Faculteit Wetenschappen

Departement Fysica

Characterization of defects, modulations and surface layers in topological insulators and structurally related compounds

Karakterisatie van defecten, modulaties en oppervlakte lagen van topologische isolatoren en structureel gerelateerde materialen

Proefschrift voorgelegd tot het behalen van de graad van

Doctor in de Wetenschappen

aan de Universiteit Antwerpen, te verdedigen door

Carolien Callaert

Promotor:

Prof. Dr. J. Hadermann

Copromotor:

Prof. Dr. D. Lamoen

Antwerpen

2020

Members of the Jury

Chairman

Prof. Dr. Bart Partoens, University of Antwerp, Belgium

(Co-)Promotors

Prof. Dr. Joke Hadermann, University of Antwerp, Belgium

Prof. Dr. Dirk Lamoen, University of Antwerp, Belgium

Members

Prof. Dr. Wim Wenseleers, University of Antwerp, Belgium

Prof. Dr. Lada Yashina, Moscow State University, Russia

Prof. Dr. Simon Clarke, University of Oxford, England

Contact information

Electron Microscopy for Materials Science
University of Antwerp

Carolien Callaert

EMAT - Electron Microscopy for Materials Science

University of Antwerp - Department of Physics

Groenenborgerlaan 171, B-2020 Antwerpen

Belgium

carolien.callaert@uantwerpen.be

Table of Contents

List of abbreviations v
Preface vii
Chapter 1 Introduction 1
1.1 Topological insulators 1
1.1.1 Characteristics 1
1.1.2 Structures 3
1.1.3 Thermoelectric properties 6
1.2 Defects, modulations and surface layers 8
1.2.1 Defects 8
1.2.2 Modulations 10
1.2.3 Surface layers 10
Chapter 2 Applied techniques 11
2.1 Experimental techniques 11
2.1.1 Transmission electron microscopy 11
2.1.2 Electron-matter interaction 12
2.1.3 Reciprocal space 13
2.1.4 Bragg equation 14
2.1.5 (3+d) reciprocal space 16
2.1.6 SAED 19
2.1.7 EDT 19
2.1.8 BF TEM and DF TEM 21
2.1.9 STEM 22
2.1.10 STEM-EDX 23
2.1.11 PXRD 24
2.2 Theoretical techniques 25
2.2.1 Schrödinger equation 25
2.2.2 Born-Oppenheimer approximation 26
2.2.3 Density functional theory 27
2.2.4 Exhange-correlation functionals 30
2.2.5 Relativistic effects 30
2.2.6 Practical implementation 32

2.2.7 Hellmann-Feynman theorem 36
2.2.8 Nudged elastic band calculations 36
2.3 Synthesis 39
2.4 TEM sample preparation 40
2.5 Software, microscopes and equipment 43
Chapter 3 Bulk structures 45
3.1 Bi_2Se_3 45
3.1.1 Introduction 45
3.1.2 Methodology 48
3.1.3 Results 51
3.1.4 Discussion 70
3.1.5 Conclusion 74
3.2 $(In_xBi_{1-x})_2Se_3$ and $Sb_2(Se_xTe_{1-x})_3$ 74
3.2.1 Introduction 74
3.2.2 $(In_xBi_{1-x})_2Se_3$ 77
3.2.3 $Sb_2(Se_xTe_{1-x})_3$ 82
3.2.4 Conclusion 88
3.3 $Ge_mBi_{2n}Te_{(m+3n)}$ 89
3.3.1 Introduction 89
3.3.2 Results 91
3.3.3 Conclusion 104
Chapter 4 Study of the surface 107
4.1 Oxidation 107
4.1.1 Introduction 107
4.1.2 Bi_2Te_3 and Sb_2Te_3 110
4.1.3 $(Sb_{0.55}Bi_{0.45})_2Te_3$ 119
4.1.4 $Ge_mBi_{2n}Te_{(m+3n)}$ 123
4.1.5 Conclusion 127
4.2 Fe deposition 128
4.2.1 Fe/Bi_2Te_3 128
Chapter 5 Structurally related materials 135
5.1 GeTe 135

5.1.1 Introduction 135
5.1.2 Results 138
5.1.3 Conclusion 144
5.2 Fe_2Ge_3 144
5.2.1 Introduction 144
5.2.2 Results 146
5.2.3 Conclusion 151
Chapter 6 General Conclusions 153
Algemene conclusies 157
References 161
Scientific contributions 177
Acknowledgement 179

List of abbreviations

ABF	annular bright field
AE	all-electron
BF	bright-field
BZ	Brillouin zone
CTR	chemical transport reaction
DF	dark-field
DFT	density functional theory
EDT	electron diffraction tomography
EDX	energy dispersive X-ray
FIB	focussed ion beam
GGA	generalized-gradient approximation
HAADF	high-angle annular dark-field
LDA	local density approximation
MEP	minimum energy path
NCL	Nowotny chimney ladder phases
NEB	nudged elastic band
PAW	Projector-Augmented Wave
PBE	Perdew-Burke-Ernzerhof
PXRD	powder X-ray diffraction
QL	quintuple layer
SAED	selected area electron diffraction
SCXRD	single crystal X-ray diffraction
SEM	scanning electron microscopy
SOC	spin-orbit coupling

SOT	spin-orbit torque
STEM	scanning transmission electron microscopy
STM	scanning tunnelling microscopy
TEM	transmission electron microscopy
VASP	Vienna Ab initio Simulation Package
VdW	van der Waals
XRF	X-ray fluorescence
XP	X-ray photoelectron
XPS	X-ray photoelectron spectroscopy

Preface

Topological insulators are a new class of fascinating materials that are only recently discovered. Ideally they are bulk insulating and surface conducting. They are intensely studied due to their special physics and possible future applications, such as in spintronics. Furthermore, certain characteristics of the studied materials that made them topological insulators also cause them to be thermoelectric materials. However, defect engineering is necessary in order to obtain the ideal properties which depend on the application.

In this thesis, defects, modulations and surface layers of topological insulators and structurally related materials are studied, mostly with transmission electron microscopy (TEM), supported in some cases with *ab initio* calculations. The structurally related materials investigated in this thesis are all still thermoelectric materials. In these materials a temperature gradient can cause an electric potential, so they can convert (waste) heat to electricity. Next to the bulk structures, the surface layers due to oxidation or due to the presence of an additional magnetic material are examined as well. How materials react upon oxidation or on interfacing them with a magnetic material is crucial for practical applications, especially when keeping in mind that for certain applications the surface properties are of interest.

The thesis itself is divided into six chapters.

Chapter 1 explains in more details the different elements contained in the title of this thesis.

Chapter 2 provides an introduction on the used experimental and theoretical techniques, followed by a short description of the synthesis of the materials made by the group of Lada Yashina, Andrei Shevelkov and Artem Abakumov. Finally, the chapter is ended with an explanation of the most commonly used TEM sample preparation techniques used in this thesis and an overview of the software, microscopes and equipment that I used to acquire the data.

Chapter 3 determines the bulk structure of topological insulators. First, the defect structure of the standard Bi_2Se_3 sample, containing a quintuple layered structure bonded with weak van der Waals interactions, is unravelled and atomic mobility around and across the van der Waals gap is detected. Second, the topological insulator-normal insulator structures $(Bi_{1-x}In_x)_2Se_3$ and $Sb_2(Te_{1-x}Se_x)_3$ are confirmed to be respectively cation and anion substituted with the same quintuple layered structure as Bi_2Se_3. However, new structural characteristics were found: interstitial defects and atomic mobility along and across the van der Waals gap in $(Bi_{1-x}In_x)_2Se_3$ and a different layered composition for $Sb_2(Te_{1-x}Se_x)_3$ where Se already occupies the outer Te layers of the quintuple layer before the middle layer is completely filled. Third, the structures of the $Ge_mBi_{2n}Te_{(m+3n)}$ series are solved, divided into the trigonal layered structure with l-layered (l=7,9,11,5-7) building blocks instead of the five-layered building blocks for Bi_2Se_3 and rock salt structures with planar defects.

Chapter 4 reveals the structure and chemical composition of the oxidized layers and sublayers of Bi_2Te_3, Sb_2Te_3, $(Sb_{0.55}Bi_{0.45})_2Te_3$ and $Ge_mBi_{2n}Te_{(m+3n)}$ and an oxidation mechanism is proposed. Also the structure and chemical composition of the interface between the (approximately) 20 nm thick Fe layer and Bi_2Te_3 is shown, unfolding the intermediate 3.5 nm amorphous FeTe interface layer, where excessive Bi migrates to the shallow bulk forming septuple layers of Bi_3Te_4.

Chapter 5 solves the bulk structures of two structurally related materials, α-GeTe and Fe_2Ge_3. For α-GeTe the planar defect structure is characterized while for Fe_2Ge_3 the space group with cell parameters of the commensurate and incommensurate structures was untangled.

Chapter 6 summarizes the general conclusions of this thesis.

Chapter 1 Introduction

In this chapter I will explain the different terms inside the title of my thesis 'Characterization of defects, modulations and surface layers in topological insulators and structurally related compounds'. In the first section I will explain what topological insulators are, how the structurally related compounds are connected to topological insulators and make a link between topological insulators and thermoelectric materials. In the second section I will discuss what defects, modulations and surface layers are.

1.1 Topological insulators

1.1.1 Characteristics

Until a few decades ago, materials could be divided into "electronic phases" of matter: an insulator, a conductor, a semiconductor, a magnet and more exotic phases like the superconductor[1]. However, a few decades ago, a new class of materials was discovered. In 1982, Thouless *et al.*[2] explained the *quantum hall effect*. The *quantum hall effect* occurs when placing a 2D material in a high magnetic field at low temperature, creating a current along the edge of the material in one direction. Later[3,4], the *quantum spin hall effect* was predicted in 2D materials, where a spin polarized surface current exists without an applied magnetic field, but due to spin-orbit coupling, a relativistic effect that couples the spin and orbital angular momentum of electrons[5]. This is followed by the generalization of the 2D quantum spin hall effect to three dimensions[6]. Finally, Hsieh *et al.*[7] confirmed experimentally the first 3D topological insulator, Bi_xSb_{1-x}. Topological insulators are bulk insulators but surface conductors. This surface conductivity is spin polarized with a 90° spin-momentum locking where the spin lies inside the surface plane and is robust against non-magnetic impurities.

In topological insulators, the spin-orbit coupling takes on the role of the magnetic field in the quantum hall effect. This makes it an important and crucial factor. Spin-orbit coupling is weak for light elements, but strong for heavy elements[5]. So, the chemical nature of the structure is important. But what does this interaction do? The spin-orbit coupling causes band-inversion, which can be observed with density functional theory (DFT). However, band-inversion on its own does not prove the topological insulator nature of the material[8].

To explain band inversion, you need to know that crystalline materials have a band structure. You have the conduction band (lowest non-filled band) and the valence band (highest filled band) and for semiconductors and insulators there exists an energy gap between them. These bands have a certain ordering. They are for example filled with s-electrons (s-like band) or p-electrons (p-like band). The strong spin-orbit coupling causes a band inversion, so the normally s-like conduction band (p-like valence band) becomes p-like (s-like) around the bandgap of the material[8,9]. In topological insulators, surface states connect the conduction and valence band (see Figure 1.1).

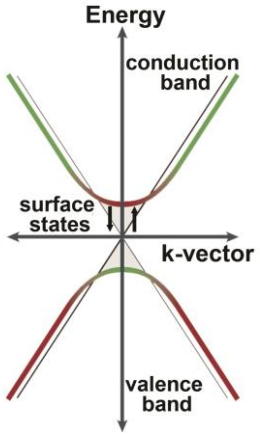

Figure 1.1 Schematics for the inverted band extrema of a topological insulator showing the conduction band, valence band and surface states. The maximum of the valence bands takes on the orbital character of the conduction band and the minimum of the conduction bands that of the valence band. The figure is adapted from Heremans *et al.*[10].

The fact that surface conductivity is robust against non-magnetic impurities is an interesting property for applications. This means that the electrons are protected from backscattering, which is a heat producer in electronics. When the electron encounters a non-magnetic impurity, the electron needs to go around the defect while moving forward with the same spin direction (Figure 1.2a) or it needs to change its spin direction to go in the opposite direction (Figure 1.2b,c). The latter two paths cancel each other due to destructive interference. In more details, the electron can go clockwise (Figure 1.2b) or counterclockwise (Figure 1.2c) around the defect, rotating the spin by π or – π. This leads to a rotation difference of the electron spin of 2π between the two backscattered paths, which are time-reversal symmetric. A 2π spin rotation difference leads to a -1 factor between the two wave functions of the electron (spin 1/2), leading to destructive interference of the two backscattered paths. However a magnetic impurity breaks time-reversal symmetry, so that the two paths do not interfere destructively anymore. Time reversal symmetry thus protects the robustness of the surface states[9].

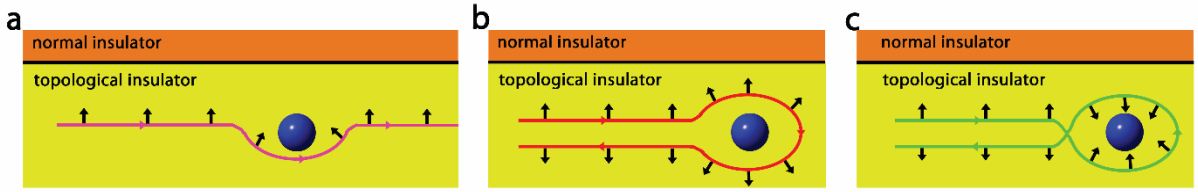

Figure 1.2 A forward moving path of an electron after encountering a non-magnetic impurity (blue atom) (a) and the backscattered paths where the spin rotes clockwise (rotation of π) (b) and counterclockwise (rotation of –π) (c). The electron spin difference between the two backscattered paths is 2π, leading to destructive interference in the case of a non-magnetic impurity. The figure is adapted from Qi *et al.*[9].

In this thesis, we will study most of the time the bulk material, because the bulk determines the surface states, more than the shape of the surface. The reason for this is captured in the name, 'topological insulator'. Topology is a branch of mathematics where quantities that do not change under continuous deformation are studied. A classic example is the donut and

the coffee cup, where the invariant quantity is the 'genus' of the surface, which is one in both cases because both contain only one 'hole'. You can change the form of a donut to a coffee cup by just bending, enlarging and shrinking, namely by continuous change. In the case of topological materials, you need to look at the electron's wave function in momentum space. This wave function is 'knotted' for a topological insulator and topological invariants are related to this knotting (usually expressed as integrals involving the wave function). Let's consider the example where the wave function of a topological insulator looks like a 'trefoil knot' and vacuum looks like a closed loop (Figure 1.3). We cannot go from the 'trefoil knot' to the closed loop by a continuous deformation. We need to cut the trefoil knot at the interface or in other words, the topological invariants need to change. Similarly, both the bulk material and vacuum are insulators, but the surface of the topological insulator cannot remain insulating by contradiction due to the changing invariants, like the cutting of the trefoil knot. This is why the surface states are so robust[1,11].

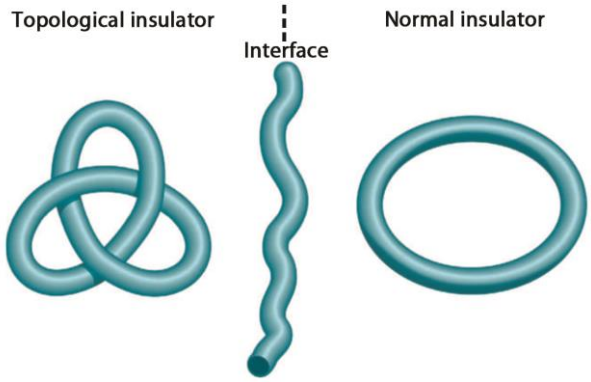

Figure 1.3 Left: 'Knotted' wave function of a topological insulator. Right: Looped wave function of an ordinary insulator like vacuum. To go from the left wave function to the right wave function is impossible by using only a continuous deformation. The string needs to be cut at the surface (middle). The image is taken from Moore *et al.*[11].

1.1.2 Structures

Topological insulators can take on a wide range of different structures. SOC driven band inversion should occur as key ingredient to obtain topological insulators. So, traditionally, one looks for topological insulator properties in semiconductors or insulators containing heavy elements. Band gap tuning is possible through *e.g*. alloying or strain, making even semimetals potential candidates. Therefore, for nonmagnetic compounds, one searches typically for compounds with an even number of electrons per unit cell. Large gap ionic compounds are avoided since their conduction and the valence bands are formed from atomic orbitals. On the other hand, intermetallics and covalent bonded materials are more suitable. To satisfy both requirements of a strong SOC and a weak ionic value, we look for compounds including Sn, Bi or Sb. One class of topological insulators consists of Bi or Sb which have a layered structure with spacegroup $R\bar{3}m$ (or similar). Another group contains Sn, where the compounds can take on the zinc-blende-type structure which is connected to α-Sn, which has a diamond structure. More information can be found in the paper of Bansil *et al*.[8].

In this section I will discuss briefly the structure of the investigated topological insulators and thermoelectric materials. All discussed structures can be divided into four different category-types: (i) Bi_xSb_{1-x}, (ii) Bi_2Se_3, Bi_2Te_3 and Sb_2Te_3, (iii) $Ge_mBi_{2n}Te_{(m+3n)}$, and (iv) Ru_2Sn_3. The first three categories belong to the Bi/Sb group, while Ru_2Sn_3 is a variant of the Sn class. They are displayed in Figure 1.4 and Figure 1.5. Note that structures with the space group $R\bar{3}m$ or R3m, which belong to the trigonal crystal system, can be displayed in a rhombohedral and hexagonal unit cell. In this thesis, we will always use the hexagonal unit cell, unless specified otherwise.

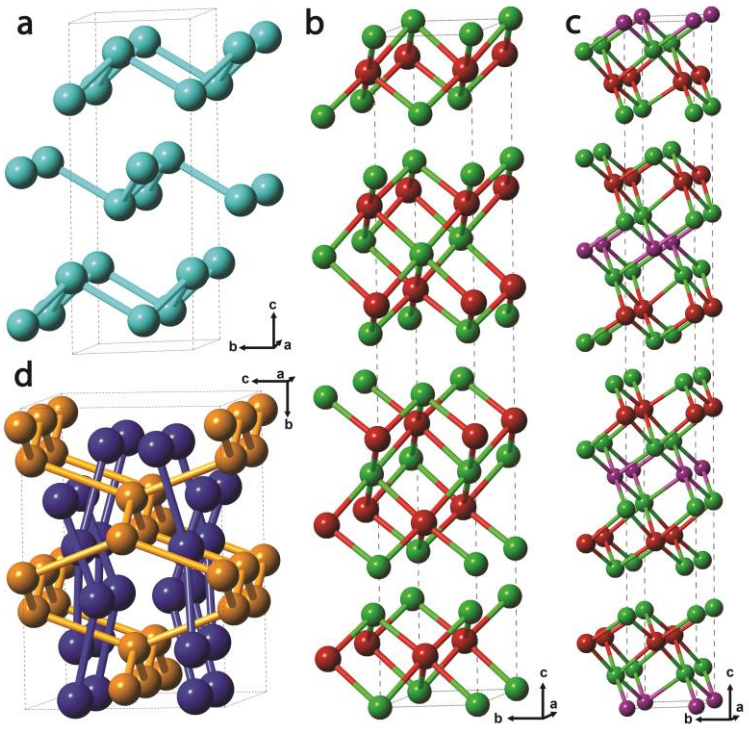

Figure 1.4 Structures of four groups of topological materials: (a) $Bi_{0.9}Sb_{0.1}$[12] (b) Bi_2Te_3[13] (c) $GeBi_2Te_4$[14] (d) Ru_2Sn_3[15] in its low temperature orthorhombic phase. Mixed Sb/Bi is displayed in light blue, Te in dark green, Bi in red, Ge in purple, Ru in orange and Sn in dark blue.

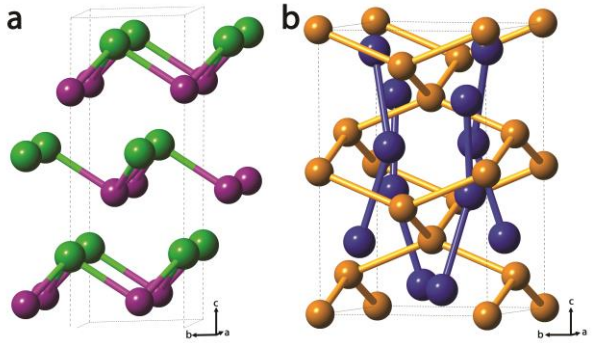

Figure 1.5 Structures related to one of the four discussed groups of topological materials (Figure 1.4). Chemical composition can be different. (a) α-GeTe[16] (b) Ru_2Sn_3[15] in its tetragonal form or Fe_2Ge_3[17] but with different cell parameters. Ge is displayed in purple, Te in green, Ru in orange and Sn in blue.

1.1.2.1 $Bi_{1-x}Sb_x$

$Bi_{0.9}Sb_{0.1}$ (Figure 1.4a) was the first 3D topological insulator that was experimentally discovered with incident-photon-energy-modulated angle-resolved photoemission spectroscopy (IPEM-ARPES) and has complex surface states[7]. The structure consists of mixed double layers, where Bi and Sb are intermixed in a 0.9:0.1 ratio[12]. Its space group is $R\bar{3}m$, with cell parameters a=b=4.539 Å and c=11.8465 Å[12].

The structure of the studied α-GeTe[18] (Figure 1.5a), which is a good thermoelectric material but not a topological insulator, is related to the structure of $Bi_{0.9}Sb_{0.1}$. In this material the columns are not intermixed, but Ge and Te rows alternate along the c-direction in the hexagonal setting. This change happens due to symmetry lowering to the substructure R3m, removing the inversion symmetry in the origin and the two fold rotation axis along [110], [010] and [100][19]. R3m is a *translationengleiche* subgroup, or in other words the translations are unchanged[19].

1.1.2.2 Bi_2Se_3, Bi_2Te_3 and Sb_2Te_3

Bi_2Se_3[20], Bi_2Te_3[13,21] and Sb_2Te_3[21,22] are second generation topological insulators[8]. They are tetradymites or crystalline M_2X_3 compounds with M a group Va metal (*e.g.* Bi and Sb) and X a group VIa anion (*e.g.* Te and Se) layered in a rhombohedral structure (Figure 1.4b). All three materials consist of five-layered building blocks -called quintuple layers (QLs)- strongly bound to each other, with a chemical sequence 'Se/Te - Bi/Sb - Se/Te - Bi/Sb - Se/Te'. In between these layers a weak van der Waals interaction exists. The materials gained a lot of interest due to their simple surface states, namely a single Dirac cone[23–27] (see Figure 1.6).

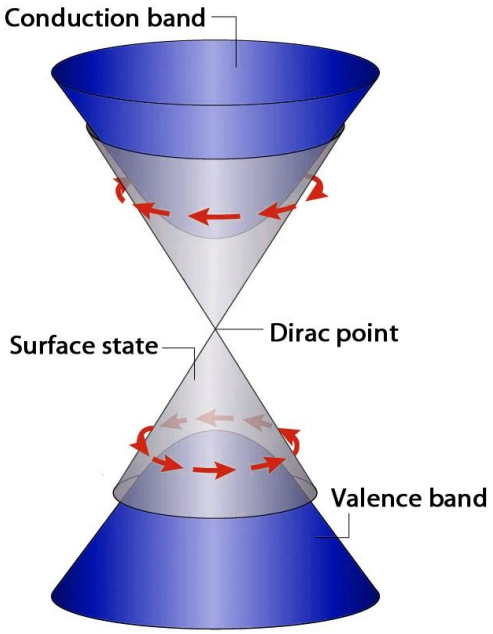

Figure 1.6 Visualisation of the surface states which consists of a Dirac cone (light blue) with the Dirac point. The conduction and valence bands are displayed in dark blue and the helical spin texture in red. This is based on a figure of Tokura *et al.*[28].

1.1.2.3 $Ge_mBi_{2n}Te_{(m+3n)}$

The $Ge_mBi_{2n}Te_{(m+3n)}$ series are part of the tetradymitelike layered topological insulators.[8] This group of materials consists also of stacked building blocks similar to Bi_2Te_3, however more variations in the size of the 'building blocks' are allowed (Figure 1.4c). For example, for n=1 and m=0, we have the Bi_2Te_3 structure with five-layered building blocks. For n=1 and m=1, we have $GeBi_2Te_4$, with an insertion of GeTe into the Bi_2Te_3 block, leading to a seven-layered building block. Adjusting the stacking and composition is a promising way to tune the electronic and spin properties[8,29]. Note that in section 3.3 we will discuss that $Ge_mBi_{2n}Te_{(m+3n)}$ series can also take on a defect-rich rock salt structure.

1.1.2.4 Ru_2Sn_3

Ru_2Sn_3 is an intermetallic compound. It belongs, more specifically, to the class of Nowotny chimney ladder phases (NCLs)[30], with the general formula T_tE_m, where T is a transition metal generally of group IVb-VIII and E is a main group IIIa-Va element[31,32]. In the crystal structure, the squared T sublattice forms 4-fold helical channels arranged in a flattened diamond network of the β-Sn-type structure, while the E atoms form helices inside the T helical channels, creating a helix-within-a-helix motif (Figure 1.5b).

Ru_2Sn_3 goes from a tetragonal non-centrosymmetric phase at high temperature to an orthorhombic centrosymmetric phase at low temperature, with a reversible phase transition[15]. To go to the orthorhombic structure (Figure 1.4d), we have a loss of translation (one of the cell parameters doubles) and symmetry elements. Ru_2Sn_3 in its low temperature orthorhombic phase is a strong topological insulator with d-p band inversion and highly anisotropic surface states[33].

The studied Fe_2Ge_3[17] has a similar structure to Ru_2Sn_3 in its tetragonal phase (Figure 1.5b) and also belongs to the class of NCLs. It is a prospective thermoelectric[17], but is not a topological insulator.

1.1.3 Thermoelectric properties

Another common factor of all the examined materials is that they all have been studied for their thermoelectric properties, which I will further discuss in Chapter 3 to 5. Many topological insulators were already studied for their thermoelectric properties before they had been identified as topological insulators[34,35]. The reason for this is that some material features that make it a topological insulator, also cause it to be a good thermoelectric material[10,36].

The figure-of-merit ZT indicates the thermoelectric performance of a material or how well a temperature gradient causes an electric potential, so that (waste) heat can be converted to electricity:

$$ZT = \frac{S^2\sigma}{\kappa}T \qquad 1.1$$

with S the Seebeck coefficient or thermopower, σ the electrical conductivity, T the temperature and κ the thermal conductivity. Both phonons and electrons contribute to the thermal conductivity, so the thermal conductivity is the sum of the electrical thermal conductivity and the lattice thermal conductivity: $\kappa = \kappa_{lat} + \kappa_{el}$. The Seebeck coefficient is an intrinsic material property and is related to the ratio of the voltage difference to the temperature difference that causes this voltage difference[37]. Doping is applied to maximize the density of states at the Fermi level to obtain high Seebeck coefficients[38]. The goal for finding good thermoelectric materials is to maximize the figure-of-merit to obtain a better energy conversion.

We can try to increase the figure-of-merit by increasing the electrical conductivity whilst simultaneously decreasing the thermal conductivity. A way to obtain this in materials is to look for a material with a narrow bandgap to achieve higher electrical conductivity and heavy atoms to increase the phonon scattering in order to decrease the thermal conductivity[36]. Topological insulators of the tetradymite or tetradymitelike layered family which we studied contain heavy elements. The heavy elements cause a high spin-orbit coupling in order to achieve a band inversion between the conduction and valence band with a narrow bulk bandgap. So, these topological insulators have a narrow bandgap and contain heavy elements, ideal for good thermoelectric properties[36]. Furthermore, when the SOC coupling is even higher, instead of the inverted band extrema as for Bi_2Se_3 we get inverted bands as for Bi_2Te_3 which result in good Seebeck coefficients and electrical conductivity[10] (Figure 1.7). Bi_2Te_3 is commonly used in commercial thermoelectric applications. Heremans *et al.*[10] specified in more details why tetradymites have a low lattice thermal conductivity and give three reasons for it. First, the atoms (Bi, Sb, Te, Se) are really heavy with weak bonds leading to low sound velocities. Second, the large unit cells in real space result in small unit cells in reciprocal space and low phonon cut-off wave vectors. Third, the bonds are anharmonic and this determines the phonon scattering probability of phonon-phonon interactions. This helps to lower the phonon lifetime when temperature increases. However, not all good thermoelectric materials are topological insulators like GeTe[39].

Furthermore, like defect engineering happens in topological insulators to achieve ideal properties, the same applies to gain better thermoelectric properties, indicating how important defect engineering is[40].

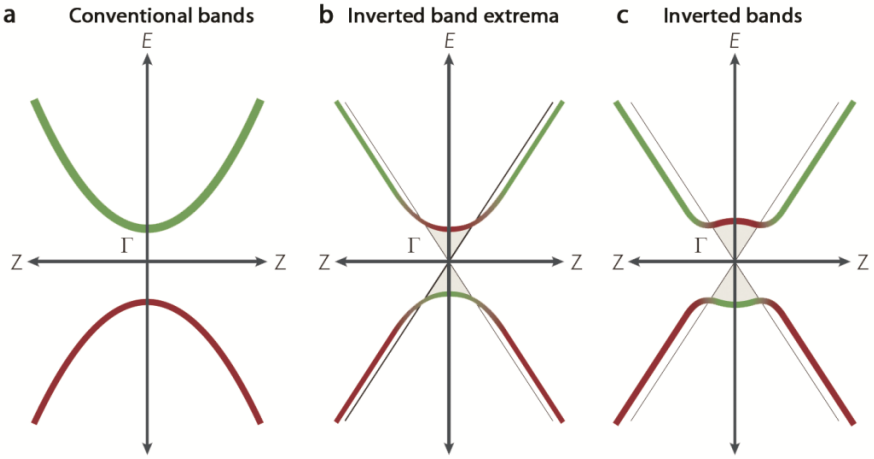

Figure 1.7 Schematics for the conventional bands of a normal insulator (a) the inverted band extrema as for Bi_2Se_3 (b) and the inverted bands as for Bi_2Te_3 (c). Near the Γ point in reciprocal space the band character is inverted for the model in (a) and (b). The conduction band takes on the orbital character of the valence band and *vice versa*. The figure is taken from Heremans *et al.*[10].

1.2 Defects, modulations and surface layers

Crystalline materials consist of atoms that are periodically ordered, so a certain unit is 'infinitely' (real crystals have a finite size) repeated in all directions. In this thesis we will study the edges of some finite crystals and periodic and non-periodic changes to the ordered structure, hence the terms used in the title of this thesis: 'surface layers', 'modulations' and 'defects'.

But why are we so interesting in this? Especially the term 'defect' has a more negative connotation. However in materials science lots of times defects, modulations and interfaces between different mediums are used to fine tune the physical properties of materials in order to have the perfect characteristics for applications[41]. Defects, modulations and interfaces will influence material properties and their understanding and control is a powerful tool for future devices[41].

1.2.1 Defects

Defects are non-periodic changes or discontinuities in the crystalline lattice structure and can be classified according to their dimensionality: zero, one, two and three dimensional.

Zero dimensional defects are point defects. Point defects are one atom defects, which you can categorize as a vacancy, an interstitial defect or a substitutional defect (Figure 1.8). A vacancy is when one atom is missing from a lattice site. When one atom is added on a non-lattice site in between the periodically ordered atoms, it's called an interstitial defect. A substitutional defect is when one atom is exchanged with another atom which normally does not occupy that site.

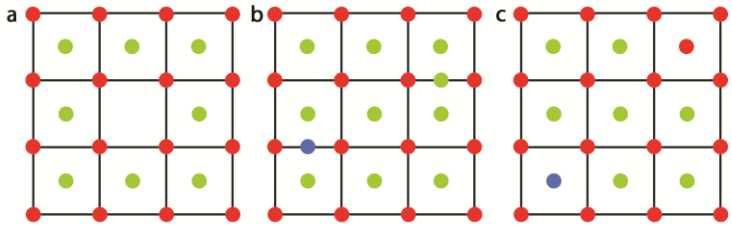

Figure 1.8 Point defects: (a) vacancy (b) interstitial defect caused by a foreign atom (blue) and a regular atom (green) (c) substitution defect caused by a foreign atom (blue) and a regular atom (red).

One dimensional defects are line discontinuities in the repeated structure. Two basic examples are edge dislocations and screw dislocations (Figure 1.9). An edge dislocation is when a half-plane of atoms is added or removed from the perfect crystal. For screw dislocations the atom planes are connected, forming a single surface with a helical form. The Burgers vector indicates the magnitude and the direction of the distortion. For edge dislocations the Burgers vector and the dislocation line are perpendicular to each other, while for the screw dislocation they are parallel.

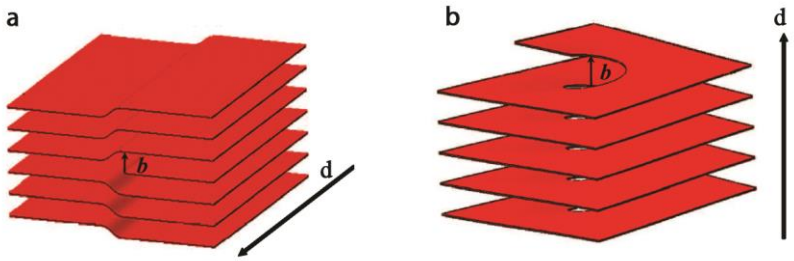

Figure 1.9 Line defects: (a) edge dislocation (b) screw dislocation where the vector **b** denotes the Burgers vector and vector **d** the direction of the dislocation line. This drawing is taken from Repula *et al.*[42].

Two dimensional defects are planar defects where a discontinuity happens across a plane. Two examples are grain boundaries and twin boundaries (Figure 1.10). A material can consist of areas with different orientations, which are called grains. The atoms in the regions between the grains deviate from the perfect structure and these regions are called grain boundaries. A twin boundary is when two domains separated by a plane are each other's mirror image.

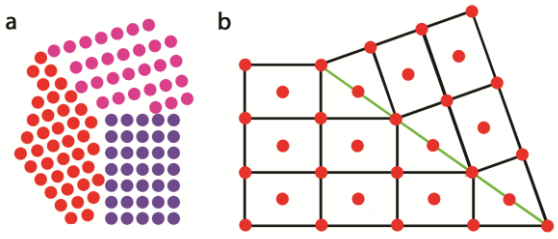

Figure 1.10 Planar defects: (a) Grain boundary (b) Twin boundary.

A special case of twinning, which will be discussed in this thesis, is deformation twinning. Usually, when an external force causes stress to be applied on the material, dislocations start

to move throughout the material to accommodate this stress. These 1D dislocations can turn into newly-formed twins which are referred to as 2D deformation twins. In case a step occurs on their twin boundary, this 'jump' is called a twinning dislocation, which is a 1D defect.

Three dimensional defects are three dimensional inclusions in the crystalline structure, called precipitates or the removal of a 3D volume, called voids.

1.2.2 Modulations

When a basic structure undergoes periodic changes or in other words a modulation by a variation of the atomic sites (positions and occupancy), we obtain a commensurately or incommensurately modulated structure. If the modulation periodicity is an integer number of the underlying basic structure period, the structure is commensurately modulated and periodic in three dimensions (3D). For an irrational amount, it is incommensurately modulated and 3D aperiodic but periodic in (3+d) dimensions, where d is the number of modulation vectors. Although incommensurately modulated crystals are 3D aperiodic, they are crystalline according to the International Union of Crystallographers definition of a crystal as 'any solid having an essentially discrete diffraction diagram'[43,44]. Commensurately modulated structures can be determined in 3D and (3+d) dimensions, however the structure of incommensurately modulated materials needs to be determined in a (3+d) dimensional space and then be reinterpreted in three dimensions. A short introduction about the (3+d) reciprocal space and its relation to a 3D model will be explained in section 2.1.5.

1.2.3 Surface layers

As mentioned before, crystals have a finite size, so an interesting question is what exactly happens with the structure at the interface with oxygen or at the interface with another material? Does the structure remain the same? Do we get a mixture of the two media at the interface? For several examples (see chapter 4) some of these questions will be discussed in more detail.

Chapter 2 Applied techniques

In this chapter, I will explain the experimental and theoretical techniques I used to examine the materials, followed by a summary of the software, microscopes and equipment I used. Finally, I will discuss the bulk sample synthesis used by the group of Lada Yashina, the group of Andrei Shevelkov and Artem Abakumov and the standardly used sample preparation methods I performed on the synthesized materials: focussed ion beam milling and crushing.

2.1 Experimental techniques

2.1.1 Transmission electron microscopy

Most techniques in this thesis are performed using a transmission electron microscope: selected area electron diffraction (SAED), electron diffraction tomography (EDT), scanning transmission electron microscopy (STEM) imaging, dark-field and bright-field transmission electron microscopy (DF and BF TEM) imaging and energy dispersive X-ray (EDX) spectroscopy.

A transmission electron microscope consists of an electron gun, electron magnetic lenses, deflection coils and stigmators and is kept under high vacuum (~10^{-5} Pa) to allow the electrons the move throughout the microscope without being scattered by air molecules.

The electron beam is first generated in the electron gun, where electrons can escape the cathode material with a velocity determined by the accelerator located underneath. Next, a series of condenser lenses consisting of two to three lenses direct the beam onto the sample. This is the illumination system. For imaging, with the condenser lenses the sample can be illuminated with a parallel beam called TEM imaging (for example for SAED) and with a scanning focussed beam which is called STEM imaging (for example for STEM-EDX). The first condenser lens determines the spot size or in other words the demagnification of the electron source onto the sample. The second and third condenser lenses (if available) focus or defocus the beam onto the sample and determine the convergence angle of the beam. A strong objective lens is placed around the sample to focus the image. It's both part of the illumination system and imaging system. Afterwards, the electron beam is projected at a chosen magnification and in a selected mode (diffraction or image mode) by the imaging system on a selected viewing system *e.g.* a CCD or a high-angle annular dark-field detector. The chosen detector depends on the selected method. With the diffraction lens you can choose image mode or diffraction mode, while with a three lens system (intermediate lens and two projector lenses) the right magnification is selected. A simplified version of how the electrons pass through all the lens systems is displayed in Figure 2.1. For example, only a two lens system instead of the four lens system for the imaging system is visualized. Every extra lens (the diffraction lens and second projector lens) is added to increase the flexibility of the system. Note that also two apertures are drawn on this figure in order to select a certain part of the electron beam.

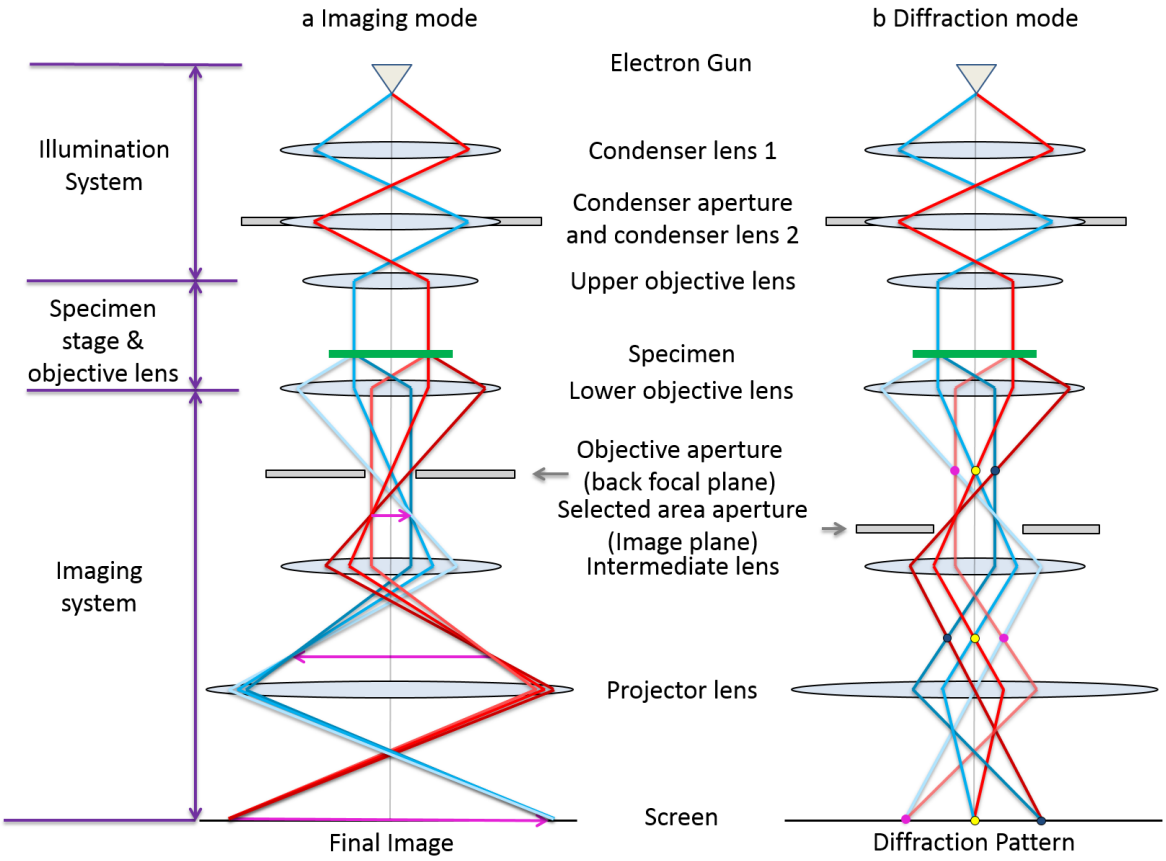

Figure 2.1 Simplified model to visualize how the electrons pass through the column in image mode (a) en diffraction mode (b), where the sample is illuminated with a parallel beam.

Due to the use of electrons electromagnetic lenses are utilized instead of the glass lenses for light. Electromagnetic lenses are even less perfect than glass lenses and due to different kinds of aberrations not all rays are focussed in the same spot. The stigmators and probe correctors, the last only exist on aberration corrected microscopes, are used to reduce these aberrations, which enables obtaining a resolution of 0.8 Å.

Different kinds of deflection coils are used to shift or tilt the beam, for example, to scan over a certain area in STEM mode or to guide the beam in a correct way through the column of the microscope.

2.1.2 Electron-matter interaction

In a transmission electron microscope an electron beam will be directed to a thin TEM sample, interact and pass through it. We can characterize two types of interactions: *elastic* and *inelastic* interactions. When no interactions happen, the electron goes through the material and these electrons form the direct beam.

Elastic scattering is an electron-nucleus interaction, inducing the incoming electrons to electrostatically deflect by the Coulomb field of the nucleus. In this case, the electron loses a

negligible amount of energy. Even backscattering can happen when the electron-nucleus interaction is strong enough.

Inelastic scattering is an electron-electron interaction, where the incoming electrons transfer energy to the material due to the Coulomb interaction between the incoming electrons and the electrons of the examined material, which result in different induced reactions: X-rays, Auger electrons, secondary electrons, electron-hole pairs, 'absorbed electrons' and light. A secondary electron is created when the incident electron provides enough energy to remove an electron from the outer atomic shell (excitation) or inner atomic shell (ionization). The atom is then in an excited and less stable state. When an electron from a higher atomic shell falls back to this empty lower shell to regain a more stable state, the energy differences between these shells will be sent out in the form of an X-ray. Or the energy difference can be given to another electron of that atom, which gains enough energy to be ejected from the atom in the form of an Auger electron. For direct-gap semiconductors, the incoming electron can excite a valence electron to the conduction band, creating an electron-hole pair. Light will be emitted when a conduction band electron falls back to fill the valence band hole. When the specimen is too thick, no electrons are transmitted through the sample, we say that the electrons are 'absorbed' by the sample.

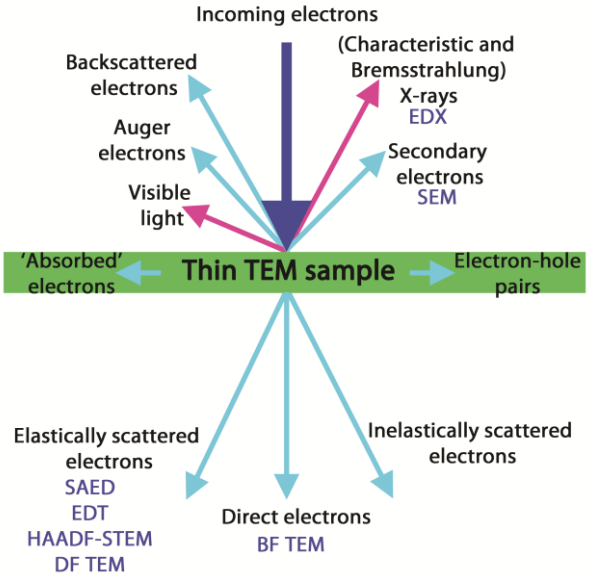

Figure 2.2 Scheme of the interactions between the incoming electron beam (dark blue) with the sample (green), where the resulting electron signals (light blue) and non-electron signals (pink) used for the techniques in this thesis written in dark blue are displayed.

2.1.3 Reciprocal space

A crystalline material consists of atoms that are periodically ordered. We can describe the crystalline structure with an atomic structure model in real space. This model has unit cell vectors **a**, **b** and **c** with angles α, β and γ in between these vectors and volume V. We can define a corresponding Fourier space or reciprocal space with lattice vectors **a***, **b*** and **c*** (Figure 2.3):

$$\boldsymbol{a}^* = \frac{\boldsymbol{b} \times \boldsymbol{c}}{V}, \boldsymbol{b}^* = \frac{\boldsymbol{c} \times \boldsymbol{a}}{V}, \boldsymbol{c}^* = \frac{\boldsymbol{a} \times \boldsymbol{b}}{V}. \quad 2.1$$

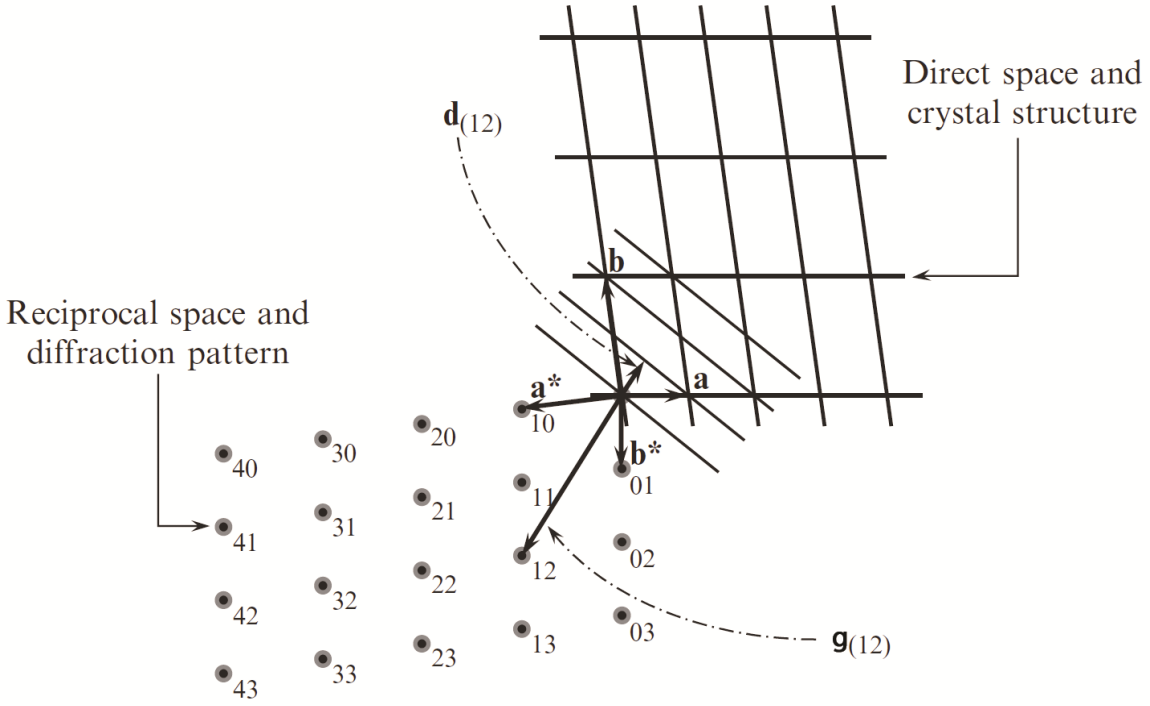

Figure 2.3 Visual 2D representation of the relationship between reciprocal and real space. This image is taken from Pecharsky *et al.*[45].

Each reciprocal lattice point hkl corresponds to a set of (hkl) planes in real space. This lattice point is characterized with a reciprocal lattice vector $\mathbf{g}_{hkl}$:

$$\boldsymbol{g}_{hkl} = h\boldsymbol{a}^* + k\boldsymbol{b}^* + l\boldsymbol{c}^* \quad 2.2$$

$\mathbf{g}_{hkl}$ is perpendicular to the (hkl) planes and its length is inversely proportional to the distance between the (hkl) planes, d_{hkl}:

$$|\boldsymbol{g}_{hkl}| = \frac{1}{d_{hkl}}. \quad 2.3$$

2.1.4 Bragg equation

Electrons can be described with plane waves with a certain wavelength λ and the atoms inside a crystal with lattice planes (hkl) with interplanar distance d_{hkl}. Diffraction can then be described as the reflection of these electron waves by the lattice planes (Figure 2.4). Two diffracted waves will only interfere constructively when both waves are in phase, or in other words when the path difference between the two paths, which is 2d sinθ (see Figure 2.4), is an integer number of the wavelength, n λ. From this, we get the Bragg equation:

$$2d \sin\theta = n\lambda. \qquad 2.4$$

From the Bragg equation in real space, we know that in a diffraction pattern bright hkl reflections appear when the electron waves reflected from the (hkl) lattices interfere constructively.

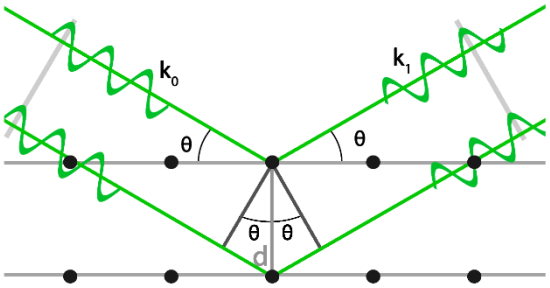

Figure 2.4 Geometric construction for the Bragg equation in real space, where $\mathbf{k_0}$ is the incoming wave and $\mathbf{k_1}$ is the diffracted wave[46]. The planes constructed from black atoms at which the electrons diffract are displayed in grey.

A plane wave can also be characterized by a wave vector **k**, where its length is equal to the inverse of its wavelength (1/ λ). A (hkl) plane can be represented by the vector $\mathbf{g_{hkl}}$. So, the geometric construction in real space for the Bragg equations (Figure 2.4) can also be depicted as in Figure 2.5a. After translating the diffracted wave vector $\mathbf{k_1}$ to the starting point of the incoming wave vector $\mathbf{k_0}$, we obtain the Bragg equation in reciprocal form (Figure 2.5b):

$$\boldsymbol{k_1} = \boldsymbol{k_0} + \boldsymbol{g}. \qquad 2.5$$

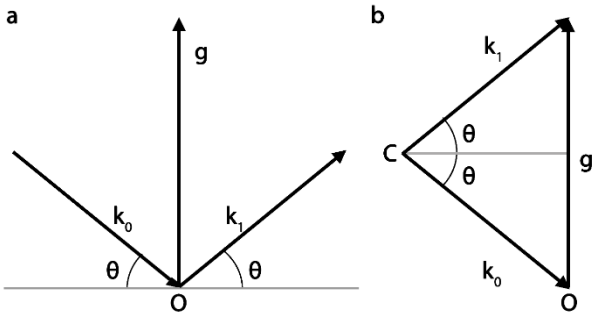

Figure 2.5 a. Geometric construction for the Bragg equation in reciprocal space, where in (b.) the diffracted wave vector $\mathbf{k_1}$ is translated to the starting point of the incoming wave vector $\mathbf{k_0}$[46]. The vector **g** represents a set of planes in real space.

Reciprocal lattice points that satisfy the Bragg condition can be visualized by reciprocal lattice points that lie on the Ewald sphere (Figure 2.6). When we have an incident beam falling in on a crystal in a certain orientation, then the end of the incoming wave vector is fixed to the origin of the reciprocal lattice. The starting point of the incoming wave vector is the centre of the sphere, called the Ewald sphere, where its length is the radius of the sphere.

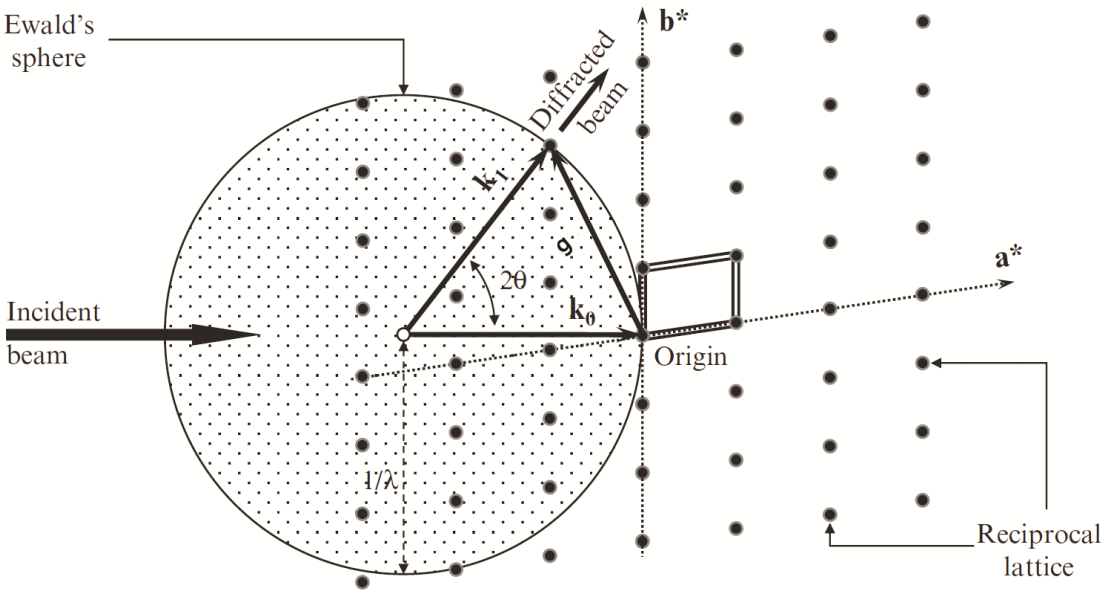

Figure 2.6 The Ewald sphere construction: reciprocal lattice points that lie on this sphere satisfy the Bragg equation. Double lines mark the unit cell in reciprocal space. This image is taken from Pecharsky *et al.*[45].

Due to the small wavelength of electrons, *e.g*. 2.51 pm at 200 keV, the Ewald sphere radius is big (~10^{12}m^{-1}), leading to an almost flat surface and enables us to view a 2D slice of reciprocal space. Moreover, more reflections than the ones perfectly satisfying the Bragg equation, are observable due to the finite size of the reciprocal lattice points caused by the finite size of the crystal. The crystal parallel to the incident beam should be very thin to allow electron transmission, causing the reflections to be elongated in this direction, forming relrods or reciprocal lattice rods.

It is possible that the electron beam diffracts multiple times inside the sample, where the corresponding probability increases with sample thickness and the atomic number of the atoms inside the material. This can lead to the visibility of certain reflections in the diffraction pattern that should normally be extinct due to glide planes and screw axes. This does not apply to extinctions caused by the centring of the unit cell. This is also called dynamical diffraction.

2.1.5 (3+d) reciprocal space

For modulated structures, the structure can be described in (3+d) dimensions. Let's assume one modulation vector, so d=1. In reciprocal space every lattice point is now characterized by the reciprocal lattice vector **H**

$$\boldsymbol{H} = h\boldsymbol{a}^* + k\boldsymbol{b}^* + l\boldsymbol{c}^* + m\boldsymbol{q} \qquad 2.6$$

with **a***, **b*** and **c*** the reciprocal basis vectors of the underlying basic structure and **q** the modulation vector described as

$$\boldsymbol{q} = \alpha\boldsymbol{a}^* + \beta\boldsymbol{b}^* + \gamma\boldsymbol{c}^* \text{ with } \alpha = \frac{a'}{a^*} < 1, \qquad \beta = \frac{b'}{b^*} < 1 \text{ and } \gamma = \frac{c'}{c^*} < 1 \tag{2.7}$$

where a' is the length of the q vector after projection onto the reciprocal **a*** basic vector (similar for b' and c'). The main reflections of the basic structure are obtained for m=0, while the satellite reflections caused by the modulation correspond to m ≠ 0 (Figure 2.7a). If at least one of the components of the q vector (α, β and γ) is irrational, then the structure is incommensurately modulated and no 3D indexing of all reflections is possible. Otherwise, it is a commensurately modulated structure where 3D indexing is achievable. In the (3+1) dimensional reciprocal space of an incommensurately modulated structure periodicity is retained. The four reciprocal basic vectors $\boldsymbol{a}_1^*$, $\boldsymbol{a}_2^*$, $\boldsymbol{a}_3^*$ and $\boldsymbol{a}_4^*$ of this (3+1) dimensional space are

$$\boldsymbol{a}_1^* = \boldsymbol{a}^* \tag{2.8}$$

$$\boldsymbol{a}_2^* = \boldsymbol{b}^* \tag{2.9}$$

$$\boldsymbol{a}_3^* = \boldsymbol{c}^* \tag{2.10}$$

$$\boldsymbol{a}_4^* = \boldsymbol{q} + \boldsymbol{e}_4, \qquad \boldsymbol{e}_4 \perp \boldsymbol{R}_3^* \tag{2.11}$$

where the unit vector $\mathbf{e}_4$ is orthogonal to the 3D reciprocal space $\boldsymbol{R}_3^*$ (reconstruction see Figure 2.7b). So, a diffraction pattern is a projection of the (3+1) dimensional reciprocal lattice onto the 3D reciprocal space $\boldsymbol{R}_3^*$ along the $\boldsymbol{e}_4$ direction.

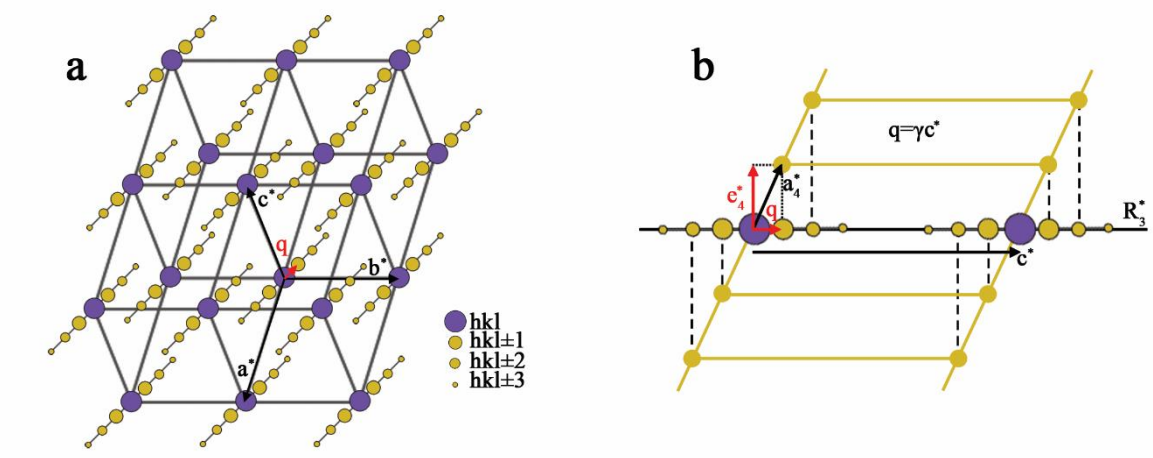

Figure 2.7 3D reciprocal space of an incommensurately modulated structure (a) with the reconstruction of its (3+1) dimensional reciprocal space (b). The 3D reciprocal space R_3^* is just represented by one line. The main reflections are indicated with purple and the satellites with yellow. This figure is based on the paper from Batuk *et al.*[47].

The structure can be periodically described in a (3+1) dimensional real space. In this space, a periodic curve defined by the modulation function $\boldsymbol{U}(\bar{\boldsymbol{x}}_4)$ describes the atomic positions. The basic vectors in this space are

$$\boldsymbol{a}_1 = \boldsymbol{a} - \alpha \boldsymbol{e}_4 \quad (2.12)$$

$$\boldsymbol{a}_2 = \boldsymbol{b} - \beta \boldsymbol{e}_4 \quad (2.13)$$

$$\boldsymbol{a}_3 = \boldsymbol{c} - \gamma \boldsymbol{e}_4 \quad (2.14)$$

$$\boldsymbol{a}_4 = \boldsymbol{e}_4, \qquad \boldsymbol{a}_i \boldsymbol{a}_j^* = \delta_{ij} \quad (2.15)$$

The intersection of the real physical space $\mathbf{R}_3$ with the (3+1) dimensional space gives the three dimensional modulated structure. In the real physical space the atomic positions are given by

$$\boldsymbol{r} = \boldsymbol{r}_0 + \boldsymbol{n} + \boldsymbol{U}(\bar{\boldsymbol{x}}_4 = \boldsymbol{q}.(\boldsymbol{r}_0 + \boldsymbol{n}) + t) \quad (2.16)$$

where $\boldsymbol{r}_0 + \boldsymbol{n}$ is the position of the atom in the unit cell of the underlying basic structure described in relation to its position in the first unit cell $\boldsymbol{r}_0$ combined with **n** translations. **U** is the modulation function and t is the initial phase of the modulation.

In Figure 2.8 an example is displayed to compare the basic structure with a commensurately and incommensurately modulated structure by shifting the coordinates of one atom type. It shows that the commensurately modulated structures can be described in (3+1) dimensions using a q vector that is 1/3 of the c* or in 3 dimensions by decreasing the unit cell by three in reciprocal space or in other words to increase the unit cell by three in real space. However, the incommensurately modulated structure can only be described in (3+1) dimensions because the modulation periodicity in an irrational amount of the underlying basic structure period.

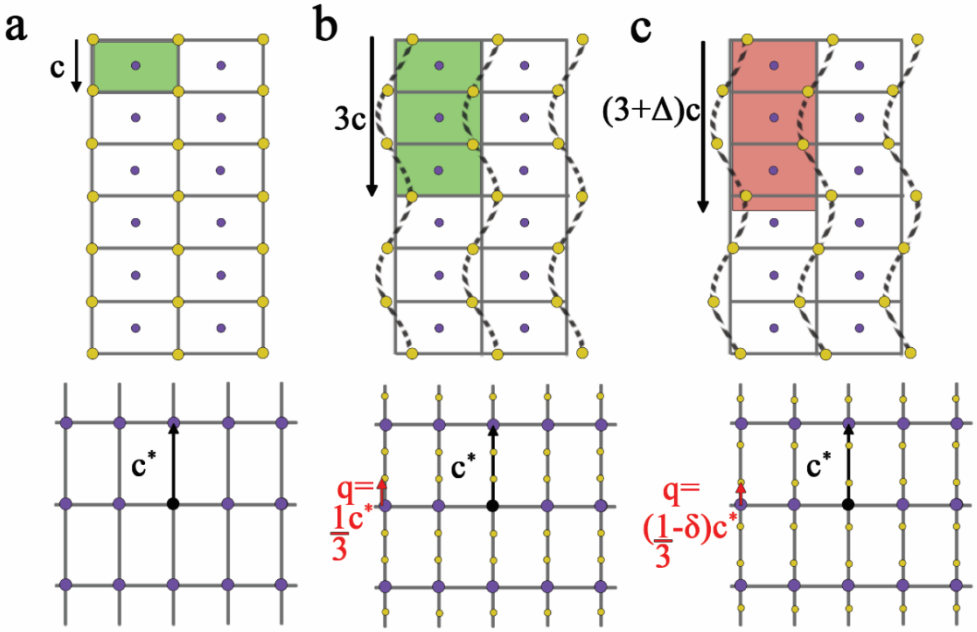

Figure 2.8 Comparison between (a) underlying basic structure (b) commensurately modulated structure (c) incommensurately modulated structure in real (top) and reciprocal space (bottom). The unit cell in real space is marked with green or red.

The symmetry of (3+1) dimensional structures can be described using a superspace group which is different from the space group notation. An example of a superspace group is $I4_1/amd(00\gamma)00ss$:

- $I4_1/amd$ is the space group of the basic structure, where the first letter 'I' denotes the centring of the lattice[1] and $4_1/amd$ the symmetry of the structure.
- (00γ) are the components of the q vector. In this case it means that the q vector lies purely along the **c*** axis.
- 00ss is the symmetry operation of the phase: 0 means that the phase shifts for 4_1 and a are zero, while s means that the phase shifts are ½ for m and d.

More information about incommensurately modulated structures can be found in the book of van Smaalen *et al.*[48] and the article of Janssen and Janner[49].

2.1.6 SAED

For a selected area electron diffraction (SAED) pattern, a parallel electron beam is directed onto the sample and an area of interest is selected with an aperture, called the selected area aperture. This aperture is placed at the image plane of the objective lens and only the electrons coming from the area of interest are not blocked and will reach the viewing device, in this case the CCD (Figure 2.1b). With the diffraction lens the diffraction space is selected to obtain the diffraction pattern.

2.1.7 EDT

With electron diffraction tomography (EDT) the 3D reciprocal space of a single crystal is reconstructed by tilting that crystal along one axis using an equidistant small step size (*e.g.* 1°) and acquiring at every step an off-zone diffraction pattern.[50,51,52] The position and amplitude of each reflection in this 3D reciprocal space is extracted and used for crystal structure determination. So, the sample is manually tilted every one degree along the goniometer axis, while taking at every degree a SAED pattern[52] (Figure 2.9). At every step, we check if the same area of interest is illuminated to get only information of the same area.

[1] I stands for body centered. Other centering types are the primitive centering (P),the base-centered (A,B or C) centering and face-centered (F) centering.

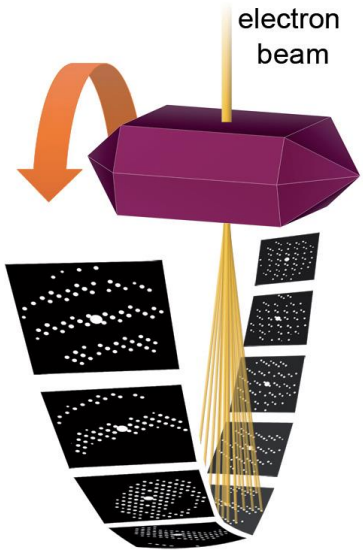

Figure 2.9 Schematics of the principle of electron diffraction tomography, taken from Karakulina[53].

EDT can be performed with and without precession. In a precessed electron diffraction pattern a tilted, parallel beam will fall onto your sample and will be rotated over 360°. In this way, a series of different out-off zone patterns are acquired, centred around the diffraction pattern obtained without tilting the sample. The intensities of these different patterns are integrated to achieve a precessed electron diffraction pattern. Due to this tilted beam, dynamical diffraction is reduced, so the dynamical effects are reduced and a more kinematic pattern is accomplished. To attain this, two sets of coils are needed. With one set of coils the parallel beam will be tilted to fall inclined onto your sample under a certain angle called the precession angle and to simultaneously rotate the beam while remaining on the same area of interest. With the second set, the beam that passed through the sample will be redirected to a parallel beam again. Working with structures containing heavy elements increases the dynamical effects and thus the need for using precessed electron diffraction tomography. Furthermore, the limited stepsize causes loss of information. By using precession, this missing information can be reduced, because during precession the intensity in the missing areas between different 2D patterns is sampled[52].

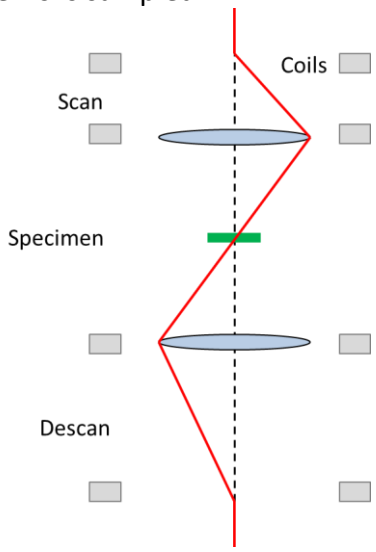

Figure 2.10: Schedule of the precession electron diffraction setup in the electron column.

After the data acquisition, the data is treated in order to find the reflections, refine the orientation matrix, perform the cluster analysis, integrate the diffracted intensities and index the cluster reciprocal space. The Rietveld method is used for the final structure refinement and is explained in more details in section 2.1.11.

2.1.8 BF TEM and DF TEM

For bright-field and dark-field transmission electron microscopy (BF TEM and DF TEM) imaging, a parallel electron beam is directed onto the sample. The central beam for BF TEM or a diffracted beam for DF TEM is selected from the diffraction pattern with the objective aperture, inserted in the back focal plane of the objective lens (Figure 2.1b). When acquiring a DF TEM image where an hkl reflection (g_{hkl}) is selected, only the areas where the electrons can scatter on these hkl planes will light up. When only the central beam is selected, the contrast in the TEM image will depend on how many electrons pass through different areas without interaction and end up in the central beam. For DF TEM, diffracted electrons are selected. These electrons travel off the optical axis and in this way undergo more aberration and astigmatism[54]. So for centred dark field TEM, the incident beam is tilted in such a way that the chosen diffracted beam travels along the optical axis.

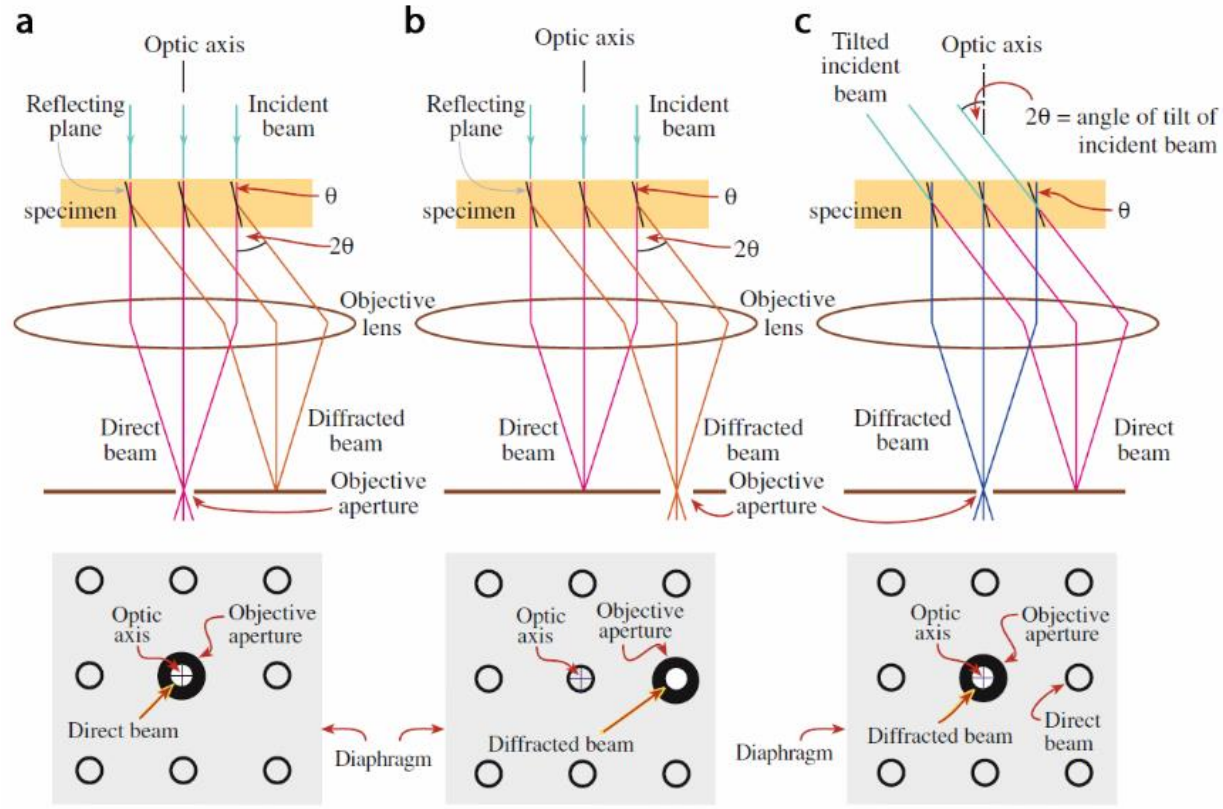

Figure 2.11 BF TEM (a) and DF TEM (b), where respectively the central beam and the diffracted beam are selected with the objective aperture. (c) For centred DF TEM, the diffracted beam is brought on the optical axis by tilting the incoming beam and selected with the objective aperture. This figure is taken from Williams and Carter[54].

2.1.9 STEM

For scanning transmission electron microscopy (STEM) imaging, the beam is focussed onto the sample and scanned (using scanning coils) in a raster pattern over the sample. The STEM magnification is not determined by the lenses of the imaging system, but by the size of the scanning area, which relies on the size of the convergent beam or electron probe. The latter depends on the lenses above the sample and their aberrations[54,55].

For STEM imaging, the imaging devices are detectors in the diffraction plane, instead of the CCD cameras in TEM. These detectors measure the intensity of a certain range of (mostly elastically) scattered beams[55,56]. Depending on the measured range of scattered beams, we obtain different kinds of STEM images *e.g.* annular bright field (ABF) and high-angle annular dark-field (HAADF). The intensity of every pixel in the STEM image relates to the combined intensity of the detected diffracted beams coming from the corresponding area of the sample.

To record a HAADF STEM image the detector measures the high angle scattered electrons: the coherent diffracted beams and the incoherent thermal diffuse scattering[57] (see Figure 2.12). At high angles, the d spacing becomes so small that it is of the order of the thermal vibration amplitude of the atoms. So we get diffuse scattering due to the absence of well-defined planes that lead to coherent Bragg scattering[57]. Integration of the signal over a large angular range causes the image itself to be mostly incoherent and directly interpretable[57]. The diffracted beams are coherent as consequence of interference effects. When only a small angular part of the diffraction pattern is selected, the image is sensitive to the details or features of the interference pattern and we obtain a non-directly interpretable image. However, when a larger angular range is selected, we are less sensitive to specific details of the interference pattern due to the fact that these details are integrated, which results in a more incoherent image, making the image directly interpretable.

Electrons scattered at high angles underwent an electron-nucleus interaction: The incoming electron is attracted towards the positive core due to Coulomb interaction, causing its path to deflect towards the core. A heavier element has a higher atomic number Z and thus a more positive core, leading to a higher Coulomb force. So, heavy elements scatter the electrons more to higher angles than lighter elements. Furthermore, the scattering probability depends on Z, so the likelihood to scatter is higher for heavier elements. Due to these two reasons atomic columns containing heavy elements appear brighter than ones with lighter elements: HAADF STEM has Z dependent contrast. The dependency is approximately Z^2, like the nuclear scattering or Rutherford scattering.[57] In practice, the squared dependency is lower, because electrons scattered at smaller scattering angles are also measured to increase the detected signal. These electrons saw a 'screened' nucleus (due to the atomic electrons), leading to a lower exponent in the Z dependency.[57] The inner and outer collection angles for the detector are ~50 mrad and ~200mrad (~≥3α, with alpha the semi convergence angle or electron probe angle).

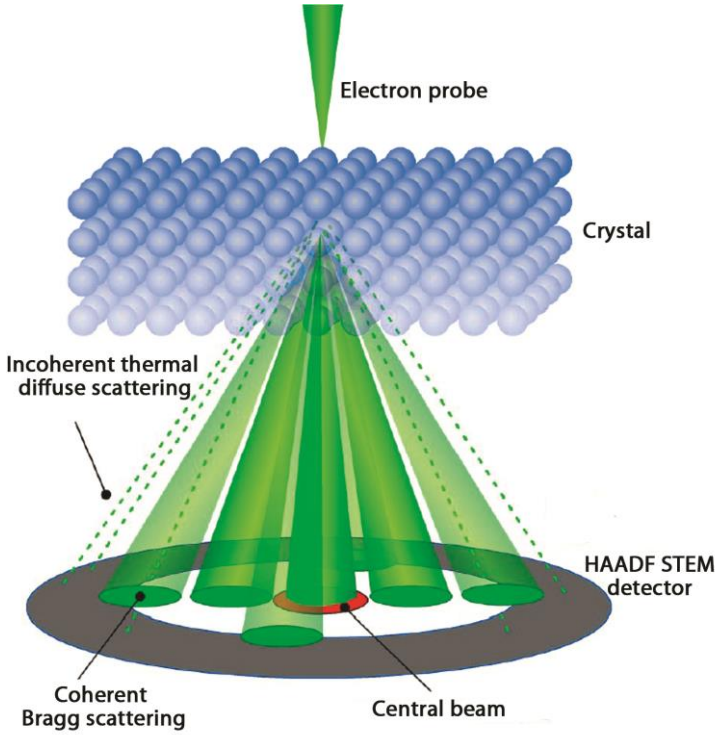

Figure 2.12 The electron probe scans over the crystal. Afterwards, the incoherent thermal diffuse scattering and the coherent Bragg scattering are recorded with the HAADF STEM detector. This figure is adapted from Zhang *et al.*[58] .

For ABF STEM imaging, the low angle scattered electrons are measured. The detector has in this case an inner and outer collection angle of ~12mrad and ~24mrad (an angular range of about half the probe angle to the full probe angle[57]). This image is not strongly depended on Z, making light and heavy elements visible in the same image[57].

2.1.10 STEM-EDX

During STEM-EDX X-rays formed due to the electron-matter interaction are collected. An atom consists of a nucleus and electrons that orbit around it in specific shells. When an incoming electron removes an electron from an atomic inner shell, then the atom is in an excited state. The atom becomes more stable again by filling the place of the removed electron with an electron from a higher atomic shell. In order to achieve this, the electron needs to lose energy by sending its excess energy, equal to the energy difference between the two shells, out in the form of an X-ray. These energy differences between different shells are characteristic for every element, so measuring this gives information about the elemental composition of the material. However, not only characteristic X-rays are being generated, but also Bremsstrahlung X-rays. So, an incoming electron can interact with the nucleus, which can cause it to change its momentum leading to energy loss, sent out in the form of an X-ray. This X-ray can have any energy up until the beam energy, but small energy losses are far more likely than high energy losses. Bremsstrahlung X-rays lead to a continuous energy spectrum, while the characteristic X-rays cause discrete peaks.

The X-rays are collected by a silicon drift detector (SDD). Four of these detectors are mounted symmetrically around the sample, forming the Super-X four detector system. This allows us to acquire more signal at all different angles, making atomic resolution STEM-EDX mapping possible.

2.1.11 PXRD

For powder X-ray diffraction (PXRD), the sample consists of small crystals randomly oriented. X-rays will hit the sample and will diffract on the crystal planes, resulting in deflection of the X-rays over a 2θ angle according to the Bragg law. A detector collects these deflected radiation and their intensities are plotted in function of the Bragg angle 2θ.

The X-rays come from an X-ray tube under vacuum consisting of a cathode which generates the electrons and a metal anode which is bombarded by the generated electrons and produced X-rays[45]. Finally, the K_α line of a Cu source (other sources are also possible such as Mo and Co) is filtered out using a filter (or monochromator) which removes the other wavelengths and this K_α line is used during the experiment.

First, a Le Bail decomposition of the PXRD pattern is performed where the cell parameters, the peak shape and the background are refined using a non-linear least squares minimization of the difference between the observed and the calculated intensities[45]. Note that in the Le Bail method the intensities of the hkl reflections are given arbitrary values to give the best fit and the method is structure independent. The quality of the fit is expressed by the profile reliability factor, R_p, the weighted profile reliability, R_{wp}, and the goodness of fit, χ^2

$$R_p = \frac{\sum_{i=1}^{n} \left| Y_i^{obs} - Y_i^{calc} \right|}{\sum_{i=1}^{n} Y_i^{obs}} \times 100\% \qquad 2.17$$

$$R_{wp} = \left[\frac{\sum_{i=1}^{n} w_i \left(Y_i^{obs} - Y_i^{calc} \right)^2}{\sum_{i=1}^{n} w_i \left(Y_i^{obs} \right)^2} \right]^{1/2} \times 100\% \qquad 2.18$$

$$\chi^2 = \frac{\sum_{i=1}^{n} w_i \left(Y_i^{obs} - Y_i^{calc} \right)^2}{n - p} \qquad 2.19$$

where n is the total number of points measured in the PXRD pattern, $Y_i^{obs\,(calc)}$ is the observed (calculated) intensity of the i^{th} data point with w_i the weight of that i^{th} data point, equal to $1/Y_i^{obs}$ and p is the number of free least squares parameters. Using weight factors ensures that every point contributes equally, independently of its intensity.

Next, in order to refine the crystal structure the Rietveld method is applied, where now the intensities of the peaks are related to the crystal structure[45]. On top of the profile parameters now also the structure parameters are refined. Extra reliability factors similar to the profile reliability factors can be defined, using the calculated structure factors F_{hkl}^{calc} and the estimated observed structure F_{hkl}^{obs} factors based on F or F^2 [59]

$$R_F = \frac{\sum_{hkl}\left|F_{hkl}^{obs}\right| - \left|F_{hkl}^{calc}\right|}{\sum_{hkl}\left|F_{hkl}^{obs}\right|} \quad 2.20$$

$$R_{F^2} = \frac{\sum_{hkl}\left(F_{hkl}^{obs}\right)^2 - \left(F_{hkl}^{calc}\right)^2}{\sum_{hkl}\left(F_{hkl}^{obs}\right)^2}. \quad 2.21$$

The observed structure factor needs to be estimated because multiple reflections can contribute to the same point in the PXRD patterns. So the final intensity is distributed among the different reflections in the same way as for the calculated model.

2.2 Theoretical techniques

In section 3.1 we will complement our measurements with first-principles electronic structure calculations using density functional theory (DFT). In this section a brief introduction on DFT is provided thereby introducing the concepts that are used in this thesis.

2.2.1 Schrödinger equation

DFT is an approach to the quantum many body problem and uses the electron density as the fundamental quantity to describe the properties of the many-particle system. The Hamiltonian describing the interaction between N electrons and M nuclei in a solid is given by

$$\begin{aligned}\widehat{H} = &-\sum_{k=1}^{M}\frac{\hbar^2}{2M_k}\nabla_{\boldsymbol{R}_k}^2 - \sum_{i=1}^{N}\frac{\hbar^2}{2m_e}\nabla_{\boldsymbol{r}_i}^2 + \frac{1}{2}\sum_{k_1\neq k_2=1}^{M}\frac{1}{4\pi\varepsilon_0}\frac{Z_{k_1}Z_{k_2}e^2}{\left|\boldsymbol{R}_{k_1}-\boldsymbol{R}_{k_2}\right|} \\ &+\frac{1}{2}\sum_{i_1\neq i_2=1}^{N}\frac{1}{4\pi\varepsilon_0}\frac{e^2}{\left|\boldsymbol{r}_{i_1}-\boldsymbol{r}_{i_2}\right|} - \sum_{k=1}^{M}\sum_{i=1}^{N}\frac{1}{4\pi\varepsilon_0}\frac{Z_{k_1}e^2}{\left|\boldsymbol{R}_k-\boldsymbol{r}_i\right|}\end{aligned} \quad 2.22$$

m_e is the mass of the electron and e its charge. M_k is the mass of the k[th] nucleus with charge $Z_k e$ at position $\boldsymbol{R}_k$. The position of the i[th] electron is represented by $\boldsymbol{r}_i$ and ε_0 is the permittivity of vacuum. The eigenvalues of the Hamiltonian and in particular the ground state energy of a system consisting of N electrons and M nuclei are found by solving the many-particle time-independent Schrödinger equation

$$\widehat{H}\Psi(\boldsymbol{r}_1,\dots,\boldsymbol{r}_N,\boldsymbol{R}_1,\dots,\boldsymbol{R}_N) = E\Psi(\boldsymbol{r}_1,\dots,\boldsymbol{r}_N,\boldsymbol{R}_1,\dots,\boldsymbol{R}_N) \quad 2.23$$

where we omitted the spin dependency of the many-particle wave function for simplicity.

For any realistic system of nuclei and electrons this equation cannot be solved exactly and we need to rely on further approximations.

2.2.2 Born-Oppenheimer approximation

The first approximation is the Born-Oppenheimer approximation[60]. Due to the fact that electrons move a lot faster than the nuclei, they perceive static nuclei. Using the short-handed notation

$$\boldsymbol{r} \coloneqq \{\boldsymbol{r}_i; 1 = 1 \dots N\} \tag{2.24}$$

and

$$\boldsymbol{R} \coloneqq \{\boldsymbol{R}_i; 1 = 1 \dots M\} \tag{2.25}$$

we can approximate the wave function in the Born-Oppenheimer approximation as[60]

$$\Psi(\boldsymbol{r}, \boldsymbol{R}) = \Psi_n(\boldsymbol{R}).\Psi_e(\boldsymbol{r}; \boldsymbol{R}) \tag{2.26}$$

where $\Psi_n(\boldsymbol{R})$ is the wave function that depends only on the nuclear coordinates and $\Psi_e(\boldsymbol{r}; \boldsymbol{R})$ is the wave function that depends on the electronic coordinates and parametrically on the nuclear coordinates. The latter wave function satisfies the Schrödinger equation for the electronic problem[61]:

$$\hat{H}_e \Psi_e(\boldsymbol{r}) = E_e \Psi_e(\boldsymbol{r}) \tag{2.27}$$

where $\hat{H}_e$ is the Hamiltonian

$$\hat{H}_e = \left[-\sum_{i=1}^{N} \frac{\hbar^2}{2m_e} \nabla_{\boldsymbol{r}_i}^2 - \sum_{k=1}^{M} \sum_{i=1}^{N} \frac{1}{4\pi\varepsilon_0} \frac{Z_{k_1} e^2}{|\boldsymbol{R}_k - \boldsymbol{r}_i|} + \frac{1}{2} \sum_{i_1 \neq i_2 = 1}^{N} \frac{1}{4\pi\varepsilon_0} \frac{e^2}{|\boldsymbol{r}_{i_1} - \boldsymbol{r}_{i_2}|} \right] \tag{2.28}$$

$$= \hat{T} + \hat{V}_{ext} + \hat{V}_{ee}. \tag{2.29}$$

The first term is the kinetic energy, the second term the external potential energy and the third term the electron-electron interaction. We omitted the dependence of the wave function and the energy E_e on the nuclear coordinates.

The total energy E of the electron-nuclei system is given by[62]

$$E = E_e + \frac{1}{2} \sum_{k_1 \neq k_2 = 1}^{M} \frac{1}{4\pi\varepsilon_0} \frac{Z_{k_1} Z_{k_2} e^2}{|\boldsymbol{R}_{k_1} - \boldsymbol{R}_{k_2}|} \tag{2.30}$$

where the kinetic energy of the nuclei is neglected. Eq. 2.27 is still too complicated to solve and further approximations are required. An historically important approximation is the so-called Hartree-Fock approximation where the many-electron wave function is written as a Slater determinant of single particle wave function or orbitals leading to a set of non-linear Schrödinger-like equations for the orbitals: the Hartree-Fock equations. The Slater determinant which is anti-symmetric is written as

$$\Psi = \frac{1}{\sqrt{N!}}\sum_{i=1}^{N!}(-)^{P(i)}\psi_{i_1}(\boldsymbol{r}_1)\dots\psi_{i_N}(\boldsymbol{r}_N) = \frac{1}{\sqrt{N!}}\begin{vmatrix}\psi_1(\boldsymbol{r}_1) & \psi_2(\boldsymbol{r}_1) & \dots & \psi_N(\boldsymbol{r}_1)\\ \psi_1(\boldsymbol{r}_2) & \psi_2(\boldsymbol{r}_2) & \dots & \psi_N(\boldsymbol{r}_2)\\ \vdots & \vdots & \ddots & \vdots\\ \psi_1(\boldsymbol{r_N}) & \psi_2(\boldsymbol{r}_N) & \dots & \psi_N(\boldsymbol{r}_N)\end{vmatrix}. \quad 2.31$$

P(i) is the number of permutations needed to change the order of the orbitals in the product term and ψ_i are the one-particle orbitals. The Hartree-Fock method accounts for the anti-symmetric nature of the many-particle wave function and correlation effects due to the Pauli exclusion principle, the so-called exchange contribution. However, no other electron-electron correlations are accounted for in the Hartree-Fock method. Several methods have been developed to go beyond the Hartree-Fock approximation and account for these correlation effects. In the next section we will mention another approach to the many-particle problem.

2.2.3 Density functional theory

2.2.3.1 Hohenberg-Kohn theorem

Density functional theory (DFT) is a different approach to the many-particle problem. Though the formalism leads to single-particle equations similar to the Hartree-Fock equation, the inclusion of correlation (and exchange) effects to the total energy is much simpler. The foundations of DFT as an exact many-body theory are given by the Hohenberg-Kohn theorems[63]. The Hamiltonian of the many-body electron system is given by Eq. 2.29.

Theorem I

The external potential $V_{ext}(\boldsymbol{r})$ is determined uniquely, apart from an additive constant, by the ground state electron density $\rho_0(\boldsymbol{r})$.

So, the density defines the external potential thus also all terms in the Hamiltonian. Therefore, the electron wave function can be determined and thus the ground state energy. In other words, E is a unique functional of the electron density, meaning that the electron density is the only quantity needed to find the ground state energy.

Theorem II

For a density *$\rho'(\boldsymbol{r})$ such that $\rho'(\boldsymbol{r})\geq 0$ and $\int \rho'(\boldsymbol{r})d\boldsymbol{r}=N$ holds, $E_0=E[\rho_0]\leq E[\rho]$.*

It represents the energy variation principle, meaning that the true ground state electron density is the one that minimizes the energy functional.

The proof of these theorems can be found in reference books[61,62].

2.2.3.2 Kohn-Sham equations

Practical calculations can be performed within the DFT approach using the Kohn-Sham scheme. Kohn and Sham assumed that the original many-body problem can be replaced by an auxiliary system of independent particles, described exactly with a Slater determinant of

single particle wave function or orbitals, with the same density and energy as the original many-body system and moving in an effective potential V_{KS}. The many particle orbitals satisfy the Kohn-Sham equations:

$$\widehat{H}_{KS}\psi_i = \varepsilon_i\psi_i \tag{2.32}$$

with ε_i the Kohn-Sham eigenvalues, ψ_i the single-particle wave functions and the Kohn-Sham Hamiltonian

$$\widehat{H}_{KS} = -\sum_{i=1}^{N}\frac{\hbar^2}{2m_e}\nabla_i^2 + \sum_{i=1}^{N}V_{KS}(\boldsymbol{r}). \tag{2.33}$$

The Kohn-Sham potential $V_{KS}(\boldsymbol{r})$ is

$$V_{KS}(\boldsymbol{r}) = V_{ext}(\boldsymbol{r}) + V_C(\boldsymbol{r}) + V_{XC}(\boldsymbol{r}) \tag{2.34}$$

with the external potential $V_{ext}(\boldsymbol{r})$, the Coulomb potential $V_C(\boldsymbol{r})$ and the exchange-correlation potential $V_{XC}(\boldsymbol{r})$ defined by

$$V_{ext}(\boldsymbol{r}) = \frac{\delta E_{ext}[\rho]}{\delta\rho} = -\sum_{k=1}^{M}\frac{1}{4\pi\varepsilon_0}\frac{Z_{k_1}e^2}{|\boldsymbol{R}_k - \boldsymbol{r}|} \tag{2.35}$$

$$V_C(\boldsymbol{r}) = \frac{\delta E_C[\rho]}{\delta\rho} = \frac{e^2}{4\pi\varepsilon_0}\int\frac{\rho(\boldsymbol{r}')}{|\boldsymbol{r} - \boldsymbol{r}'|}d\boldsymbol{r}' \tag{2.36}$$

$$V_{XC}(\boldsymbol{r}) = \frac{\delta E_{XC}[\rho]}{\delta\rho}. \tag{2.37}$$

They are the functional derivatives with respect to the density of the corresponding energy terms .The energy can then be written as

$$E[\rho] = T_S[\rho] + E_C[\rho] + E_{ext}[\rho] + E_{XC}[\rho] \tag{2.38}$$

with the kinetic energy of the non-interacting system $T_S[\rho]$, the classical Coulomb interaction $E_C[\rho]$ and the electron-nuclei interaction $E_{ext}[\rho]$:

$$T_S[\rho] = -\frac{\hbar^2}{2m_e}\sum_{i=1}^{N}\langle\psi_i|\nabla_i^2|\psi_i\rangle \tag{2.39}$$

$$E_C[\rho] = \frac{1}{2}\int V_C(\boldsymbol{r})\rho(\boldsymbol{r})d\boldsymbol{r} \tag{2.40}$$

$$E_{ext}[\rho] = \int V_{ext}(\boldsymbol{r})\rho(\boldsymbol{r})d\boldsymbol{r}. \tag{2.41}$$

The density is

$$\rho(\boldsymbol{r}) = \sum_i f_i \psi_i^*(\boldsymbol{r})\psi_i(\boldsymbol{r}) \text{ with } f_i = 0,1,2\,. \tag{2.42}$$

f_i gives the occupation of the single particle wave function $\psi_i(\boldsymbol{r})$. The last term in Eq. 2.38 is the exchange-correlation energy functional and contains all unknown elements. It accounts for the exchange contribution and the correlation effects beyond that of the Hartree-Fock approximation.

The Kohn-Sham equations are solved self-consistently (Figure 2.13). First, we fix the positions of the nuclei and use a trial electron density to calculate the effective potential and solve the Kohn-Sham equations to obtain the single electron wave functions. Next, the electron density is recalculated using Eq. 2.42. If the calculated electron density is the same as the trial electron density, then we found the true ground state density, otherwise we will start over and the calculated electron density becomes the new trial electron density. In this way, one obtains the ground state electron density for the fixed nuclei positions.

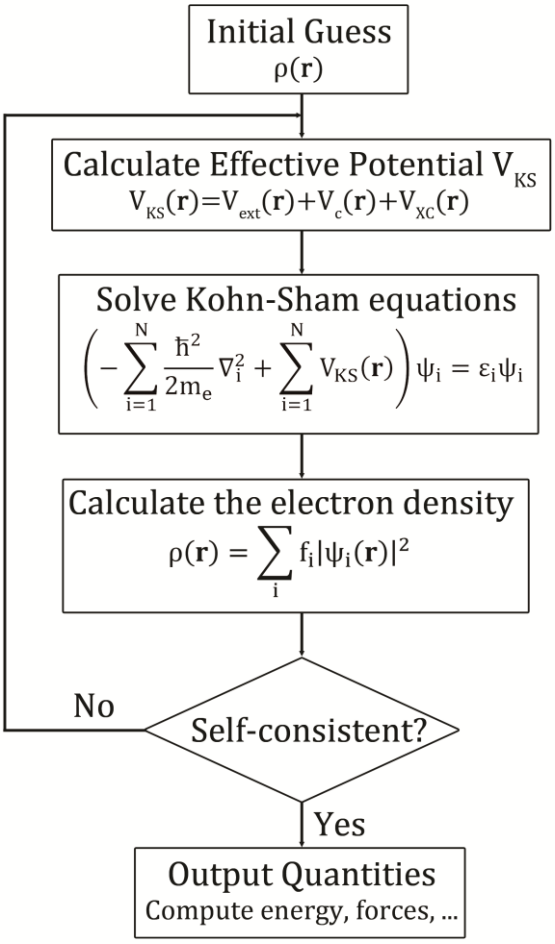

Figure 2.13 Flowchart that explains how the Kohn-Sham equations are solved self-consistently.

2.2.4 Exhange-correlation functionals

2.2.4.1 Local density approximation and generalized gradient approximation

Since the exact exchange-correlation energy is not known one has to rely on approximations. One of the approximations of the exchange-correlation functional is the local density approximation (LDA), which only depends on the local electron density. In this approximation, the inhomogeneous electron gas is locally replaced by a homogeneous electron gas, where the exchange correlation energy of the homogeneous electron gas is taken as the exchange correlation energy of the inhomogeneous electron gas. The total exchange-correlation energy is then the sum over all local contributions. The generalized gradient approximation (GGA) goes beyond the LDA and is based not only on the local electron density but also on its gradient. In this thesis the generalized-gradient approximation of Perdew-Burke-Ernzerhof (PBE)[64] was used for the exchange and correlation energy.

2.2.4.2 Van der Waals functional

In this thesis we also needed to include the influence of the van der Waals forces or more specifically the London dispersion forces and thus we use the van der Waals density functional (vdW-DF) method which is based on the electron density. Non-local electron-electron correlations cause these van der Waals forces. Or in other words, instantaneous charge density fluctuations in one region can create an instantaneous dipole which in turn influences the density in another region leading to an induced dipole[65]. So, the exchange correlation is of the form[66–68]

$$E_{XC} = E_X^{GGA} + E_C^{LDA} + E_C^{NL} \qquad 2.43$$

consisting of an exchange energy term taken from the GGA functional (*e.g.* PBE), a correlation energy term obtained within the local density approximation and a non-local energy term approximating the non-local electron correlation effects. The VdW interaction in this thesis was included using the optB86b-VdW density functional in VASP[66,67].

2.2.5 Relativistic effects

Until now, we used the time-independent Schrödinger equation, which does not include relativistic effects. However, for heavy elements as the ones studied in this thesis the electron velocity becomes sufficiently high so that relativistic effects should be included. The time-independent Dirac equation[69] reads:

$$E\psi(\boldsymbol{r}) = (c\boldsymbol{\alpha}.\boldsymbol{p} + \beta m_e c^2)\psi(\boldsymbol{r}). \qquad 2.44$$

This describes a single particle with spin ½, in our case an electron, where c is the speed of light, $\boldsymbol{p}$ is the quantum mechanical momentum operator (-i$\hbar\boldsymbol{\nabla}$), m_e is the rest mass of the electron and $\boldsymbol{\alpha}$ and $\boldsymbol{\beta}$ are 4x4 matrices

$$\boldsymbol{\alpha} = \begin{pmatrix} 0 & \boldsymbol{\sigma} \\ \boldsymbol{\sigma} & 0 \end{pmatrix}, \qquad \beta = \begin{pmatrix} I & 0 \\ 0 & -I \end{pmatrix} \tag{2.45}$$

with the Pauli matrices $\boldsymbol{\sigma}$

$$\boldsymbol{\sigma} = \left(\begin{pmatrix} 0 & 1 \\ 1 & 0 \end{pmatrix}, \begin{pmatrix} 0 & -\mathrm{i} \\ \mathrm{i} & 0 \end{pmatrix}, \begin{pmatrix} 1 & 0 \\ 0 & -1 \end{pmatrix} \right) \tag{2.46}$$

and I is the 2x2 identity matrix. The wave function $\psi(\boldsymbol{r})$ is a four-component (bi-spinor) function, which can be written using two two-component spinor:

$$\psi(\boldsymbol{r}) = \begin{pmatrix} \psi_1(\boldsymbol{r}) \\ \psi_2(\boldsymbol{r}) \end{pmatrix}. \tag{2.47}$$

In a more general case, when a particle moves with charge q, which is $-e$ in the case of an electron, in an electromagnetic field described by the vector and scalar potentials $\boldsymbol{A}(\boldsymbol{r})$and $\phi(\boldsymbol{r})$, Eq. 2.44 can be rewritten as

$$\big(E - q\phi(\boldsymbol{r})\big)\psi(\boldsymbol{r}) = \big(\boldsymbol{\alpha}.\big(c\boldsymbol{p} - q\boldsymbol{A}(\boldsymbol{r})\big) + \beta mc^2\big)\psi(\boldsymbol{r}) \tag{2.48}$$

where $\boldsymbol{p}$ was replaced by $\boldsymbol{p} - (q/c)\boldsymbol{A}(\boldsymbol{r})$ and E by $E - q\phi(\boldsymbol{r})$. Eq. 2.48 can also be written in a two-component form using the Pauli matrices:

$$\boldsymbol{\sigma}.(c\boldsymbol{p} - q\boldsymbol{A}(\boldsymbol{r}))\psi_2(\boldsymbol{r}) + (mc^2 + q\phi(\boldsymbol{r}) - E)\psi_1(\boldsymbol{r}) = 0 \tag{2.49}$$

$$\boldsymbol{\sigma}.(c\boldsymbol{p} - q\boldsymbol{A}(\boldsymbol{r}))\psi_1(\boldsymbol{r}) - (mc^2 - q\phi(\boldsymbol{r}) + E)\psi_2(\boldsymbol{r}) = 0. \tag{2.50}$$

Rewritten the first equation, we obtain

$$\psi_1(\boldsymbol{r}) = \frac{\boldsymbol{\sigma}.(c\boldsymbol{p} - q\boldsymbol{A}(\boldsymbol{r}))}{(-mc^2 - q\phi(\boldsymbol{r}) + E)}\psi_2(\boldsymbol{r}). \tag{2.51}$$

In order to estimate the relative magnitude of $\psi_1(\boldsymbol{r})$ and $\psi_2(\boldsymbol{r})$, we approximate with $\boldsymbol{\sigma}.\boldsymbol{p} \approx mv$, $E - mc^2 \approx ½mv^2$ and neglect the electromagnetic field. The ratio ψ_1/ψ_2 then becomes $2c/v$. v is the averaged velocity of the particle. In the case of an electron in a solid, the average velocity v is much smaller than the speed of light, making $\psi_1$the large component and thus the most important one. ψ_2 is the small component. After substituting the second equation into the first equation, we obtain

$$(E' - q\phi(\boldsymbol{r}))\psi_1(\boldsymbol{r}) = \frac{1}{2m}(\boldsymbol{\sigma}.\boldsymbol{\pi})\frac{1}{1 + \left[\dfrac{E' - q\phi(\boldsymbol{r})}{2mc^2}\right]}(\boldsymbol{\sigma}.\boldsymbol{\pi})\psi_1(\boldsymbol{r}) \tag{2.52}$$

with $E' = E - mc^2$ which is the 'normal' energy without rest mass energy and $\boldsymbol{\pi} = \boldsymbol{p} - (q/c)\boldsymbol{A}$. Next, we will assume the absence of a magnetic field which is the case in our situation. When we approximate Eq. 2.52 to order v^2/c^2, we get[70]

$$(E' + e\phi(\boldsymbol{r}))\psi_1(\boldsymbol{r}) = \left[\frac{p^2}{2m} - \frac{p^4}{8m^3c^2} - \frac{e\hbar^2}{8m^2c^2}\boldsymbol{\nabla}.\boldsymbol{\nabla}\phi(\boldsymbol{r}) - \frac{e\hbar}{4m^2c^2}\boldsymbol{\sigma}.\boldsymbol{\nabla}\phi(\boldsymbol{r})\times\boldsymbol{p}\right]\psi_1(\boldsymbol{r}). \quad 2.53$$

This looks similar to the Schrödinger equation with three extra terms added:

- $-\frac{p^4}{8m^3c^2}$: mass-velocity term, which is a relativistic correction to the kinetic energy:

$$E = \sqrt{|\boldsymbol{p}|^2c^2 + m^2c^4} \approx mc^2 + \frac{|\boldsymbol{p}|^2}{2m} - \frac{(|\boldsymbol{p}|^2)^2}{8m^3c^2} \pm \cdots \quad 2.54$$

- $-\frac{e\hbar^2}{8m^2c^2}\boldsymbol{\nabla}.\boldsymbol{\nabla}\phi(\boldsymbol{r})$: The Darwin term, which produces an energy shift in the s-states. It[71] is due to the very rapid oscillatory motion, called the 'Zitterbewegung', making the electrons feel on average a smeared-out Coulomb potential from the nuclei.
- $-\frac{e\hbar}{4m^2c^2}\boldsymbol{\sigma}.\boldsymbol{\nabla}\phi(\boldsymbol{r})\times\boldsymbol{p}$: The spin-orbit coupling term, due to the interaction of the electron spin with its orbital angular momentum.

As one can see, the first two terms, the mass-velocity term and the Darwin term, do not depend on the Pauli matrices making it possible to include them directly into the Hamiltonian as corrections to the one-electron potential[72]. This leads to the scalar-relativistic approach, where the first two terms are included and the spin-orbit coupling neglected. Using the scalar-relativistic wave functions, the spin-orbit coupling can then be included through a perturbation using the second variation method[73].

2.2.6 Practical implementation

2.2.6.1 Bloch theorem and k point sampling

The effective potential V_{KS} is periodic due to the translation symmetry in crystals. Thus the Kohn-Sham equations only need to be solved for the unit cell with cell parameters **a**, **b** and **c**:

$$V_{KS}(\boldsymbol{r}) = V_{KS}(\boldsymbol{r} + \boldsymbol{T}) \quad 2.55$$

with **T** the translation vector in real space equal to the sum of an integer amount of the basis vectors.

$$\boldsymbol{T} = n\boldsymbol{a} + m\boldsymbol{b} + p\boldsymbol{c} \quad 2.56$$

Bloch[43] proved that the solutions of the Schrödinger equation with a periodic potential (see Eq. 2.32, movement of one electron in the effective potential V_{KS}) are of the form

$$\psi_{n\boldsymbol{k}}(\boldsymbol{r}) = \exp(i\boldsymbol{k}.\boldsymbol{r})\, u_{n\boldsymbol{k}}(\boldsymbol{r}) \quad 2.57$$

with $u_{n\boldsymbol{k}}(\boldsymbol{r})$ a function with the crystal periodicity, where **k** is the wave vector and n the band index: $u_{n\boldsymbol{k}}(\boldsymbol{r}) = u_{n\boldsymbol{k}}(\boldsymbol{r} + \boldsymbol{T})$. The latter can be expanded as a Fourier series

$$u_{n\boldsymbol{k}}(\boldsymbol{r}) = \sum_{\boldsymbol{g}} c_{n,\boldsymbol{k}+\boldsymbol{g}} e^{i\boldsymbol{g}.\boldsymbol{r}}. \tag{2.58}$$

Eq. 2.57 thus becomes

$$\psi_{n\boldsymbol{k}}(\boldsymbol{r}) = \sum_{\boldsymbol{g}} c_{n,\boldsymbol{k}+\boldsymbol{g}} e^{i(\boldsymbol{g}+\boldsymbol{k}).\boldsymbol{r}} \tag{2.59}$$

with **g** the reciprocal lattice vectors. Also the energy eigenvalues are periodic in reciprocal space

$$\varepsilon_n(\boldsymbol{k}) = \varepsilon_n(\boldsymbol{k}+\boldsymbol{g}). \tag{2.60}$$

The electron density for an infinitely extended crystal can be written as

$$\rho(\boldsymbol{r}) = \frac{1}{V_{BZ}} \sum_n \int_{BZ} f_{n\boldsymbol{k}} |\psi_{n\boldsymbol{k}}(\boldsymbol{r})|^2 d\boldsymbol{k} \tag{2.61}$$

where V_{BZ} is the volume of the first Brillouin zone (BZ), which is the unit cell in reciprocal space. Next, a weighted summation over a finite number of **k**-points can approximate this integral over the first Brillouin zone, because the wave functions with closely located **k** points are almost identical:

$$\rho(\boldsymbol{r}) = \sum_{n\boldsymbol{k}} w_{\boldsymbol{k}} f_{n\boldsymbol{k}} |\psi_{n\boldsymbol{k}}(\boldsymbol{r})|^2 d\boldsymbol{k} \tag{2.62}$$

with $w_{\boldsymbol{k}}$ the weight of **k**. So, the situation is simplified to a calculation of the wave function at a finite number of **k** points in the first Brillouin zone and for a finite number of bands. In fact, only the **k** points in the irreducible Brillouin zone (only the non-symmetrical equivalent **k** points) need to be calculated (see Figure 2.14). In this thesis the Γ point (center of the BZ) is always included in the calculation, *i.e.* we use Γ-centered **k** point grids.

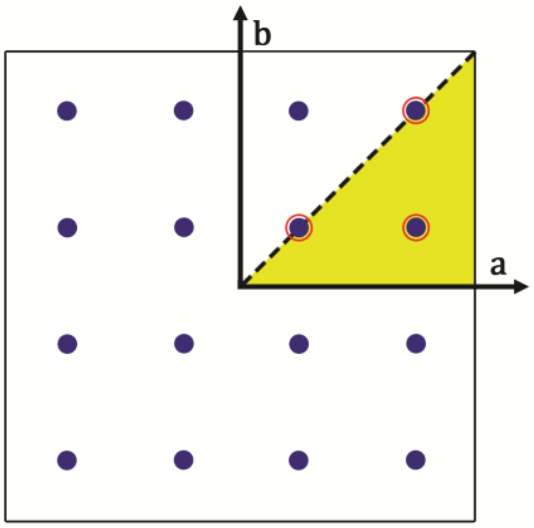

Figure 2.14 Visualization of a square 2D Brillouin zone (black encircled) and the three non-symmetrical equivalent **k** points encircled in red. The irreducible Brillouin zone is displayed in yellow.

2.2.6.2 Plane wave basis set

To solve the Kohn-Sham equations the single electron orbitals need to be expanded in a certain basis set. In this thesis we used a plane wave basis set. Only plane waves with a kinetic energy $(\hbar/2m)|\boldsymbol{k}+\boldsymbol{g}|^2$ smaller than a particular cut-off energy E_{cut}

$$\frac{\hbar}{2m}|\boldsymbol{k}+\boldsymbol{g_{max}}|^2 = E_{cut} \qquad 2.63$$

are accounted in the series. The cut-off energy will thus determine how many plane waves are included in the basis set, so increasing E_{cut} will improve the accuracy of the calculation, however it will also increase the calculation cost.

2.2.6.3 Projected-Augmented-Wave method

Practically speaking, it is a problem to describe the spatially strongly localized states and rapid oscillations of the orbitals near the nucleus with plane waves. The number of plane waves will be too high for practical calculations. For example, the Projected-Augmented-wave (PAW) method[74] first introduced by Blöchl will offer a solution to this problem. This method is applied in this thesis. The PAW method keeps the all-electron (AE) character, but it uses a decomposition of the AE wave function in terms of a smooth pseudo-wave function, and a rapidly varying contribution localized within the core region[61].

Two regions are defined: the augmentation region Ω_{R_a} which is the enclosed spherical volume around each atom with radius r_c^a, and the interstitial region, which is the remaining space in between these spherical volumes. The core of the method is a transformation that maps the true electron wave function on an auxiliary 'smooth' pseudo-wave function which can be easily expanded in plane waves. The AE wave functions $\psi_{n\boldsymbol{k}}$ are reconstructed from the pseudo-wave functions $\tilde{\psi}_{n\boldsymbol{k}}$ through a linear transformation $\hat{T}$:

$$|\psi_{n\boldsymbol{k}}\rangle = \hat{T}|\tilde{\psi}_{n\boldsymbol{k}}\rangle. \qquad 2.64$$

Reconstruction of the true wave functions is possible in order to calculate the physical properties of the system. The Kohn-Sham equations become

$$\hat{T}^{\dagger}\hat{H}\hat{T}|\psi_{n\boldsymbol{k}}\rangle = \varepsilon_n\hat{T}^{\dagger}\hat{T}|\tilde{\psi}_{n\boldsymbol{k}}\rangle. \qquad 2.65$$

$\hat{T}$ has to be constructed in such a way that the pseudo-wave functions become smooth in the augmentation region due to the strong oscillations of the AE wave function close to the nucleus, while simultaneously staying identical to the AE wave function in the interstitial space, so $\hat{T}$ becomes

$$\hat{T} = 1 + \sum_a \hat{T}^a \qquad 2.66$$

where a is defined as atom index and $\hat{T}^a$ is the null operator outside the augmentation region of atom a, implying that it reduces every state to zero in the interstitial space. Inside

each augmentation region, the pseudo- and AE wave function can both be respectively expanded in partial wave functions $|\tilde{\phi}_i^a\rangle$ and $|\phi_i^a\rangle$:

$$|\tilde{\psi}_{n\boldsymbol{k}}\rangle = \sum_i c_i^a \, |\tilde{\phi}_i^a\rangle \tag{2.67}$$

$$|\psi_{n\boldsymbol{k}}\rangle = \sum_i c_i^a \, |\phi_i^a\rangle \tag{2.68}$$

where we go from Eq. 2.67 to Eq. 2.68 with

$$|\phi_i\rangle = \hat{T}|\tilde{\phi}_i\rangle. \tag{2.69}$$

Because $\hat{T}$ is a linear operator, the coefficients c_i^a should be linear functionals of the pseudo-wave functions:

$$c_i^a = \langle \tilde{p}_i^a | \tilde{\psi}_{n\boldsymbol{k}} \rangle \tag{2.70}$$

where $\tilde{p}_i^a$ are the projector functions. From this, it follows that the one-center expansion of the pseudo-wave function is equal to itself inside the augmentation region:

$$|\tilde{\psi}_{n\boldsymbol{k}}\rangle = \sum_i \langle \tilde{p}_i^a | \tilde{\psi}_{n\boldsymbol{k}} \rangle |\, \tilde{\phi}_i^a\rangle \Rightarrow \sum_i |\tilde{\phi}_i^a\rangle \langle \tilde{p}_i^a| = 1. \tag{2.71}$$

As a consequence, this leads to $\langle \tilde{p}_{i_1}^a | \tilde{\phi}_{i_2}^a \rangle = \delta_{i_1,i_2}$ inside the augmentation region. This implies that inside the augmentation region the projector functions $\tilde{p}_i^a$ are orthonormal to the partial wave functions $\tilde{\phi}_i^a$. These projector functions can now be applied to write the transformation operator as

$$\hat{T} = 1 + \sum_a \sum_i (|\phi_i^a\rangle - |\tilde{\phi}_i^a\rangle)\langle \tilde{p}_i^a| \tag{2.72}$$

using

$$\hat{T}^a = \sum_i \hat{T}^a |\tilde{\phi}_i^a\rangle \langle \tilde{p}_i^a| = \sum_i (|\phi_i^a\rangle - |\tilde{\phi}_i^a\rangle)\langle \tilde{p}_i^a|. \tag{2.73}$$

Finally, the AE wave function can be written as

$$|\psi_{n\boldsymbol{k}}\rangle = |\tilde{\psi}_{n\boldsymbol{k}}\rangle + \sum_a \sum_i (|\phi_i^a\rangle - |\tilde{\phi}_i^a\rangle)\langle \tilde{p}_i^a | \, \tilde{\psi}_{n\boldsymbol{k}}\rangle. \tag{2.74}$$

A schematic representation of this Eq. 2.74 can be found in Figure 2.15. More information can be found in the papers of Blöchl[74] and Rostgaard[75].

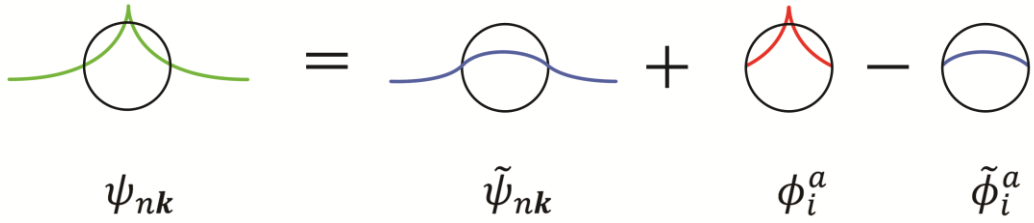

Figure 2.15 Schematic representation of the all-electron wave function using the projector augmented wave method.

2.2.7 Hellmann-Feynman theorem

When the Hamiltonian depends on a parameter λ, then the Hellmann-Feynman theorem[76,77] connects the derivative of the total energy to this parameter λ with the expectation value of the derivative of the Hamiltonian to this parameter λ. If $\mathrm{E}(\lambda)$ is the eigenvalue of the normalized eigenfunction $\Psi(\lambda)$ of the Hamiltonian $H(\lambda)$,

$$\hat{H}(\lambda)|\Psi(\lambda)\rangle = E(\lambda)|\Psi(\lambda)\rangle \qquad 2.75$$

and

$$\langle\Psi(\lambda)|\Psi(\lambda)\rangle = 1, \qquad 2.76$$

then the Hellmann-Feynman theorem states:

$$\frac{\mathrm{d}E(\lambda)}{\mathrm{d}\lambda} = \left\langle\Psi(\lambda)\left|\frac{\mathrm{d}\hat{H}(\lambda)}{\mathrm{d}\lambda}\right|\Psi(\lambda)\right\rangle. \qquad 2.77$$

Proof of this theorem can be found in text books[62].

The forces on the nuclei are calculated by taking the negative derivative of the total energy to the atomic positions $\mathbf{R}_i$ and using the Hellmann-Feynman theorem we get for an atom I the force

$$\boldsymbol{F}_I = -\nabla_{\boldsymbol{R}_I} E = -\langle\Psi|\nabla_{\boldsymbol{R}_I}\hat{H}|\Psi\rangle. \qquad 2.78$$

In equilibrium the forces acting on the nuclei are zero. This allows us to optimize the atomic positions of a structure.

Nudged elastic band calculations

Nudged elastic band calculations (NEB) can be performed using DFT. NEB is a method that allows one to find saddle points and minimum energy paths (MEPs) between two atomic configurations. The movement of atom(s) causes the change from one to the other atomic configuration (Figure 2.16a-b). From this an energy barrier is obtained that the system needs to overcome in order to undergo that transition (Figure 2.17).

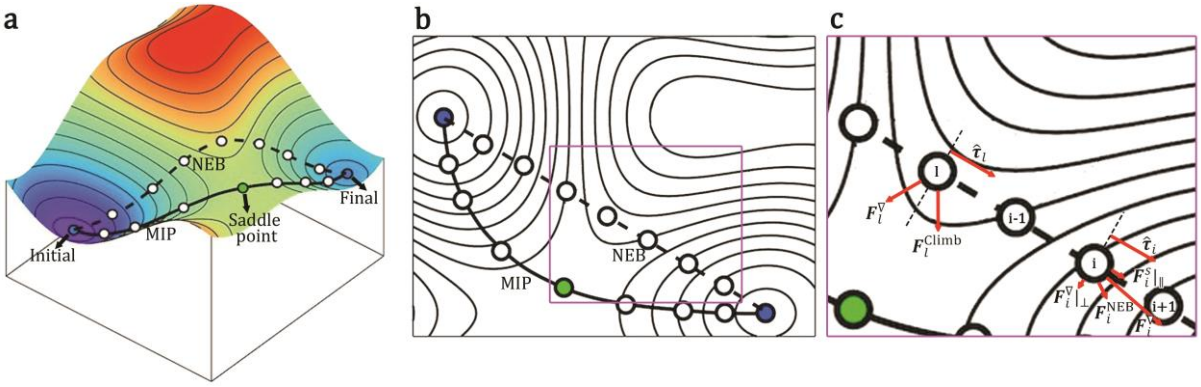

Figure 2.16 (a) 3D overview of the minimal energy path (MIP, solid black line) from the initial (blue) to final (blue) state passing through a saddle point (green) and intermediate points (white) found from a linear starting nudged elastic band path (NEB, dashed line). (b) 2D representation of the 3D representation in (a). The purple rectangle is enlarged in (c), where the different forces are represented from Eqs. 2.79 and 2.84, where image I represent the image with highest energy. Part of this image is adapted from ref. 78.

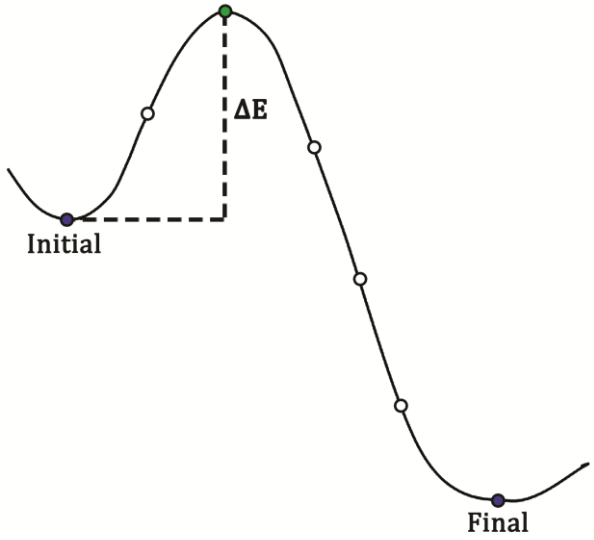

Figure 2.17 Energy barrier with energy ΔE that a system needs to overcome to go from the initial state to the final state (blue) passing to intermediate states (white) and a saddle point (green). This figure is adapted from ref. 43.

The initial and final states are known, but the intermediate states of the MIP are not. So we start from an initial guess. Next, the given intermediate images between these two atomic configurations are optimized, so each image will take on an atomic configuration with the lowest energy possible perpendicular to the path while maintaining equal spacing to neighbouring images. This is done by adding a spring interaction between adjacent images forming an 'elastic band'. The position of the N+1 images are noted as $[\boldsymbol{R}_0, \boldsymbol{R}_1, \boldsymbol{R}_2, \ldots, \boldsymbol{R}_N]$ where index 0 corresponds to the initial state and index N to the final state. The spring force $\boldsymbol{F}_i^s$ and the true force $\boldsymbol{F}_i^\nabla$, related to the potential energy gradient, are split in components parallel and perpendicular to the band, where only the perpendicular component of the true force $\boldsymbol{F}_i^\nabla|_\perp$ and the parallel component of the spring force $\boldsymbol{F}_i^s|_\parallel$ are used. The total force used during the calculation $\boldsymbol{F}_i^{\mathrm{NEB}}$ is thus the sum of both components (Figure 2.16c):

$$\boldsymbol{F}_i^{\mathrm{NEB}} = \boldsymbol{F}_i^s|_{\parallel} + \boldsymbol{F}_i^{\nabla}|_{\perp} \quad 2.79$$

with

$$\boldsymbol{F}_i^{\nabla}|_{\perp} = -\nabla E(\boldsymbol{R}_i)|_{\perp} = -\nabla E(\boldsymbol{R}_i) + (\nabla E(\boldsymbol{R}_i).\hat{\boldsymbol{\tau}}_i)\hat{\boldsymbol{\tau}}_i \quad 2.80$$

$$\boldsymbol{F}_i^s|_{\parallel} = k(|\boldsymbol{R}_{i+1} - \boldsymbol{R}_i| - |\boldsymbol{R}_i - \boldsymbol{R}_{i-1}|)\hat{\boldsymbol{\tau}}_i \quad 2.81$$

where k is a spring constant and $\hat{\boldsymbol{\tau}}_i$ is the normalized local tangent at image i. This force projection is called 'nudging'. In this way the spring force only affects the distance between the images avoiding influence on the convergence of the elastic band to the minimum energy paths and the true force doesn't cause the images to go towards the minima.

How the normalized local tangent at image i is calculated depends on the energy of image i, $i-1$ and $i+1$. If only image $i-1$ or $i+1$ has a higher energy than image i then the coordinates of image *i* and the image with the higher energy will be used to calculate the local tangent $\boldsymbol{\tau}_i$.

- if $E_{i+1} > E_i > E_{i-1}$ then $\boldsymbol{\tau}_i = \boldsymbol{\tau}_i^+ = \boldsymbol{R}_{i+1} - \boldsymbol{R}_i$
- if $E_{i+1} < E_i < E_{i-1}$ then $\boldsymbol{\tau}_i = \boldsymbol{\tau}_i^- = \boldsymbol{R}_i - \boldsymbol{R}_{i-1}$

However, if images $i-1$ and $i+1$ have both a higher or lower energy than image i then the local tangent $\boldsymbol{\tau}_i$will be calculated as a weighted average

- if $E_{i+1} > E_{i-1}$ then $\boldsymbol{\tau}_i = \boldsymbol{\tau}_i^+ \Delta E_i^{\max} + \boldsymbol{\tau}_i^- \Delta E_i^{\min}$
- if $E_{i+1} < E_{i-1}$ then $\boldsymbol{\tau}_i = \boldsymbol{\tau}_i^+ \Delta E_i^{\min} + \boldsymbol{\tau}_i^- \Delta E_i^{\max}$

with

$$\Delta E_i^{\max} = \max(|E_{i+1} - E_i|, |E_{i-1} - E_i|) \quad 2.82$$

$$\Delta E_i^{\min} = \min(|E_{i+1} - E_i|, |E_{i-1} - E_i|) \quad 2.83$$

The final used local tangent is then normalized $\hat{\boldsymbol{\tau}}_i$.

In the Climbing Image-nudged elastic band there is one modification, namely the image with the highest energy is driven up to the saddle point. The force on the image with the highest energy now becomes the image's true force with its component along the elastic band inverted to push this image up along the band and maximize the energy along the band while minimizing in all other directions in order to find the true saddle point (Figure 2.16c).

$$\boldsymbol{F}_{i_{\max}}^{\mathrm{climb}} = -\nabla E\left(\boldsymbol{R}_{i_{\max}}\right) + 2(\nabla E\left(\boldsymbol{R}_{i_{\max}}\right).\hat{\boldsymbol{\tau}}_{i_{\max}})\hat{\boldsymbol{\tau}}_{i_{\max}} \quad 2.84$$

This image does not feel the spring forces so the spacing of the images on both sides of this image will be different. More information about NEB calculations can be found in *e.g.* papers of Henkelman *et al.*[79,80].

2.3 Synthesis

The group of Lada Yashina made most of the studied samples, but $FeGe_\gamma$ was fabricated by the group of Andrei Shevelkov and Bi_2Se_3 by Artem Abakumov. A small summary of the used techniques are mentioned in this section.

All bulk samples, except Bi_2Se_3, some $Ge_mBi_{2n}Te_{(m+3n)}$ samples, GeTe and $FeGe_\gamma$, were made using the Bridgman technique[81], a melt based technique. A silica crucible containing the molten mixture is slowly pulled through a furnace, so that the negative temperature gradient solidifies the melt[82]. For Fe/Bi_2Te_3, the Fe was deposited in situ from an e-beam evaporator with the sample kept at the cleavage temperature. The evaporation rate was typically of the order of 0.05 monoatomic layers per minute.

The bulk material of Bi_2Se_3 was prepared by melting stoichiometric amounts of Bi and Se in an evacuated sealed silica tube at 800 °C for 10h, cooling down to 670 °C for 2 days, and annealing at 670 °C for 5 days. Afterwards, we determined the Bi/Se ratio as 40.6(1.8)/59.4(1.8) using energy dispersive X-ray analysis (EDX) on a scanning electron microscope (SEM).

Part of the $Ge_mBi_{2n}Te_{(m+3n)}$ single crystals were synthesized using the chemical vapor transport method. This method is based on the use of chemical transport reactions (CTR), which means all heterogeneous, reversible chemical reactions accompanied by the transfer of the original solid or liquid substance from one temperature zone to another as a result of the formation and decomposition of intermediate gaseous compounds. The crystals were grown in evacuated quartz ampoules using a two-zone horizontal furnace with a linear temperature gradient between the zones (10 degrees/cm). For synthesized crystals cold and hot zone temperatures were 400 and 500 ^oC correspondingly. The synthesis was carried out from a mixture of binary tellurides. Molecular iodine was used as a transport agent. The mass of the transporting agent was chosen so that the pressure created by it under the conditions of the transport reaction was in the range from 1 to 2 atmospheres.

The GeTe crystals were grown by direct solidification from melt enriched in Te (51 at. %). This composition lies inside the homogeneity range. High purity elemental Ge and Te were crushed in mm size species, weighted and sealed in evacuated quartz ampoules. The mixture was melted and then quenched at room temperature. Next, the ingots were annealed at 775 °C during one month with subsequent slow cooling to room temperature.

The polycrystalline samples of $FeGe_\gamma$ underwent a two-step synthesis process. First, a Fe and Ge mixture with a total mass of 0.5g with Ge/Fe ratio 1.5 was prepared. The mixture was placed inside a quartz ampoule, evacuated to the residual pressure of 1×10^{-2} torr and then sealed. The ampoules were annealed at 900 C for 5 days, cooled down to room temperature in the shut off furnace, ground and annealed again at 700 °C for 7 days. A mixture of FeGe (*P*6/*mmm*, CoSn-type) and $FeGe_2$ (*I*4/*mcm*, $CuAl_2$-type) is formed. Second, these mixtures together with 5mg of I_2 crystals (purified by sublimation) were placed into quartz ampoules,

evacuated, sealed, annealed at 480 °C for 7 days, and cooled down to room temperature in the shut off furnace. Next, the ground mixtures were annealed at 500 °C for another 7 days.

2.4 TEM sample preparation

All studied samples were bulk crystals in the order of cm, except for Fe_2Ge_3, which was a powder sample. In order to examine them in a transmission electron microscope, the size needs to be reduced to allow the electrons to pass through, hence the term 'transmission'.

The Fe_2Ge_3 powder sample was made by crushing the powder in a mortar and mixing it with ethanol. Next, this mixture is dripped onto a TEM grid, consisting of a Cu ring with a Cu raster pattern overlaid with a carbon layer containing holes. Finally, the small crystals lying on this C layer can be studied in a TEM.

All other samples were prepared using focussed ion beam (FIB) milling. For Bi_2Se_3 also other sample preparation techniques are tried but this will be discussed in more details in section 3.1. A Thermo Fisher dual beam FIB/SEM Helios NanoLab 650 was utilized to prepare FIB lamellas. It combines scanning electron microscopy (SEM) using electrons to generate an electron-mode image with focussed ion beam (FIB) microscopy using ions to generate an ion-mode image, hence the name 'dual beam'. Both beams have a cross-sectional point on the sample with an intermediate angle of 52° (Figure 2.18a). Both the ions and the electrons react with the material, resulting in the emission of secondary electrons, which are detected by the camera. Furthermore, the FIB/SEM contains a GAS Injection system (GIS) and an omniprobe (Figure 2.18a). The GIS is necessary to insert gaseous Pt inside the chamber which can be fixed onto the material using the electron or ion beam. With the omniprobe we can manoeuvre the lamella.

All the used settings during the FIB preparation are shown in Table 2.1. Before starting the FIB procedure to remove a thin slice of the bulk material, the top surface needs to be protected to avoid its removal or damage during sample preparation. First, a carbon layer outside the FIB/SEM, using a carbon coater, is applied over the surface. Inside the FIB/SEM an electron deposited Pt layer (slow deposition) is applied to the slice of interest, followed by an ion-beam deposited Pt layer (fast deposition) (Figure 2.18b,c). The layers are placed in order from the least to the most damaging. The material above and below the FIB slice is milled away with a depth of ~10 µm (Figure 2.18d-e). The milling patterns to perform this consist of multiple but overlapping patterns: the first pattern is wide while the others ones are smaller in order to remill the area closer to the slice. During the removal of the material, it should be able to sputter outside the hole, necessitating the first wide pattern. Due to material resputtering in the hole after the first wide pattern, a smaller area close to the slice is remilled. The top mill should be large enough in order to cut the slice on all sides except for one connection to the bulk material (Figure 2.18f). Then the omniprobe is connected to the sample using Pt, followed by cutting the last connection point to the bulk (Figure 2.18g). The FIB slice or FIB lamella can then be removed from the bulk (Figure 2.18h).

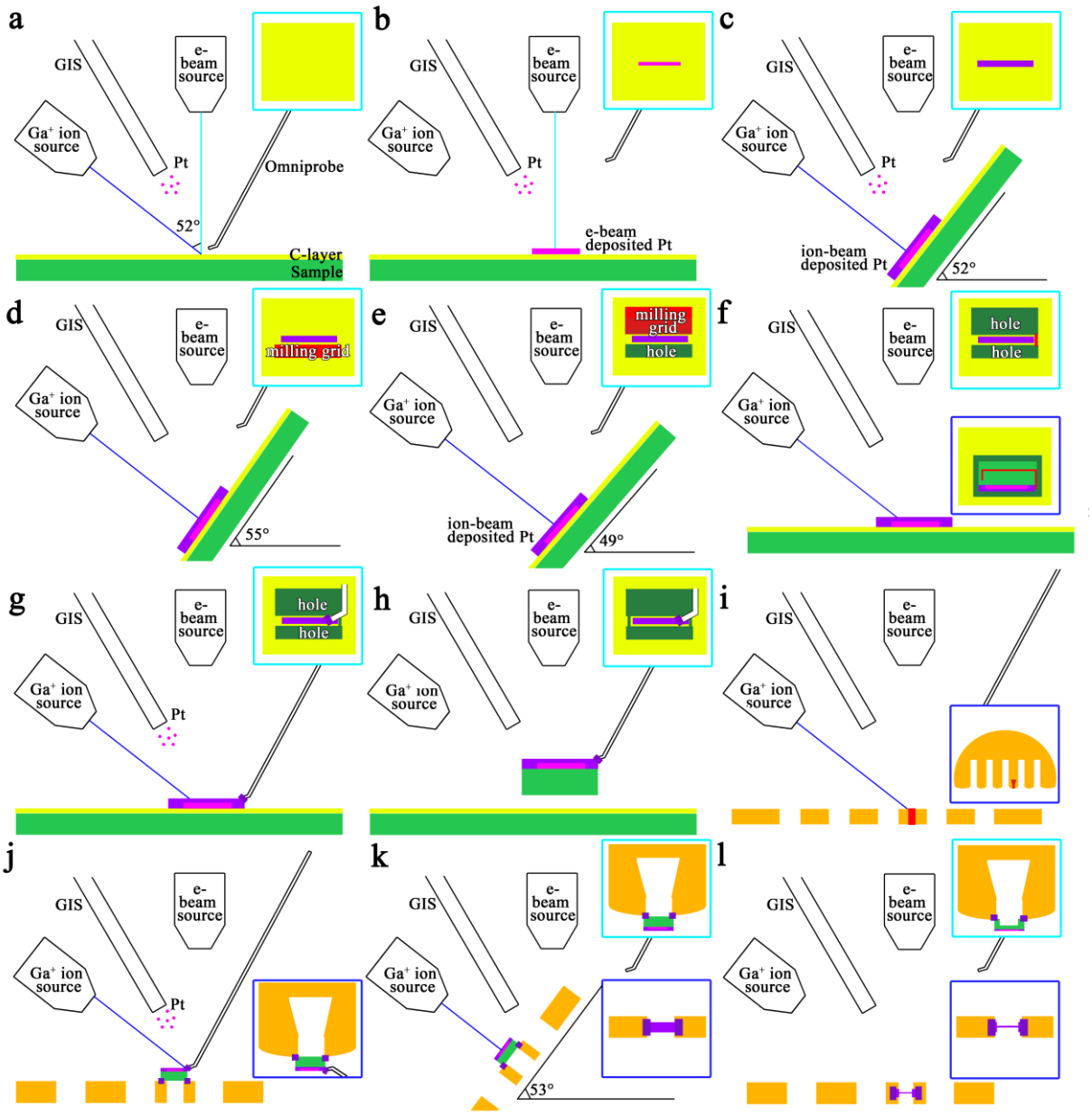

Figure 2.18 FIB procedure, where respectively in the top and bottom right corner the electron view and ion view is displayed: The sample coated with a carbon layer using a carbon coater is placed inside the FIB/SEM (a). An electron deposited Pt layer (b) followed by an ion deposited Pt layer (c) is placed onto the material to protect the surface of the sample during preparation. The material below (d) and above (e) the sample is milled away with Ga^+ ions in order to lift a slice of material out the bulk, called the FIB lamella. The slice is cut loose with Ga^+ ions from the bulk, only one small connective bridge remains in order to not let the sample fall down (f). The Pt omniprobe is attached to the FIB lamella using an ion deposited Pt bridge. The last connection to the bulk material is milled away with Ga^+ ions, and the lamella is removed from the bulk sample. The Cu grid (orange) is prepared for attaching the sample to it, by removing the red area (i). The sample is fixated to the grid using Pt (j), afterwards the omniprobe is cut loose using Ga^+ ions. The sample is thinned on both sides using different settings of current and voltage, and tilt angles. The result is a thinned FIB lamella (l).

The FIB sample is attached onto a Cu grid that is prepared by drilling two connected holes in the grid: one trapezium hole with high voltage and current to speed up the milling process and one rectangular hole with lower current so that the wide op the hole is correct for

mounting the sample (Figure 2.18i). Afterwards the sample is connected by two rectangular Pt bridges to the Cu grid (Figure 2.18j), followed by the detachment of the omniprobe by milling their connection point.

The sample is thinned in five different steps with decreasing voltage and current. The settings inside Table 2.1 are guidelines that work well for the studied materials. However, small adaptions from sample to sample were necessary. If the sample thickness perpendicular to the Pt layer is decreasing too fast compared to the Pt thickness, then the tilt angles should be decreased. If the opposite occurs, higher tilt angles should be applied. Most often the first situation happened because the studied samples were soft. For this reason, we should start with a thick enough sample (~6 µm perpendicular to the Pt layer). Furthermore, the thinning settings can change slightly depending on what we want to study: the bulk and/or the surface. If we are only interested in the bulk, it doesn't matter if the sample is still thick close to the Pt layer, however for surface examination it does matter.

Removing a slice from the bulk material

Name	Figure 2.18	Ion/e^-	Voltage [kV]	Current [nA]	Tilt [°]	X [µm]	Y [µm]	Z [µm]
e- beam deposited Pt	b	Pt, e^-	5	0.80	0	5.0	1.5	2.4
Ion-beam deposited Pt	c	Pt, ion	30	0.23	52	11	2	1.7
Bottom mill (2 patterns)	d	Ga^+	30	9.3	55	16/16	4.5/2.15	1.5
Top mill (3 patterns)	e	Ga^+	30	9.3	49	16/16/16	8/4/2	1
Undercut (3 patterns)	f	Ga^+	30	0.79	0	0.6/14/0.6	1.7/0.7/~5	'30'[1]
Pt securing	g	Pt, ion	30	0.23	0	~0.4	~0.4	1
Disconnect slice from bulk	h	Ga^+	30	0.23	0	~0.6	~3.5	'30'[1]

Preparing Cu grid and attach sample to grid

Name	Figure 2.18	Ion/e^-	Voltage [kV]	Current [nA]	Tilt [°]	X [µm]	Y [µm]	Z [µm]
Trapezium area grid	i	Ga^+	30	65	0	14.5(top)/ 10(bottom)	18	40
Rectangle area grid	i	Ga^+	30	9.3	0	8	10	40
Attach sample to Grid (2 patterns)	j	Pt, ion	30	0.23	0	3.7/3.7	3.6/3.6	1
Cutting omniprobe	j	Ga^+	30	0.23	0	8	10	1

Thinning conditions

Name	Figure 2.18	Ion/e^-	Voltage [kV]	Current [nA]	Tilt [°]	Pt thickness [µm]	X [µm]	Z [µm]
Thinning step1	k	Ga^+	30	0.79	51-53	1	7	1
Thinning step2	k	Ga^+	30	0.23	51-53	0.4	6.5	1.5
Thinning step3	k	Ga^+	30	0.08	51-53	0.15	6	2
Thinning step4	k	Ga^+	8	0.066	50-54	<0.1[2]	5.5	15s[3]
Thinning step5	k	Ga^+	2	0.023	48-56	<0.1[2]	5	15s[3]

Table 2.1 FIB settings related to the scheme is Figure 2.18. The z values used for the Ga^+ milling correspond to how deep we would mill a Si material using these setting. The viewing ion beam conditions are 0.0077 nA at 30kV and the electron beam conditions 0.80nA at 5kV. [1]Mill until you have removed all needed material. [2]The material is thin, thus observe the sample during thinning. [3]Use small thinning intervals to prevent milling the complete sample.

2.5 Software, microscopes and equipment

The SAED data was acquired on a Thermo Fisher Tecnai G2 or on a Phillips CM 20 operating at 200 kV. The HAADF STEM and STEM-EDX data was collected on aberration-corrected Thermo Fisher Titan Transmission Electron Microscopes operating at 200 kV or 300 kV with an ultimate resolution of 0.8 Å, one of which is equipped with a Super-X four detector system. The HAADF STEM simulations were performed using the MULTEM software package[83] and the QSTEM package[84]. Powder X-ray diffraction (PXRD) data was collected on a Huber G670 diffractometer. The first-principles calculations were carried out using density functional theory (DFT), encoded in the Vienna Ab initio Simulation Package (VASP)[85–88]. The

programs PETS[89] (Process Electron Tilt Series) and Jana2006[90] are used for the data treatment for EDT. Jana2006[90] is also used for the data analysis of PXRD. To prepare most of our TEM samples a Thermo Fisher dual beam FIB/SEM Helios NanoLab 650 was utilized, otherwise crushing or cryo-crushing was performed.

Chapter 3 Bulk structures

In this chapter I will determine the bulk structures of different kinds of topological insulators. First, I will solve the defect structure of a standard prototype example of a topological insulator, Bi_2Se_3. Then, I will unravel the structure of In doped Bi_2Se_3, followed by Se doped Sb_2Te_3. Both material systems are a mixture of a topological insulator with a normal insulator. Finally, I will reveal the different structures of the $Ge_mBi_{2n}Te_{(m+3n)}$ series.

Almost all structures in chapters 3 to 5 are represented in a hexagonal unit cell. If there can be confusion about the type of unit cell, the type is explicitly mentioned: H stands for hexagonal, R for rhombohedral and C for cubic. From now on, the following colour scheme is used: Red and yellow colours indicate the cations and the cation defects (mixed sites are orange); Green and purple colours represent the anions and the anion defects; and blue colours depict another type of material (oxygen or Fe addition).

3.1 Bi_2Se_3

This section is based on the paper: Callaert Carolien, Bercx Marnik, Lamoen Dirk, Hadermann Joke, *Interstitial defects in the van der Waals gap of Bi_2Se_3*, Acta Crystallographica B, Structural Crystallography and Crystal Chemistry B75 (2019), p 717-732[91].

3.1.1 Introduction

Bi_2Se_3 is both a thermoelectric material[34] and topological insulator. Nevertheless, Bi_2Se_3 slightly conducts in its bulk due to the presence of defects[25,92]. Compared to other materials like Bi_2Te_3, Bi_2Se_3 has a larger bandgap of 0.3 eV[25,27], which opens the door to spintronic applications at room temperature, such as memory devices. For example, recently Han *et al*.[27] observed a high spin-orbit torque efficiency on the magnetic layer CoTb by Bi_2Se_3. Bi_2Se_3 is also an ideal study sample and application-friendly due to its robust and simple surface states where the Dirac point lies inside the bandgap[25].

Defects influence the physical material properties, *e.g.* electrical[93,94], optical[94], mechanical[94] and transport[95,96] properties. They also determine the carrier concentration[97] and can modify the band structure by shifting the Dirac point energy and Fermi energy[95,98]. The Fermi level affects whether the bulk character is insulating or conducting. To achieve the ideal properties for a specific application, the native defects need to be optimized[99]. In theory, native and intrinsic point defects differ: intrinsic point defects are point defects in stoichiometric materials, native point defects in non-stoichiometric materials. In practice, however, people are less strict with these terms[99]. The thermoelectric performance depends *i.a.* on the Seebeck coefficient, the electrical conductivity and the carrier thermal conductivity. These parameters are influenced by the carrier concentration, which in turn depends on the amount and the character of the defects. Note that extrinsic doping can influence the formation energy of these defects, thus increasing or decreasing their chance of existence and consequently affecting the carrier concentration[99].

Not only the static point defects, but also the movement of point defects is important. For example, Bi_2Se_3 shows potential for Li-ion batteries[100,101], and Bi_2Se_3 integrated with carbon has already been proven to be a high-performance sodium-ion battery anode material[102]. Related topological insulators also already have applications in phase change devices. The phase transition is induced by temperature, laser or electric field, necessitating the study of the movement of defects as these can be the first step towards the transition. For example, the switching energy decreased for a structure consisting of alternating GeTe (normal insulator) and Sb_2Te_3 (topological insulator) layers, a material designed for interfacial phase-change memory (IPCM) devices[103–105]. Furthermore, Bi_2Te_3 nanowires are promising for phase-change random access memory (PRAM) applications[106].

The basic structure of Bi_2Se_3 consists of quintuple layers (QLs), Se1-Bi-Se2-Bi-Se1, where the QLs are weakly bound by van der Waals (VdW) interactions (Figure 3.2a)[20,107]. However, different kinds of native defects are observed or theoretically predicted for Bi_2Se_3: Se and Bi vacancies[95,98,108–114], substituted atoms[95,98,108,112–116], interstitial Se atoms[95], interstitial Bi atoms[93,117,118] and Bi_2 layers in the VdW gap[116] (Figure 3.2). Different settings, for example growth kinetics (*e.g.* fast/slow cooling)[95], the Bi/Se ratio[95,99,117], extrinsic doping[99], deformation after synthesis[99], and annealing[99], lead to different defect concentrations. Se substituted at the Bi sites and Bi vacancies have so far only been found with theoretical calculations for Se-rich samples[108,112,114]. For Bi_2Se_3, Se vacancies V_{Se}, especially on the outer Se layers, and in lesser amount Bi substituted at the Se positions Bi_{Se}, are the most commonly accepted defects [95,98,108–110,112–115].

In the equilibrium phase diagram of the Bi-Se system (Figure 3.1) a Bi_2Se_3 homogeneity range bounded by a (curved) solidus line is present wherein the material takes on the Bi_2Se_3 structure. In this homogeneity range the structure does not change, while the selenium concentration varies continuously[119]. The compound with the 40:60 stoichiometric ratio will contain Bi_2Se_3 combined with an addition of Se or liquid, because it falls outside the homogeneity range of Bi_2Se_3. The deviation from stoichiometry towards the Bi side is realised by increasing the Se vacancy concentration. For this reason, Bi_2Se_3 crystals are always of n-type.

Several examples in the literature indicate the existence of Se and Bi interstitials: Dai *et al.*[95] suggested the presence of Se interstitials (Figure 3.2c) in the VdW gap based on their high resolution scanning tunnelling microscopy (HR STM) observations combined with first-principles simulations. However, others[92,98,111] previously proposed Se vacancies based on analogous observations. Despite their thorough argumentation, the Se interstitial atoms were not unambiguously determined. Urazhdin *et al.*[118] mentioned Bi interstitial defects in the VdW gap observed with scanning tunnelling microscopy and scanning tunnelling spectroscopy (STM-STS). However, interpretation of these data is not straightforward, especially without simulations, as follows from the work of Dai *et al.*[95]. Jia *et al.*[117] used indirect observations (increase of the cell parameters and a shift on the diffraction peak (015)) to suggest the presence of Bi interstitial defects for a 2:1.5 Bi:Se ratio prepared sample. Finally, Tumelero *et al.*[93] found two stable Bi interstitial sites in the VdW gap using

theoretical calculations: Bi in an octahedral coordination, Bi_{oct}, and in a tetrahedral coordination, Bi_{tetra} (Figure 3.2c). They optimized the lattice parameters of the structures with defects and determined that Bi_{oct} had a lower formation energy than Bi_{tetra}. In fact, Bi_{oct} possessed the lowest formation energy among all defects for a Bi-rich sample and lowest or second lowest for a Se-rich sample, which indicates that its existence is plausible.

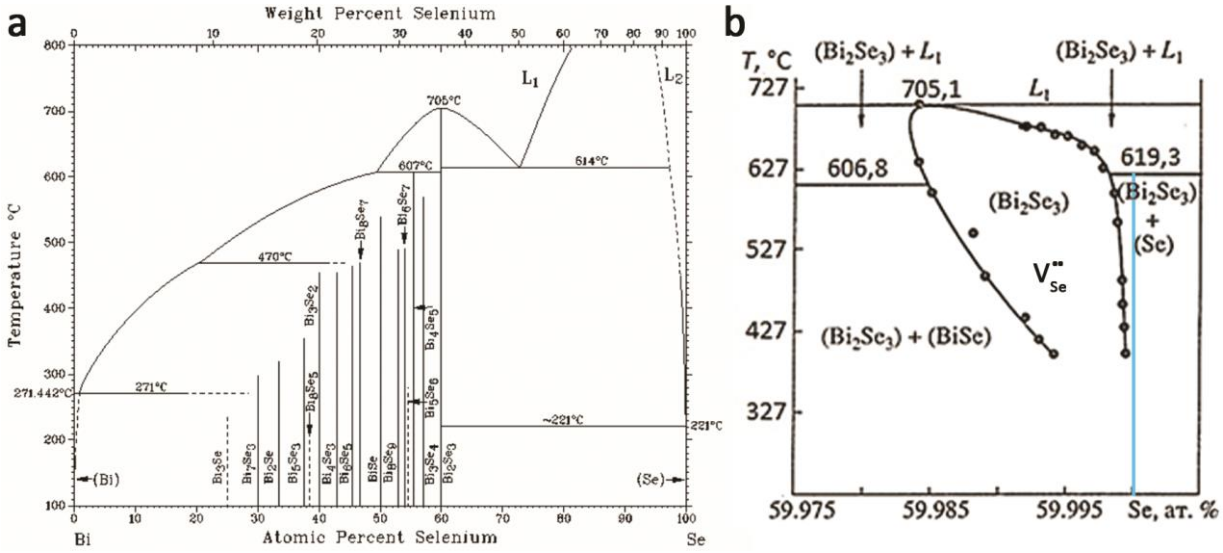

Figure 3.1 (a) Phase diagram of the Bi-Se system[120]. (b) Fragment of the phase diagram near the Bi_2Se_3 compound[121]; the 40:60 Bi:Se composition is marked with a blue line. When the material has the 40:60 Bi:Se composition, it falls outside the homogeneity range, where the material would take on the structure of Bi_2Se_3 without the addition of Se, BiSe or liquid. The material in this homogeneity range is n-type, and contains $V_{Se}^{\bullet\bullet}$ defects. The •• symbol indicates that the defect has a +2 charge.

Although these examples from the literature suggest the existence of Bi and Se interstitial defects, clear and direct experimental evidence is still lacking. In this section, we show the existence of interstitial defects inside the VdW gap using a combination of state-of-the-art techniques: scanning transmission electron microscopy (STEM) using an aberration corrected TEM, energy dispersive X-ray (EDX) spectroscopy using a four-detector Super-X configuration and precession electron diffraction tomography (PEDT). We compare our experimental results with first-principles calculations using density functional theory (DFT) to study the formation energy of the defects and their movement across and along the VdW gap. We also discuss our attempts at structure characterization with X-ray powder diffraction (PXRD) and single crystal X-ray diffraction (SCXRD). We show that for this specific case, PEDT with dynamical refinement seems the most reliable method to investigate the occurrence of interstitial defects.

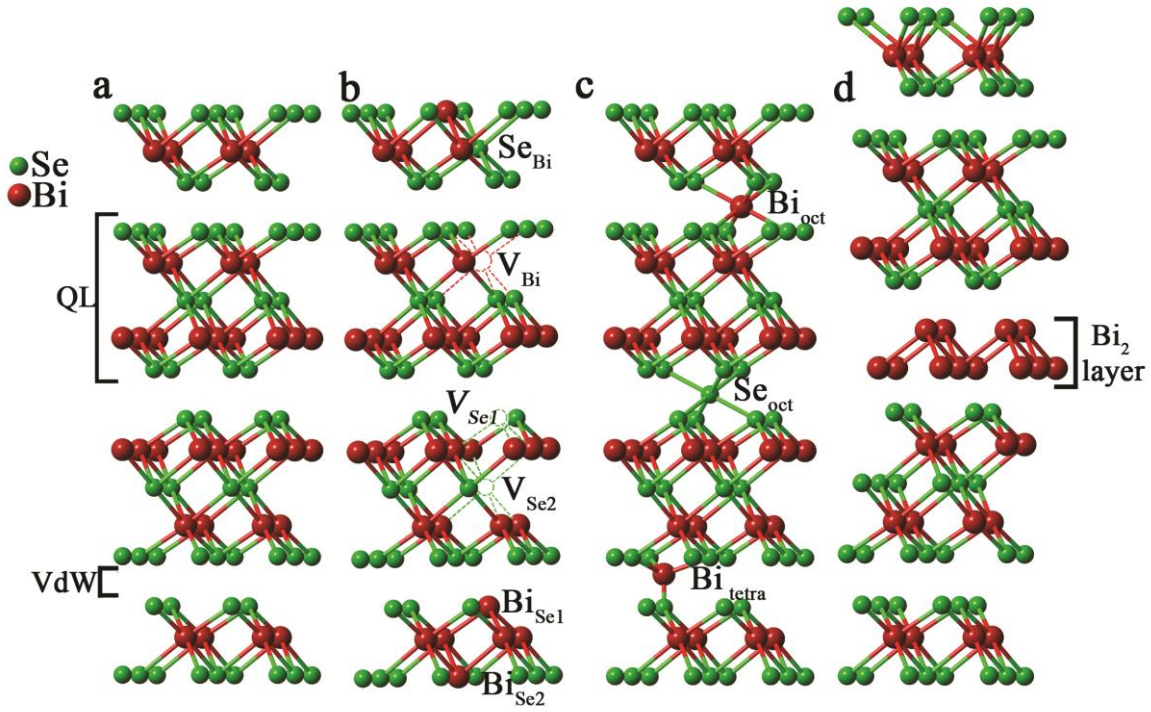

Figure 3.2 (a) Basic structure[20] of Bi_2Se_3, consisting of quintuple layers (QLs), Se1-Bi-Se2-Bi-Se1, with van der Waals (VdW) interactions between the QLs. (b) Visualization of the Se vacancies in the outer layers of the QL (V_{Se1}) and central Se layer (V_{Se2}), Bi vacancies (V_{Bi}), the substituted defects where Bi is substituted in the inner and outer layers of the QL (respectively Bi_{Se2} and Bi_{Se1}) and Se on the Bi sites (Se_{Bi}). (c) Interstitial Bi defects in the van der Waals gap in the octahedral (Bi_{oct}) and tetrahedral coordination (Bi_{tetra}) and interstitial Se in an octahedral coordination. (d) Bi_2 layer modelled from the HAADF STEM images of Huang *et al.*[116]. Green spheres are Se; red spheres are Bi. The corresponding references can be found in the main text.

3.1.2 Methodology

3.1.2.1 TEM

The STEM and EDX data were acquired on aberration-corrected Thermo Fisher Titan transmission electron microscopes operating at 300kV with an ultimate resolution of 0.8 Å. The EDX data is obtained with a Super-X four detector system. Calculated STEM images were made with QSTEM[84].

Precession electron diffraction tomography (PEDT) data was acquired on a Thermo Fisher Tecnai G2 electron microscope at 200kV, using a CCD camera (2048x2048 pixels) and equipped with the ASTAR system from Nanomegas. Every 1° a precessed selected area electron diffraction pattern was taken from -21° to 76° (98 images) using a precession angle of 1° to minimize dynamical effects, and by tilting over the goniometer axis. The crystal had a random orientation at the start of the tilt series.

The program PETS[89] (Process Electron Tilt Series) was used to find the reflections, refine the orientation matrix, perform the cluster analysis and integrate the diffracted intensities. Next, the cluster reciprocal space was indexed using Jana2006[90], software which we also used to perform the structure refinement. The model for the kinematical refinement was the basic

quintuple layer structure without defects. Afterwards, a dynamical refinement was performed, as implemented in the module Dyngo (refinement parameters: R_{sg} = 0.4 , g_{max} = 2, 128 integration steps)[122–124]. An optimization of the orientation of each pattern was performed, and the frames with a tilt angle deviation higher than 0.5° were removed (9 frames). The refined parameters are the scale factors of the 89 frames, the occupancies, the positional parameters and the isotropic displacement parameters for all atoms, with some restrictions which are discussed in section 3.1.3.2. The cell parameters were updated to those determined from the PXRD data, which provides more accurate values, as the exact magnification of electron diffraction patterns can be anisotropic due to microscope aberrations and the total magnification can vary slightly during the series due to voltage instabilities and slight differences in sample height.

3.1.2.2 XRD

Powder X-ray diffraction (PXRD) data was acquired on a Huber G670 diffractometer, using Cu-K_α radiation (λ = 1.54059 Å). Lebail and Rietveld refinement were performed in Jana2006[90]. Pseudo-Voigt functions consisting of the Gaussian parameters U, V, and W and the Lorentzian parameters X and Y, combined with an asymmetric correction by divergence[125] were used to fit the PXRD data. Anisotropic strain broadening using the tensor method was applied. Ten Legendre Polynomials fit the background and a shift correction was introduced. The preferred orientation was corrected in the March Dollase approach[126–128].

3.1.2.3 DFT

First-principles calculations were carried out using density functional theory (DFT), encoded in the Vienna Ab initio Simulation Package (VASP)[85–88]. The generalized-gradient approximation of Perdew-Burke-Ernzerhof (PBE)[64] was used for the exchange and correlation energy. The Projector-Augmented Wave (PAW) method[129,130] was applied to describe the interactions between the ionic cores and the valence orbitals. $5d^{10}$ $6s^2$ $6p^3$ are the valence electrons for Bi and $4s^2$ $4p^4$ for Se. The VdW interaction was included using the optB86b-VdW density functional in VASP[66,67]. A plane wave basis with cut-off energy of 400 eV was utilized to describe the atoms in a 3x3x1 hexagonal cell. For the structural relaxation a 3x3x1 Γ-centred k-point grid was used to sample the Brillouin zone.

The lattice parameters, volume and atomic positions were optimized for the bulk structure without defects. For the structures with defects, only the positions of the atoms in the three layers above and below the interstitial defect inside the VdW gap along the c-axis were optimized, as explained in more detail in section 3.1.3.4. For the electronic self-consistency loop, convergence is achieved when the total free energy change and band structure energy change are both smaller than 10^{-5} eV between electronic steps. The structure is considered converged when the forces on the atoms are smaller than 0.01 eV/Å. Finally, an additional electronic optimization including spin-orbit coupling (SOC) was performed, based on the geometry obtained from the structural optimization and without using the VdW interaction.

The equilibrium concentration of a defect D is determined by the defect Gibbs free energy of formation $G_f[D]$[131]

$$c \sim e^{-\frac{G_f[D]}{k_B T}} \quad 3.1$$

where $G_f[D]$ depends in principle on pressure P and temperature T, and k_B is Boltzmann's constant. However for solids this (P,T) dependence can be neglected in a first approximation[131] and $G_f[D]$ then reduces to the defect formation energy $E_f[D]$, which for a defect in a charge state q is defined by

$$E_f = E_{tot}[D] - E_{tot}[bulk] - \sum_i \Delta n_i \mu_i + q\, \mu_e\ , \quad 3.2$$

where $E_{tot}[D]$ is the total energy of the structure with a defect and $E_{tot}[bulk]$ that of the ideal defect-free structure. Δn_i is the number of added (positive) or removed (negative) atoms of element i, μ_i are the chemical potentials of element *i* (*i* =Bi, Se) and μ_e is the chemical potential of the electrons (the "Fermi energy"). Since the bandgap of Bi_2Se_3 is rather small we limit ourselves to neutral point defects ($q = 0$) in this work[132].

The chemical potentials μ_i ($i =$ Bi, Se) reflect the influence of the reservoirs with which atoms are exchanged to create the defect and the actual value depends on the experimental growth conditions. The chemical potentials are considered as variables[133], but are subjected to several constraints. An upper bound follows from the fact that precipitation of the elemental phase should be avoided

$$\mu_i \leq \mu_i^0\ (i = \text{Bi, Se})\ , \quad 3.3$$

where μ_i^0 is the chemical potential of the elemental phase and where *e.g.* $\mu_{Bi} = \mu_{Bi}^0$ corresponds to Bi-rich (or Se-poor) conditions.

The hexagonal R$\bar{3}$m structure (6 atoms) is used to calculate μ_{Bi}^0 and the trigonal $P3_121$ structure for μ_{Se}^0 (3 atoms)[112,132]. Hexagonal unit cells were chosen for all materials (Bi_2Se_3, Se and Bi), resulting in a maximal error cancellation when the same k-point density in reciprocal space is used[132], leading to a 9x9x3 mesh for Bi and a 9x9x9 for Se.

Since the numerical value of μ_i depends on the used reference, we prefer to work with

$$\Delta\mu_i = \mu_i - \mu_i^0, (i = \text{Bi, Se}). \quad 3.4$$

The formation enthalpy of Bi_2Se_3, defined by

$$\Delta H_f = E_{tot}[\text{Bi}_2\text{Se}_3] - 2\,\mu_{Bi}^0 - 3\mu_{Se}^0\ , \quad 3.5$$

can then be rewritten as

$$\Delta H_f = 2\,\Delta\mu_{Bi} + 3\,\Delta\mu_{Se}\ . \quad 3.6$$

In Eq. 3.5 $E_{tot}[Bi_2Se_3]$ is the total energy per formula unit. The upper bounds of Eq. 3.3 in combination with Eq. 3.6 provide also lower bounds for $\Delta\mu_{Se}$ and $\Delta\mu_{Bi}$,

$$\Delta\mu_{Bi} \leq 0 \Longrightarrow \Delta\mu_{Se} \geq \frac{1}{3}\Delta H_f \qquad 3.7$$

$$\Delta\mu_{Se} \leq 0 \Longrightarrow \Delta\mu_{Bi} \geq \frac{1}{2}\Delta H_f \,. \qquad 3.8$$

The defect formation energy, given by Eq. 3.2, can be written in a more convenient form by using Eqs. 3.4 and 3.6,

$$E_f(\Delta\mu_{Se}) = E_f^0 - \frac{1}{2}\Delta H_f \Delta n_{Bi} + \left(\frac{3}{2}\Delta n_{Bi} - \Delta n_{Se}\right)\Delta\mu_{Se} \,, \qquad 3.9$$

where E_f^0 is the defect formation energy of Eq. 3.2 as a function of the reference chemical potentials μ_{Bi}^0 and μ_{Se}^0. Equation 3.9 will be used later when discussing the various defects and shows that the defect formation energy depends linearly on the chemical potential $\Delta\mu_{Se}$. A similar expression can be derived for $E_f(\Delta\mu_{Bi})$.

Finally, the minimum energy path for certain defect migrations is calculated using the climbing image modification of the nudged elastic band (NEB) method[79,80] using seven intermediate images between start- and final configuration with inclusion of the VdW interaction. Afterwards, SOC was applied to the images with the lowest and highest total energy in order to determine the energy barrier of the path including SOC but without optimizing the atomic coordinates or lattice parameters.

3.1.3 Results

3.1.3.1 STEM/EDX

Preparation techniques can introduce or affect defects, so we tried completely different sample preparations to rule out, as much as possible, the effects of sample preparation on our results: (i) focussed ion beam (FIB) milling (ii) scotch tape method (iii) liquid-phase-exfoliation (iv) cryo-crushing.

The explanation about the first method, FIB milling, can be found in section 2.4. The second method was the Scotch tape method. The Scotch tape method was first utilized to obtain a single layer of graphite, *i.e*. graphene[134]. Due to the weak van der Waals interaction between the quintuple layers of Bi_2Se_3, this method was also tried out on Bi_2Se_3. First, the tape is placed onto the bulk material, followed by pulling the tape off to remove pieces of the bulk. Repeating this procedure further reduces the size. Next, the tape is soaked in acetone to extract the small crystals from the tape. Then, the crystals are mixed with ethanol and placed on a TEM grid. This TEM grid is a Cu ring with crossed Cu bars inside forming a raster. Over these bars a carbon layer with holes is deposited. The dissolved glue is mostly present as contamination on the Cu grid, rendering this sample preparation unsuccessful. Without

using acetone and pasting the tape directly on the Cu grid destroys large areas of the C layer of the TEM grid, resulting in a low amount of crystals rendering this method not useful.

The third method was the liquid-phase-exfoliation method, which is a chemical exfoliation method in comparison to the mechanical exfoliation method, the Scotch tape method. Also this method is used for obtaining few layers of graphene[135]. The settings are based on the ones used by Sun *et al.*[136] who obtained few-layer Bi_2Se_3. The basic principle comprises of placing the material inside a small tube filled with a suitable solvent inside an ultrasonic bath. After sonification and letting the material rest without movement the top part of the liquid is deposited in a centrifuge in order to filter out the smallest crystals from the liquid. The centrifuge part was not necessary in our case.

In an ultrasonic bath high frequency waves are generated in the liquid and propagate inside it. The acoustic pressure wave compresses (molecules are close together) and rarefies (molecules are far from each other) while propagating. When the pressure inside the rarefied part of the wave is lower than the vapour pressure of the liquid, a void or cavity bubble is created inside the liquid. When it explodes close to the material, the cavity is filled rapidly with liquid leading to an intense shock wave enabling the removal of contamination[137] or in our case pieces of material due to the breakage of the weak van der Waals bonding.

The bulk crystal itself is cut at room temperature to obtain a crystal with a size of about 1 cm^2 x 1 mm. This small crystal is placed in a glass tube filled with isopropanol in an ultrasonic bath filled with tap water for a total of four hours. Due to the ultrasonic waves the water heats up, so every 30 min the water is replaced to avoid damaging the material due to high temperatures. The maximum temperature was 40 °C. Next, we let the liquid rest, so that the heavy particles can sink faster to the bottom than the smaller particles. After a couple of hours when the top part of the liquid in the veil becomes transparent, this transparent part is dripped onto a Cu grid overlaid with a carbon layer using a pipet.

The fourth sample preparation method is cryo-crushing. A small crystal of mm size, cut at room temperature, is placed in a metal bowl which is in contact with liquid nitrogen (77 K) achieving the same temperature. The material itself is crushed with a ceramic mortar. The crushed pieces are placed into a glass tube filled with ethanol and put inside an ultrasonic bath. After 5 minutes, this mixture is dripped onto a TEM grid.

Bi_2Se_3 is a layered material where visualization of this layering is important. Furthermore, the resolution of a transmission electron microscope is limited, so the distances between the projected columns should be large enough (>0.8 Å) to be able to separate them in a STEM image. Due to the latter two reasons, the $<100>_H$ or $<110>_H$ zones are ideal zones for STEM imaging. The samples should also be translucent or thin enough and the tilting range of the holder is limited, so the preferred zone should be in tilt range.

Like previously mentioned, the Scotch tape method was not a good method due to the low particle quantity or high contamination. Furthermore, the zone limitation rendered the

method 'liquid-phase-exfoliation' not useful for STEM, because the crystals laid dominantly along the <001> zone or a close neighbouring zone, making the tilt degree for the <100> zone too high (~90°). However, it prepares nice TEM samples, so for EDT where a specific zone is not necessary this method is useful.

FIB was the easiest method to prepare samples to study the <100> zone. The layered structure was parallel with the surface and due to the limitless cutting angle (360°) the right zone was always accessible. However, sample preparation can damage the structure of a material, so care should be taken. A second successful method was cryo-crushing, but preferential orientation of the crystals along the <001> zone complicated the search for the right crystal zone. Furthermore, crushing can also damage the structure. Only FIB and cryo-crushing produced samples in the right zone axis for STEM. So, these two methods will be used for the STEM imaging and we choose cryo-crushing for EDT.

The stacking of the quintuple layers (QLs) is visible in the high-angle annular dark-field scanning transmission electron microscopy (HAADF STEM) images along the [010] zone (Figure 3.3). The samples contained the same defects, independently of the used preparation technique: Bi substituted at the Se outer layers of the QLs, interstitial defects in the van der Waals (VdW) gap and interstitial defects in the middle and outer Se layers of the QLs. The first defect can be recognized by some atom columns in the outer Se layers (indicated by blue arrows in Figure 3.3) being brighter than those in the central Se layers of the QLs. The grey scale of an atomic column in HAADF STEM scales with the averaged atomic number Z of the atoms in that column. Thus, a Se column that contains Bi atoms at some of the Se positions appears brighter than a pure Se column (Figure 3.4). The interstitial defects can be recognized by the appearance of extra dots in between the regular atom columns (purple, green and yellow arrows in Figure 3.3). The interstitial defects have a tendency to cluster. A similar example of cluster formation was found in $(Bi_{1-x}In_x)_2Se_3$ where substituted In atoms have this cluster inclination on the Bi positions[138], which is in agreement with the thermodynamically proneness to demix in the equilibrium phase diagram of Bi_2Se_3-In_2Se_3 [139]. The reason why the defects cluster in Bi_2Se_3 is not known. Comparison with HAADF-simulations suggests that the interstitial defect inside the VdW gap occupies an octahedral site rather than a tetrahedral site (Figure 3.5). We found Bi substituted on the middle Se layers only in the cryo-crushed sample, which might be because on the crushed particles we study the edges of the sample, while the FIB samples are made from sections through the bulk.

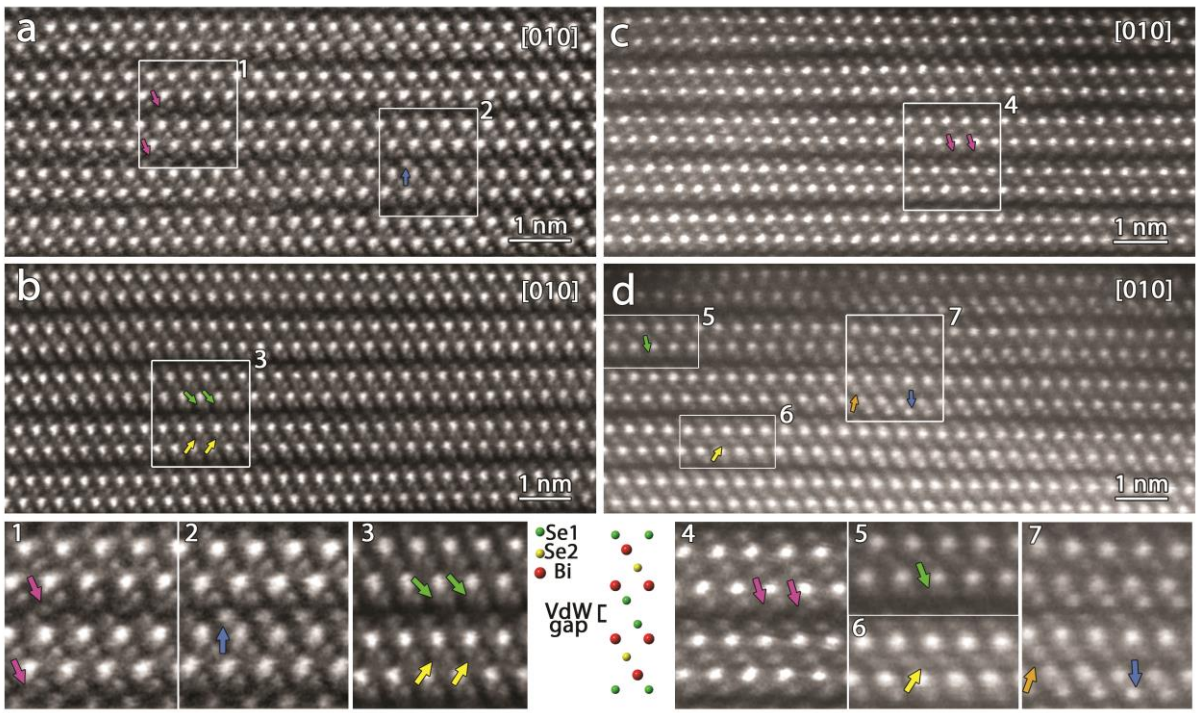

Figure 3.3 HAADF STEM images from a FIB prepared sample (a and b) and a cryo-crushed sample (c and d), with magnified areas displayed at the bottom of the figure combined with a unit cell of a defect free structure at the same scale as the magnified images (1-7). Purple arrows (1 and 4) mark the interstitial defects in the VdW gap. Yellow arrows highlight the interstitial atoms in the central Se layer of the quintuple layer (QL) (3 and 6) and green arrows in the outer Se layers (3 and 5). Bi also occupies Se sites in the outer Se layers of the QLs, indicated with blue arrows in 2 and 7. An orange arrow marks Bi in the middle Se layer (7).

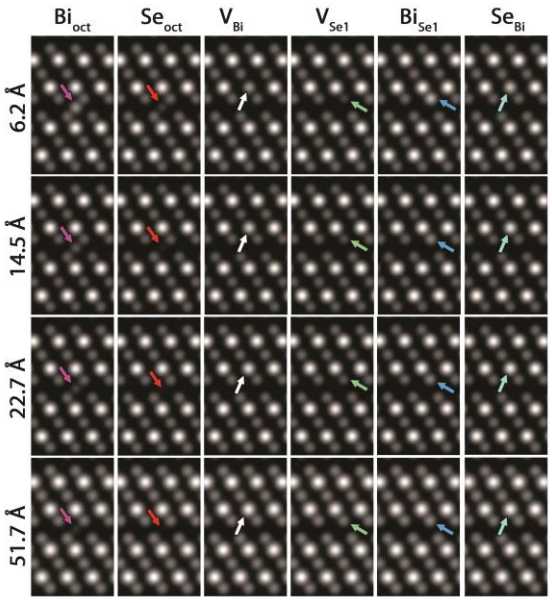

Figure 3.4 HAADF STEM simulations using QSTEM[84] of different defects at different thicknesses when accounting for one defect: interstitial Se (red arrows) and Bi (purple arrows) defects in the van der Waals gap, Bi (white arrows) and Se (green arrows) vacancies and substitutional defects (Bi_{Se1} is marked with bright blue arrows and Se_{Bi} with light blue arrows). An expected trend due to the Z dependency of HAADF STEM images throughout the simulations is that the defects caused by Bi (Bi_{oct}, V_{Bi} and Bi_{Se1}) are more visible at the same thickness than the corresponding Se caused defects (Se_{oct}, V_{Se} and Se_{Bi}).

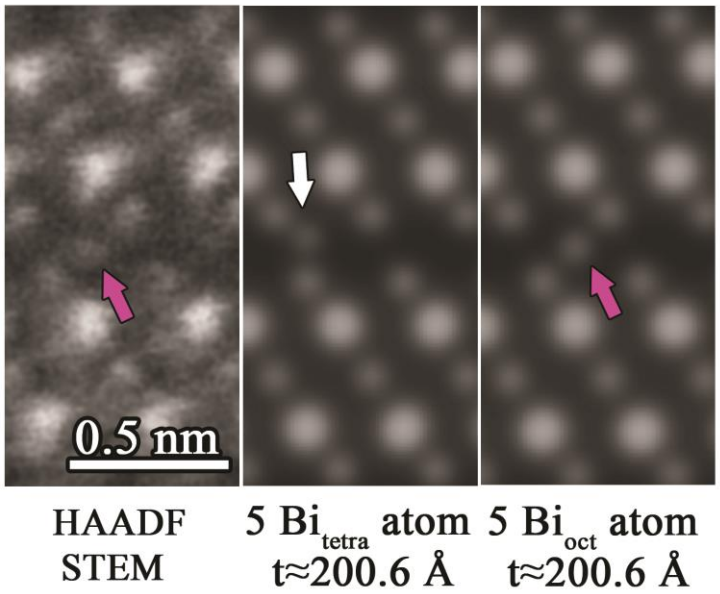

Figure 3.5 HAADF STEM (left, smaller area of Figure 3.3a.1) with simulated images using QSTEM[84] of zone [010] with five Bi atoms at the tetragonal site (Bi_{tetra}) (middle, white arrow) and five at the octahedral site (right, purple arrow) in the VdW gap to verify the coordination of the interstitial defect. The thickness of the simulated samples is 200.6 Å, a realistic thickness for a FIB sample prepared as described in the method section[140]. The edges of a crushed sample can be as thin as a few Å. The amount of defects is chosen in such a way that the relative contrast of all columns is similar to the experimental image for a sample thickness of 200.6 Å.

The interstitial defect in the VdW gap appears mobile in the cryo-crushed sample. Figure 3.6 display one specific trajectory: an atom jumps from the Se outer layer through the VdW gap to the outer Se layer of the neighbouring QL, resulting in temporary interstitial defects in the VdW gap. The STEM-EDX map (Figure 3.7) shows that the chemical nature of this defect is mainly bismuth. Furthermore, if only one atom shifts its position, the movement of Bi would be more visible than of Se in a HAADF STEM image, due to the lower Z value of Se (Figure 3.4). The line profile of the STEM-EDX map shows several small Bi peaks away from the Bi layers of the ideal Bi_2Se_3 structure. The position marked on the EDX map (Figure 3.7) with a pink arrow shows a clear Bi signal at the octahedral position, however, the profile shows the corresponding peak shifted more towards the upper Se layer. We propose that this apparent discrepancy is due to the mobility of the Bi atoms. In the EDX map, Bi is clearest where it does not overlap with the strong Se signal, but the profile cumulates the different signals of Bi along its path, undisturbed by the Se signal. Similarly the peaks of other interstitial positions deviate from their expected positions. One Se signal is present in the centre of the VdW gap in the line profile, and the outer Se layer of the QL above has a smaller peak height than the Se peak of the QL below (Figure 3.7). This suggests that Se moved from the Se layer above the VdW gap to the VdW gap. On the HAADF STEM image of the EDX map the interstitial defects are not seen, because the HAADF STEM image is only one instance of a time series of images of the area while the maps are the sum of the different scans of the area over the whole time interval. A small Bi peak, indicated with a Bi_{Se1} arrow, exists in the line profile at the same position as an outer Se peak, in Figure 3.7. The outer Se peak also

has a lower signal in comparison to the other Se peaks, implying Bi substituted at the outer Se layer.

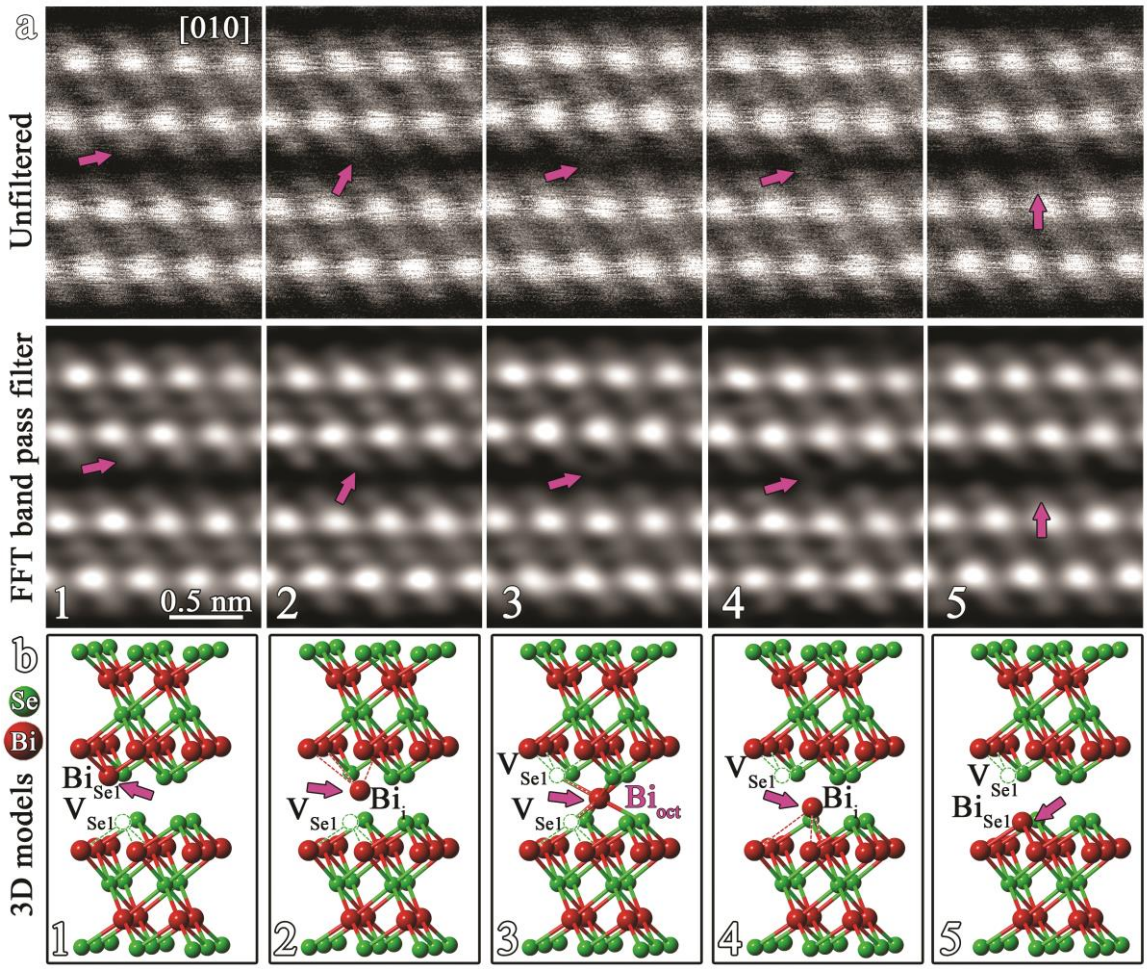

Figure 3.6 (a) Time series (every 20.1s) of the unfiltered (top) and FFT band pass filtered (bottom) HAADF STEM images from the cryo-crushed sample along [010] of the temporary creation of an interstitial defect in the VdW gap, marked with purple arrows. (b) Schematic model of the observation in Figure 3.6a: a Bi atom at the Se1 position (Bi_{Se1}) (1) migrates toward the VdW gap, moving through a temporal displaced non-octahedral site (Bi_i) (2) and finally creates a Se1 vacancy (V_{Se1}) and an interstitial Bi atom (Bi_{oct}) (3). Next, the atom goes to a non-octahedral site (Bi_i), removing the interstitial defect in the octahedral site (4) and jumps into a vacancy in the neighbouring Se layer (5).

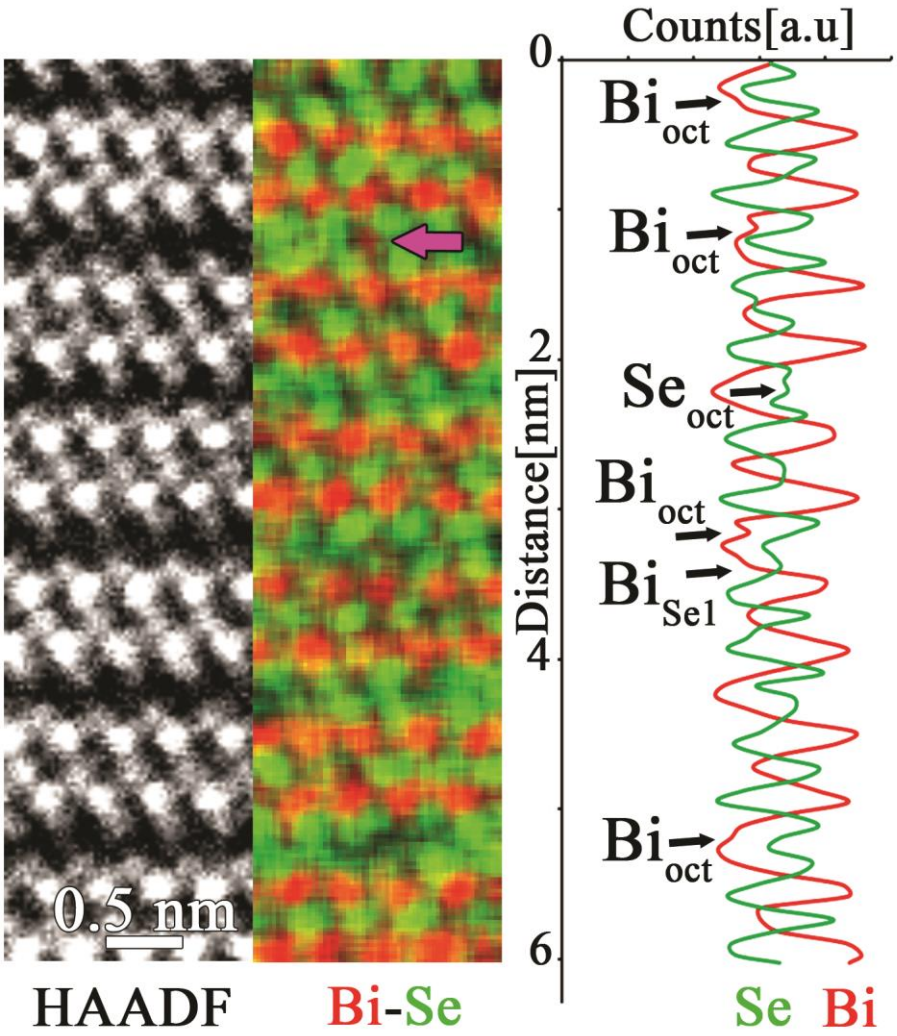

Figure 3.7 HR-EDX map. Bi occupies the interstitial position in the VdW gap (purple arrow). In the line profile three types of defects are visible: Bi_{oct}, Se_{oct} and Bi_{Se1} (black arrows).

The interstitial defect in the outer Se layers of the QL is also mobile, observed for the cryo-crushed sample: an atom jumps briefly in an interstitial position and disappears again (Figure 3.8). The observed path deviates slightly from the linear path between the start- and end configuration; a small deviation towards the VdW gap is visible. We could not determine the chemical character of this defect with EDX due to the small interatomic distances in the Se layer. Presumably, mainly Se occupies this interstitial defect, because of the dominant Se character of this layer. Of course, the argument that a moving Bi atom is more easily observable than a moving Se atom due to the Z contrast of a HAADF STEM image also applies here (Figure 3.4).

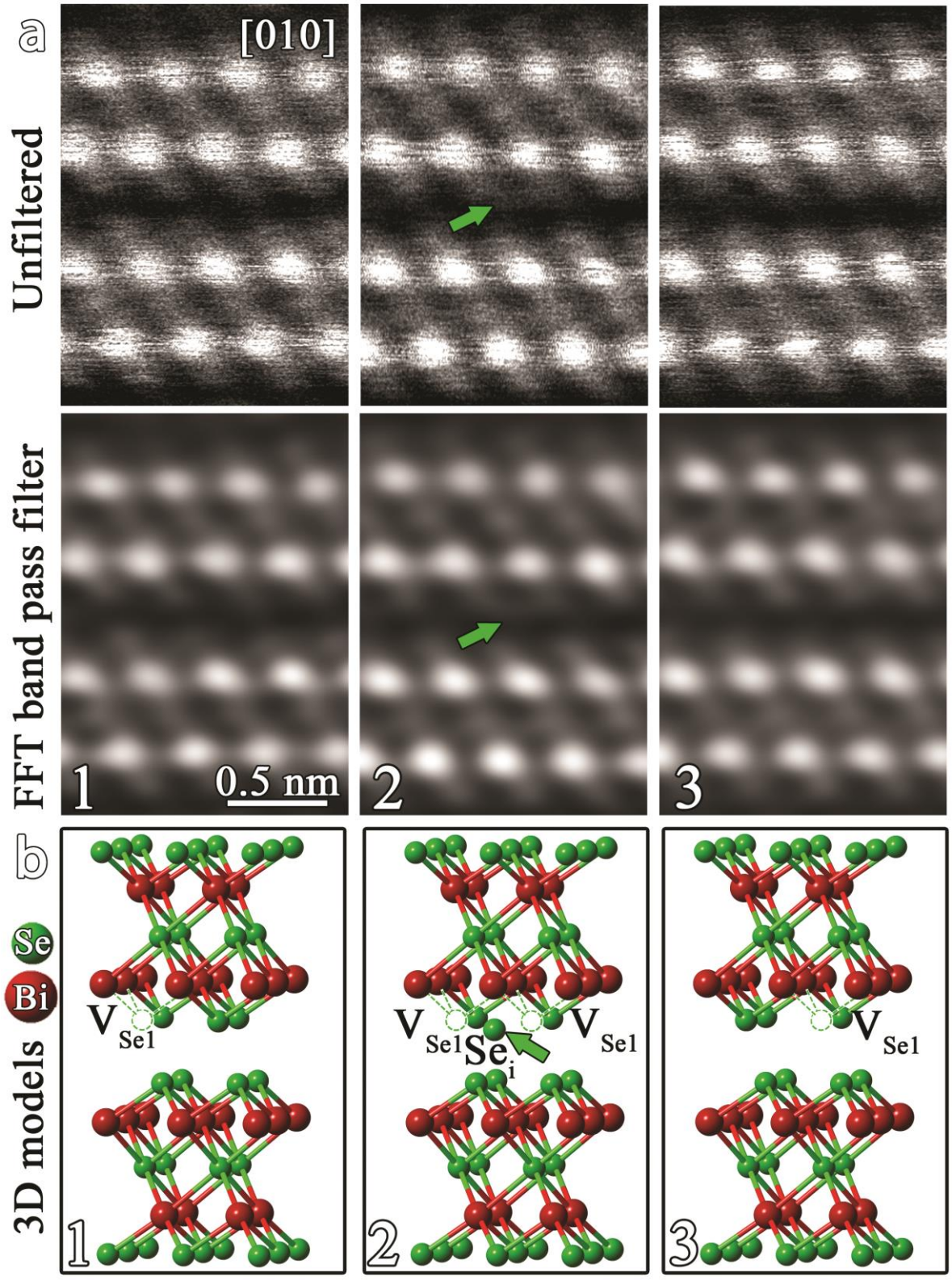

Figure 3.8 (a) Time series (0s, 40.2s, 60.3s) of the unfiltered (top) and FFT band pass filtered (bottom) HAADF STEM images from the cryo-crushed sample along [010] of the temporary creation of an interstitial defect inside the Se1 layer, marked with green arrows. (b) Schematic model of the observation in Figure 3.8a: a Se atom displaces from its original position (1), creating a vacancy and an interstitial atom in the Se layer (2), the interstitial atom occupies the neighbouring Se vacancy (3). The direction of vacancy diffusion is indistinguishable from the HAADF STEM images.

As high resolution STEM imaging is known to cause defects by itself in other compounds[141–144], we decided to supplement these images by determining the structure from quantitative electron diffraction data, as this type of data can be taken at a much lower electron dose rate, allowing to accurately solve the structure of even very beam sensitive materials, like hydrogen storage materials, organic materials, pharmaceuticals and proteins[50,145,146].

3.1.3.2 PEDT

The crystal made using the cryo-crushing method used for PEDT had a diameter of ~200nm. Dynamical refinement was essential due to the heavy elements. We started the dynamical refinement from the ideal Bi_2Se_3 structure without defects and determined a rough estimate for the global thickness parameter for the dynamical refinement from low magnification TEM images of the crystal taken every 5°. To know the thickness of the sample at 0° tilt angle, we require a TEM image at 90°. However, the maximum tilt angle limit was 76°. From every TEM image, the projected width is determined by calculating the area of the crystal divided by its length. Next we extrapolate the determined projected width values to 90° to obtain an estimate for the final thickness, namely 367 Å. The same thickness was used for all diffraction patterns. Determining the thickness parameter experimentally was a crucial factor for the successful refinement as the thickness plots generated by Dyngo of the diffraction patterns led to a different thickness parameter (~50-200 Å). We decided to use the one determined directly from the low magnification images.

Refining the Se occupancies suggests the presence of Bi on these Se sites, Bi_{Se}, as the occupancy refinement consistently gives an occupancy >1 for these positions. We speculate that an even higher Bi concentration is present on these sites, as several examples in the literature indicate the existence of Se vacancies, especially on the outer Se layers of the quintuple block[95,98,108–114]. Vacancies could not be taken into account, because an unknown amount of vacancies on the already mixed Bi_{Se1}/Se1 sites leaves too many degrees of freedom (an excess of Bi can be compensated by more vacancies). The displacement parameters of elements on the same crystallographic site are constrained to be equal, neglecting the chemical dependence. This limits the number of parameters and is a reasonable approximation in EDT, where the determination of displacement parameters is less accurate compared to techniques as SCXRD. Moreover, the occupancy of Bi on the Bi sites of the basic Bi_2Se_3 structure was fixed to one to avoid a meaningless value higher than one.

The obtained difference Fourier map (F_{obs}-F_{calc}) suggests that there are interstitial atoms on the octahedral sites inside the VdW gap and in a distorted octahedral site between the inner and outer Se layers, positioned close to the Bi layers (Figure 3.9). The obtained signal at these positions is higher than three times the standard deviation (3σ) of the difference Fourier map. The coordinates of this intermediate model are shown in Table 3.1. We propose Bi as the chemical character for both interstitial sites, respectively labelled from now on as Bi_{oct} and Bi_{int}. For the octahedral site inside the VdW gap, we base this decision on the STEM and EDX data. For the interstitial position inside the QL, the distance between the

interstitial defect inside the QL and the closest Bi atom (2.39 Å) is too small for an interstitial Se or Bi atom. We therefore suggest that Bi occasionally moves from its ideal position towards the interstitial position, so that both sites are not occupied at the same time. The sum of the occupancy of the Bi position in the ideal structure and the interstitial Bi inside the QLs was thus fixed to one. The atoms in the outer Se layers are less tightly bound due to the weak VdW interaction on one side, leading to the highest displacement parameters for this structure. The observed movement of the interstitial defects indicate high displacement parameters and weaker bonding, which is similar to the outer Se site. So, the displacement parameters for the interstitial defects were restricted to the displacement parameters of Se1 and Bi_{Se1}. Up to this point, we constrained the coordinates of Se_1 and Bi_{Se1} to be identical. By removing this constraint, the Bi_{Se1} defect moves ~0.5 Å towards the VdW gap. This movement is in agreement with the DFT calculations in section 3.1.3.4.

The refined structure with interstitial defects suggests 1.5(6)% Bi on the octahedral site in the VdW gap and 1.9(5)% on the interstitial position inside the QLs (Table 3.2). The reliability factors improve with only about 1%, probably due to the low quantity of defects (Table 3.3).

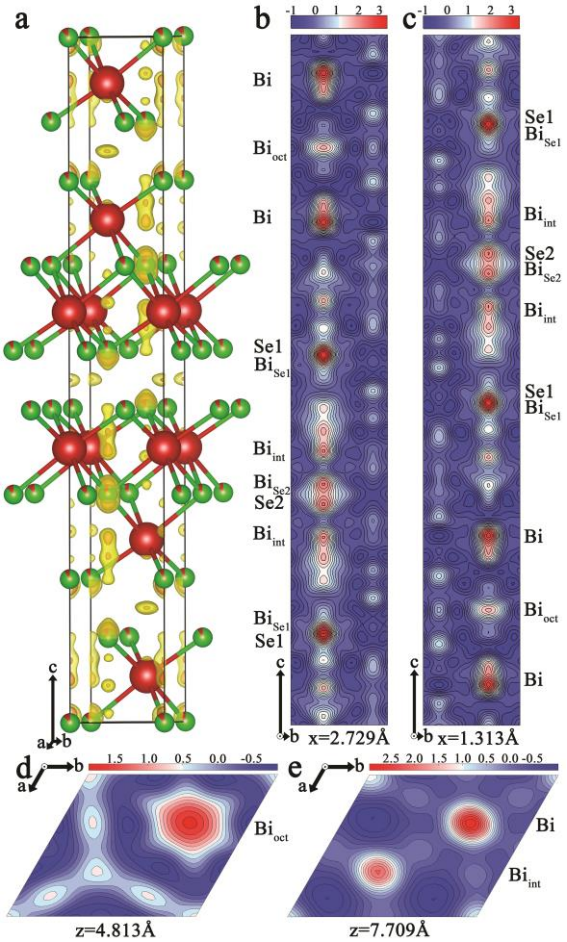

Figure 3.9 (a) 3D-difference Fourier map overlaid with the basic Bi_2Se_3 structure model including Bi substituted on the Se sites but without interstitial defects (Table 3.1) (Green spheres are Se; red spheres are Bi), plotted using VESTA[147]. The yellow (orange) areas contain values that are higher than 2σ (3σ) with σ the standard deviation, equal to 1.99 e/Å. (b-c) 2D-difference Fourier map of the b-c plane at respectively x=2.729 Å and x=1.313 Å. (d-e) 2D difference Fourier map of the a-b plane at respectively z=4.813 Å and z=7.709 Å.

Atom	Occupancy	x	Y	z	U_{iso}[Å²]
Bi	1	0	0	0.40045(11)	0.0228(3)
Se2	0.87(2)	0	0	0	0.0246(15)
Bi_{Se2}	0.13(2)	0	0	0	0.0246(15)
Se1	0.906(17)	0	0	0.20997(17)	0.0273(13)
Bi_{Se1}	0.094(17)	0	0	0.20997(17)	0.0273(13)

Table 3.1 Model from EDT based on the dynamical refinement with Bi substituted on the Se sites, Bi_{Se1} and Bi_{Se2}.

Atom	Occupancy	x	y	z	U_{iso} [Å²]
Bi	0.974(10)	0	0	0.40034(11)	0.0225(5)
Se2	0.92(3)	0	0	0	0.0243(16)
Bi_{Se2}	0.08(3)	0	0	0	0.0243(16)
Se1	0.91(2)	0	0	0.2122(5)	0.0268(11)
Bi_{Se1}	0.09(2)	0	0	0.198(2)	0.0268(11)
Bi_{oct} in VdW	0.015(6)	0	0	0.5	0.0268(11)
Bi_{int} in QL	0.019(5)	0.333333	0.666667	0.606(6)	0.0268(11)

Table 3.2 Model from EDT based on the dynamical refinement with Bi substituted on the Se sites (Bi_{Se1} and Bi_{Se2}) and interstitial defects (Bi_{oct} and Bi_{int}) in an octahedral site in the VdW gap and in a distorted octahedral site in the QL layer.

	PXRD					EDT	
	Le Bail fit of the PXRD data	Model with only Bi_{Se1}, with U_{ani} (Table 3.5)	Model with only Bi_{Se1}, with U_{iso} (Table 3.4)	Model with only Bi_{Se1} and Bi_{Se2} (Table 3.1)	Model with Bi_{Se1}, Bi_{Se2}, Bi_{oct} and Bi_{int} (Table 3.2)	Model with only Bi_{Se1} and Bi_{Se2} (Table 3.1)	Model with Bi_{Se1}, Bi_{Se2}, Bi_{oct} and Bi_{int} (Table 3.2)
Chemical formula		$Bi_{2.024}Se_{2.976}$	$Bi_{2.032}Se_{2.968}$	$Bi_{2.318}Se_{2.682}$	$Bi_{2.261}Se_{2.740}$	$Bi_{2.318}Se_{2.682}$	$Bi_{2.261}Se_{2.740}$
a [Å]	4.14096(3)	4.14070(3)	4.14078(4)	4.14006(10)	4.14004(10)	4.1407	4.1407
b [Å]	4.14096(3)	4.14070(3)	4.14078(4)	4.14006(10)	4.14004(10)	4.1407	4.1407
c [Å]	28.6592(5)	28.6564(6)	28.6579(6)	28.6475(12)	28.6479(11)	28.6564	28.6564
R (F_0) [all/obs]		4.37/4.37	6.40/6.40	9.15/8.80	8.47/8.11	28.73/14.86	28.08/14.23
wR(F_0) [all/obs]		5.96/5.96	8.06/8.06	12.07/12.03	11.49/11.46	16.61/16.13	15.92/15.44
R_p	2.24	3.13	3.70	4.75	4.61		
R_{wp}	3.45	4.70	5.41	6.89	6.66		
χ^2	8.87	12.06	13.89	17.69	17.10	6.57/9.49	6.34/9.15

Table 3.3 Differences in cell parameters and reliability factors for different models.

3.1.3.3 XRD

In order to compare the results to more standardly used techniques, we also performed XRD analysis of the crystals.

We tried single crystal XRD. For this, five different SCXRD preparation methods were done. We tested two different cryo-cutting methods. For the first method, the material was fixed on a holder with superglue and cooled with liquid nitrogen right before cutting it with a Well diamond wire to obtain a slice of 180 µm with thickness smaller than 180 µm. The thickness was not chosen, but determined by how the sample broke off after cutting it with the Well diamond. The last dimension was cut manually after re-cooling it with liquid nitrogen. For the second method, the sample was manually cut while being submerged in liquid nitrogen and thus continuously cooled. Also here the thickness is determined by how the small pieces broke off.

The third sample preparation method is cryo-crushing with the same procedure as described in section 3.1.3.1 for the TEM sample preparation. Only in this case, a crystal of the right size was selected using a light microscope.

The fourth sample preparation is the Scotch tape method. We first pasted the tape onto the bulk material and pulled it off attaining small crystalline pieces. Afterwards these fragments

were disconnected from the tape by resolving the glue with dichloromethane. Next, part of the mixture containing dichloromethane and crystals is placed in a glass vial under the fume hood to evaporate the dichloromethane. However, the crystals were stuck to the bottom of the vial, so ultrasonic bathing in ethanol for 60 seconds was performed to remove the crystals from the bottom. Compared to the TEM preparation here dichloromethane was used instead of acetone to remove the crystals from the tape due to the easier removal using dichloromethane.

For the fifth preparation method we tried to chemically remake the Bi_2Se_3 sample in a small enough size. Bi and Se crystals were separately hand milled inside a mortar. A 2:3 ratio of Bi:Se mixture was ground in a ball mill at 400 rpm (revolution per minute) for 2 minutes, 5 minutes of no movement, rotation at 400 rpm in the opposite direction for 2 minutes, followed by 5 minutes of no movement. This sequence is repeated for three hours. Next, the grinded material is pressed in a pellet. This pellet is placed in an evacuated sealed silica tube. Finally this tube is heated at 800 °C for 10h, cooled down to 670 °C in 45h and kept at this temperature for 120h.

All five different sample preparation methods we tried were unsuccessful. The reduction of the crystal size by cutting, crushing or exfoliation resulted in poorly crystalline samples which showed smeared out reflections on the single crystal XRD patterns. An example of this is shown in Figure 3.10. Remaking the sample resulted in a crystallite size unavoidably larger than required for SCXRD (0.15-0.2 mm). Therefore we turned to powder XRD.

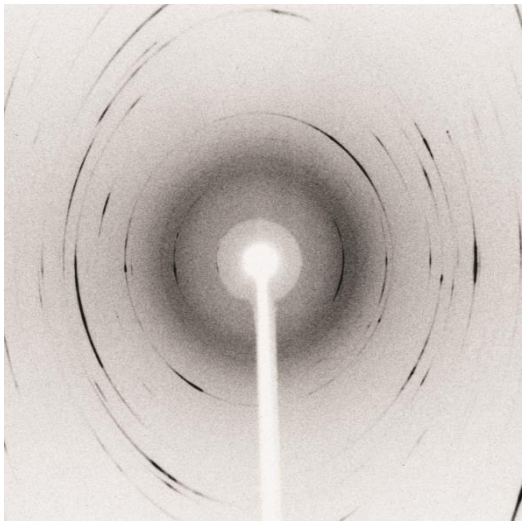

Figure 3.10 Single-crystal X-ray diffraction pattern of a cryo-crushed Bi_2Se_3 sample.

We tested two different sample preparation methods: cryo-crushing and liquid-phase-exfoliation in ethanol.

For the liquid-phase-exfoliation PXRD sample preparation we used ethanol compared to the isopropanol for the liquid-phase-exfoliation TEM sample preparation. Ethanol was not mentioned in the paper of Sun *et al.*[136], however, it also works, is easier in use than isopropanol (no fume hood is necessary) and is a standard liquid used for TEM and PXRD

sample preparation. A small crystal with a size of about 1 cm² x 1 mm was cut from the bulk material. This small crystal was submerged in ethanol and placed in an ultrasonic bath. The broken off Bi_2Se_3 fragments were collected five times after 10 minutes each in the ultrasonic bath and deposited onto the holder. With each cycle, the ethanol was refilled. The procedure was paused every 5 minutes to regulate the water temperature of the ultrasonic bath to reduce the impact of heating.

For cryo-crushing, a small crystal with ~1 cm² x 1 mm size was cut from the bulk material. This small crystal was cryo-crushed and afterwards directly placed onto the holder.

The sample prepared by ultrasonic bathing contained a very high intensity $1\bar{1}5$ reflection compared to the calculated pattern using the ideal Bi_2Se_3 structure. Addition of starch to the Bi_2Se_3 powder sample increased the random orientation of the Bi_2Se_3 sample which resulted in a decrease of the intensity of the $1\bar{1}5$ reflection. This proved that this high intensity was caused by preferential orientation. However, the starch introduced a high background at low 2θ-angles, making the patterns with less preferential orientation unusable. In the cryo-crushed sample the preferential orientation was less pronounced compared to the Bi_2Se_3 sample made by ultrasonic bathing without starch addition. Therefore, data treatment was only performed on the best data set, that of the cryo-crushed sample.

The ideal quintuple-layered structure was the starting model for the Rietveld refinement. The displacement parameters for both Se layers were constrained to be identical due to the negative displacement parameter for Se2 when refined separately. Refining the occupancies of both Se positions resulted in an occupancy value higher than 1, so Bi was added to these sites. The occupancy of Bi_{Se2} was 0.061%, whereas for Bi_{Se1} only 0.004%. The occupancy for the Bi site was kept fixed at 1, due to its unrealistic value (>1). Next, preferred orientation along the $[20\ \overline{20}\ 3]$ direction, using the March-Dollase approach, was included to account for the unusually high $1\bar{1}5$ reflection. Preferential orientation along the c-axis provided a worse visual fit of the PXRD profile and this option was thus discarded. Further refinement led to a negative Bi_{Se2} occupancy, resulting in the removal of Bi_{Se2} and the restriction of the Se2 occupancy to 1. This intermediate model is shown in Table 3.4. Also, harmonic, anisotropic displacement parameters were tested (Table 3.5). Separate refinement of the Se1 and Bi_{Se1} coordinates moved the substituted Bi toward the QL instead of towards the VdW gap, which is in disagreement with EDT and DFT. Therefore, the coordinates of both elements were held constrained. No signs of any interstitial defects were observed during this refinement. The final fit is shown in Figure 3.11.

Next, to compare, we used the EDT models with and without interstitial defects inside the VdW gap and QLs to fit the PXRD data, restarting from the original Le Bail fit. All profile parameters, including the cell parameters, were refined and the same preferential orientation direction was again introduced. The R factors of these models were worse compared to the model found from PXRD (Table 3.3).

Atom	Occupancy	x	y	z	U_{iso} [Å²]
Bi	1	0	0	0.40037(4)	0.0092(3)
Se2	1	0	0	0	0.0105(7)
Se1	0.984(3)	0	0	0.21063(6)	0.0105(7)
Bi_{Se1}	0.016(3)	0	0	0.21063(6)	0.0105(7)

Table 3.4 Model from PXRD with isotropic displacement parameters.

Atom	Occupancy	x	y	z	U_{ani} [Å²]
Bi	1	0	0	0.40052(4)	0.0112(4)
Se2	1	0	0	0	0.0192(9)
Se1	0.988(2)	0	0	0.21014(7)	0.0192(9)
Bi_{Se1}	0.012(2)	0	0	0.21014(7)	0.0192(9)

Atom	U_{11} [Å²]	U_{22} [Å²]	U_{33} [Å²]	U_{12} [Å²]	U_{13} [Å²]	U_{23}[Å²]
Bi1	0.0034(3)	0.0034(3)	0.0267(9)	0.00168(17)	0	0
Se1/Se2/ Bi_{Se2}	0.0044(6)	0.0044(6)	0.049(2)	0.0022(3)	0	0

Table 3.5 Model from PXRD with harmonic, anisotropic displacement parameters.

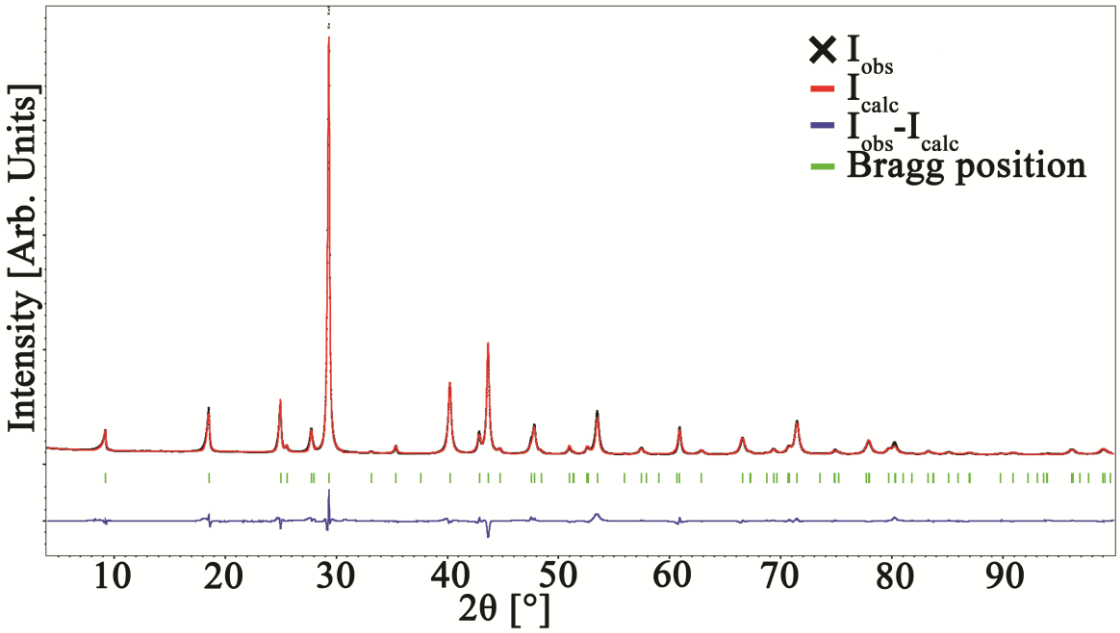

Figure 3.11 Observed PXRD diffractogram (black), with its fit (red) where the PXRD model with anisotropic displacement parameters is used (displayed in Table 3.5). The difference between both is displayed (blue) at the bottom. Green ticks indicate Bragg peaks.

3.1.3.4 DFT

For the structure optimization with defects, all atoms in the 3x3x1 cell are fixed except for the six layers along the c axis around the interstitial defect. Optimizing all atomic positions causes a small displacement of the two complete QL blocks around the interstitial defect, which corresponds more to a defect structure rather than a rare local defect. The binding forces between the atoms in the QL are significantly higher than the weak VdW interaction, causing the QLs to displace when all atomic positions are allowed to optimize within the periodic boundary conditions of VASP. The energy difference of the optimized intermediate configuration with two vacancies and a Bi atom in the octahedral site corresponding to the saddle point of Figure 3.12 c with and without fixing the chosen positions is 117 meV for the complete 3x3x1 cell or ~0.9 meV per atom. We also tested the influence of fixing the atomic positions on the energy barrier. For comparison, the path displayed in Figure 3.12c has an energy barrier of 1.716 eV when optimizing all atoms versus 1.766 eV when optimizing only the atomic coordinates of the atoms in the six layers closest to the defect. This indicates that fixing the atomic positions of the atomic layers has only a minor influence on the kinetic barriers of the defect migrations. Furthermore, only the octahedral interstitial site in de VdW gap (and not the tetrahedral one) was studied, based on the STEM and EDT data.

Using Eq. 3.5 (section 3.1.2.3) we obtain a formation enthalpy (per formula unit) for Bi_2Se_3 of -1.83 eV including SOC, and -1.96 eV without SOC. Both values agree well with the experimental result of -1.60(17) eV (at 298K) with a somewhat better agreement for the SOC calculation[148]. Furthermore, we calculated the defect formation energy using Eq. 3.9 (section 3.1.2.3). We use the Se-poor regime to compare the calculated formation energies to the experimental defect occupancies derived from our EDT results (section 3.1.4), because the material is Se deficient. This suggests rather Se-poor than Se-rich conditions. Figure 3.13c-Figure 3.13d show the formation energies of different single defects without and with including spin-orbit coupling (SOC): Bi substituted on Se1 and Se2 (Bi_{Se1} and Bi_{Se2}), Se substituted on Bi (Se_{Bi}), Se1 and Se2 vacancies (V_{Se1},V_{Se2}), Bi vacancies (V_{Bi}) and interstitial Bi and Se inside the VdW gap (Bi_{oct} and Se_{oct}). For the Se-poor regime, Bi_{Se1} has the lowest formation energy, followed by V_{Se1}, V_{Se2}, Bi_{Se2}, V_{Bi} and Bi_{oct} when we include SOC. Without SOC, V_{Bi} is removed from this ranking. For the Se-rich limit, V_{Bi} has the lowest formation energy when including SOC, followed by Se_{Bi}, V_{Se1}, V_{Se2}, Se_{oct}, Bi_{Se1}, Bi_{oct} and Bi_{Se2}. Without SOC, Se_{Bi} has the lowest formation energy, followed by V_{Se1}, V_{Se2}, Bi_{Se1}, V_{Bi}, Se_{oct}, Bi_{Se2} and Bi_{oct}. In the case of the Se-rich limit (or Bi-poor limit) the SOC results seem intuitively more logical: if more Se is present, it is more likely that Bi vacancies exist and that Se substitutes Bi. When SOC is neglected, however, Se1 vacancies are second in the ranking of having the lowest formation energy. Also, Se_{oct} is lower in the ranking in the calculation with SOC compared to the calculation without SOC. In general, we notice a strong decrease in formation energy for V_{Bi} for the results including SOC.

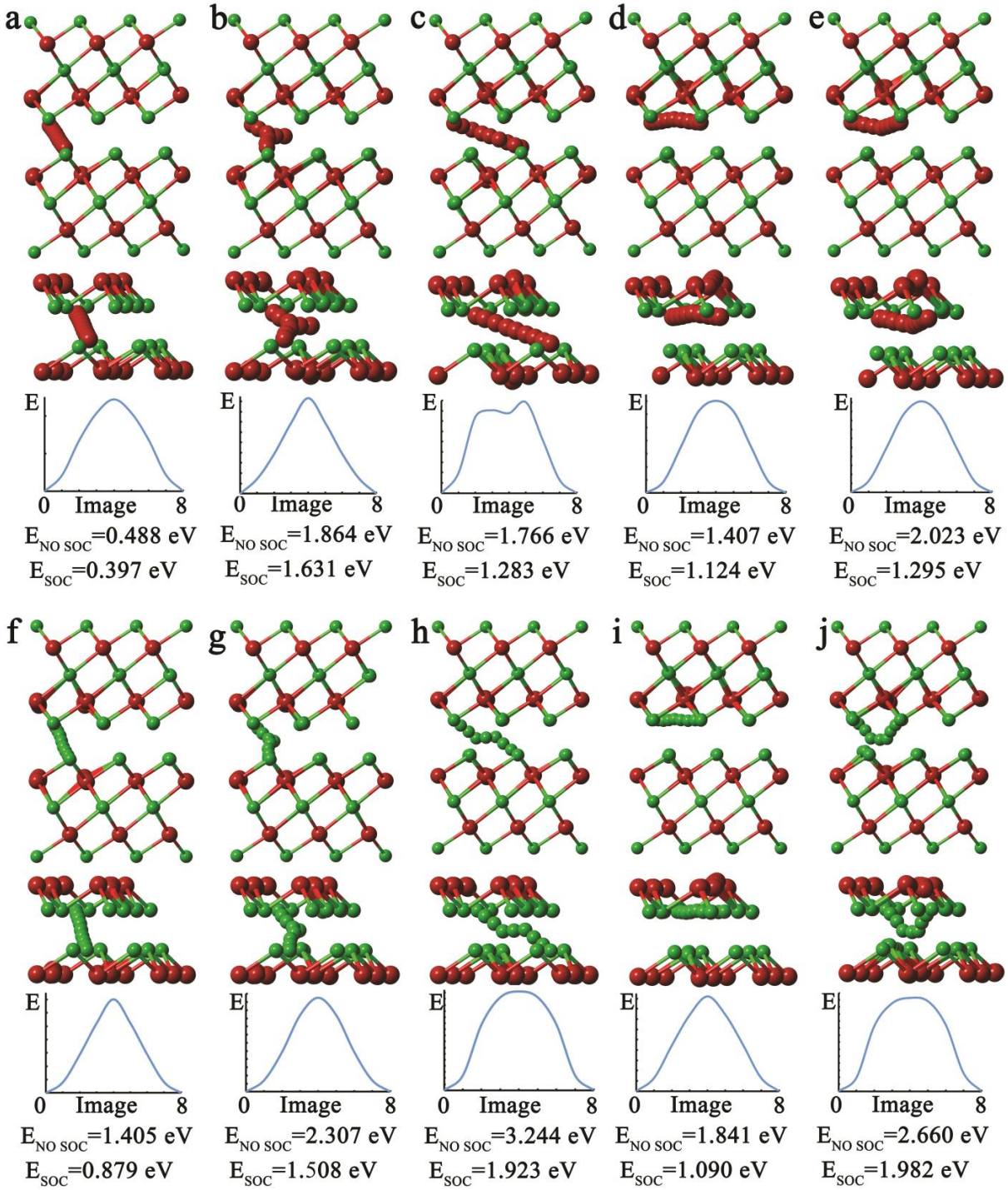

Figure 3.12 Top row (a-e): Different migration paths for Bi_{Se1} diffusion towards the Se1 layer on the opposite side of the VdW gap or towards a neighbouring Se1 vacancy in the same layer. Middle row (f-j): Se1 diffusion towards the VdW gap to the opposite Se1 layer or towards a neighbouring V_{Se1} vacancy in the same layer. For every migration path (top to bottom) the projected structure along the **b** axis is displayed, then a close up of the environment around the moving atom, followed by a plot displaying the total energy change for the images along the path with the calculated energy barrier with and without including SOC. For the models itself, the positions of all atoms of the nine images of the migration path are integrated into one image.

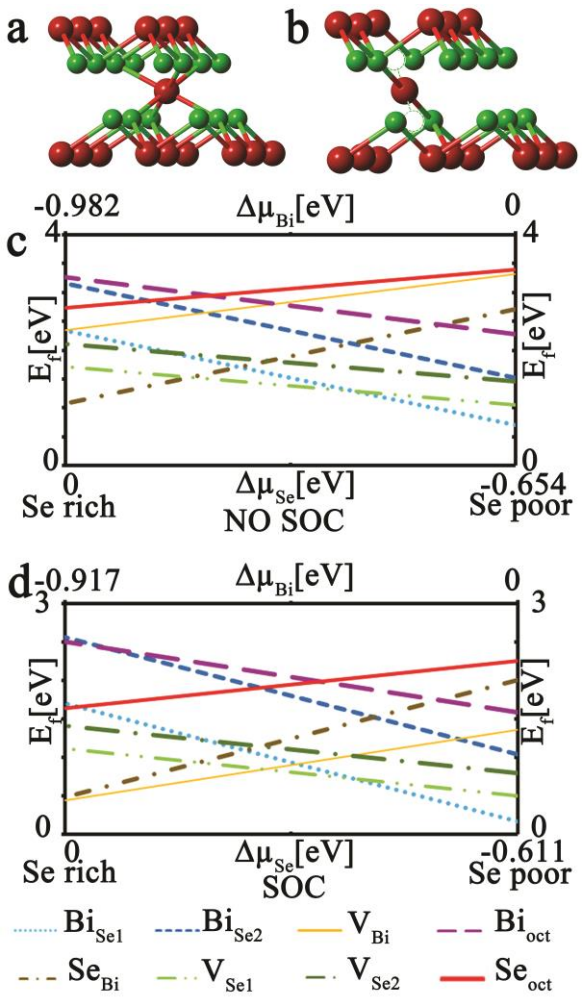

Figure 3.13 Bi coordination for an octahedral site (a) and a planar site (b) in the VdW gap. The Bi-Se bonding distance is ~2.7 Å for the octahedral site in (a). The V_{Se1}-Bi distance is ~1.8 Å and the Bi-Se bonding distance is ~3.4 Å for the planar site in (b). Defect formation energies as a function of the chemical potentials $\Delta\mu_{Bi}$ and $\Delta\mu_{Se}$ without SOC included (c) and with SOC included (d).

To study the migration of defects across the VdW gap and inside the Se1 layer, several paths between different configurations of vacancies were studied, where crystallographically equivalent paths were assumed equal. For every crystallographically distinct two vacancy configuration, combined with an interstitial defect in an octahedral setting inside the VdW gap, the total structure is optimized. Except for one configuration for an interstitial Bi atom (Figure 3.13b), all final geometries correspond to a distorted octahedral configuration (see Figure 3.13a for the octahedral site). This planar configuration is only possible due to the free space provided by the vacancies. Paths passing through the distorted octahedral site and linear paths between two Se vacancies in an adjacent or the same Se layer were studied. When the octahedral position does not lie on the linear path between the two Se vacancies, we always interpolate via the optimized intermediate structure when setting up the initial path. One Bi path (Figure 3.12b) is an exception to the latter. When we optimized the intermediate position (two Se vacancies and one Bi atom on the octahedral site) of the path shown in Figure 3.12b the interstitial Bi moved to a planar configuration (Figure 3.13b). Because we are interested in the migration of Bi along the octahedral site, we constructed

an initial path along this octahedral site. Furthermore, to speed up convergence we used the Fast Inertial Relaxation Engine (FIRE) force based optimizer[149]. However, as the path converged to the path displayed in Figure 3.12a, we fixed Bi on the octahedral site, resulting in the optimized path shown in Figure 3.12b.

When including SOC, a diffusing Bi atom needs to overcome an energy barrier of 1.283 eV or 1.631 eV to jump towards a V_{Se1} in the adjacent layer along the Bi_{oct} position. Without SOC, the corresponding energy barriers are 1.766 eV and 1.864 eV. The linear Bi path along the planar position has a low energy barrier of only 0.397 eV with SOC and 0.488 eV without SOC. A calculated energy barrier including SOC of 1.124 eV or 1.295 eV, respectively for a linear path and a path passing through a distorted octahedral position, should be overcome to allow a Bi atom to jump to a neighbouring Se position inside the same Se layer. Without SOC, the energy barriers are respectively 1.407 eV and 2.023 eV. In general, the energy barriers for Bi and Se become significantly lower on including SOC. These energy barriers, especially the ones including SOC, are similar or even lower than those found for α-GeTe, which has a comparable structure with a two-layered block of Ge and Te with weak VdW interactions in between. There, the activation barriers for Ge diffusion using also a vacancy mechanism range from 0.95 eV to 2.44 eV, depending on the path (linear or curved) and the number of Ge vacancies present (Ge vacancies helped to decrease the barrier)[150]. As a rule of thumb, reactions with an energy barrier of 21 kcal/mol (≈0.9 eV per atom) or lower, will happen readily at room temperature[151,152]. An activation barrier of 1.4 eV was also experimentally determined for Ge diffusion, probably by a vacancy mechanism, inside PbTe[153].

Similar trajectories are found for a migrating Se atom. The energy barriers to jump towards the adjacent Se layer are higher than for a Bi atom, except for the Se path displayed in Figure 3.12g when including SOC. The latter can be explained by the required fixation of Bi on the octahedral site for the corresponding Bi path (see Figure 3.12b). The fact that the activation energy for a Se migration across the VdW gap is generally higher than that of the corresponding Bi path agrees with our expectations: more energy is required to remove a Se atom from its ideal position in the bulk structure than for a Bi_{Se1} defect. This is also clear from the amount of energy necessary to move a Bi or Se atom from the Se1 layer towards the octahedral interstitial position: 2.149 eV without SOC or 1.687 eV with SOC for a Bi atom and respectively 3.677 eV and 2.537 eV for a Se atom. However, the energy barrier for a Se atom to linearly jump to a neighbouring V_{Se1} position inside the same Se layer (Figure 3.12i) is lower than for Bi when including SOC, probably due to its smaller size and thus smaller local distortion. Note that for the non-linear path of the Se atom jumping to a neighbouring Se vacancy of the same Se layer along an octahedral site (Figure 3.12j), the FIRE force-based optimizer was used. The interstitial Se_{oct} at the saddle point forms a Se-Se bond with a Se1 atom of the adjacent layer of size 2.37 Å (standard Se-Se bonding is ~2.4 Å). This path has a high energy barrier compared to the corresponding Bi path.

3.1.4 Discussion

With STEM we observed interstitial defects inside the VdW gap with mainly Bi character determined by EDX. Both samples prepared with different methods contained these defects, suggesting that they are not induced by sample preparation. Moreover, through simulations using QSTEM[84], we verified that one Bi atom in the VdW gap is indeed still detectable in STEM images of thin samples of around 50 Å (a plausible thickness for the imaged areas in cryo-crushed samples) in the $[010]$ zone. The fact that the defects are also observed in EDT performed with a parallel, spread electron beam, *i.e.* at a much lower electron dose rate, supports that these defects are not simply induced by the electron beam. Furthermore, the calculated defect formation energies support the EDT results.

We use the Se-poor regime to compare the calculated formation energies to the experimental defect occupancies derived from our EDT results, because the material is Se deficient. Bi_{Se1} has the lowest formation energy for a Se-poor sample, followed by V_{Se1}, V_{Se2}, Bi_{Se2}, V_{Bi} and Bi_{oct} when we include spin-orbit coupling. Without SOC, V_{Bi} is removed from this ranking. Of the calculated single defects, Bi_{Se1} is indeed the defect present with the highest occupancy in EDT, followed by Bi_{Se2} and Bi_{oct}. Vacancies could not be taken into account, since the mixed occupancy of a site by Se, Bi and vacancies would require too many refinable parameters. All defects except the vacancies are also observed with STEM. The fact that the vacancies were not observed does not mean they are absent, however, to count the atoms in a column from HAADF STEM images, one needs a binary possibility for the occupation, and, also here, the possibility to have Se, Bi or a vacancy at each position prevents quantification. For PXRD only the defect with the lowest formation energy is found *i.e.* Bi_{Se1}. So, PXRD does not indicate the presence of interstitial defects. However, we are inclined to consider the EDT data as more reliable for several reasons. First, the EDT data is measured from a single crystal. Second, the preparation of the sample for PXRD was challenging: all samples had a preferential orientation, which makes Rietveld refinement more difficult since a preferred orientation influences the peak intensity, next to anisotropic peak broadening (caused for example by an anisotropic sample size or complex defect structure). Moreover, in our attempts to collect single crystal X-ray data we observed reduced crystallinity after the application of any type of mechanical stress or size reduction, which implies that the crystallinity in the crystallites in the powder sample is probably also reduced. For EDT, on the other hand, we can filter out a perfect crystal that was not damaged during sample preparation. In PXRD this is not possible: the data is taken from the whole crushed sample, and for single crystal XRD, we did not succeed in creating a sufficiently undamaged crystal with a suitable size (≈0.15 mm per dimension).

Our findings on the interstitial Bi atoms in the VdW gap are also supported by the computational results of Tumelero *et al.*[93] who found that the Bi interstitial defect in an octahedral setting has the lowest formation energy in a Se-poor material and the lowest or second lowest in a Se-rich material depending on the simulation settings. Jia *et al.*[117] and Urazhdin *et al.*[115] propose the existence of interstitial Bi through indirect evidence. However, Dai *et al.*[95] suggested the existence of interstitial Se atoms, where the concentration of

interstitial Se increased for samples synthesized under Se-rich conditions. This is in line with our results for the calculated formation energies. The synthesis procedure clearly influences the presence of defects. This can explain why we observed a Bi dominant character for the interstitial defects, whereas Dai *et al.*[95] found Se interstitial defects. In summary, STEM and EDX show the existence of interstitial Bi defects in the VdW gap and both the EDT and DFT results support that they are not beam induced.

Based on the calculations of the transition state including SOC, we expect the Bi and Se migration paths in respectively Figure 3.12a and Figure 3.12f to occur easily and in Figure 3.12i to happen exceptionally at room temperature. The Bi and Se path across the VdW gap have a calculated energy barrier of 0.397 eV and 0.879 eV respectively, which is lower than the rule of thumb energy barrier of 21 kcal/mol (≈0.9 eV per atom), at which the transition will happen readily at room temperature[151,152]. The Se path inside the Se layer is 1.090 eV, which is slightly higher than 0.9 eV. The diffusion coefficient *D* is described by the Arrhenius equation[154–156]:

$$D = D_0 e^{-E/k_B T}, E = E_m + E_{f_v} \tag{3.10}$$

with D_0 a pre-exponential factor, T the temperature, k_B Boltzmann's constant and E the activation energy, where the latter is the sum of the energy barrier E_m and the formation energy E_{f_v} of a vacancy in the case of a vacancy mechanism. The formation energy is included in the equation because a vacancy should be present in the adjacent layer in order to jump toward this site, which has a probability proportional to $\exp\left(-E_{f_v}/k_B T\right)$. From Eq. 3.10, we estimate that migrations along the Se path inside the Se layer occur about 1000 times less frequently than something that should happen readily. Without SOC, only the Bi path in Figure 3.12a can exist easily at room temperature. Reasons why we did not directly observe Se movement within the outer Se layers (Figure 3.12i) and Bi and Se migration across the VdW gap (Figure 3.12a and Figure 3.12f) calculated with SOC or only the Bi path (Figure 3.12a) without SOC include the limited resolution of the microscope, the possibility that this migration is too rapid for us to record, or, in the case of the Se path, that the Z value is too low to see the movement of one Se atom considering the thickness of the sample.

The observed path in Figure 3.8a can correspond to the model of Figure 3.12e, whereas the path in Figure 3.6a can correspond to the model in Figure 3.12b or Figure 3.12g. The similarity of the paths in Figure 3.12e and Figure 3.12i is high, except for the slight deviation of the atom of the path in Figure 3.12e towards the VdW gap. The latter combined with the fact that a moving Bi atom is more readily visible in STEM than a moving Se atom, suggests that we observed in Figure 3.8a the path in Figure 3.12e rather than Figure 3.12i. This does not exclude that the path in Figure 3.12i cannot happen, only that it is less probable that we observed it. For the observed path in Figure 3.6a, one jumping Bi atom should be more readily visible in STEM, however for the calculated path in Figure 3.12b the Bi atom in the octahedral site is fixed in order to force the path along this position. In the path in Figure 3.12g a Se atom follows a similar route and for Se it is a true minimum energy path,

however, the low Z value for Se suggests that multiple Se atoms should have moved at the same time for this to be visible. Due to the higher energy barriers of the paths in Figure 3.12b, Figure 3.12e and Figure 3.12g, these migrations are probably caused by the electron beam irradiation. Moreover, it is possible that these paths are more easily visualized in STEM because the atoms pass along the octahedral position, which is represented by a larger empty space than the shortest projected distance between the two opposing Se layers. Hence, the presence of an atom in the octahedral site is more easily recorded. In comparison, the atomic movement between atom columns that are closer together in projection could be more readily interpreted as noise. Even though the paths that are observed are likely to be influenced by the electron beam, the existence of these interstitial defects itself is probably not beam induced, because the interstitial Bi atoms are also observed using PEDT, which is considerably less beam damaging than STEM and EDX. The occupancy probability of the defects determined by EDT is also inversely proportional to their corresponding DFT calculated formation energies, which further supports the proposition that the interstitial defects are not merely a result of the electron beam.

The influence of the beam on the sample merits a detailed discussion. Ionization damage - causing radiolysis damage, thermal damage and electrostatic charging- and knock-on displacement damage are the main damage mechanisms inside a material due to the interaction with the electron beam[157,158]. Beam damage depends on a lot of different parameters such as specimen thickness and orientation, beam voltage, beam current density and beam size[143].

Radiolysis, electrostatic charging and heating are caused by inelastic scattering of electrons: the Coulomb interaction between the incoming electrons and the electrons of the atoms inside a material creates secondary electrons[144]. The incident electron provides enough energy to remove an electron from the outer atomic shell (excitation) or inner atomic shell (ionization) of atoms, creating a vacancy and a secondary electron[157]. If this vacancy exists long enough, as it does in insulators and certain semiconductors, the ionized atom can move by breaking its chemical bonds, whereas movement is avoided when electrons fill this vacancy fast enough, as for metals[157]. The atom can only move when the excitation energy is changed into momentum due to thermal vibration and local Coulomb repulsion [143,159]. This is *ionization damage* or *radiolysis*. These secondary electrons can travel a few nanometres, creating even more damage[157]. For example, Hobbs proposed a model for the oxygen movement in tetrahedral silica due to radiolysis, where the oxygen in a Si-O bond moves off-centre and makes an O-O peroxy linkage, creating an O vacancy and interstitial[160]. Many of the created secondary electrons due to the inelastic scattering have enough energy to leave the sample and can cause a local positive charge inside poorly conducting specimens, *i.e.* lead to *electrostatic charging*. This introduces an electric field that can cause atomic movement depending on the ionic and electrical conductivity of the material[157,159]. Furthermore, the local increase in temperature due to this inelastic scattering, *i.e.* the *heating* of the sample, remains small, even when using STEM, due to its logarithmic dependence on the beam diameter[144,157]. For example, for silicon nitride the local temperature was increased by 2.0 °C and 9.8 °C for respective beam currents of 2.11nA and

10.31nA with a 300 nm beam diameter[158], we used less than 50pA for atomic resolution STEM.

Knock-on damage inside the material and surface sputtering –respectively moving atoms inside the material or out of the material- are caused by elastic scattering of the electrons. Elastic scattering is an electron-nucleus interaction, inducing the incoming electrons to electrostatically deflect by the Coulomb field of the nucleus[143,144,157]. The necessary displacement energy (E_d) depends on the bond strength, crystal lattice and atomic weight of the elements inside the material and the direction of the knock-on atomic momentum[144,157]. This mechanism is especially present in electrically conducting materials, like metals and some semiconductors[157]. When the transferred energy is high enough, the displaced atom can move to another (meta)stable site through a saddle point position, creating Frenkel pairs – a vacancy and an interstitial atom[157].

Due to the small temperature rise, heating damage can be neglected in Bi_2Se_3. Furthermore, Bi_2Se_3 is not a poor conductor: Bi_2Se_3 conducts at the surface and also in the bulk it is slightly conductive due to defects[25,92]. The two mechanisms that are most likely to cause the observed movement of the defects in Bi_2Se_3 are knock-on damage and radiolysis. The Se atoms in the outer Se layers are on one side only weakly bound with VdW interactions, which makes them more vulnerable to knock-on damage. Radiolysis is also still an option, because the material is only slightly conducting in the bulk, which can cause the vacancy to exist too long, so that the ionized atom can displace from its position.

We observed interstitial defects with mainly Bi character with STEM and EDX, supported with PEDT and the DFT calculated formation energy of the different defects. Intrinsic and native defects are an important topic, because they influence the material's properties and thus device-based applications. Wang. *et al.*[156] discovered that Cu interstitial defects act as donor defects in Bi_2Se_3 and Dai *et al*.[95] proposed the same for interstitial Se defects in Bi_2Se_3. This suggests that the observed interstitial defects will probably make the Bi_2Se_3 material more n-doped. The defects and the higher electric conductivity can positively influence the thermoelectric characteristics, but are negative when we want to use the conducting surface states due to the higher bulk conductivity, like for spintronic applications. These defects also impact material engineering using doping, since doping can influence the formation energy of an intrinsic defect[99]. Furthermore, DFT including SOC suggests that one Bi and Se path from one Se layer towards the adjacent Se layer can occur easily and the Se movement inside the outer Se layers is rather exceptional at room temperature. Without SOC, only the Bi path is easily present at room temperature. We have also shown that SOC strongly influences the energy barriers and formation energies. The formation enthalpy calculated with SOC agrees slightly better with the experiment. Knowledge about the mobility of atoms is necessary, because of its influence on many physical properties and processes, such as mechanical deformation and chemical degradation[94]. Furthermore, information on the intrinsic migration of atoms around the VdW gap is specifically needed for battery applications[100–102], because these migrations can tamper with the mobility of the dopants. Self-diffusion gives us also a lower limit for the diffusion of dopants, when the dopants do

not have excess charge and are smaller, and thus do not cause any lattice distortions [161]. On the other hand, this atomic mobility indicates that Bi_2Se_3 can withstand a certain amount of external stimuli before completely deforming.

3.1.5 Conclusion

We observed with high resolution-scanning transmission electron microscopy and high resolution-energy dispersive X-ray spectroscopy the presence of interstitial defects in the van der Waals gap of Bi_2Se_3, independent of the sample preparation technique. Their observation is supported by a structural refinement based on precession electron diffraction tomography data, indicating that they are not merely induced by the electron beam. Furthermore, the defect occupancy probability determined by EDT is inversely proportional with their corresponding DFT calculated formation energies, excluding the vacancies which could not be taken into account in EDT due to the mixed occupancy (Bi, Se and vacancies) of the sites. These interstitial defects are at an octahedral site, occupied mostly by Bi atoms and only in rare cases by Se atoms. After comparison with literature, we propose that the interstitial defects will make the material more n-doped, which is negative for spintronic applications where we want to use the conducting surface states and positive for the thermoelectric properties. However, the paths that are energetically probable at room temperature (Se movement within the outer Se layers and Bi and Se migration across the VdW gap calculated with SOC or only the Bi path without SOC) were not observed directly in the TEM. Instead, the paths that were directly observed are less likely to occur according to DFT and thus those specific observed paths might be beam induced. We suggest that the energetically favourable paths were not observed because they need a higher resolution in both time and space than was available during the observations. This atomic mobility is negative for *e.g.* Li or Na battery applications, because it will hinder the movement of the Li and Na atoms. On the other hand, it indicates that it can endure a certain amount of external stimuli, like the electron beam, without completely deforming. Finally, we also have shown that SOC strongly influences the energy barriers and defect formation energies.

3.2 $(In_xBi_{1-x})_2Se_3$ and $Sb_2(Se_xTe_{1-x})_3$

3.2.1 Introduction

Bi_2Se_3 and Sb_2Te_3 are topological insulators that slightly conduct in their bulk due to the presence of defects[25,92,162–164]. For Bi_2Se_3, Se vacancies V_{Se}, especially on the outer Se layers, and in lesser amount Bi substituted at the Se positions Bi_{Se}, are the most commonly accepted defects[95,98,108–110,112–115]. However, recently we discovered that interstitial defects exist in the van der Waals gap. More detailed information about our found defect structure of Bi_2Se_3 can be found in section 3.1. Different defects are suggested for Sb_2Te_3: Sb vacancies V_{Sb}[165], Sb on Te1 antisite defects Sb_{Te1}[165], Te vacancies[164] V_{Te}, Sb on the Te antisite defects Sb_{Te}[164,166] and under more Te rich sample conditions Te on the Sb antisite defects Te_{Sb}[165], but the most common defect for Sb_2Te_3 is the Sb_{Te} antisite defect[164–167].

Similar to the Bi_2Se_3 case, for Sb_2Te_3 the stoichiometric composition does not fall inside the homogeneity range, which is completely shifted to the chalcogen-rich side, so a material containing only the Bi_2Se_3 or the Sb_2Te_3 structure with the stoichiometric composition does not exist in either case (see the equilibrium phase diagrams in Figure 3.1, Figure 3.14). In contrast to Bi_2Se_3, Sb_2Te_3 is always p-type since the dominating native defects are Sb_{Te} antisite defects.

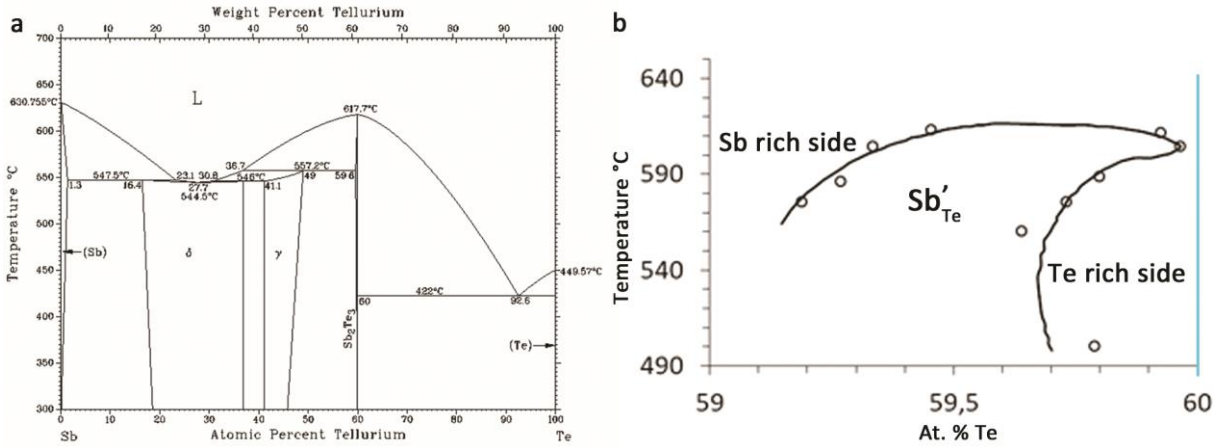

Figure 3.14 (a) Phase diagram of the Sb-Te system[120]. (b) Fragment of the phase diagram near the Sb_2Te_3 compound[168]; the 40:60 Sb:Te composition is marked with a blue line. When the material has the 40:60 Sb:Te composition, it falls outside the Sb_2Te_3 homogeneity range. In the homogeneity range, the material is p-type, and contains Sb'_{Te} defecten. The ' symbol means that the defect has a -1 charge.

The bulk conductivity is unwanted for certain applications like low-power spintronics[169]. The absence of backscattering at the surface could greatly reduce energy losses when using this surface current. Furthermore, if the topological insulator has an isolated Dirac cone and a Fermi level that lies in the bulk bandgap, the scattering from the bulk bands decreases. Extrinsically doping can influence the formation energy of intrinsic point defects, thus increasing or decreasing their chance of existence and consequently affecting the carrier concentration[99]. For example, Horák *et al.*[164] studied the point defects in $Sb_2Te_{3-x}Se_x$ crystals and proposed that the Sb_{Te} antisite defects decrease, in agreement with Karamazov *et al.*[170] and Lošťák *et al.*[171], and the anion vacancies slightly drop with increasing Se content. Defects also modify the band structure by shifting the Dirac point energy and Fermi energy[95,98]. Extrinsic doping the material by adding another element to the structure and optimizing these extrinsic defects is thus a way to obtain perfect properties[99]. So for both materials a third element is added in order to gain control over the band structure and in order to make these materials truly bulk insulating. The continuous compositional change will slowly nudge the character of the band structure in a certain direction. For example, Sb_2Te_2Se, a topological insulator (p-type) has an isolated Dirac cone where the Fermi level lies above the maximum of the bulk valence band[172], while for Sb_2Te_3 the Fermi level lies below the bulk valence band[173] and Sb_2Se_3 is not a topological insulator[27,174]. Characterizing the bulk structure is important, because the interesting feature of topological insulators, the conducting surface states, is controlled by the bulk. The surfaces are just the terminating layers of the bulk, and by themselves show no topological properties. The reason for this is

that the surface conduction is a consequence of the topological invariants needing to change when going from the topological insulator to the vacuum.

Another reason why these specific materials are interesting lies in the choice of elements. $(Bi_{1-x}In_x)Se_3$ is a mixture of Bi_2Se_3 and In_2Se_3, whereas $Sb_2(Se_xTe_{1-x})_3$ is a mixture of Sb_2Se_3 and Sb_2Te_3. Sb_2Te_3[26,27] and Bi_2Se_3[27,175] are both topological insulators[27], while In_2Se_3[176] and Sb_2Se_3[27,177] are normal insulators. In summary, both studied materials are a mixture of a topological insulator with a normal insulator. So at a certain composition a "topological phase transition" will occur, the phase transition from a topological insulator to a normal insulator. Accurate knowledge about the exact structure of this type of materials is the first step in aiding to understand this transition better by providing the correct structures as input for calculations and to explain measurements of the physical properties and thus to understand more about the physics of topological insulators.

Both chosen mixtures are different. $(Bi_{1-x}In_x)_2Se_3$ is cation substituted and $Sb_2(Se_xTe_{1-x})_3$ is anion substituted. Furthermore, Bi_2Se_3[20], β-In_2Se_3[178,179] (stable above 200 °C) and Sb_2Te_3[21,22] have a quintuple-layered structure, while Sb_2Se_3[180] has an orthorhombic structure displayed in Figure 3.15. However, phase diagrams based on bulk powder diffraction show that the orthorhombic Sb_2Se_3 structure turns to the quintuple-layered Sb_2Te_3 structure as soon as even a little Te is added to Sb_2Se_3[170,181].

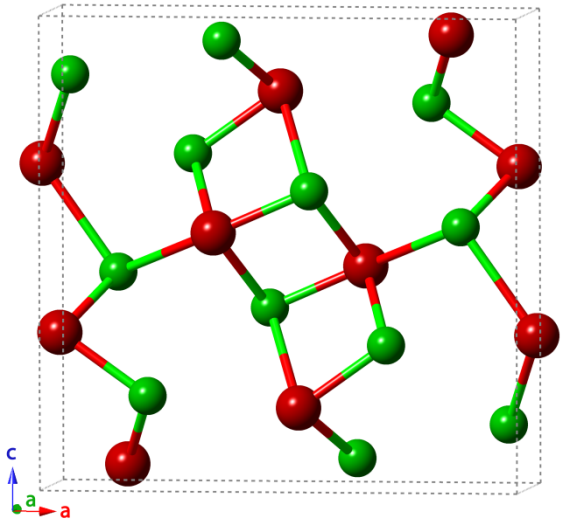

Figure 3.15 Sb_2Se_3 structure with two crystallographic distinct Sb sites, where the Sb-Se bonding distances up until 3.486 Å are taken into account, similar to Voutsas *et al.*[180]. Red sphere are Sb; green spheres are Se.

For Bi_2Se_3 doped with In, Horák *et al.*[182] suggest a decrease of the concentration of Bi_{Se} antisite and the creation of In_{Bi} defects upon In addition in the Bi_2Se_3 structure. Ji *et al.*[183] also observed these In_{Bi} defects in the quintuple-layered structure for $(In_{0.88}Bi_{0.12})_2Se_3$ using single crystal X-ray diffraction. Furthermore, the Se atoms in the middle Se layer deviate from their ideal 3b position to a partially occupied 18g position, leading to local variations on the coordinates of the middle Se atomic position[183]. Bouanani *et al.*[139] found that in the phase diagram of the Bi_2Se_3-In_2Se_3 system a region exists where there is demixing of the two

structures. Close towards the pure In_2Se_3 limit Bi substitutes on the In sites, while towards the pure Bi_2Se_3 limit In substitute on the Bi sites.

For Sb_2Te_3 doped with Se, literature disagrees on how Se is incorporated inside the Sb_2Te_3-Sb_2Se_3 system. Procarione *et al.*[184] suggest that Se more likely substitutes onto the outer Te layers, while Anderson *et al.*[22] proposed the opposite. Both used indirect measurements. Procarione *et al.*[184] based their conclusions on the decrease of the band gap with increasing Se content combined with the transition from the hexagonal structure to an admixture of the hexagonal structure and the orthorhombic structure at Sb_2TeSe_2. Anderson *et al.*[22] based their findings on the variation of the c parameter with increasing Sb_2Se_3 content. Two nearly linear regions existed with a discontinuity at Sb_2Te_2Se. The suggestion of Anderson *et al.*[22] is supported by Ullner *et al.*[185] who found that Se occupies the middle layer in the QL in Sb_2Te_2Se using powder X-ray diffraction. Lošťák *et al*.[186] assume that Se fills the Te sites without preference using indirect measurements: the reflectivity spectra in the plasma resonance frequency range, the Hall constant and the electrical conductivity. According to Zhang *et al.*[187] the topological phase transition occurs at $Sb_2(Se_{0.94}Te_{0.06})_3$ where the doping is modelled using the virtual crystal approximation method (the mixed site is replaced by a virtual atom that interpolates between the behaviour of the elements that occupy that mixed column).

We studied the local ordering of the bulk structure of $(Bi_{1-x}In_x)Se_3$ and $Sb_2(Se_xTe_{1-x})_3$ using atomic resolution HAADF STEM imaging combined with EDX mapping.

3.2.2 $(In_xBi_{1-x})_2Se_3$

We studied two different $(In_xBi_{1-x})_2Se_3$ concentrations, x=0.049 and x=0.135. The TEM samples themselves are made using FIB. The same quintuple-layered stacking as for Bi_2Se_3 is visible in the high-angle annular dark-field scanning transmission electron microscopy (HAADF STEM) images along the [010] zone. Both In-doped samples exhibited the same kind of defects: interstitial defects in the van der Waals (VdW) gap and interstitial defects in the middle and outer Se layers of the QLs, similar to Bi_2Se_3 (see section 3.1.3.1). Note that in Figure 3.16a.1 the interstitial atom is not always in the octahedral coordination site (see Figure 3.5) and that deviations on the position occur.

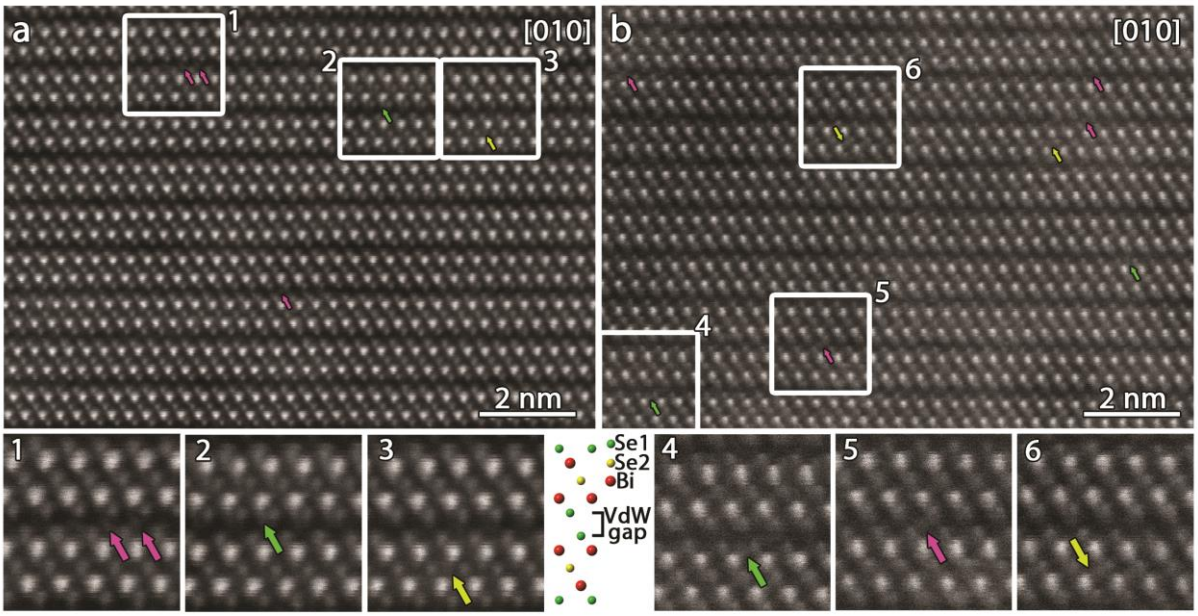

Figure 3.16 HAADF STEM images from a FIB prepared $(In_xBi_{1-x})_2Se_3$ sample with x= 0.049 (a) and x=0.135 (b), with the magnified areas displayed at the bottom of the figure combined with a unit cell of an undoped and defect free Bi_2Se_3 structure at the same scale as the magnified images (1-6). Purple arrows (1 and 5) mark the interstitial defects in the VdW gap. Yellow arrows highlight the interstitial atoms in the central Se layer of the quintuple layer (QL) (3 and 6) and green arrows in the outer Se layers (2 and 4).

These interstitial defects in the van der Waals gap appear mobile in the In-doped materials, similar to Bi_2Se_3. An example where the position of one specific interstitial atom is followed is shown in Figure 3.17c-d. The interstitial atom is present, disappears and appears again. This indicates that the interstitial defect moves from an interstitial site inside the VdW gap towards a Se vacancy in the outer Se layers and back. Bi_2Se_3 is known for its high amount of Se vacancies, so we assume that still some Se vacancies exist despite the small In addition. When the complete stack of 12 images of the same area is averaged, the interstitial defects are visible (Figure 3.17e). This indicates that most of the time the interstitial defects are present in the VdW gap. From the study of all HAADF STEM images from Bi_2Se_3, $(In_{0.049}Bi_{0.951})_2Se_3$ and $(In_{0.135}Bi_{0.865})_2Se_3$, we also suggest that the amount of interstitial defects went up with increasing In content. This increase of interstitial defects suggests that In is present on this site. The latter is further supported by EDX (see later). Also the STM data made by the group of Lada Yashina[138] indicate In defects inside the VdW gap. In section 3.1 we suggested that the interstitial defect in Bi_2Se_3 had mainly a cation character (Bi) which is in line with our current suggestion, in this case indium.

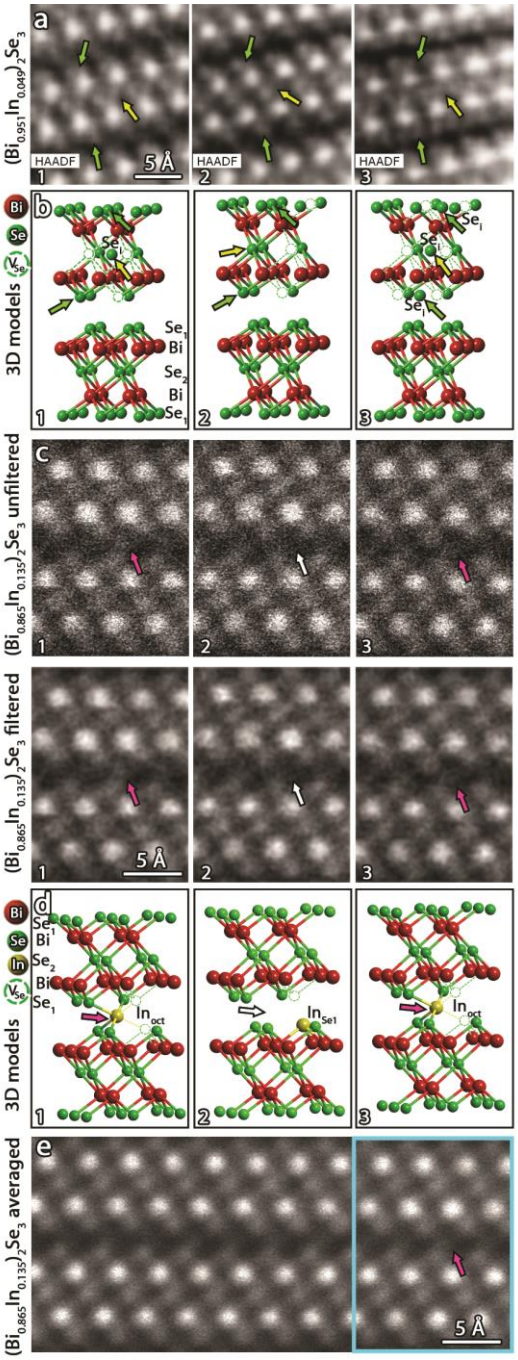

Figure 3.17 (a) HAADF STEM images along [010] of $(Bi_{0.951}In_{0.049})_2Se_3$ acquired during an EDX experiment showing the temporary creation of interstitial defect inside the Se1 and Se2 layers, marked with corresponding green and yellow arrows. (b) Schematic model of the observation in Figure 3.17a.: a Se1 atom displaced from its original position creates a vacancy and an interstitial atom in the Se1 layer (1), the Se1 atom relocate to its original position in the structure (2), followed by a repeated displacement creating a vacancy and an interstitial atom in the Se1 layer (3). A similar situation is observed for the Se2 atom. The direction of vacancy diffusion or if the atom moves to its original position is indistinguishable from the HAADF STEM images. (c) Time series (0s, 24s, 28s) of the unfiltered (top) and the Gaussian Blur filtered (bottom) HAADF STEM images along [010] of $(Bi_{0.865}In_{0.135})_2Se_3$ displaying the movement of an interstitial defect in the VdW gap. The interstitial defect is marked with purple arrows, while the empty VdW gap is marked with a white arrow. (d) Schematic model of the observation in Figure 3.17c: an In atom in an octahedral coordinated interstitial site in the VdW gap (In_{oct}) (1) moves towards an empty Se1 vacancy (In_{Se1}) (2) and back to an octahedral coordinated interstitial position in the VdW gap (In_{oct}) (3). (e) Averaged image of a stack of 12 images where three single frames of this stack are partly displayed in Figure 3.17c. The area of these single frames is marked in blue in Figure 3.17e.

The interstitial defects inside the Se layers also appear mobile, analogous to Bi_2Se_3. An example for $(Bi_{0.951}In_{0.049})_2Se_3$ is displayed in Figure 3.17a-b, showing a sequence of HAADF STEM images saved during EDX mapping. Interstitial defects clearly appear and disappear while mapping the same area. No conclusion could be made about the chemical character of these interstitial defects. Also, the direction of vacancy diffusion or if the atom moves back to its original position is indistinguishable from the HAADF STEM images and all mentioned situations are plausible. Note that Ji *et al.*[183] did observe local variations on the coordinates of the Se site in the middle Se layer for $(In_{0.88}Bi_{0.12})_2Se_3$, there each Se site is split into six partially occupied positions summing up to one atom occupancy.

We propose that the effect of the beam is to induce the movement, but not the interstitial defect itself based on our investigation of the undoped Bi_2Se_3 (section 3.1). However, like in the case of undoped Bi_2Se_3, some paths will probably exist which are possible at room temperate without the aid of external stimuli. The induced mobility in this type of materials indicates that a certain amount of mobility is possible without completely deforming the five-layered structure, which is a good indication of the stability of the material. However, the atomic mobility along and across the van der Waals gap is problematic if these materials should be used for *e.g.* Li or Na battery applications. In that case, the intrinsic mobility would hinder the mobility of the added Li or Na.

HR-EDX mapping was performed on both samples (Figure 3.18-Figure 3.19), showing the substitutional behaviour of In on the Bi sites. This was further supported by STM data of Sánchez-Barriga *et al.*[138] for $(Bi_{0.951}In_{0.049})_2Se_3$. Furthermore, the EDX map of $(In_{0.135}Bi_{0.865})_2Se_3$ contains In signal in octahedral coordinated sites and displaced sites inside the VdW gap and some inside the Se layers (Figure 3.19). The smeared out In signal along and across the VdW gap can be caused by the mobility of the interstitial defects (Figure 3.17c-d).

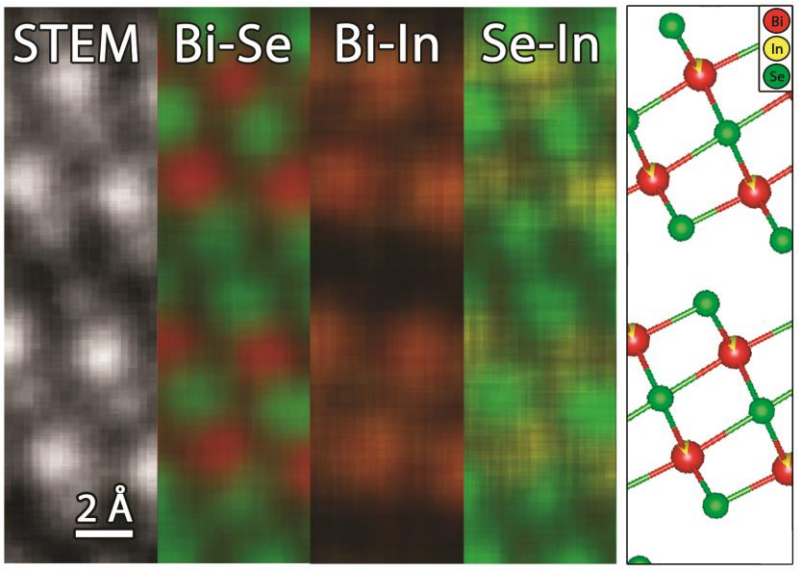

Figure 3.18 HR averaged EDX map from one large EDX map for $(In_{0.049}Bi_{0.951})_2Se_3$ with the HAADF STEM image and the partial composition maps. Bi-M is represented with red, Se-K with green and In-L with yellow, clearly showing the substitutional behavior of In on the Bi sites. The corresponding model is displayed on the right with mixed layers coloured by approximated fraction.

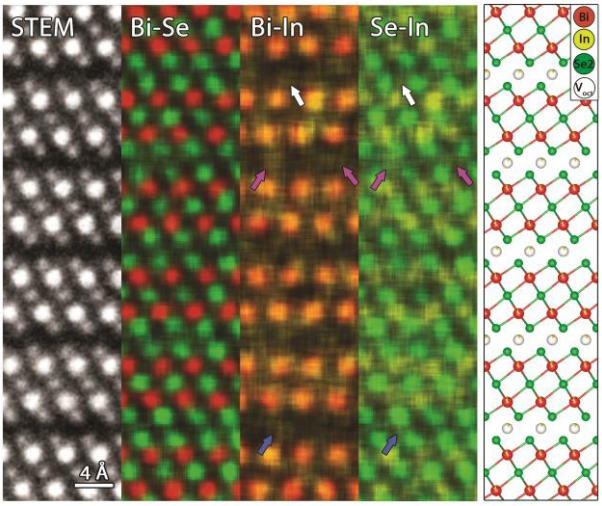

Figure 3.19 HR averaged EDX map of different areas for $(In_{0.135}Bi_{0.865})_2Se_3$ with the HAADF STEM image and the partial composition maps. Bi-M is represented with red, Se-K with green and In-L with yellow, clearly showing the substitutional behavior of In on the Bi positions. Furthermore, this map shows In signal in an octahedral coordinated site (purple arrow) and displaced site (blue arrow) inside the van der Waals gap, and some in the Se layers (white arrow). The corresponding model is displayed on the right with mixed layers coloured by approximated fraction.

Sánchez-Barriga *et al.*[138] studied the topological to normal insulator phase transition of these samples using spin- and angle resolved photoemission spectroscopy and relativistic many body calculations. They found that the inversion of the bulk bands happen for x=0.55. However, the surface states already opened at the Dirac point before this point. The reason why the surface states are already gapped before the phase transition is due to small In_2Se_3 clustering inside the structure. We did not observe local In_2Se_3 clustering using STEM imaging. A possible explanation could be that the size of the local ordering is too small (couple of atoms), resulting in a too small contrast difference inside the Z dependent cation columns in HAADF STEM. At the surface (vacuum-topological insulator interface) we have a Dirac cone but also on the topological to normal insulator domain formed by the In_2Se_3 clusters. When the wave function decays too slowly (when the spin-orbit coupling is too weak) then the wave functions of both Dirac cones overlap and we get a surface bandgap. The surface band states are also gapped when the material is a normal insulator. Furthermore, both on the topological insulator side and the normal insulator side a non-zero in plane spin polarization exists that decreases exponentially with increasing x (so towards the normal insulator side) and depends on the spin-orbit coupling. The out of plane polarization is negligible and independent of the spin-orbit coupling.

The measurements in the paper of Sánchez-Barriga *et al.*[138] show among other things the influence of the atomic structure, or more specifically of the local In_2Se_3 clustering on the properties of $(Bi_{1-x}In_x)_2Se_3$: a surface bandgap already opens at the Dirac cone while the bulk band inversion still exists. This is important to know when we want to use these surface states for applications. Also for certain applications like spintronic devices the bulk conductivity in Bi_2Se_3 is unwanted. Scattering from the bulk bands decreases when the Fermi level and the Dirac cone lie inside the bulk bandgap. For Bi_2Se_3 the Dirac cone is positioned inside the bulk bandgap, however the Fermi level is located inside the conduction bulk

band[25]. Wang H. *et al.*[188] found that In interstitial defects inside the van der Waals gap in InSe, a four-layered structure with sequence Se-In-In-Se, are donor defects. Similarly, Wang Y.-L. *et al.*[156] found that Cu interstitial defects in Bi_2Se_3 behave as donor defects. This suggests that In interstitial defects inside the van der Waals gap make the material more n-doped with a higher Fermi level, leading to more bulk conductivity instead of less. However, for thermoelectric applications, a high electrical conductivity is good and defects could lower the lattice thermal conductivity. For In ($5s^2\ 5p^1$) on the Bi ($6s^2\ 6p^3$) site, we expect negatively charged substitutional defects, thus leading to a hole concentration increase: $\mathrm{In} \rightarrow \mathrm{In}''_{\mathrm{Bi}} + 2\mathrm{h}^{\bullet}$. The symbol " means that In_{Bi} has a -2 charge and the symbol • indicates that the hole h has a positive charge. However, Horák *et al.*[189] suggest that the In_{Bi} defect is uncharged, where the In ($5s^2\ 5p^1$) undergoes an electronic transition to In ($5s^0\ 5p^3$). The bond polarity (the difference between the electronegativity of the two elements forming the bond) of the In-Se bonds increases compared to the Bi-Se bonds, which leads to a decrease of the antisite defects Bi_{Se}: $\mathrm{Bi} \rightarrow \mathrm{Bi}'_{\mathrm{Se}} + \mathrm{h}^{\bullet}$. This initially increases the free carrier concentration due to the drop of hole concentration with which the electron can recombine. At x=0.075, the free electron concentration drops because the incorporation of In increases the ionicity, lowering the deviation from stoichiometry and thus decreases the Se vacancies $\mathrm{V}^{\bullet\bullet}_{\mathrm{Se}}$. So, Horák *et al.*[189] proposed that In on the Bi site doesn't directly influence the Fermi level; instead, it influences the concentration of other defects and changes the Fermi level in this way.

3.2.3 $Sb_2(Se_xTe_{1-x})_3$

We studied this system at three different concentrations, where the concentration itself was determined with SEM-EDX: $Sb_{2.07(3)}(Se_{0.09(2)}Te_{0.89(1)})_3$, $Sb_{2.01(4)}(Se_{0.33(3)}Te_{0.67(2)})_3$ and $Sb_{2.05(4)}(Se_{0.52(3)}Te_{0.47(2)})_3$ (Figure 3.20). These concentrations were the result of using correspondingly x=0.1, x=0.3 and x=0.6 during sample preparation. From the HAADF STEM image of the sample $Sb_{2.05(4)}(Se_{0.52(3)}Te_{0.47(2)})_3$. (Figure 3.20c) it is already clear that the Se atoms preferentially substitute the middle Te layer in the quintuple layer due to the Z contrast in HAADF STEM images. Se has a Z number of 34, while Te has one of 52, so columns that contain more Se atoms will appear darker than columns with more Te atoms. In contrast to the $(Bi_{1-x}In_x)_2Se_3$ system no interstitial defects were observed.

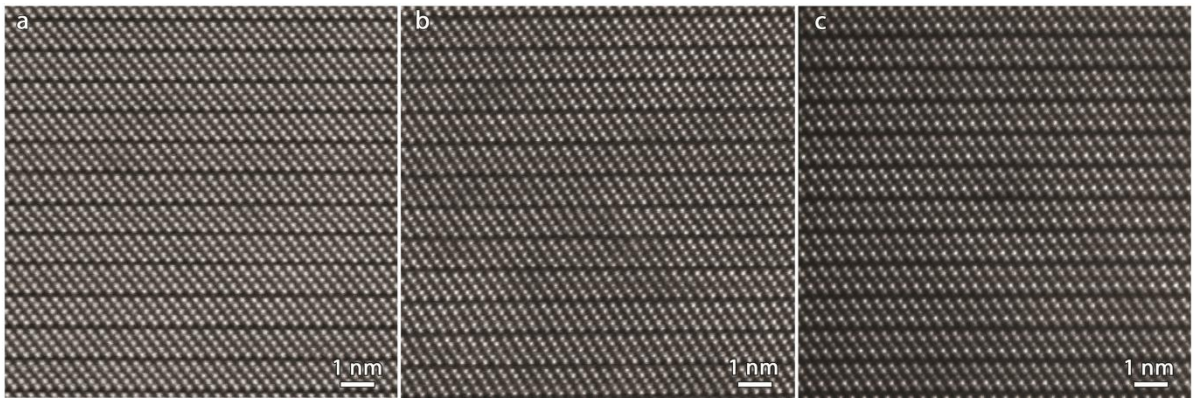

Figure 3.20 HAADF STEM images of zone [010] for $Sb_{2.07(3)}(Se_{0.09(2)}Te_{0.89(1)})_3$ (a), $Sb_{2.01(4)}(Se_{0.33(3)}Te_{0.67(2)})_3$ (b) and $Sb_{2.05(4)}(Se_{0.52(3)}Te_{0.47(2)})_3$ (c).

The samples contain, however, 3D defects of different sizes (Figure 3.21). The pure Sb_2Te_3 sample also contained these defects. These 3D defects still show the quintuple layer in projection, but a darker contrast is observed.

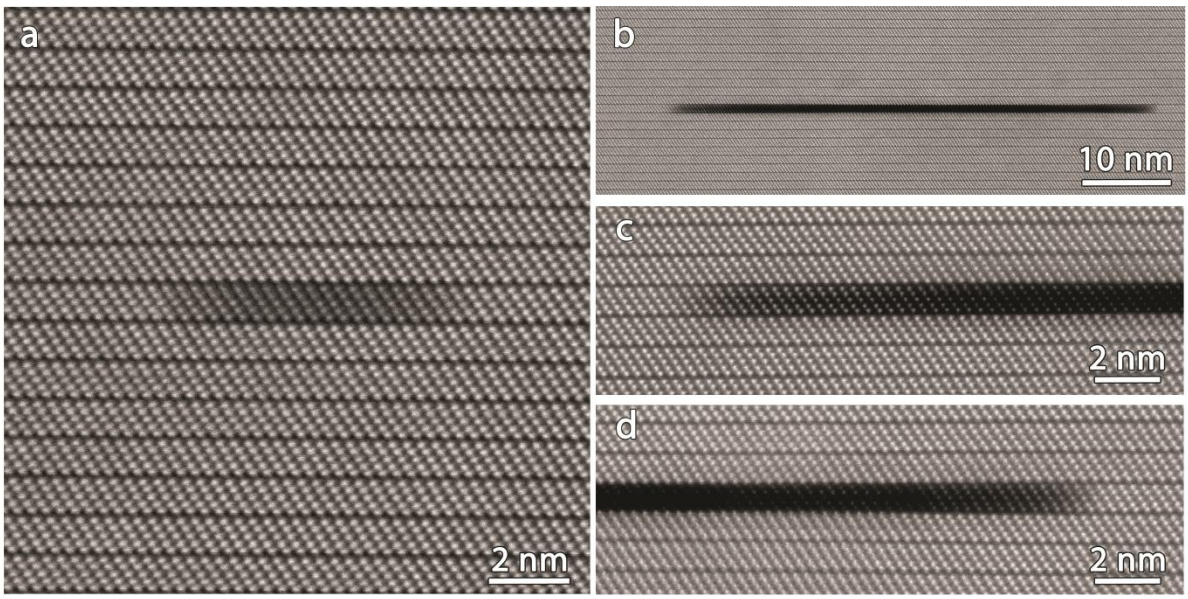

Figure 3.21 HAADF STEM images of the 3D defects in $Sb_{2.07(3)}(Se_{0.09(2)}Te_{0.89(1)})_3$: (a), (b) An overview of two 3D defects of different size. (c), (d) Close ups of the edges of the 3D defect in (b).

A possible explanation for the change of contrast could be that a chemically different composition exists in these areas, similar to the CaSe nanoclusters found in Ca-doped Bi_2Se_3. However, EDX (Figure 3.22) shows a decrease of Sb, Te and Se with no other chemical element present. This suggests that the contrast difference is caused by a decrease in thickness and not a change of chemical composition. Another explanation could be that the defects are caused by the FIB sample preparation, however, no reports were found in literature of any similar defects caused by FIB in any other materials. Furthermore, they were also not present in any of the other samples that we made, which were all prepared with similar sample preparation settings. Another suggestion is that oxygen is captured in these areas. For example, oxygen might be present in the sample when the raw bulk Bi material used for sample preparation was oxidized. However, in this case the question remains why the void only consists of one quintuple layer. Wu *et al.*[190] observed in $(GeTe)_{0.975}(Bi_2Te_3)_{0.025}$ vacancy clusters, however, a specific size was not mentioned. Another proposition is that these materials contained another phase consisting for example only of Se which is the lightest of the three elements. This can explain the excess of Se in the outer layer of the QL bordering the line defect (Figure 3.22). Due to the different structural properties between the two phases the milling effect can be different, causing the removal of the extra phase by FIB. However, such a big difference in milling on such a local scale is still highly unlikely. Also annealing can remove secondary phases[191], however no annealing after the sample preparation is performed on these samples. So, the origin of these 3D defects, consisting of the partial removal of one quintuple layer in the depth of the material, is not clear. But it would be interesting to know their effect on the properties of this

material. Khan *et al.*[191] found that nano- to micrometre sized pores in for example $Co_{23.4}Sb_{69.1}Si_{1.5}Te_{6.0}$, which were irregularly shaped and were randomly oriented, lowered the lattice thermal conductivity caused by a wide spectrum of phonon scattering. This was very beneficial for the thermoelectric properties of the material and enhanced the ZT with more than 100% compared to the material without pores.

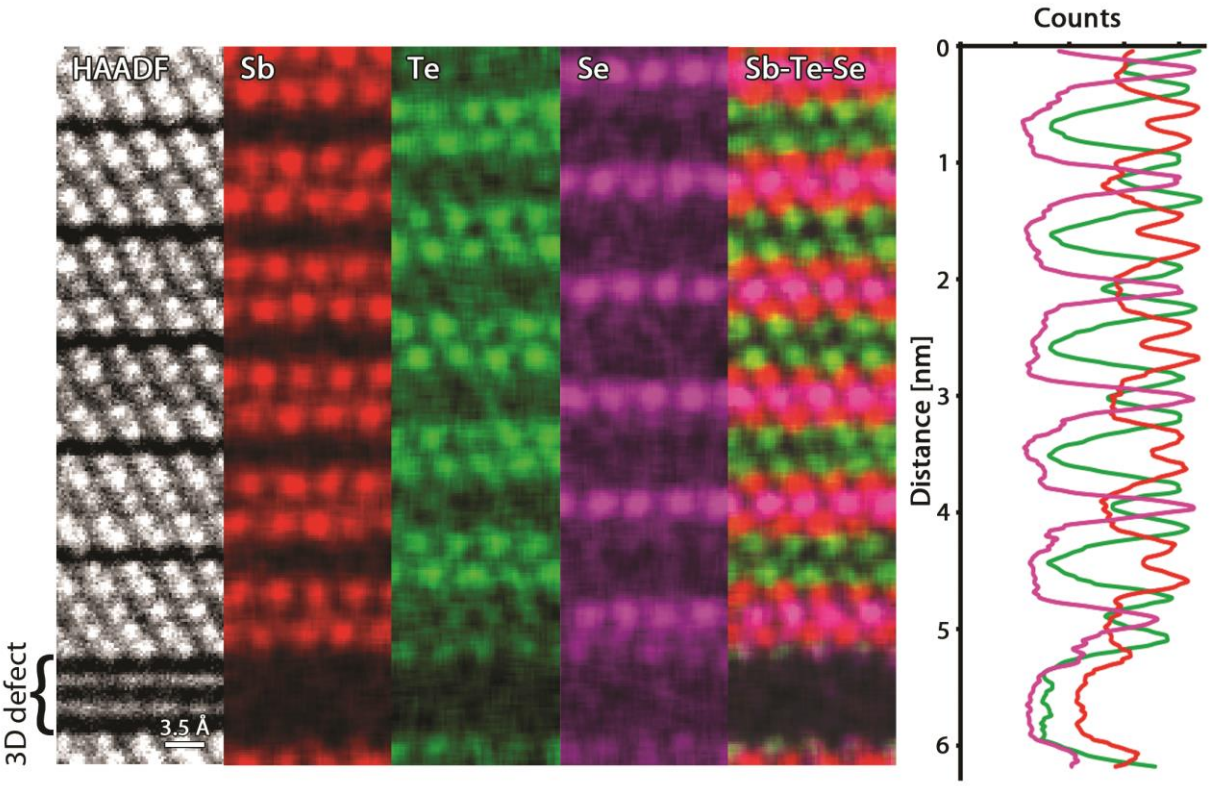

Figure 3.22 EDX map of zone [010] from $Sb_{2.01(4)}(Se_{0.33(3)}Te_{0.67(2)})_3$ with a vertical line profile: Se occupies dominantly the central layer of the QL , but are also present in the outer layers of the QL. The EDX signal of Sb, Se and Te drops at the position of the 3D defect.

The Se map of the EDX maps from $Sb_{2.07(3)}(Se_{0.09(2)}Te_{0.89(1)})_3$ and $Sb_{2.01(4)}(Se_{0.33(3)}Te_{0.67(2)})_3$ each averaged (Figure 3.23) indicate that the outer layers of the QL layer already contain Se before the middle layer is completely filled, contradicting literature which indicated that Se had a site preference on the middle Te layer, the outer Te layers or no site preference at all[22,185,186,192].

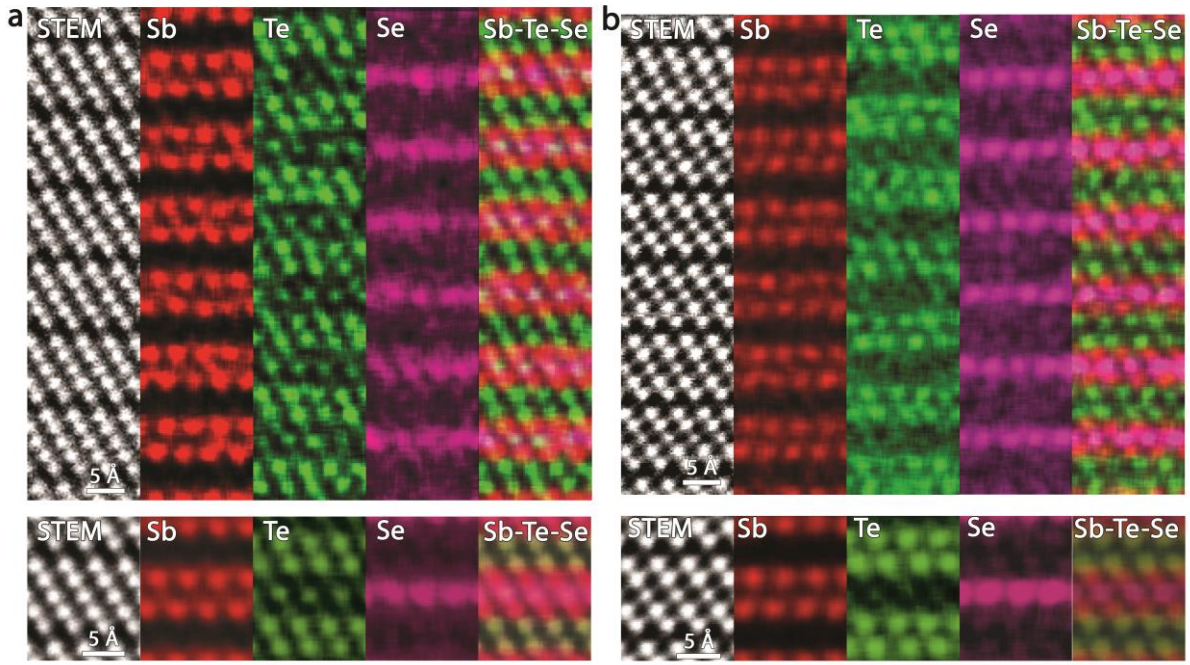

Figure 3.23 Atomic resolution EDX maps of (a) $Sb_{2.07(3)}(Se_{0.09(2)}Te_{0.89(1)})_3$ and (b) $Sb_{2.01(4)}(Se_{0.33(3)}Te_{0.67(2)})_3$. The small EDX map at the bottom is obtained from the top EDX map by averaging over the different quintuple layers.

We performed a more detailed EDX investigation to obtain a rough estimate of the chemical layer composition of the chemically different Te/Se layers. We followed a similar procedure described by Lu *et al.*[193,194], using the Sb-L (6.603 keV), Te-L (3.767 keV) and Se-K (11.210 keV) lines. First, we average the atomic resolution map (Figure 3.23) to increase the signal to noise ratio. Next, we fit the line profile of the elemental maps of the mixed positions with a combination of Gaussian functions using the program Fityk[195] (Figure 3.24). The FWHM of the Gaussian peaks for each element was constrained to have the same value for the different layers. Small differences can occur, because the FWHM depends on the beam spreading and channelling which on its own depends on the chemical distribution of the column[194]. However, thin film conditions weaken the dependence. The fitted FWHM of Te-L is 0.27 nm and of Se-K is 0.25 nm. Then, we determine our own k factors of the Cliff-Lorimer method[54] –assuming thin film conditions- which is the scaling factor between the concentration ratio of two elements, C_{Te}/C_{Se} ,and their corresponding characteristic X-ray intensity ratio I_{Se}/I_{Te}: $\frac{C_{Te}}{C_{Se}} = k_{Te,Se}\frac{I_{Te}}{I_{Se}}$ .The counts ratio I_{Te}/I_{Se} is determined by taking the ratio of the sum of the areas under the Gaussian peaks of Te and Se. The concentration ratio in atomic percent, C_{Te}/C_{Se}, was obtained from the STEM-EDX data. We choose the STEM-EDX data due to the small difference with the SEM-EDX data that could be explained by small local concentration differences (Table 3.6). Knowing the k factors we can use the formulae '$\frac{C_{Te}}{C_{Se}} = k_{Te,Se}\frac{I_{Te}}{I_{Se}}$' combined with '$C_{Te}+C_{Se}$ =1' to determine the layer composition of the chemically different Te/Se layers (see Table 3.7-Table 3.8). The error is calculated through error propagation with the k factor variation Δk/k ~0.1 and assuming that the error on the

counts is equal to $\sqrt{I}$. The count variation (ΔI/I) is thus negligible compared to the k factor variation, when using a reasonable amount of counts per element.

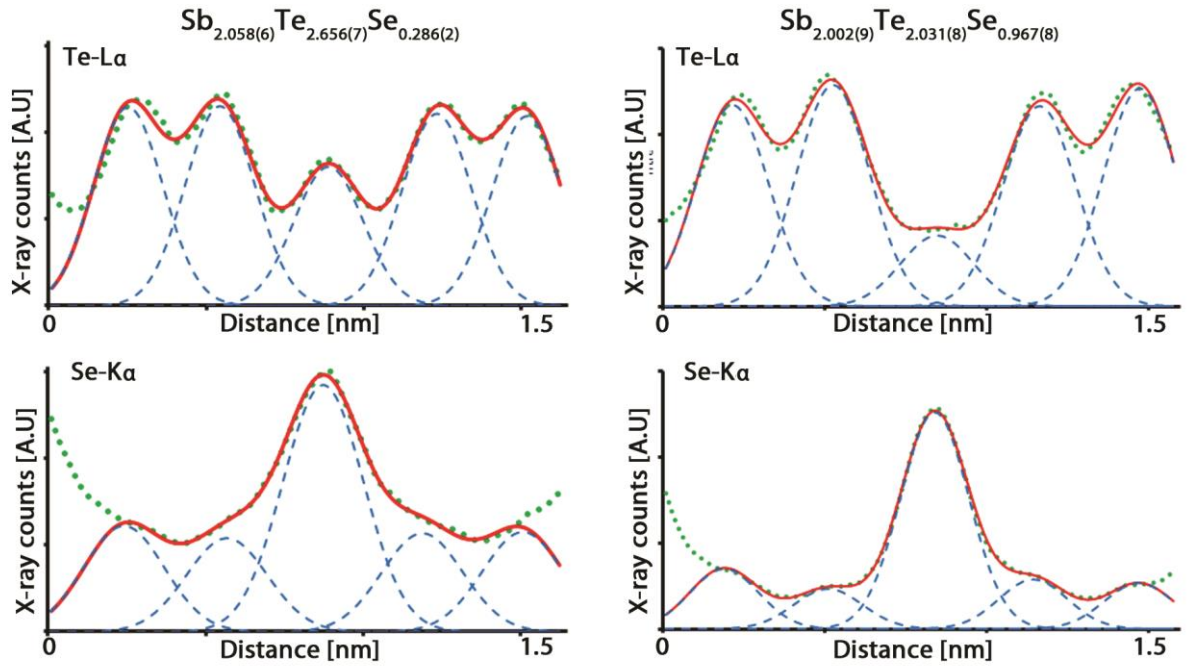

Figure 3.24 The elemental Se and Te line profiles of the averaged HR-EDX maps in Figure 3.23: the experimental data (green) where Gaussian peaks are fitted at the different peak positions (blue) with the overall sum (red).

Label name	SEM-EDX	STEM-EDX
$Sb_2(Te_{0.4}Se_{0.6})_3$	$Sb_{2.05(2)}Te_{1.40(2)}\ Se_{1.55(3)}$	
$Sb_2(Te_{0.7}Se_{0.3})_3$	$Sb_{2.01(2)}Te_{2.01(3)}\ Se_{0.98(3)}$	$Sb_{2.002(9)}Te_{2.031(8)}Se_{0.967(8)}$
$Sb_2(Te_{0.9}Se_{0.1})_3$	$Sb_{2.07(2)}Te_{2.67(2)}\ Se_{0.26(3)}$	$Sb_{2.058(6)}Te_{2.656(7)}Se_{0.286(2)}$

Table 3.6 The measured SEM-EDX and STEM-EDX[2] data for the different samples.

[2]To calculate the error only the variation of the different measurements is taken into account, not the error of the method itself.

	$Sb_{2.058(6)}Te_{2.656(7)}Se_{0.286(2)}$			$Sb_{2.002(9)}Te_{2.031(8)}Se_{0.967(8)}$		
	Sb-L	Te-L	Se-K	Sb-L	Te-L	Se-K
Layer 1	0	94.3(6)	5.7(6)	0	88(2)	12(2)
Layer 2	100	0	0	100	0	0
Layer 3	19	81(2)	19(2)	0	30(3)	70(3)
Layer 4	100	0	0	100	0	0
Layer 5	0	93.7(6)	6.3(6)	0	84(2)	16(2)

Table 3.7 More detailed EDX investigation of the chemical composition of the different layers of one QL for $Sb_{2.058(6)}Te_{2.656(7)}Se_{0.286(2)}$ and $Sb_{2.002(9)}Te_{2.031(8)}Se_{0.967(8)}$.

	$Sb_{2.058(6)}Te_{2.656(7)}Se_{0.286(2)}$		$Sb_{2.002(9)}Te_{2.031(8)}Se_{0.967(8)}$	
	Te-L	Se-K	Te-L	Se-K
Middle layer QL	94.0(4)	6.0(4)	86(1)	14(1)
Outer layer QL	81(2)	19(2)	30(3)	70(3)

Table 3.8 Averaged result over equivalent layers of the more detailed EDX investigation for $Sb_{2.058(6)}Te_{2.656(7)}Se_{0.286(2)}$ and $Sb_{2.002(9)}Te_{2.031(8)}Se_{0.967(8)}$.

So, the more detailed EDX investigation confirms that before the middle Te layer of the quintuple layer is completely filled with Se, Se is already present in the outer Te layers. When we compare HAADF STEM simulations using the found concentration with the averaged experimental HAADF STEM image, we can conclude that the match is reasonable, confirming the found layer composition (Figure 3.25).

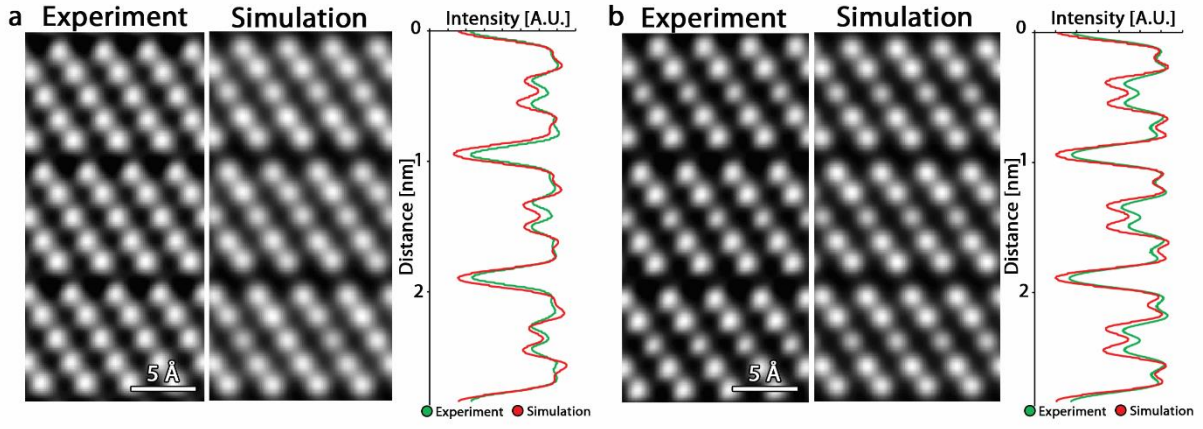

Figure 3.25 Comparison between the averaged experimental HAADF STEM images and the simulated HAADF STEM images calculated using QSTEM[84] using the found layered composition displayed in Table 3.8 and their corresponding line profiles for $Sb_{2.07(3)}(Se_{0.09(2)}Te_{0.89(1)})_3$ (a) and $Sb_{2.01(4)}(Se_{0.33(3)}Te_{0.67(2)})_3$ (b).

For Sb_2Te_3 the Dirac cone lies inside the bulk bandgap and the Fermi level below the top of the bulk valence band, indicating p-doped characteristics[29]. Horák *et al.*[164] proposed that the increase of uncharged Se defects on the Te sites in $Sb_2(Se_xTe_{1-x})_3$ leads to a decrease of the concentration of Sb_{Te} antisite defects ($Sb \rightarrow Sb'_{Te} + h^{\bullet}$) and a small drop in the concentration of anion vacancies ($V^{\bullet\bullet}_{Te}$). This is due to the increase in the band polarity caused by the higher electronegativity of Se compared to Te. This makes the $Sb_2(Se_xTe_{1-x})_3$ material less p-doped compared to the undoped Sb_2Te_3 material. No explicit distinction was made between the outer and inner Te layers of the quintuple layer. In Sb_2Te_3 the antisite defect Sb_{Te1} has a lower formation energy compared to Sb_{Te2}[112] and Jiang *et al.*[165] only observed Sb_{Te1} using STM. Therefore, most or all antisite defects are positioned on the outer Te layers. We found that a small quantity of Se occupies the outer Te layers before the middle Te layer is completely filled. It is possible that the small quantity of Se atoms in the outer Te layers influence the amount of antisite defects on the outer Te layers more than the Se atoms do in the middle Te layers. More research needs to be done on this, however, this lies outside the scope of this thesis.

3.2.4 Conclusion

$(Bi_{1-x}In_x)_2Se_3$ was cation substituted with interstitial defects inside the van der Waals gap with In character indicated by EDX. We propose that the interstitial defect is not beam induced based on our investigation of the undoped Bi_2Se_3. Literature suggests that these interstitial defects will make the material even more n-doped, leading to more bulk conductivity instead of less which is not optimal when the aim is to use the conducting surface states like in spintronics. On the contrary, for thermoelectric applications we want a higher electrical conductivity combined with a lowering of the lattice thermal conductivity due to the point defects. Furthermore, atomic mobility along and across the van der Waals gap is observed and we suggest that this is beam induced, again based on our examination of the undoped Bi_2Se_3. This atomic mobility indicates that the material can withstand a certain amount of external stimuli, in our case the electron beam, without completely deforming the structure which is a good property. However, for *e.g.* Li and Na battery applications this property is not ideal because it can hinder the mobility of the Li and Na atoms.

$Sb_2(Se_xTe_{1-x})_3$ was anion substituted with no interstitial defects. We observed a clear ordering on the anion sites different from literature: Se occupies mostly the middle layer of the quintuple layer, however, a low Se amount already fills the outer Te layers before the middle layer is completely filled. Literature indicates that uncharged Se defects on the Te sites lead to a decrease of the Sb_{Te} antisite concentration. Furthermore, the antisite defects seem to be located mostly or only on the outer Te layers. It is possible that the small quantity of Se atoms on the outer Te sites react with these antisite defects instead of the inner Se atoms; more research needs to be done on this. The material also contained 3D defects consisting of the removal of part of the quintuple layer. Their effect on the material's properties would be interesting, especially since Khan *et al.* [191] found that this sort of defects

can heavily enlarge the thermoelectric properties of a material. However, this lies outside the scope of this thesis.

3.3 $Ge_mBi_{2n}Te_{(m+3n)}$

3.3.1 Introduction

In the previous two sections we talked about how intrinsic and extrinsic defects can influence the material properties and that defect engineering should lead to the perfect characteristics for applications like low-power spintronics[169]. In this section the same goal applies but the way to obtain it is different. This time the conducting surface states will be tuned not by extrinsic doping of the quintuple-layered structure but by forming homologous series by adding Ge to Bi_2Te_3[196] to form $Ge_mBi_{2n}Te_{(m+3n)}$ series or written in another way $mGeTe\text{-}nBi_2Te_3$ systems. Eremeev *et al.*[197] demonstrated the tunability of the surface states with ab-initio calculations, spin-resolved photoemission and scanning tunnelling microscopy for the $mPbTe\text{-}nBi_2Te_3$ homologous series of topological insulators. Furthermore, Xu *et al.*[198] proved that $GeBi_2Te_4$ is a topological insulator with a single Dirac cone with an isolated Dirac point. Knowing the chemical composition per layer is important for the material's properties, like their topological insulator character.

Series of structures made by stacking the same structural slabs but in different amounts are called a homologous series. For example, in $mGeTe\text{-}nBi_2Te_3$, for m=0, n=1 you have Bi_2Te_3, the common quintuple-layered structure, while for m=1 and n=1 you obtain $GeBi_2Te_4$ or $GeTe\text{-}Bi_2Te_3$, suggesting a seven-layered structure. Agaev *et al.*[14] and Karpinskii *et al.*[199] indeed found for $GeBi_2Te_4$ a seven-layered structure. However, they disagreed on the composition of the single layers. Furthermore, others[200,201] found metastable structures with a cubic rock salt structure for the $Ge_mBi_{2n}Te_{(m+3n)}$ series instead of the trigonal layered structures.

So, the $GeTe\text{-}Bi_2Te_3$ system mostly occurs in two different structure types: (i) a stable trigonal layered structure containing building blocks of an odd number of alternating stacked Te and mixed Ge/Bi layers along the c_H axis (hexagonal cell) where the Te-Te layers of adjacent building blocks are connected with weak van der Waals interactions[14,199,201–205], while the other type (ii) is a metastable cubic rock salt structure consisting of equidistant and alternating stacked Te and mixed Ge/Bi layers along the $[111]_C$ direction (cubic cell) containing vacancies on the Ge/Bi positions[200,201] (Figure 3.26). The building blocks of the trigonal layered structure can be roughly viewed as a finite sized rock salt structure. An exception to these two structure types is the domain rich α-GeTe structure for the $GeTe\text{-}Bi_2Te_3$ system with low addition of Bi_2Te_3 ($(GeTe)_{1-x/2}(Bi_2Te_3)_{x/2}$ with x= 0%, 3%, 5% and 7%)[190]. The sample preparation method[201,206] *e.g.* an additional annealing step[201] or slow cooling[206] can influence in which structure type the material will occur. Also temperature can cause a phase transition from one structure type to another[201]. It is important to know which structure type will appear under which conditions, because the atomic structure will influence the properties, which can for example affect the topological insulator character.

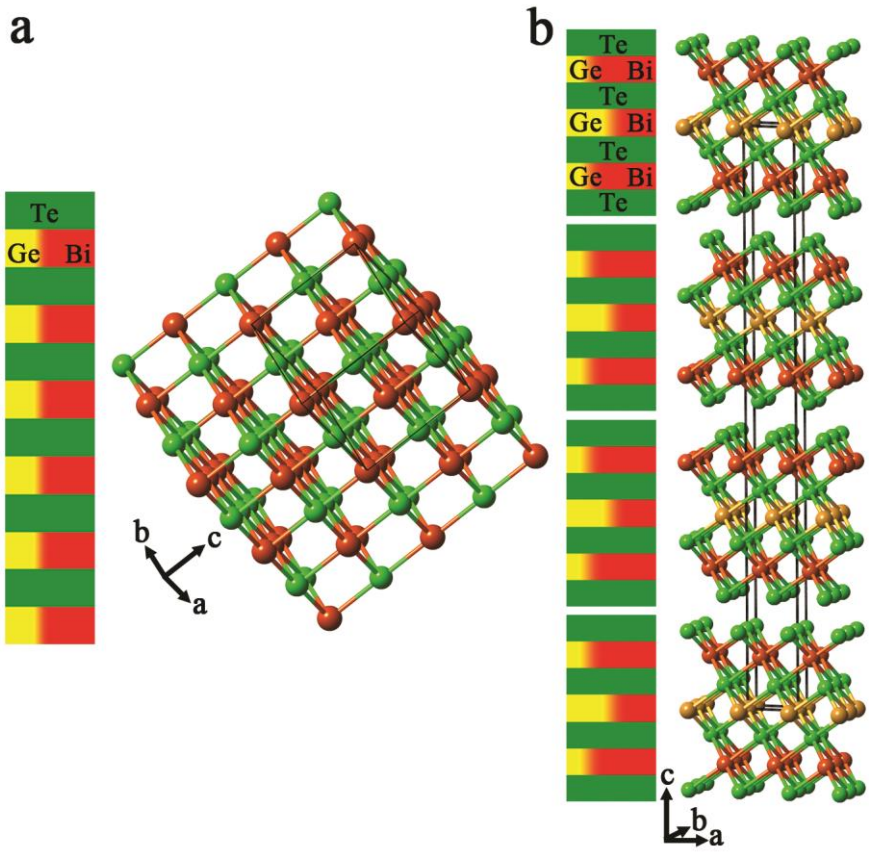

Figure 3.26 The cubic rock salt type structure (a) and an example of the trigonal layered structures (b) for the GeTe-Bi_2Te_3 system with mixed Ge/Bi layers. Our results for the trigonal layered structures indicated that more Bi is present in the outer Bi/Ge layers than in the inner Bi/Ge layers, which is taken into account in the displayed model. Green represents Te, red Bi, yellow Ge and orange a mixture of Bi and Ge.

Temperature induces a phase transition from the metastable rock salt structure to the trigonal layered structure. For example, $Ge_2Bi_2Te_5$ undergoes this phase transition at 650K passing a two-phase coexistence[201]. The metastable rock salt structure contains 20 atomic percent vacancies in the Ge/Bi layers[201]. These vacancies lead to the crystal chemical stability of the rock salt structure[207]. Furthermore, heating aids the diffusion of these random vacancies into ordered planes[208]. Zhang *et al.*[209] showed through ab-initio calculations that the rearrangement of the vacancies from vacancy clusters to ordered vacancy layers causes the insulator (rock salt structure) to metal (trigonal layered structure) transition in the closely related GeTe-Sb_2Te_3 system, while substitution disorder and the structural distortion between the two structure types aren't crucial[209].

The GeTe-Bi_2Te_3 system could be interesting for phase-change memory application due to its amorphous to crystalline phase transformation similar to the closely related GeTe-Sb_2Te_3 system. For applications the speed of crystallization is important, because the principle is based on the amorphization and recrystallization of the material by use of e.g. laser or current pulses. Lee *et al.*[210] reported their fast crystallization, where the temperature and the minimum time for crystallization are smaller than the closely related GeTe-Sb_2Te_3 system. For rewritable optical storage devices the phase change material should also have a

large optical difference between the two states, which is the case for the related GeTe-Sb_2Te_3 system already used in applications[211]. Furthermore, the characteristic material features for optical storage applications, such as the octahedral-like atomic arrangement and vacancies, also exist in GeTe-Bi_2Te_3. For non-volatile electronic storage devices the two states of the material should have a large change in electrical conductivity, which is the case for the GeTe-Sb_2Te_3 system[209]. Furthermore, the GeTe-Bi_2Te_3 material is also a good thermoelectric material[212,190].

These trigonal layered structures are also van der Waals heterostructures, an emerging research area[213]. Van der Waals heterostructures are structures where different 2D crystals are stacked on top of each other. So, an artificial material can be made by adding monolayer or few-layer crystals on top of each other in a chosen sequence. Within the 2D crystals strong covalent bondings exist, while weak van der Waals forces bind the different building blocks.

We studied seven different concentrations of $Ge_mBi_{2n}Te_{(m+3n)}$: $GeBi_2Te_4$, $GeBi_2Te_4$+I, $GeBi_4Te_7$, $Ge_3Bi_2Te_6$+I, $Ge_3Bi_2Te_6$, $Ge_4Bi_2Te_7$ and $Ge_{6.8}Bi_2Te_{9.8}$. After two samples '+I' is noted, because they were made with a chemical transport reaction (CTR) and thus contain iodine (~ 1%) which was the transport agent. The other five samples were made with the Bridgman technique. We observed using HAADF STEM and EDX spectroscopy that $GeBi_2Te_4$, $GeBi_2Te_4$+I, $GeBi_4Te_7$ and $Ge_3Bi_2Te_6$+I have a trigonal layered structure with van der Waals gaps, while $Ge_3Bi_2Te_6$, $Ge_4Bi_2Te_7$ and $Ge_{6.8}Bi_2Te_{9.8}$ have the rock salt structure with twin boundaries and Ge vacancies. We will first discuss the trigonal layered structures and then the rock salt structures.

3.3.2 Results

3.3.2.1 Trigonal layered structures

3.3.2.1.1 HAADF STEM

Until now all studied structures (Bi_2Se_3, $(Bi_xIn_{1-x})_2Se_3$ and $Sb_2(Se_xTe_{1-x})$) consisted of a stacking of five-layered building blocks –also called a quintuple layer- along the c-axis with weak van der Waals interactions in between them. These van der Waals gaps are recognized in HAADF STEM images by a larger distance separating two building blocks in comparison to the layers inside these building blocks. $GeBi_2Te_4$, $GeBi_2Te_4$+I, $GeBi_4Te_7$ and $Ge_3Bi_2Te_6$+I have a similar layered structure, however the amount of layers inside these building blocks are now different (Figure 3.27). The structure of $GeBi_2Te_4$ prepared with the Bridgman method consists of blocks of nine layers, while $GeBi_2Te_4$+I made using CTR consists of seven-layered blocks. $GeBi_4Te_7$ made with the Bridgman technique contains on average an alternation of quintuple and septuple layers. $Ge_3Bi_2Te_6$+I created using CTR is built with eleven-layered building blocks.

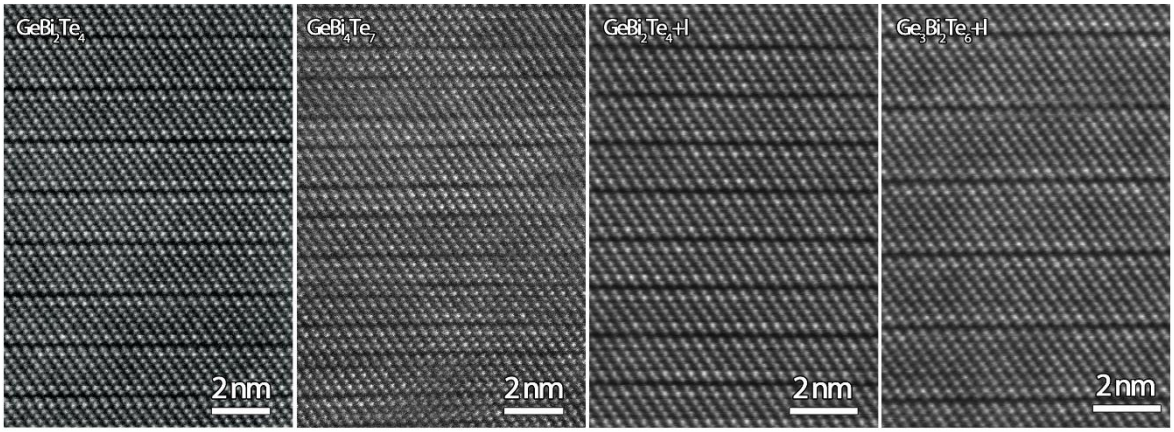

Figure 3.27 Trigonal layered structures: $GeBi_2Te_4$ contains nine-layered building blocks, $GeBi_4Te_7$ five-seven-layered building blocks, $GeBi_2Te_4$+I seven-layered building blocks and $Ge_3Bi_2Te_6$+I eleven-layered building blocks. The first two materials are made using the Bridgman technique, while the last two are made using CTR.

3.3.2.1.2 EDX study

Two of these four samples, $GeBi_2Te_4$ and $GeBi_2Te_4$+I, are studied in more details using HR EDX. We start with the assumption that the Te columns are pure, while the Ge/Bi columns are mixed. Our EDX maps show no clear proof of other intermixing behaviour, for example Bi on the outer Te layers. The EDX maps are in the same way analysed as described by Lu *et al.*[193,194] which is discussed in section 3.2.3. The used averaged EDX maps together with the pre-averaged EDX maps are shown in Figure 3.28. The fitting of the line profiles of these averaged elemental Bi and Ge maps are displayed in Figure 3.29.

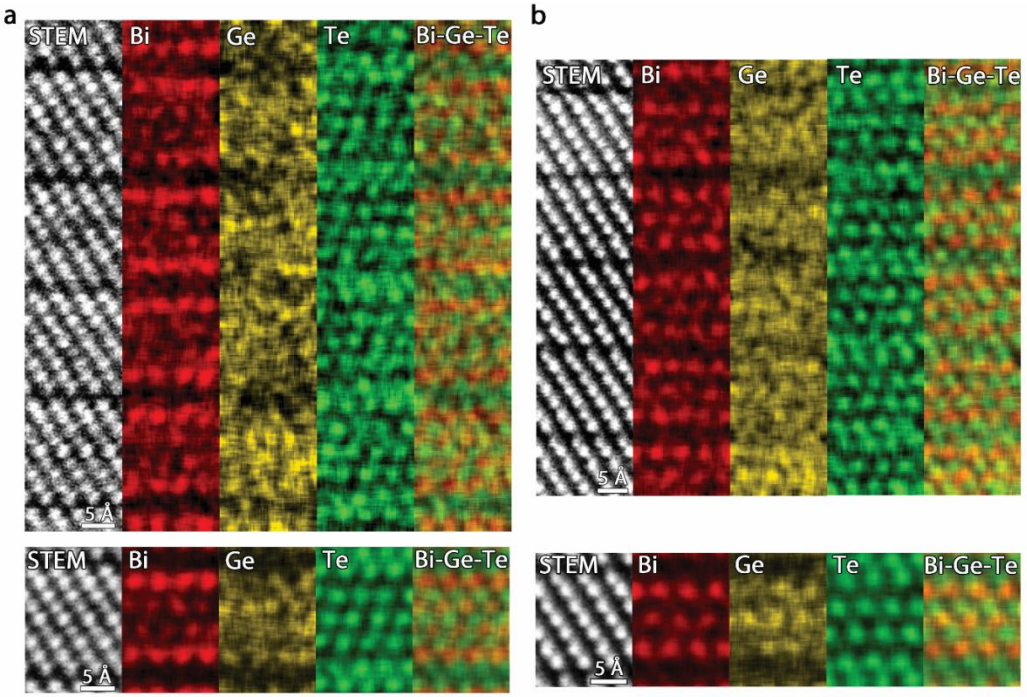

Figure 3.28 Atomic resolution EDX maps (top) and their respectively averaged EDX maps (bottom) for (a) $GeBi_2Te_4$ and (b) $GeBi_2Te_4$+I.

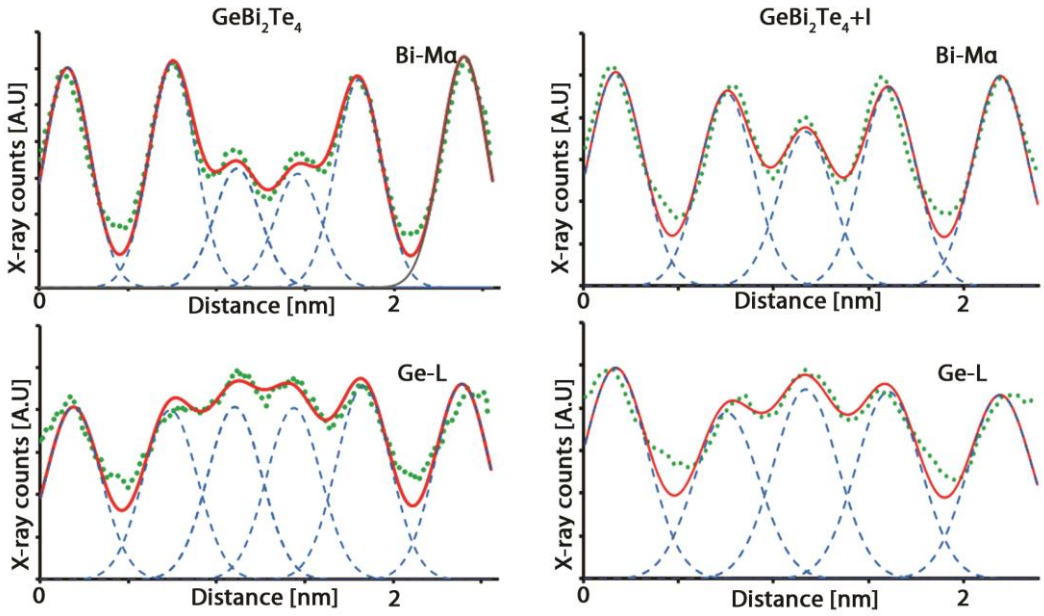

Figure 3.29 The Bi and Ge elemental line profiles of the HR-EDX maps in Figure 3.28: experimental data (green) where Gaussian peaks are fitted at the different peak positions (blue) with the overall sum (red).

However, during the investigation we observed that the average STEM-EDX data of the $GeBi_2Te_4$+I sample disagreed with the X-ray fluorescence (XRF) data of the group of Lada Yashina (Table 3.9). Therefore, we performed a SEM-EDX study, the results of which matched the XRF data. So, during the treatment of the EDX data we used the SEM-EDX composition for $GeBi_2Te_4$+I and the STEM-EDX composition for $GeBi_2Te_4$.

Name	XRF	SEM-EDX	STEM-EDX
$GeBi_2Te_4$	$\approx Ge_{14}Bi_{29}Te_{57}$		$Ge_{12.6(2)}Bi_{26.4(2)}Te_{60.9(2)}$
$GeBi_2Te_4$+I	$\approx Ge_{14}Bi_{29}Te_{57}$+1%I	$Ge_{13.4(2)}Bi_{29.98\,(8)}Te_{56.6(2)}$	$Ge_{8.4(2)}Bi_{31.3(2)}Te_{60.40(7)}$

Table 3.9 Comparison between the XRF data, SEM-EDX data and the STEM-EDX[3] data of the $GeBi_2Te_4$ and $GeBi_2Te_4$+I samples.

There are different explanations possible for why the STEM-EDX data differs from the XRF data taken by the group of Lada Yashina. The composition can vary locally and the STEM-EDX data is obtained from a small, local area. Deviations on the composition can also be caused due to strong channelling effects because the EDX map is taken in zone[214]. Furthermore, shadowing of the detectors by certain parts of the holder can affect the quantification of an element with a low to medium atomic number[215]. Or the sample is not thin enough, which was one of the criteria of Lu *et al.* [193,194].

Channelling effects of the electrons along a column depend on the exact composition of that column. However, the composition variation between different Bi/Ge mixed columns is still

[3] To calculate the error only the variation of the different measurements is taken into account, not the error of the method itself.

not too large. So, it is reasonable to assume that the channelling effects are similar in all mixed Ge/Bi columns. Also the effect of the shadowing will be the same for identical elements in different atomic columns. So, we expect that the ratio of one element in column 1 to column 2 is still correct. This means that if column 1 contains more Bi, that this will be reflected in our experiment. Even if the ratio between one to another element is incorrect, we can counter this problem by using the SEM-EDX data to rescale the intensity values correctly:

$$\frac{C_{Bi}}{C_{Ge}} = k_{Bi,Ge}\frac{I_{Bi}}{I_{Ge}} \qquad 3.11$$

where $C_{Bi(Ge)}$ is the Bi(Ge) concentration, $I_{Bi(Ge)}$ is the characteristic X-ray intensity of Bi(Ge) and $k_{Bi,Ge}$ is our own determined k factor of the Cliff-Lorimer method.

3.3.2.1.3 Comparison with literature

In this section, the layered composition of the nine-, seven-, eleven and five-seven layered structures are discussed in detail and compared with the literature. A schematic overview of this is represented in Figure 3.31. At the end, we also link our found results for the GeTe-Bi_2Te_3 system with the similar GeTe-Sb_2Te_3 system from literature.

$GeBi_2Te_4$ consists of a nine-layered structure and the layered composition determined using the in depth EDX investigation is displayed in Table 3.10 and Table 3.11. In Table 3.11 the compositions of equivalent layers are averaged. Nine-layered structures for this material type are already observed: Karpinskii *et al.*[199] determined a nine-layered structure with all layers intermixed each with a unique Bi:Ge:Te ratio for $Ge_{1.5}Bi_{2.5}Te_5$ (or equivalently $Ge_{1.2}Bi_2Te_4$) using SCXRD, while Matsunaga *et al.*[201] observed only intermixed Bi/Ge layers with a Bi:Ge ratio of 0.64:0.36 for $Ge_2Bi_2Te_5$ (or equivalently $Ge_{1.6}Bi_{1.6}Te_4$) using PXRD. The $Ge_{1.6}Bi_{1.6}Te_4$ thin film samples of Matsunaga *et al.*[201] were made by sputtering the Ge, Bi, Te elements onto a glass disk. Afterwards, it was crystallized by laser irradiation. The thin film was powdered and annealed at 578 °C for 5min. The $Ge_{1.2}Bi_2Te_4$ sample of Karpinskii *et al.*[199] was synthesized by melting the Ge, Bi and Te elements for 5h in an evacuated quartz tube, followed by annealing at 497 °C for 1000h.

Due to the different sample preparation methods and slightly varying Ge:Bi:Te ratios, we expect to observe differences between our model and the models from literature. However, comparison with literature is useful to see if similar 'trends' exist. With the latter we mean if *e.g*. a trend exists that Ge and Bi have a site preference or if they are intermixed. HR EDX indicates clearly that the composition in the inner and outer Ge/Bi layers are dissimilar, excluding the model of Matsunaga *et al.*[201]. Our model also differs from the model of Karpinskii *et al.*[199] (see Table 3.12). But the HAADF STEM simulation using our layered composition does not match perfectly with the averaged experimental HAADF STEM image. The height of the inner mixed Ge/Bi layers of the line profile from the simulation is too high; indicating that less Bi should be present in these layers due to the Z dependency of a HAADF STEM image (Z_{Bi}=83, Z_{Ge}=32 and Z_{Te}=52). If the total composition in the building block is

correct, then this means more Bi should be present in the outer mixed Ge/Bi layers or in the Te layers. If more Bi is added to the outer mixed Ge/Bi layers, then the peak height of these layers will enlarge, further increasing their peak height difference with the Te layers, making the relative height of the Te layers too low. So, this suggests that Bi is present in the Te layers. This is supported by the misfit, visible at Te-Te sites bonded with VdW interactions, between the fitted line profile (red) and the experimental Bi line profile (green) of the EDX map (Figure 3.29). Furthermore, Karpinskii *et al.*[199] already suggested complete intermixed layers with a unique Bi:Ge:Te ratio. But because no clear indications of Bi on the Te layers are present in the EDX map, we chose to keep the Te layers pure without intermixing. Furthermore, the intensity in HAADF STEM images is almost Z^2 dependent, so only a small Bi quantity on a Te column is already sufficient to increase the intensity of that mixed column. Note that the Ge map is too noisy to justify anything more than that Ge is present on the Bi columns.

	Our EDX results $GeBi_2Te_4$			*Our EDX results* $GeBi_2Te_4$+I		
Layer	Bi [at. %]	Te [at. %]	Ge [at. %]	Bi [at. %]	Te [at. %]	Ge [at. %]
1	0	100	0	0	100	0
2	75(2)	0	25(2)	72(2)	0	28(2)
3	0	100	0	0	100	0
4	60(3)	0	40(3)	64(3)	0	36(3)
5	0	100	0	0	100	0
6	60(3)	0	40(3)	70(2)	0	30(2)
7	0	100	0	0	100	0
8	70(3)	0	30(3)			
9	0	100	0			

Table 3.10 The layered chemical composition of the nine-layered building block of $GeBi_2Te_4$ (left) and the seven-layered structure of $GeBi_2Te_4$+I (right) determined from EDX.

	Our EDX results $GeBi_2Te_4$			*Our EDX results* $GeBi_2Te_4$+I		
Layer	Bi [at. %]	Te [at. %]	Ge [at. %]	Bi [at. %]	Te [at. %]	Ge [at. %]
1	0	100	0	0	100	0
2	73(2)	0	27(2)	71(2)	0	29(2)
3	0	100	0	0	100	0
4	60(2)	0	40(2)	64(3)	0	36(3)
5	0	100	0	0	100	0
6	60(2)	0	40(2)	71(2)	0	29(2)
7	0	100	0	0	100	0
8	73(2)	0	27(2)			
9	0	100	0			

Table 3.11 The layered chemical composition of the nine-layered building block of $GeBi_2Te_4$ (left) and the seven-layered structure of $GeBi_2Te_4$+I (right) determined from EDX, where equivalent layers are averaged.

	Our EDX results			*Literature Model 1*[199]			*Literature Model 2*[201]		
Layer	Bi [at. %]	Te [at. %]	Ge [at. %]	Bi [at. %]	Te [at. %]	Ge [at. %]	Bi [at. %]	Te [at. %]	Ge [at. %]
1	0	100	0	0	96	4	0	100	0
2	73(2)	0	27(2)	63	20	17	64(1)	0	36(1)
3	0	100	0	6	94	0	0	100	0
4	60(2)	0	40(2)	46	0	54	64(1)	0	36(1)
5	0	100	0	21	79	0	0	100	0
6	60(2)	0	40(2)	46	0	54	64(1)	0	36(1)
7	0	100	0	6	94	0	0	100	0
8	73(2)	0	27(2)	63	20	17	64(1)	0	36(1)
9	0	100	0	0	96	4	0	100	0

Table 3.12 The layered chemical composition (equivalent layers are averaged) of the nine-layered building block of $GeBi_2Te_4$ determined from EDX (left) compared to the layered composition for $Bi_2Ge_{1.2}Te_4$ determined by Karpinskii *et al.*[199] (middle) and for $Bi_{1.6}Ge_{1.6}Te_4$ by Matsunaga *et al.*[201] (right).

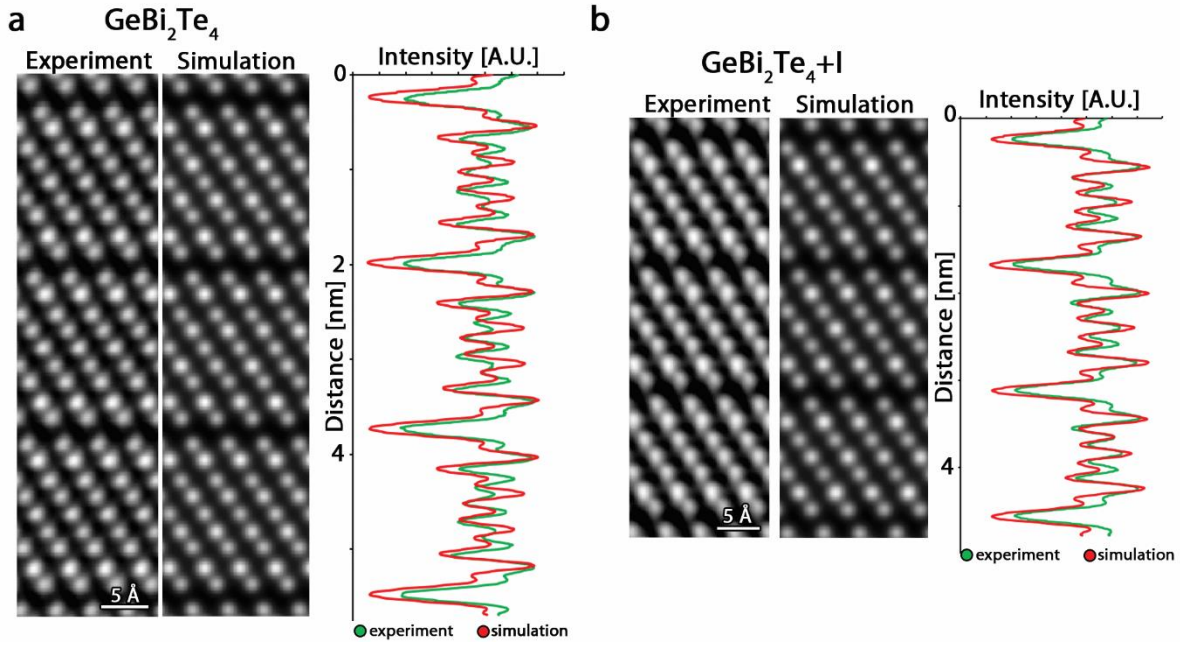

Figure 3.30 Comparison between the averaged experimental HAADF STEM image and the simulated HAADF STEM images calculated using QSTEM[84] using the found layered composition displayed in Table 3.12 and their corresponding line profiles for $GeBi_2Te_4$ (a) and $GeBi_2Te_4$+I (b).

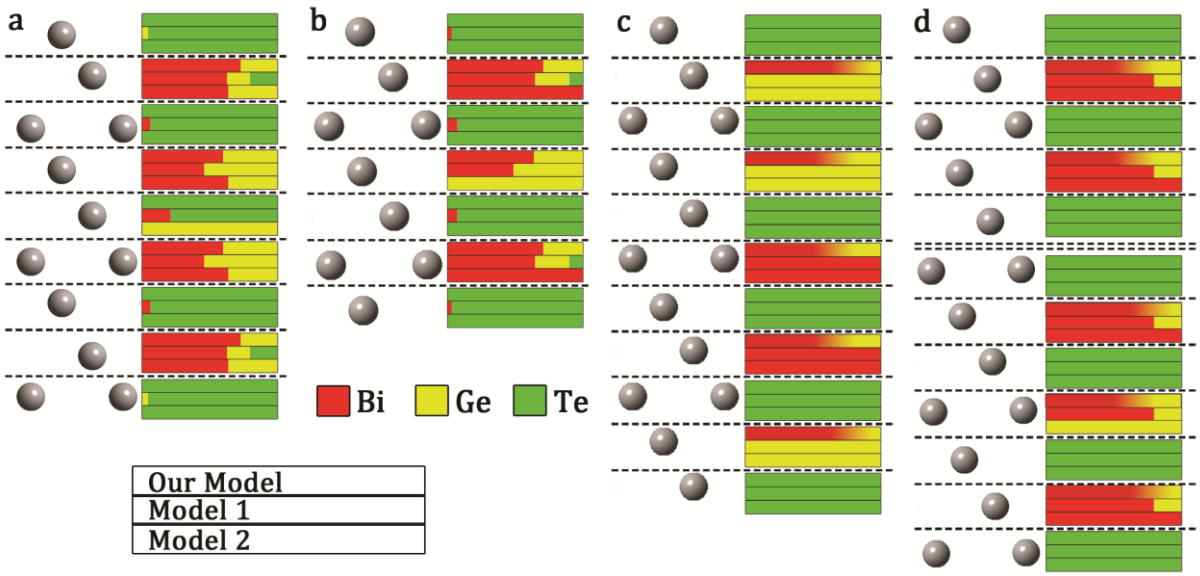

Figure 3.31 Layered composition of the nine- (a), seven- (b), eleven- (c) and five-seven (d) layered structure with on the left the atomic model and on the right the atomic percentage of the different elements Bi (red), Ge (yellow) and Te (green). The top indication is always as according to our model, while in (a) model 1 (middle) is derived from Karpinskii *et al.*[199] and model 2 (bottom) from Matsunaga *et al.*[201] (b) model 1 from Karpinskii *et al.*[199]and model 2 from Agaev *et al.*[14]. (c) model 1 from Petrov *et al.* [202] and model 2 from Karpinskii *et al.* [203]. (d) model 1 from Zhukova *et al.*[205] and model 2 from Agaev *et al.*[204].

$GeBi_2Te_4$+I contains a seven-layered structure and the layered composition determined with the in depth EDX investigation is displayed in Table 3.10 and Table 3.11. In Table 3.11 the composition of equivalent layers are averaged. Agaev *et al.*[14] and Karpinskii *et al.*[199] also observed a seven-layered structure for $GeBi_2Te_4$ determined with respectively powder electron diffraction and SCXRD data. However, the chemical composition per layer is different: Agaev *et al.*[14] determined single element layers (Te-Bi-Te-Ge-Te-Bi-Te), while Karpinskii *et al.*[199] detected intermixed layers with a unique Bi:Ge:Te ratio (Table 3.13). The $GeBi_2Te_4$ films samples of Agaev *et al.*[14] were made by evaporating the stoichiometric ratio of $GeBi_2Te_4$ in vacuum onto a NaCl crystal heated at 150 °C. Afterwards the sample was annealed in vacuum at 180-200 °C for 2h. The $GeBi_2Te_4$ sample of Karpinskii *et al.*[199] was synthesized by melting the Ge, Bi and Te elements for 5h in an evacuated quartz tube, followed by annealing at 497 °C for 1000h. Except for the small concentration of Iodine in our $GeBi_2Te_4$+I samples, the Ge:Bi:Te ratio of our sample is in agreement with the samples of the literature. However, the sample preparation method is different, which can result in a different structure. EDX shows mixed Bi/Ge layers, excluding the similarity with the model of Agaev *et al.*[14]. It also indicates differences between our found layered composition and the model of Karpinskii *et al.*[199] (see Table 3.13). The fit between the line profile of the simulated HAADF STEM image using the found layered composition and the averaged HAADF STEM image is better than for the nine-layered sample. However, the same observation can be made here. The difference between the two line profiles indicate that Bi is also present on the Te layers, again supported by literature[199] who already suggested mixed Te layers.

	Our EDX results			*Literature*[199]		
Layer	Bi [at. %]	Te [at. %]	Ge [at. %]	Bi [at. %]	Te [at. %]	Ge [at. %]
1	0	100	0	3	97	0
2	71(2)	0	29(2)	65	10	25
3	0	100	0	7	93	0
4	64(3)	0	36(3)	49	0	51
5	0	100	0	7	93	0
6	71(2)	0	29(2)	65	10	25
7	0	100	0	3	97	0

Table 3.13 (left) The averaged layered chemical composition of the seven-layered building block determined from EDX compared to (right) the atomic percentage determined for $GeBi_2Te_4$ by Karpinskii *et al.*[199].

$Ge_3Bi_2Te_6$ is an eleven-layered structure in agreement with the observed structures for $Ge_3Bi_2Te_6$ by Petrov *et al.*[202] and Karpinskii *et al.*[203]. The $Ge_3Bi_2Te_6$ films of Petrov *et al.*[202] were made by evaporating $Ge_3Bi_2Te_6$ onto NaCl heated to 160 °C and annealed for 3-4h at 160-180 °C. The $Ge_3Bi_2Te_6$ sample of Karpinskii *et al.* [203] is made by melting the Ge, Te and Bi elements in an evacuated quartz tube at 800 °C, followed by annealing at 500 °C for 1000h and then quenching. The preparation methods from literature differ from our sample preparation method. Both literature models propose the building block sequence 'Te-Ge-Te-Ge-Te-Bi-Te-Bi-Te-Ge-Te.' However, HAADF STEM images of the studied $Ge_3Bi_2Te_6$ sample suggest another type of sequence. Like $GeBi_2Te_4$ and $GeBi_2Te_4$+I the outer Bi/Ge mixed columns have a lighter colour than the inner Bi/Ge columns, indicating more Bi in the outer Bi/Ge columns than in the inner Bi/Ge columns. So, for this sample we expect similar results as for $GeBi_2Te_4$ and $GeBi_2Te_4$+I, although no HR EDX mapping was performed: More Bi in the outer Bi/Ge columns than in the inner ones and mixed Bi-Te layers.

$GeBi_4Te_7$ consists of on average an alternation of quintuple and septuple layers in agreement with $GeBi_4Te_7$ determined by Agaev *et al.*[204] using single crystal electron diffraction and Zhukova *et al.*[205] using powder diffraction data. The thin $GeBi_4Te_7$ sample studied by Agaev *et al.*[204] were formed at 564 °C using vapour condensation in high vacuum on celluloid films and crystals of rock salt. Zhukova *et al.*[205] made the $GeBi_4Te_7$ samples by fusion of the Ge, Bi, Te elements in the stoichiometric ratio in sealed quartz vessels at 800-850 °C. Afterwards, they were annealed for 30-50h at 450-500 °C. Zhukova *et al.*[205] observed Ge/Bi mixed layers with a 0.20:0.80 Ge:Bi ratio, where Agaev *et al.*[204] detected Bi_2Te_3 quintuple layers combined with 'Te-Bi-Te-Ge-Te-Bi-Te' septuple layers. No HR EDX mapping was performed for this sample. However, using the HAADF STEM images we excluded the 'Te-Bi-Te-Ge-Te-Bi-Te' septuple layer sequence. In that case the middle Ge column should have been observably lighter due to the Z dependency of the HAADF STEM image and the high Z value difference between Bi and Ge (Bi has Z number 83, while Ge has 32). Furthermore, all other samples ($GeBi_2Te_4$, $GeBi_2Te_4$+I and $Ge_3Bi_2Te_6$) made with the same and even another sample technique (CTR) already indicate mixed Bi/Ge columns. Also the other samples showed different Bi:Ge ratio for the inner and outer Bi/Ge layers, excluding the model of Zhukova *et al.*[205].

In short, we suggested that all trigonal layered structures contained mixed Ge/Bi layers with more Bi in the outer layers of the building block. This is in contradiction with Frangis *et al.*[206] who suggested that more Ge was present in the outer layers of the building block in this type of layered structures. Similarities and differences were also found between the studied GeTe-Bi_2Te_3 system and the GeTe-Sb_2Te_3 system from literature.

If you look into the differences, for the GeTe-Sb_2Te_3 system they found a lot of different defects. For $GeSb_2Te_4$ a domain structure was found where the trigonal building blocks were inverted from one domain to another[216], while the studied GeTe-Bi_2Te_3 systems were single crystal without domain formation. Single crystals allow us to determine the physical properties of the material, for example the study of the conducting surface states, without the additional complication of domains[217]. Furthermore, the binary swapping defects[216] and the disordered size of the building blocks[218] in m GeTe-nSb_2Te_3 systems were also not observed. Binary swapping defects are when a bilayer from one building block moves to the adjacent building block, while inverting the chemical character of the layers combined with intermixing of Sb and Te for stability[216]. We detected these binary swapping defects in Bi_2Te_3 and $(Sb_{0.55}Bi_{0.45})_2Te_3$ samples made using the Bridgman technique, however, they were probably caused by oxidation or by addition of an extra layer (see chapter 4). The disordered size of the building blocks and the domain structure can be a consequence of the use of different sample preparation techniques in literature: Molecular Beam Epitaxy (MBE)[218] and a magnetron sputtering technique combined with annealing[216].

Atomic reconfiguration of the VdW gap by combining or splitting of building blocks[219] or induced bilayer swapping[220] by external stimuli observed for the GeTe-Sb_2Te_3 system could be relevant for phase change applications, so it is important to know which defects exist in which type of material. Sometimes, the atomic columns in the two layers closest to the VdW gap were not round anymore, but more oval suggesting two or more atomic columns close together instead of one. But no clear reconfiguration as for the GeTe-Sb_2Te_3 system was observed, suggesting that this type of material is more stable under the electron beam. However, areas that were too heavily damaged by FIB preparation contained crystalline areas where the VdW gaps were removed. No further attention was attributed to this, due to the overall sensitivity of this type of material to the electron beam especially around the VdW gap where the bindings are weaker, discussed in sections 3.1 and 3.2.2.

A similarity between the trigonal GeTe-Sb_2Te_3 and trigonal GeTe-Bi_2Te_3 systems is how the two types of cations are distributed over the different mixed cation layers. Similar to the trigonal layered GeTe-Sb_2Te_3 system more Ge is present in the middle layers of the building blocks than in the outer layers[218]. A similar explanation described by Momand *et al.*[218] for the GeTe-Sb_2Te_3 system applies here. Bulk GeTe in its rock salt form[221] is a three dimensional bonded material versus the two dimensional bonded Bi_2Te_3 structure due to the weak van der Waals (VdW) bonding. So, the outer layers of the Bi_2Te_3 building blocks are passive, leading to their dislike to bond with the dangling bonds of GeTe. This leads to a structural preference where the GeTe structure is incorporated inside the Bi_2Te_3 building block. Mixing of the Ge/Bi layers can be expected because configuration entropy can lower the free energy

at higher temperatures. Furthermore, it is probably due to the high concentration of Bi in the outer layers of the building blocks that the van der Waals bonding appears between the different building blocks similar to Bi_2Te_3 and unlike the rock salt structure.

3.3.2.2 Rock salt structures

Thermodynamic stable $Ge_4Bi_2Te_7$[222] and $Ge_3Bi_2Te_6$[202,203] take on a trigonal layered structure with van der Waals gaps: $Ge_4Bi_2Te_7$[222] consists of thirteen-layered building blocks with alternating Te and mixed Ge/Bi layers determined using PXRD, while $Ge_3Bi_2Te_6$ is built using eleven-layered building blocks with a 'Te-Ge-Te-Ge-Te-Bi-Te-Bi-Te-Ge-Te' sequence determined using SCXRD[202] and PXRD[203]. However, the HAADF STEM images of $Ge_3Bi_2Te_6$, $Ge_4Bi_2Te_7$ and $Ge_{6.8}Bi_2Te_{9.8}$ and their corresponding FFT match with the cubic rock salt structure, similar to the structure determined by Urban *et al*.[200] for $Ge_4Bi_2Te_7$ and Matsunaga *et al.*[201] for $Bi_{1.6}Ge_{1.6}Te_4$ (Figure 3.32a and Figure 3.33a). This can be caused by a difference in sample preparation. The $Ge_4Bi_2Te_7$ sample of Shelimova *et al.*[222] was made by melting Ge, Bi, Te in an evacuated quartz tube at 800 °C for 5h, followed by air quenching and annealing at 347 °C in argon atmosphere for 1200h. The $Ge_4Bi_2Te_7$ sample of Urban *et al*.[200] is synthetized using chemical vapour transport with Iodine as a transport agent. The sample preparation of $Ge_3Bi_2Te_6$[202,203] and $Bi_{1.6}Ge_{1.6}Te_4$[201] is mentioned in section 3.3.2.1.3. All sample preparation methods are different from the Bridgman technique we used. Matsunaga *et al.*[201] proposed intermixed Ge/Bi layers containing 20 atomic percent vacancies, while Urban *et al*.[200] also suggested intermixed Ge/Bi layer but discussed a specific defect structure. In our case a specific defect structure is observed, disagreeing with the model of Matsunaga *et al.*[201]. The structure for $Ge_4Bi_2Te_7$ determined by Urban *et al.*[200] deviates slightly from the rock salt structure. It has space group $Fm\bar{3}m$, cell parameter 6.055 Å, Te position (0.5, 0.5, 0.5) and Bi/Ge (0.34:0.74 ratio) position (0.0228,0.0228,0.0228) (Figure 3.32a). They suggest that the cations are placed at a 32f split position instead of the 4a site, however the deviation is too small to observe with HAADF STEM. Because $Ge_3Bi_2Te_6$, $Ge_4Bi_2Te_7$ and $Ge_{6.8}Bi_2Te_{9.8}$ have similar structures and defects, only a representative example using $Ge_3Bi_2Te_6$ will be shown for each situation.

Urban *et al.*[200] found around the Ge vacancy layers a higher Bi content on the cation positions and a structural deformation to α-GeTe double layers. In our case, two different types of planar defects exist in $Ge_3Bi_2Te_6$. The first defect type are Ge vacancies existing in the $(11\bar{1})_C$ and $(1\bar{1}\bar{1})_C$ Ge planes with an excess of Bi on the Ge positions around these planar defects without structural deformation (Figure 3.33 and Figure 3.34). This excess of Bi is visible due to the intensity increase of the Ge columns around the planar defect. The second defect type are the removal of complete $(11\bar{1})_C$ and $(1\bar{1}\bar{1})_C$ Ge planes combined with a shorter distance between the $(11\bar{1})_C$ and $(1\bar{1}\bar{1})_C$ Te planes (Figure 3.33 and Figure 3.34). Around the defect the rock salt structure deforms to the α-GeTe structure (Figure 3.32b), which has a lower symmetry, with an excess of Bi on the Ge positions.

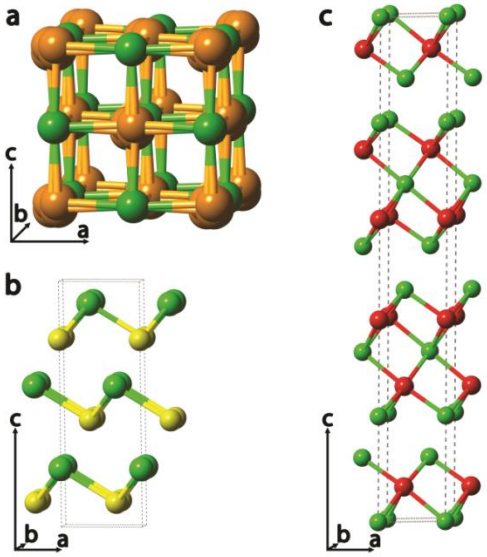

Figure 3.32 (a) Cubic structure for $Ge_4Bi_2Te_7$ by Urban *et al.*[200] (b) α-GeTe[16] (c) Bi_2Te_3[13]. Green spheres are Te; red spheres are Bi; yellow spheres are Ge; and orange sphere are Bi/Ge mixed sites.

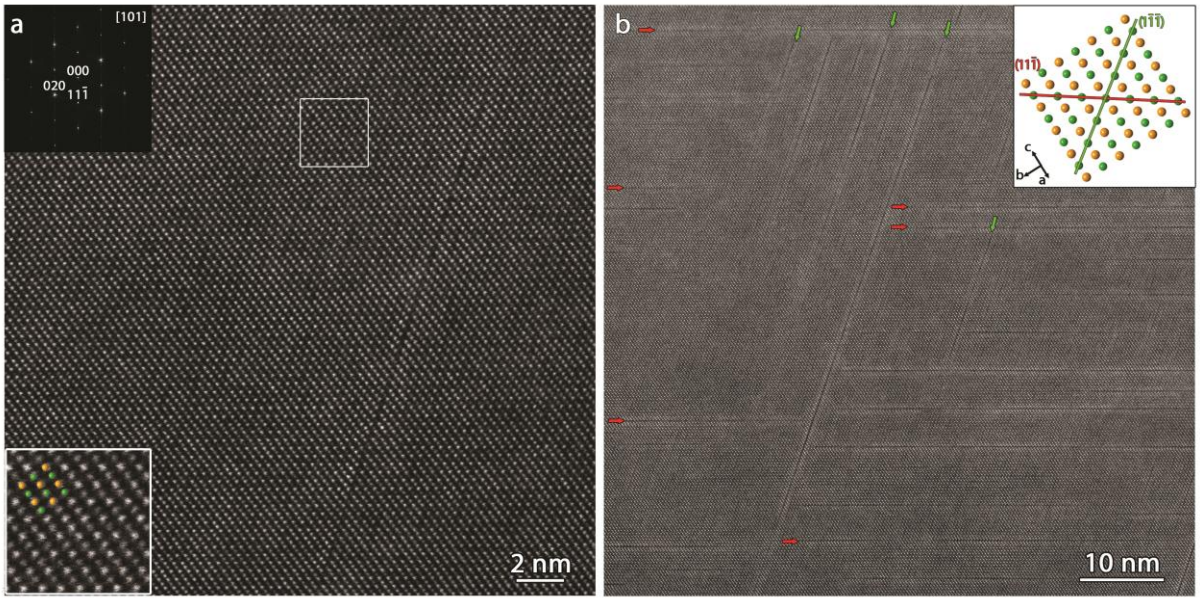

Figure 3.33 (a) HAADF STEM image of zone $[101]_C$ of $Ge_3Bi_2Te_6$ with its FFT in the left top corner. The area indicated by a white rectangle is magnified in the left bottom corner overlaid with the structure of Urban *et al*.[200], where the Ge/Bi position is placed at the 4a site instead of the 32f site for simplification and because it's indistinguishable in HAADF STEM images. The mixed Ge/Bi columns are displayed in orange and Te in green. (b) Overview of the defects in $Ge_3Bi_2Te_6$ in the $(11\bar{1})_C$ plane (red arrows, see inset where orange (green) atoms indicate the Ge/Bi (Te) sites) and the $(1\bar{1}\bar{1})_C$ plane (green arrows, see inset where orange (green) atoms indicate the Ge/Bi (Te) site). The neighbouring columns are lighter around these planar defects where the $(11\bar{1})_C$ and $(1\bar{1}\bar{1})_C$ Ge planes are partly or completely removed due to the increase of Bi at the Ge sites.

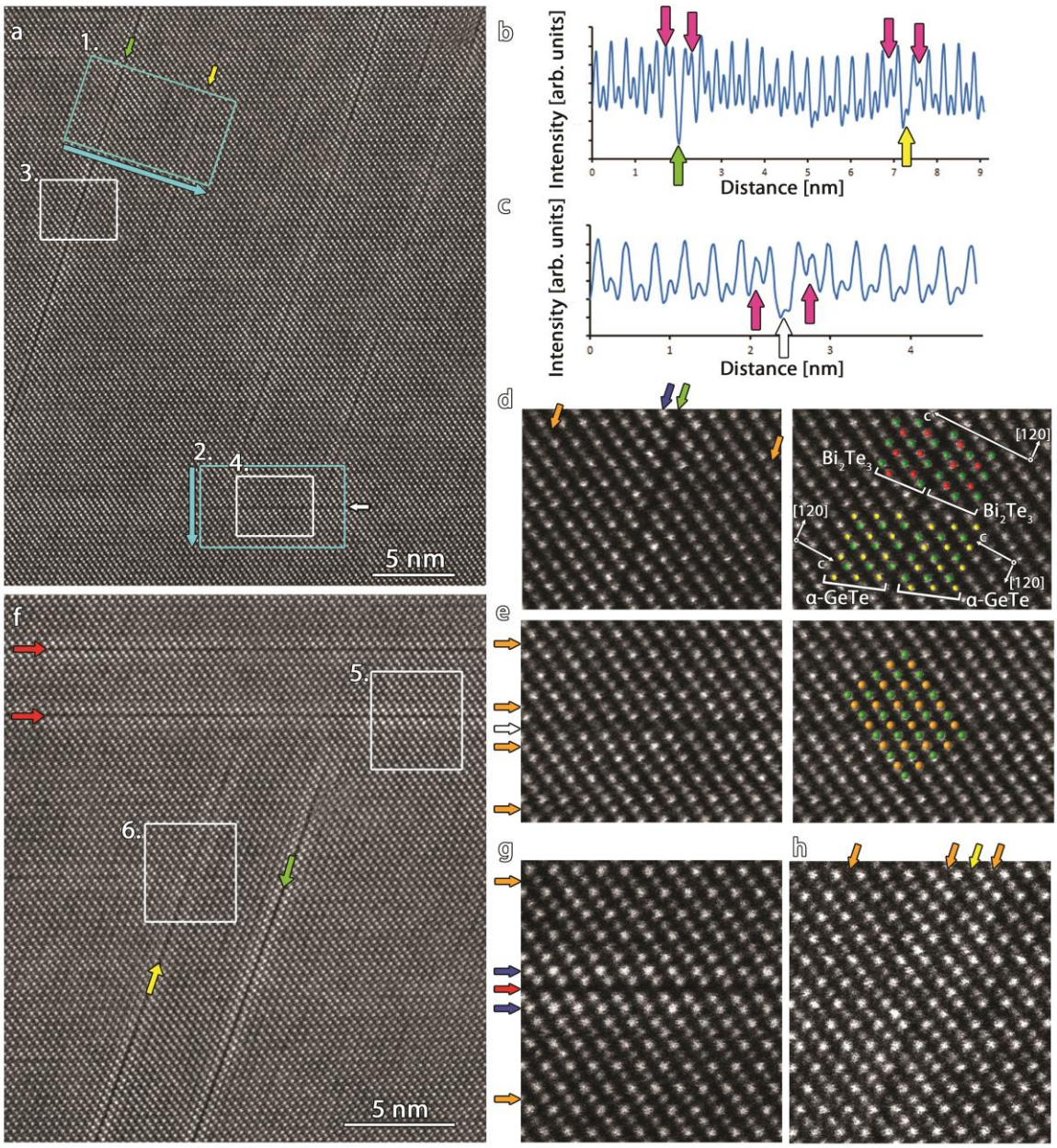

Figure 3.34 (a), (f) HAADF STEM images of zone $[101]_C$ showing the defects in $Ge_3Bi_2Te_6$ in the $(11\bar{1})_C$ plane (horizontal line defects) and in the $(1\bar{1}\bar{1})_C$ plane (sloped planar defects). Red (green) arrows indicate examples of twin boundaries along the $(11\bar{1})_C$ ($(1\bar{1}\bar{1})_C$) plane and white (yellow) arrows Ge vacancies in the $(11\bar{1})_C$ ($(1\bar{1}\bar{1})_C$) plane. The line profiles from area 1 and 2 in (a), marked with light blue, are displayed in (b) and (c). The white marked regions 3, 4, 5 and 6 in (a) en (f) are enlarged in corresponding (d), (e), (g) and (h). (b), (c) Around the Ge vacancies and twin domains an increase of the Bi content at the Ge rows is observed by the increase in intensity, were purple arrows point out the clearest examples. (d), (g) At the twin boundary, the surrounding structure deforms, which is most clearly seen by the difference in Ge/Bi position indicated with respectively blue and orange arrows. Two models are overlaid on the HAADF STEM image in (d): The top model indicates that around the defect the structure is distorted to Bi_2Te_3 (hexagonal unit cell) where the absence of the Ge plane coincide with the van der Waals gap, while the bottom model shows the twinning of the α-GeTe structure (hexagonal unit cell), where both domains are correlated by a 180° rotation around the *a* axis of the α-GeTe structure. Green, yellow and red represent respectively Te, Ge and Bi. (e), (h) No distortion around the planar defect exist when we have only a limited amount of Ge vacancies in the $(11\bar{1})_C$ ($(1\bar{1}\bar{1})_C$) Ge plane. The rock salt structure is overlaid with the HAADF STEM image in (e), where green (orange) spheres represent the Te (mixed Ge/Bi) columns.

The second defect type can be described in two different ways. One way to characterize this defect are twin boundaries. The twins differ by a 180 degree rotation around the axis a_H of the α-GeTe structure. Twin boundaries appear along the $(001)_H$ and $(01\bar{1})_H$ planes in the α-GeTe structure which match with the $(11\bar{1})_C$ and $(1\bar{1}\bar{1})_C$ planes –symmetrically equivalent planes due to a mirror plane perpendicular to axis b_C in the higher symmetry structure of the rock salt structure. We observed this defect also in α-GeTe, however in this case twin boundaries only appeared along the $(001)_H$ plane of α-GeTe. The stress due to the shorter distance between the $(11\bar{1})_C$ and $(1\bar{1}\bar{1})_C$ Te planes can be released by pushing the Ge atoms out or similarly by accumulation of Ge vacancies. This type of defect will be discussed in more details in section 5.1. Another way to describe this defect is by the local existence of the Bi_2Te_3 structure (Figure 3.32c), where the removal of the complete $(11\bar{1})_C$ or $(1\bar{1}\bar{1})_C$ Ge plane coincides with the van der Waals gap. Due to the Bi on the Ge positions the Te-Te layers want to create a van der Waals bonding, leading to a shorted distance between these layers and thus making the position between these Te layers more favourable for vacancy accumulation. HAADF STEM simulations of both models, one where the Bi_2Te_3 structure is used and one where the twin structure of α-GeTe is modelled, agree with the experimental data (Figure 3.35). This suggests that enough Bi around the planar defect can distort the structure to Bi_2Te_3 (Figure 3.32c).

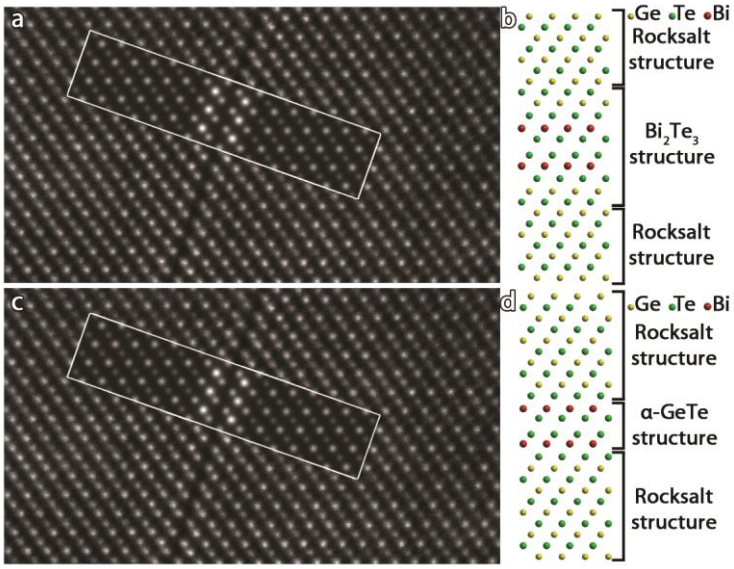

Figure 3.35 (a), (c) Averaged HAADF STEM image of zone $[101]_C$ with lower dwell time to limit scan distortions of the defects in $Ge_3Bi_2Te_6$ overlaid with STEM simulations using two different models calculated with QSTEM[84]. (a) displays the model where the planar vacancy defect corresponds with the VdW gap of the Bi_2Te_3 structure. One quintuple layer block above and below the planar defect exist in the model where the Bi layer furthers away of the VdW gap is filled with Ge, because Bi is more localized around the defect. Around these two Bi_2Te_3 building blocks the rock salt structure is used. The schematic representation of this model is shown in (b). Around the planar vacancy defect in (c) the α-GeTe structure is modelled. The α-GeTe structure on opposite sides of the defect are related by a 180° rotation around the a_H axis of the α-GeTe structure. Above and below the alpha-GeTe structure the rock salt structure is present. Its schematic representation is displayed in (d).

$Ge_4Bi_2Te_7$ has both defect types like $Ge_3Bi_2Te_6$, while $Ge_{6.8}Bi_2Te_{9.8}$ only contains the first defect type, *i.e.* the Ge vacancies in the $(11\bar{1})_C$ and $(1\bar{1}\bar{1})_C$ Ge planes with excess of Bi on the

Ge sites around this planar defect without structural distortion. $Ge_3Bi_2Te_6$, $Ge_3Bi_2Te_6$ and $Ge_3Bi_2Te_6$ can also be written as $3GeTe+Bi_2Te_3$, $4GeTe+Bi_2Te_3$ and $6.8GeTe+Bi_2Te_3$. $Ge_{6.8}Bi_2Te_{9.8}$ contains a lot less Bi_2Te_3 compared to the other two materials, which indicates that the low amount of Bi cannot cause the structural change to the Bi_2Te_3 structure and the complete removal of the Ge plane to create the van der Waals gap.

Until now we made a close comparison between our observations for $Ge_3Bi_2Te_6$, $Ge_4Bi_2Te_7$ and $Ge_{6.8}Bi_2Te_{9.8}$ with the rock salt structures from literature[200,201]. However, similarities and dissimilarities with the $(GeTe)_{0.975}(Bi_2Te_3)_{0.025}$[190] structure are worth noting. Wu *et al.*[190] also observed these van der Waals gaps for $(GeTe)_{0.975}(Bi_2Te_3)_{0.025}$. However, in between these van der Waals gaps another domain wall type, a 180° domain wall, existed due to the off-centred position of the Ge atom in between the Te layers in α-GeTe structure. This second domain type does not exist in our materials due to the centred Ge position between the Te layers in the rock salt structure. Furthermore, no excess Bi around these defects are mentioned. Also other types of domain walls were observed[190], which were absent in our samples. They[190] further concluded that the van der Waals gaps which also exist in our studied materials have a positive influence on the lattice thermal conductivity *i.e.* they must make it smaller, increasing the figure of merit for thermoelectric materials.

3.3.3 Conclusion

We found that $Ge_mBi_{2n}Te_{(m+3n)}$ samples made with the chemical transport growth method always resulted in a l-trigonal layered structure (l=7,9,11,5-7), while the ones grown using the Bridgman technique occurred in a trigonal layered structure or a rock salt structure with planar defects. Both structure types are different and this will affect the material's properties for example the topological insulator character. So, it is important to know which conditions lead to which type of structure.

$GeBi_2Te_4$, $GeBi_2Te_4$+I, $GeBi_4Te_7$ and $Ge_3Bi_2Te_6$+I have a trigonal layered structure with van der Waals gaps and respectively nine, seven, five-seven and eleven-layered building blocks, while $Ge_3Bi_2Te_6$, $Ge_4Bi_2Te_7$ and $Ge_{6.8}Bi_2Te_{9.8}$ have a rock salt structure with planar defect types. The first defect type is Ge vacancy rich $(11\bar{1})_C$ or $(1\bar{1}\bar{1})_C$ Ge planes with excess Bi on the Ge position around this planar defect. The second defect type is the removal of a complete $(11\bar{1})_C$ or $(1\bar{1}\bar{1})_C$ Ge plane with addition of Bi on the Ge position around the planar defect causing structural distortion to the α-GeTe structure. The latter can be described by twin domains or the formation of a van der Waals gap like in Bi_2Te_3. All three samples contained the first defect, while the second defect only exists in Bi rich $mGeTe\text{-}nBi_2Te_3$ samples thus not in $Ge_{6.8}Bi_2Te_{9.8}$. The fact that the vacancies are ordered instead of randomly distributed is important, since this will influence the material's properties. For example, literature suggests that especially the formation of the van der Waals type planar defect enhances the thermoelectric property of a material due to its positive influence on the lattice thermal conductivity, *i.e.* it makes the lattice thermal conductivity smaller. The effect of the other defect type is not known. For the trigonal layered materials, knowing the amount of layers in a building block and the Ge/Bi cation intermixing with a Bi increase on

the outer cation layers of the building block is necessary in order to identify these materials as topological insulators and their characteristics. Furthermore, differences with the structurally similar GeTe-Sb_2Te_3 system were observed. For example, the GeTe-Bi_2Te_3 system appears more stable against external stimuli like the electron beam, because no clear atomic reconfiguration of the van der Waals gap was observed. The latter could be relevant for phase change applications.

Chapter 4 Study of the surface

In this chapter I will first discuss the addition of an oxygen layer on top of Bi_2Te_3, Sb_2Te_3, $(Sb_{0.55}Bi_{0.45})_2Te_3$ and $Ge_mBi_{2n}Te_{(m+3n)}$ and then the addition of an Fe layer on top of Bi_2Te_3. The studied materials are topological insulators, interesting among other things due to their protected conducting surface states. These conducting states could be useful for spintronics[223]. In spintronic devices the spin of the electron can be used instead of the charge of the electron. The number one can for example be encoded with spin up and the number zero with spin down in hardware instead of one corresponding to current and zero to no current. However, for application purposes, the influence of oxidation or adding a magnetic layer needs to be understood[224], especially since the Dirac states are surface sensitive [225,226,227].

4.1 Oxidation

Section 4.1.2 is based on the paper: Sirotina Anna, Callaert Carolien, Volykhov Andrey, Frolov Alexander, Sánchez-Barriga Jaime, Knop-Gericke Axel, Hadermann Joke, Yashina Lada, *Mechanistic Studies of Gas Reactions With Multicomponent Solids: What Can We Learn by Combining NAP XPS and Atomic Resolution STEM/EDX?,* Journal of Physical Chemistry C 123(2019), p.26201-26210. Section 4.1.3 is based on the paper: Volykhov Andrey A., Sanchez-Barriga Jaime, Batuk Maria, Callaert Carolien, Hadermann Joke, Sirotina Anna P., Neudachina Vera S.,Belova Alina I., Vladimirova Nadezhda V., Tamm Marina E., Khmelevsky Nikolay O., Escudero Carlos, Perez-Dieste Virginia, Knop-Gericke Axel, Yashina Lada V., *Can surface reactivity of mixed crystals be predicted from their counterparts? A case study of topological insulators*, Journal of materials chemistry C : materials for optical and electronic devices 6(2018), p.8941-8949[228]. I performed the TEM study, EDX study and FIB preparation of the Bi_2Te_3, Sb_2Te_3 and three-years-oxidized $(Sb_{0.55}Bi_{0.45})_2Te_3$ samples. For the Bi_2Te_3 and Sb_2Te_3 samples, the bulk crystals were stripped with tape to obtain a clean surface, oxidized for one week followed by FIB preparation. For Bi_2Te_3 a second sample was made without one week of oxidization to verify the existence of the seven-layered lamella. The study of the two months oxidized $(Sb_{0.55}Bi_{0.45})_2Te_3$ sample was performed by Maria Batuk. After FIB preparation the samples were exposed to oxygen for around one hour due to transport. Other techniques, including DFT, were performed by the co-authors of the paper[228].

4.1.1 Introduction

Studying the surface oxidation is important in order to understand the surfaces' stability during preparation, handling and operation of future devices, because the surface properties can be oxidation sensitive. Analytis *et al.*[225] observed for $(Sb,Bi)_2Se_3$ that after ~1h atmospheric exposure the conducting surface states were almost completely absent. Kong *et al.*[226] proved for Bi_2Se_3 that air exposure resulted in environmental n-doping, which lowers the relative contribution of the topological surface states to the total conductivity. Yashina *et al.*[229] found that the surface reaction towards oxygen, water and a combination of both

for Bi_2Te_3 and Bi_2Se_3 is negligible, but still has an effect, *e.g.* water still makes these materials slightly p-doped. Furthermore, Ngabonziza *et al.*[230] measured high bulk electron mobility in Bi_2Te_3 after air exposure, unfavourable for certain applications. In contrast, surface oxidation in Bi_2Te_2Se did not remove the special surface properties, however small differences were still observed[224].

Bi_2Te_3 and $(Bi_{1-x}Sb_x)_2Te_3$ are interesting for p-n junction applications *e.g.* diodes, sensors, solar cells and transistors. On one hand, Bi_2Te_3 topological p-n junctions can be made operational at room temperature, because the preparation conditions (Te poor or Te rich) influence the type and the amount of defects, resulting in a p-doped Bi_2Te_3 material (Te poor) or an n-doped Bi_2Te_3 material (Te rich)[231] (Figure 4.1a). Te poor samples contain Te vacancies in the outer and inner Te layers, V_{Te1} and V_{Te2}, and Bi_{Te1} antisite defects on the outer Te layers, while Te rich samples have Te_{Bi} antisite defects and Bi vacancies V_{Bi}[231]. For a n-doped material, the Fermi level lies above the Dirac point leading to electron conductivity and for a p-doped material the Fermi level lies below the Dirac point leading to hole conductivity[231]. This also reverses the helical spin texture[231]. When the Fermi level coincides with the Dirac point, the carrier concentration becomes minimal, creating an intrinsic topological insulator[231]. On the other hand, $(Bi_{1-x}Sb_x)_2Te_3$ is promising for designing topological p-n junctions due to compositional graded doping to spatially modify the Dirac cone structure (moving the Dirac point) or due to electrostatic gating using the global back gate to adapt the surface Dirac cone position in the bulk gap, combined with the local top gate to locally modify the density and carrier type[232] (Figure 4.1). Furthermore, $(Bi_{1-x}Sb_x)_2Te_3$ can be tuned to be bulk insulating at x=0.88[233] and to maximize the thermoelectric properties at x=0.775[234]. Specific examples for applications and interests of $Ge_mBi_{2n}Te_{(m+3n)}$ are already discussed in section 3.3.1 and will not be repeated here.

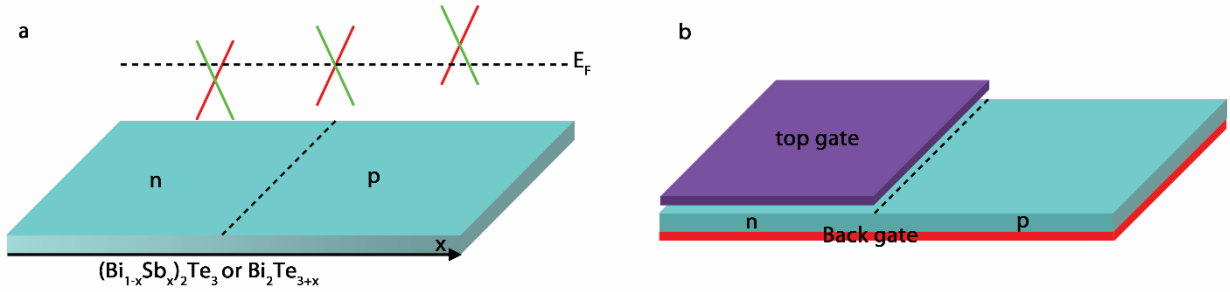

Figure 4.1 Schematic of a p-n junction due to composition graded doping (a) or electrostatic grating (b).

The oxidation mechanism depends on the diffusion element, which step of the oxidation process in which rate-limited situation is studied and the types of materials (metals[235–240], alloys[241–243], elemental semiconductors[244,245], and compound semiconductors[246,247]). Generally oxidation happens in different steps. First, oxygen adsorbs onto the metal surface. Second, electron transfer from the bulk toward the surface occurs, creating a potential difference. Third, due to this potential difference an electric field is created allowing cations and/or anions to move and an oxide layer to form. Some common models for elemental

metals which will also apply for the studied materials are the fast oxidation[236] and the Cabrera and Mott theory[237,238].

The first two to three layers undergo a fast linear oxidation[236]. So, each oxygen molecule adsorbed onto the surface dissociates and forms an oxide[236]. The theory of Cabrera and Mott[237] describes at an atomic level the diffusion in the metal substrate/oxide film/oxygen gas system when the oxidation layer is thin. An assumption that is made is that electrons can freely move from the metal to the ionized absorbed oxygen atoms or molecules at the oxygen/gas interface. The Fermi level of the metal and the absorbed layer are the same. This leads to a positive metal surface and negative oxygen ions, causing a uniform electrical field between them. Due to this electrical field the positive metal ions can slowly move through the film, thickening the oxidized layer. No electrical current is present because the electron transfer and the ion transfer balance each other. The electrons travel through the oxidized layer by tunnelling (3 nm[244]-10 nm[238]) or thermionic emission (<30 nm). With thermionic emission the electrons use the holes in the valence band of the oxidized layer or the electron channels in the conduction band to move through the oxidized layer. When assuming thermionic emission the potential difference across the oxidized layer differs slightly from the Cabrera and Mott theory[237,244]. The step that controls the rate is the movement of the ions through the oxide layer or their movement into the oxide. If the oxide layer is too thick the electric field becomes too small to be able to efficiently move the ions[238].

However, when more than one element exist inside the material like for alloys and compound semiconductors the reactivity of each element with oxygen is important. So usually it is supposed that the oxidation starts with the element which is the most reactive or in other words the element which has the lowest free energy of the oxide formation per Mole of O^{2-} basis[242,241]. Later, the oxidation process is influenced by different parameters such as the evaporation of one of the elements or formed oxides, the thermodynamic stability of the oxides, the mutual solubility of the oxides and the diffusion rates of the elements through the oxide[247]. For $A^{III}B^{V}$ semiconductors the oxidation is studied with X-Ray photoelectron spectroscopy depth profiling with a relatively moderate (tens of nm) in-depth resolution[248]. Until now no direct atomic resolution information of the oxidized material for any compound solids is known.

The oxidation models for Sb_2Te_3, Bi_2Te_3 and $(Sb_{0.55}Bi_{0.45})_2Te_3$ are based on in situ/ex-situ XP-spectra, HAADF STEM imaging and EDX mapping. For Sb_2Te_3 and Bi_2Te_3 DFT modelling was also applied. For $Ge_mBi_{2n}Te_{(m+3n)}$ we only performed HAADF STEM imaging and EDX mapping. Through similarities with the $(Sb_xBi_{1-x})_2Te_3$ samples, oxidation models for $Ge_mBi_{2n}Te_{(m+3n)}$ are suggested. We performed the STEM imaging and the EDX mapping, while the other techniques and bulk sample preparation were performed by the co-authors of the manuscript and the paper mentioned in section 4.1.

4.1.2 Bi_2Te_3 and Sb_2Te_3

4.1.2.1 STEM

The one-week-oxidized Sb_2Te_3 contains three different layers: an amorphous layer, partly intertwined with a distorted crystalline layer, followed by the bulk structure Sb_2Te_3 (Figure 4.2). Sb_2Te_3 has a non-planar oxide layer, where the highly oxidized regions are about 12 nm apart along the a-b plane (thus parallel with the surface).

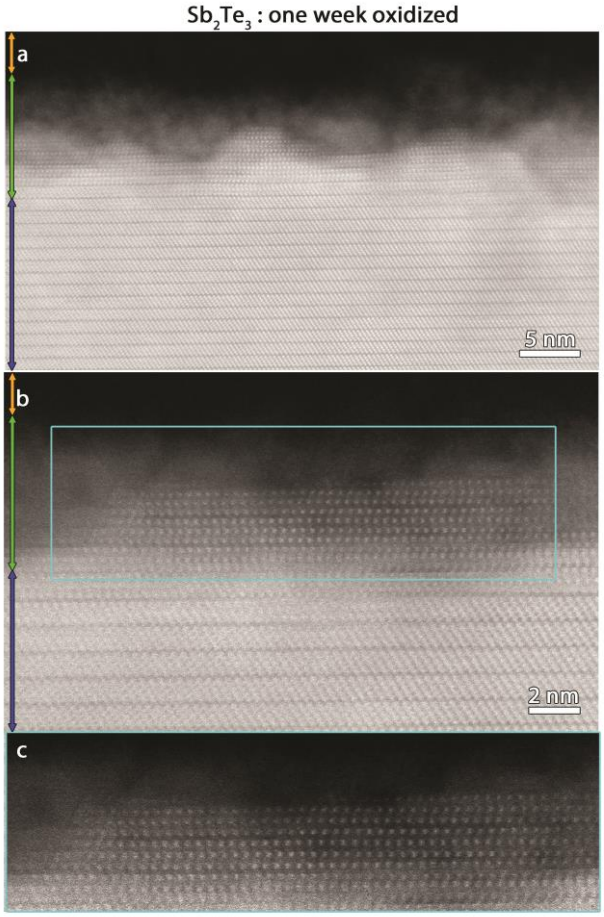

Figure 4.2 Cross-sectional overviews and close-up HAADF STEM images of the oxidized layers and the subsurface region of the one-week-oxidized Sb_2Te_3. From top to bottom, a carbon protection layer (orange) is visible, followed by an amorphous layer intermixed with a distorted crystalline structure (green), and the Sb_2Te_3 structure (blue). The areas in blue rectangles in (b) are enlarged with improved contrast in (c). (c) displays the distorted crystalline structure at the top surface of Sb_2Te_3.

The one week oxidized Bi_2Te_3 contains four different layers: an amorphous layer, intermixed with a distorted crystalline layer, a defect-rich layer and the bulk structure, where the oxide layer is planar (Figure 4.3a-c). Sb_2Te_3 did not contain this defect-rich area. The defect-rich layer (~20 nm) contains mostly seven-layered defects (Figure 4.3c). Only in rare cases interstitial defects were observed.

A seven-layered defect in this type of material is a defect where a seven-layered building block with sequence Te-Bi-Te-Bi-Te-Bi-Te exists instead of the normal five-layered building

block. Its existence was already observed by Frangis *et al.*[206,249] in bulk $Bi_{2+\delta}Te_3$ and by Ying Jiang *et al.*[250] in the bulk of Bi_2Te_3. Ying Jiang *et al.*[250] also discovered that these septuple layers do not stay at a fixed depth from the interface but this depth fluctuates stepwise parallel to the interface of the material, which is also clearly visible in our case (Figure 4.3c). However, the quantity of defects at the surface is high, while in the bulk these defects are not observed. The intensity of the atomic columns in the HAADF STEM image (which scales with the averaged atomic number of the elements inside the column) suggests that the sequence of a seven-layered lamella is Te-Bi-Te-Bi-Te-Bi-Te.

This seven-layered defect that changes in depth in reference to the surface of the material can also be described by the fact that a bilayer moves from one building block toward the adjacent building block while changing the order of the layers, so a Bi-Te layered ordering becomes a Te-Bi layered ordering. The same bilayer switching is also observed in the layered $GeSb_2Te_4$ structure by Wang *et al.*[216]. They found that the stability of this bilayer switching is due the intermixing of Sb and Te in the bilayers when it changes in depth in reference to the surface and that the energy cost of these bilayer defects is small. Furthermore, the intermixing explained the blurriness of the projected atomic columns in the HAADF STEM images caused by the distortion due to the Sb-Te intermixing disorder. This same blurriness can be observed in our case (Figure 4.3c).

To determine if oxidation caused these seven-layered defects, a non-oxidized Bi_2Te_3 sample was made. Non-oxidized means in this case that the sample is not explicitly oxidized for a certain time. However, during sample preparation the sample itself is limited exposed to air, explaining the observed oxidation layer in STEM. The non-oxidized sample has a ~0.5-1 nm thick amorphous layer, followed by a defect-free quintuple-layered structure (Figure 4.3d-e). This suggests that the seven-layered defects are a consequence of oxidation. The reason why these seven-layered defects exist at the surface is not clear. However, the existence of these seven-layered defects enables atomic mobility. If we assume that before oxidation the Bi:Te ratio is the same as in the bulk, $2/3 \approx 0.67$, and that oxidation caused these defects, then many cation positions should be empty in these septuple layers because the Bi:Te ratio in a septuple layer is $3/4=0.75$. Thus, these seven-layered defects contain cation vacancies which enable the atomic mobility.

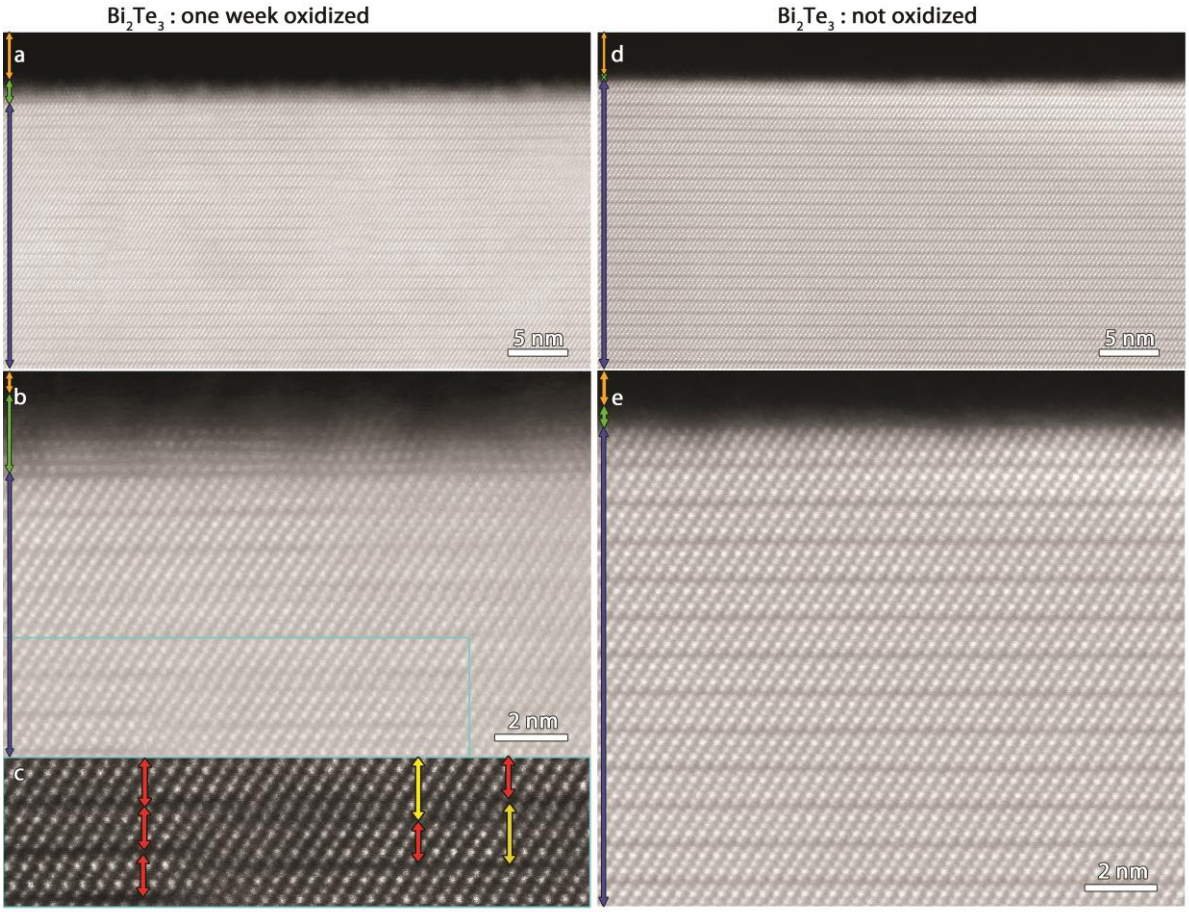

Figure 4.3 Cross-sectional overviews and close-up HAADF STEM images of the oxidized layers and the subsurface region of the one-week-oxidized Bi_2Te_3 (a, b) and the not explicitly oxidized Bi_2Te_3 (d,e). From top to bottom, a carbon protection layer (orange) is visible, followed by an amorphous layer intermixed with a distorted crystalline structure (green), and the Bi_2Te_3 structure (blue). The top part of the one-week-oxidized Bi_2Te_3 structure contains seven-layered defects (b,c), while the non-oxidized sample does not contain these defects (e). The areas in blue rectangles in (b) are enlarged with improved contrast in (c). (c) shows the stepwise displacement of the septuple layers (yellow arrows) in Bi_2Te_3 in the depth of the material, which is in agreement with the model of Jiang *et al.*[250]. The quintuple layers are marked with red arrows.

So, Bi_2Te_3 has a planar oxide layer, while Sb_2Te_3 has a non-planar oxide layer. To understand the cause of this difference, we need to look deeper into the possible point defects inside both materials and the Bi/Sb/Te-O bonding.

Bi_2Te_3 can be n-type or p-type (see phase diagrams, Figure 4.4) due to the fact that the homogeneity range is roughly symmetric with respect to the stoichiometric composition[251]. Te excess induces n-doping due to dominating ansitite defects Te_{Bi}, whereas Bi excess results in p-doping. The dominating defects here are Bi_{Te}. Practically, both n- or p-type Bi_2Te_3 can be obtained from melt depending on melt enrichment in Te or Bi correspondingly. In contrast, Sb_2Te_3 is always p-type since the dominating native defects are the Sb_{Te} antisite defects (see phase diagram, Figure 3.14). The Sb-O standard formation enthalpy comprises approximated -355 kJ/mol[252], -287 kJ/mol[253] for Bi-O and -319 to -323 kJ/mol[254] [253] for Te-O. For this estimation we divided the formation enthalpy of Bi_2O_3 (-574kJ/mol[253]) and Sb_2O_3 (-710

kJ/mol[252]) by two, and took the formation enthalpy of TeO_2. So, the ranking from more to less beneficial bonding is Sb-O, Te-O and Bi-O.

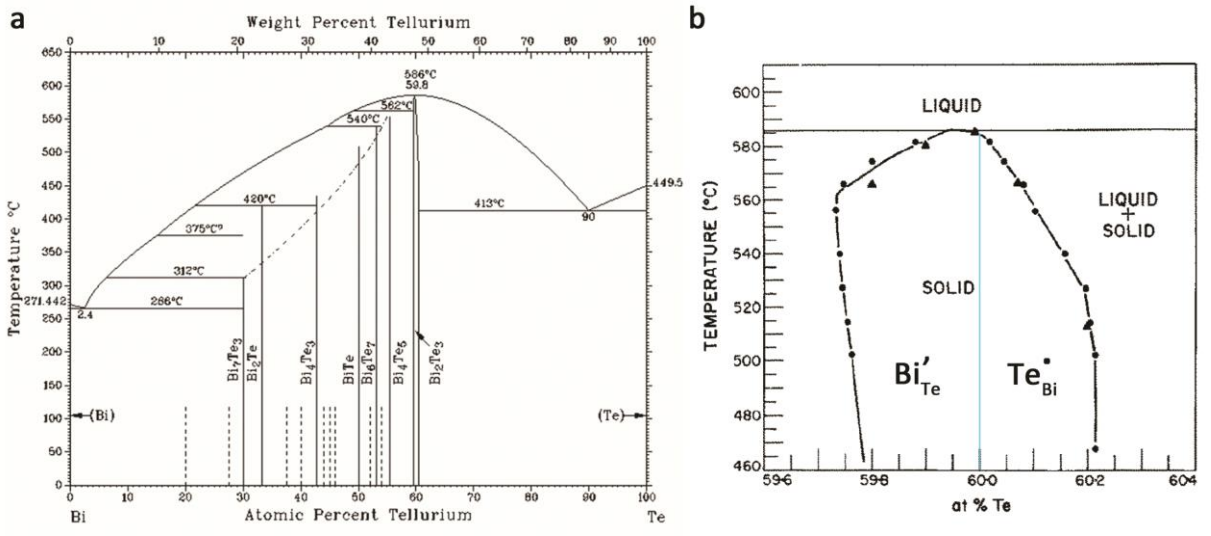

Figure 4.4 (a) Phase diagram of the Bi-Te system[120]. (b) Fragment of the phase diagram near the Bi_2Te_3 compound[251,168]; the 40:60 Bi:Te composition is marked with a blue line. On the left side of the line we have a p-type compound containing Bi'_{Te} defects and on the right hand side a n-type compound containing $Te^{\bullet}_{Bi}$ defects. The triangular data points came directly from measurements, while the round points came from interpolation.

In the case of Sb_2Te_3, we have Sb_{Te1} antisite defects and the Sb-O bonding is more beneficial than the Te-O bonding, making the Sb_{Te1} antisite defects reaction centres for the oxidation, creating a rough oxidation layer. Furthermore, DFT calculated by the group of Lada Yashina[255] proved that oxygen reacts preferentially with these antisite defects. Also STEM confirms it: the highly oxidized regions are about 12 nm apart along the a-b plane (thus parallel with the surface). One extra Sb atom per 100 atoms correspond to a ~1 at.% Sb excess which means that there is one Sb atom extra instead of a Te atom in ≈7 hexagonal unit cells. This atom can occupy six possible Te1 positions or nine Te (Te1 and Te2) positions, so only once every 40 or 60 unit cells an extra Sb atom is present at the surface, or in other words, one extra Sb atom is present in a surface of (12 nm x 45 nm) or (12 nm x 68 nm). FIB lamellas are approximate 20 nm or thicker. Furthermore, a sample thickness of 68 nm is overestimated because two closely-located oxidation centres cannot be distinguished when they overlap indicating that the averaged value of 12 nm between the oxidized regions is a top limit and the formation energy of a Sb_{Te1} defect is lower than a Sb_{Te2} defect[256], meaning that the anti-site defects prefer the outer Te layer above the middle Te layer. So, the 12 nm along the a-b plane (thus parallel with the surface) between the highly oxidized regions corresponds to Sb excess of the order of ~1 at.% typical for these crystals. In the case of Bi_2Te_3, we can have Bi_{Te1} antisite defects, although they are less probable. But the Te-O bonding is more preferential than the Bi-O bonding. So, this suggests that the antisite defects will not be reaction centres for the oxidation and we get a planar top surface in agreement with STEM. In contradiction, DFT calculations[255] proved that oxygen preferentially reacts with the Bi_{Te1} antisite defects. However, in Bi_2Te_3 the antisite defects

are less probable than in Sb_2Te_3[97] and oxygen reacts slightly less preferentially with the antisite defects of Bi_2Te_3 compared to Sb_2Te_3. This can explain the planar oxide layer found by STEM although DFT indicated that these antisite defects were reaction centres. The preference for the Te-O bonding compared to the Bi-O bonding can explain that the Te surface layer oxidizes, followed by the congruent oxidation of the first quintuple layer, creating $Bi_2(TeO_3)_3$. Congruent oxidation means that the Bi:Te ratio of the oxidation layer is identical to the Bi:Te ratio of the bulk structure. The oxidation itself happens via oxygen transport, because the size of the Te ions makes the mobility of the Te ions in Bi_2Te_3 hardly possible.

4.1.2.2 EDX

For Sb_2Te_3, EDX analysis proved that the amorphous area consists mostly of Sb and O, whereas the intertwined distorted crystalline top layer becomes strongly depleted in Sb until a tellurium layer almost completely free from Sb is formed (Figure 4.5a). This pseudomorphic layer includes up to three QLs and can be clearly seen in the EDX map in Figure 4.5a. Pseudomorphic means that a crystal with a different chemical composition takes the place of the original crystal, however, their volume and structure show similarities. It is remarkable that the clearly visible tellurium atoms roughly preserve the initial positions that they occupied in the Sb_2Te_3 lattice. The corresponding large interatomic Te-Te distances imply that there is no bonding between them. However, based on general chemistry considerations, we expect them to be bonded to each other by strong covalent bonds. Therefore, the only possible explanation for the obtained data is that such tellurium atoms are bonded to some atoms randomly positioned between the ordered Te layers. Furthermore, at certain positions in the HAADF STEM image of the EDX map in Figure 4.5a atoms are present in between these layers. The EDX data gives no clear answer as to what the nature of the disordered atoms is.

The bulk structure has the expected 2:3 Sb:Te ratio, found from quantifying the bulk EDX map in Figure 4.6a. Except for the short contact with air of the sides of the FIB lamella upon transport, we do not expect oxygen to be present in the bulk. When the EDX map is quantified using Sb, Te and O, we find 2 to 3 percent oxygen. This can be due to the short contact of the sides of the FIB lamella during transport and/or due to the overlapping of the Mz-line of Te (0.464 keV) with the K-line of O (0.525 keV). Due to this, the elemental oxygen map in counts of the surface structure is visually misleading (Figure 4.5a) and also small oxygen contributions are found for the quintuple layers furthest away of the surface, which have nothing to do with the oxidation of the original top surface. This also applies to the O maps of other materials.

For the non-oxidized Bi_2Te_3 sample no significant difference in the chemical composition of the shallow quintuple layers (Bi:Te ratio of 40.1(1):59.9(1)) in Figure 4.5c compared to the bulk quintuple layers (Bi:Te ratio of 39.6(2):60.4(2)) in Figure 4.6b, was observed. The quantification of the amorphous layer is not performed due to the low amount of counts coming from this area caused by its limited thickness. Low amount of counts leads to

inaccurate quantification. The two layers closest to the top part, deform rapidly under the electron beam.

Due to the high amount of seven-layered defects in the sublayer of Bi_2Te_3 EDX mapping becomes more difficult, leading to a lower spatial resolution compared to the EDX map of Sb_2Te_3. The drift corrector used during EDX mapping has difficulties following a certain VdW gap, causing the scanning region to 'jump' between neighbouring regions with fluctuating VdW gap depth. Kolobov *et al.*[219] even observed that before and after STEM mapping of a GeTe-Sb_2Te_3 area the stacked 2-5-2-layered structure changes to a nine-layered structure, suggesting the reconfiguration by external stimuli due to the electron beam. Also, Lotnyk *et al.*[220] detected for Ge-Sb-Te based systems that bilayer switching where the bilayer moves from one building block toward the adjacent building block while switching the order of the two layers can happen under the influence of a focused scanning electron beam. On the other hand, Wang *et al.*[257] did not observe any effect from the electron beam on the bilayers after exposing it during a standard STEM experiment up to 10 minutes. In our case, induced defects could also have occurred while repeatedly scanning the same area during EDX mapping, however this was not observed for this material.

Although the distorted crystalline top layer which is intertwined with the amorphous layer for the one-week-oxidized Bi_2Te_3 sample is thinner *i.e*. the depth size is smaller compared to Sb_2Te_3, we can still conclude that also there the intertwined distorted crystalline top layer becomes strongly depleted in the cation element, Bi for Bi_2Te_3 and Sb for Sb_2Te_3 (Figure 4.5). The distorted crystalline top layer is similar as for Sb_2Te_3 (Figure 4.2b, Figure 4.3a), which suggests that likewise the tellurium atoms are bonded to some atoms randomly positioned between the ordered Te layers. Also here the EDX data gives no clear answer as to what the nature of the disordered atoms is. The amorphous layer of Bi_2Te_3 consists, similar to Sb_2Te_3, mostly of a mixture of the cation element and oxygen.

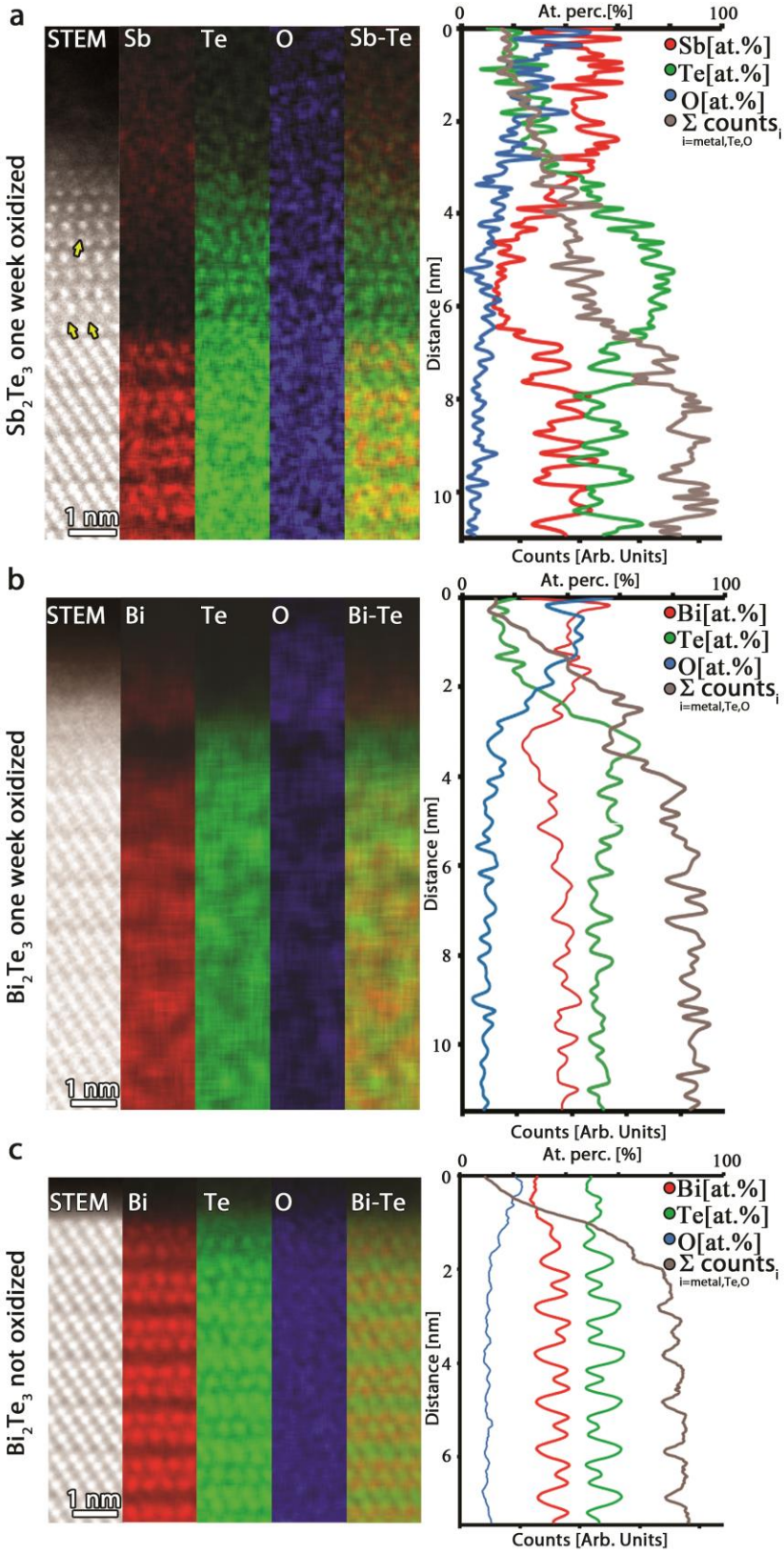

Figure 4.5 High resolution EDX maps in counts of the reaction zone of one week oxidized Sb_2Te_3 where in the HAADF STEM image some of the atomic columns in between the Te layers are marked with yellow arrows (a), one week oxidized Bi_2Te_3 (b) and non-oxidized Bi_2Te_3 (c) with the corresponding line profiles in atomic percent. On all graphs, the sum of the metal (Bi or Sb), Te and O in counts (grey) is also displayed to illustrate that the top layer consists of less material, resulting in lower counts and accuracy.

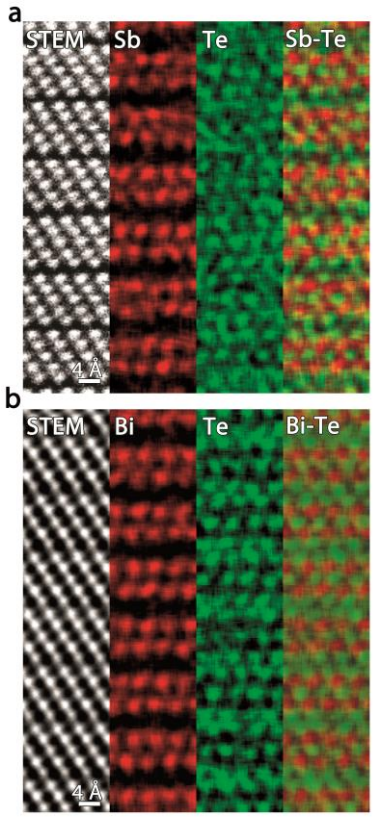

Figure 4.6 Atomic resolution-EDX maps of the bulk structure of Sb_2Te_3 (a) and Bi_2Te_3 (b).

4.1.2.3 Reaction mechanism

The following oxidation models for Sb_2Te_3 and Bi_2Te_3 are based on in-situ/ex-situ XP-spectra, HAADF STEM imaging and EDX mapping.

The reaction mechanism of Sb_2Te_3 is a two-step process. First, the oxide layer gets enriched in Sb, forming Sb_2O_3, which is clearly seen in Figure 4.2a-c and Figure 4.5a. To make this happen, the Sb-Te bonds will heterolytically break (the shared electrons are taken away by Te) followed by electron tunnelling from the Fermi-level of Sb_2Te_3, *i.e.* from Te^{-2}, to oxygen, leading to a negatively charged surface layer. Thus Te is 'oxidized' to Te^0 at the oxide-crystal interface. This negatively charged surface layer creates a potential causing the Sb^{3+} cations to migrate towards the surface, thus leaving the Sb_2Te_3 crystal and forming the Sb_2O_3 layer. The formation of the submonolayer-thickness Sb_2O_3 layer obeys a linear law typical for the initial fast oxidation of metals, where oxygen chemisorption is the rate limiting factor[236].

After a while we suppose that the electron tunnelling probability exponentially decreases upon oxide layer growth. When the oxide layer and the Te^0 layer underneath are too thick, the oxidation of this Te^0 layer can be more advantageous than the deeply located Te^{-2}. This leads to step two. Elemental tellurium, Te^0, will gradually bond to three oxygen atoms, converting into Te^{+4} and thus leading to the formation of a $Sb_nTe_mO_x$ oxide layer. The rate limiting factor is the cation diffusion in the constant potential in agreement with the Cabrera-Mott theory, visible due to the fact that one over the mean oxide layer thickness

follows the logarithmic law. The mechanism of the Te migration towards the surface is unclear.

The reaction mechanism of Bi_2Te_3 is at least a two-step process. Due to the fact that the Te-O bond is more advantageous than the Bi-O bond, the Te oxidizes first, followed by the congruent oxidation of the first quintuple layer, forming the $Bi_2(TeO_3)_3$ layer. The oxidation itself happens via oxygen transport, because the size of the Te ions makes the mobility of the Te ions in Bi_2Te_3 hardly possible. The second oxidation step of Bi_2Te_3 is similar to the first oxidation step for Sb_2Te_3.The switch from first step to the second one (cation diffusion, metal enrichment of the oxide layer and elemental Te layer) occurs because the $Bi_2(TeO_3)_3$ layer suppresses further oxygen diffusion. $Bi_2(TeO_3)_3$ can only be stable at the surface, because it has a larger volume than Bi_2Te_3 and the stress caused by the expansion due to oxidization can be only released upwards at the surface. The XPS experiment for Bi_2Te_3 ended before the completion of the second step due to the lower reactivity of Bi_2Te_3 compared to Sb_2Te_3. The second oxidation step for Sb_2Te_3 was not observed by XPS nor clear proof was provided by STEM-EDX for Bi_2Te_3. In the EDX maps, only a clear metal enrichment of the oxide layer is observed similar to Sb_2Te_3. The envisioned third oxidation step would involve mixing of Bi, Te and O, however, this has already occurred in the first step for Bi_2Te_3, therefore no conclusion can be made with EDX about the occurrence of a third step either.

Different models for the distorted crystalline structure can be proposed. STEM and EDX prove that a distorted structure exists in the subsurface layer with ordered Te layers and disordered layers in between (Figure 4.2, Figure 4.3 and Figure 4.5). The disordered layers can be Te, O or Sb and O, combined with vacancies. The model that fitted all data the best was disordered Te in between the Te layers. Te chains (space group $P3_121$) and Sb_2Te_3 have similarities: both consist of hexagonal layers along the c-axis with a=4.267 Å for Sb_2Te_3 and 4.456 Å for the Te chains (Figure 4.7). However, in Sb_2Te_3 Sb layers and van der Waals layers exist in between the Te layers, while in the Te chains only Te layers exist. So, these Te chains can be obtained by replacing the Sb atoms with Te atoms. Therefore, the distorted structure can be explained as a Te-like structure where the Sb atoms are replaced by disordered Te.

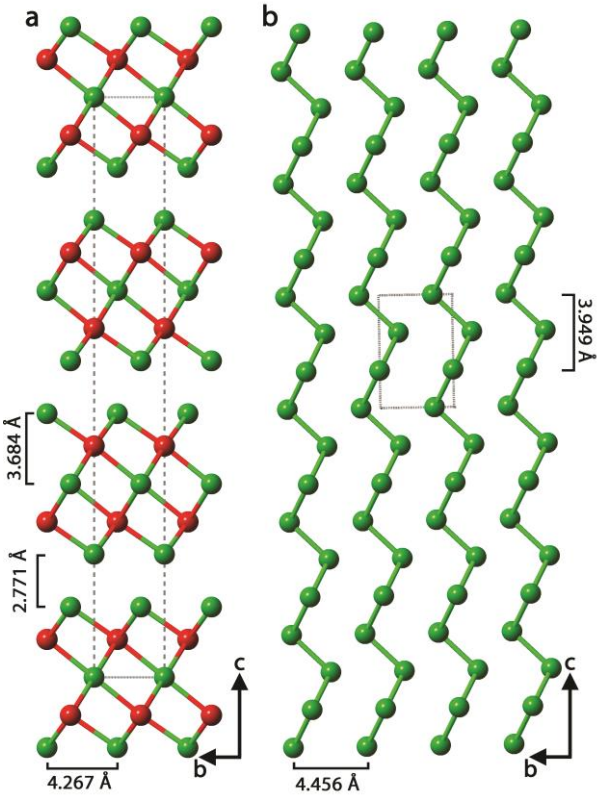

Figure 4.7 Structure of Sb_2Te_3[258] (a) and Te chains[259] (b) where the red sphere represent Sb and the green spheres Te.

4.1.3 $(Sb_{0.55}Bi_{0.45})_2Te_3$

4.1.3.1 STEM

$(Sb_{0.55}Bi_{0.45})_2Te_3$, a mixture of Sb_2Te_3 and Bi_2Te_3, is studied after two months of oxidation and also after three years of oxidation. The sample after two months of oxidation contains three different layers: an amorphous layer, intermixed with a distorted structure and the bulk structure (Figure 4.8a-c). The amorphous oxide layer covers the whole surface after two months (~1500 h) of air exposure and is planar, like for Bi_2Te_3. The interface between the amorphous layer intermixed with a distorted structure and the bulk structure is sharp. However, prolonged oxidation (about 3 years) results in certain structural changes (Figure 4.8d-f). The subsurface layer contains a significant amount of seven-layered defects (Figure 4.8f), similar to the Bi_2Te_3 sample. These seven-layered defects have a higher cation to anion ratio of atomic positions, hence many cation positions are vacant, which enables atomic mobility. So, four different layers exist in the three years oxidized sample: an amorphous layer, intermixed with a distorted structure, a defect-rich layer and the bulk structure. However, the thickness of the amorphous layer practically did not change.

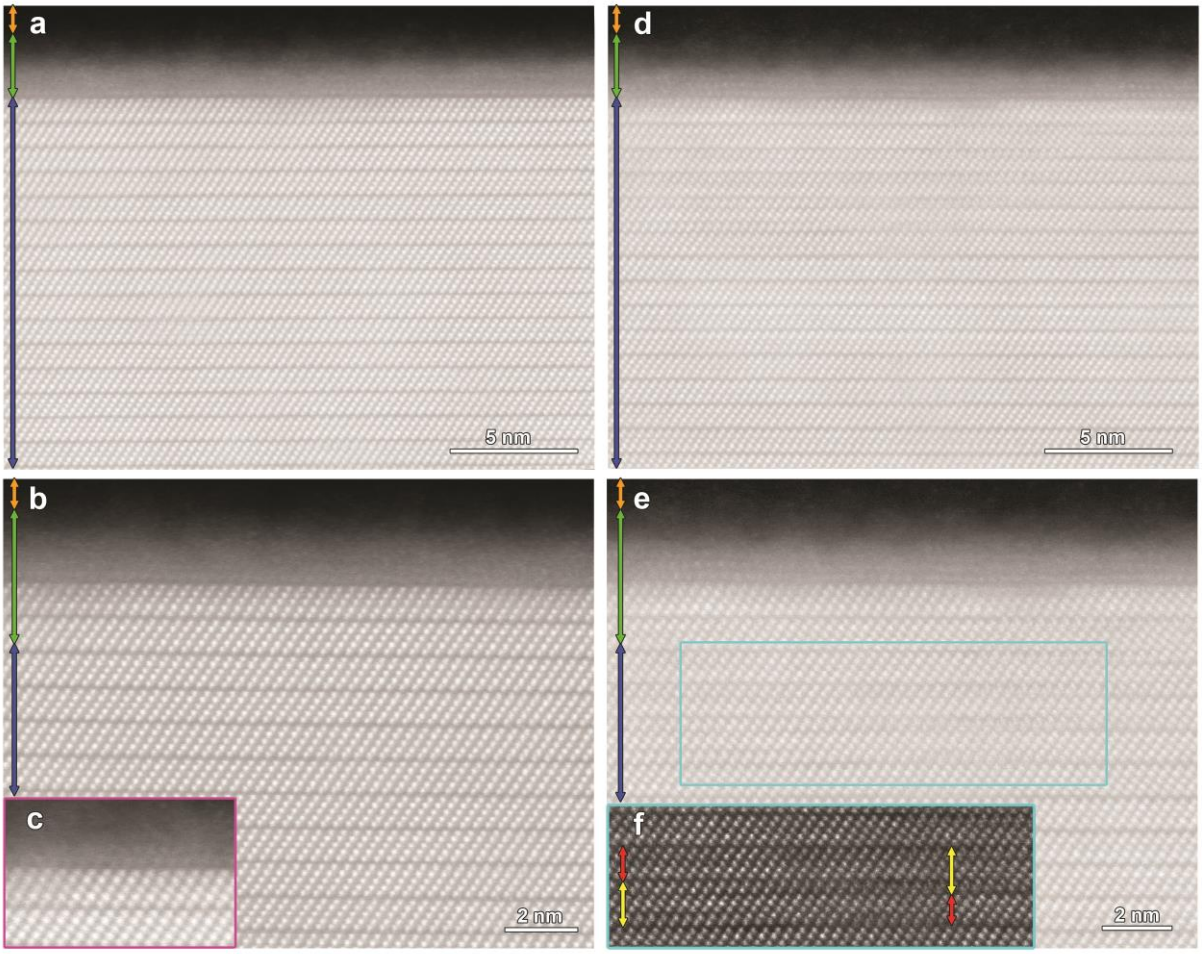

Figure 4.8 Cross-sectional overviews and close-up HAADF STEM images of the oxidized layers and the subsurface region of the two months oxidized (a, b, c) and the three years oxidized $(Sb_{0.55}Bi_{0.45})_2Te_3$ (d, e). From top to bottom, a carbon protection layer (orange) is visible, followed by an amorphous layer intermixed with indications of a distorted crystalline layer (green), and the $(Sb_{0.55}Bi_{0.45})_2Te_3$ structure (blue). The top part of the three years oxidized $(Sb_{0.55}Bi_{0.45})_2Te_3$ structure contains seven-layered defects (e,f), while the two months oxidized sample does not contain these defects (b). The area in the blue rectangle in (e) is enlarged with improved contrast in (f). (f) shows the stepwise displacement of the septuple layers (yellow arrows) in the depth of the material, which is in agreement with the model of Jiang *et al.*[250]. The quintuple layers are marked with red arrows. (c) and (e) display indications of a distorted crystalline structure at the top surface intermixed with the oxidized layer. (c) comes from another area than displayed in (b) as the Te columns were more clear there.

4.1.3.2 EDX

First, it is important to know how the three elements are distributed in the material, because they do not have the same preference for bonding with oxygen. The ranking from more to less beneficial bonding is Sb-O, Te-O and Bi-O. The EDX map of the bulk material (Figure 4.9) proves that Bi and Sb are evenly intermixed on the cation sublattice and that Te occupies the anion positions. XPS data of Volykhov *et al.*[228] further showed that the cations are statistically distributed with no surface enrichment either in Sb or Bi.

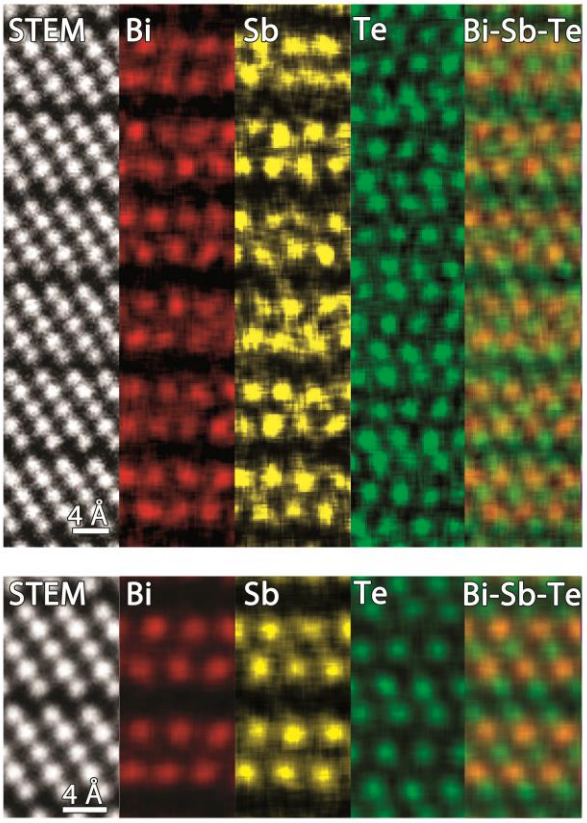

Figure 4.9 Atomic resolution EDX maps of $(Sb_{0.55}Bi_{0.45})_2Te_3$ (top) with its averaged EDX map (bottom).

The EDX map from the two months oxidized sample taken with atomic resolution and the corresponding composition profiles (Figure 4.10) clearly indicate that the upper part is composed of antimony oxide (region 0), whereas strong depletion of Sb from the first quintuple layers of the crystal is observed (regions 1 and 2). Both areas contain a certain amount of oxygen. At the same time, the Bi density slightly increases towards the interface with the amorphous layer, while the Te density is the same as in the bulk. This indicates generation of Sb vacancies in the surface layers of the crystal while the crystal structure remains intact.

However, prolonged oxidation (about 3 years) results in certain structural changes, which was already seen from the STEM data. By comparing the two EDX datasets we conclude that although the thickness of the amorphous layer practically does not change, certain Te redistribution is observed. The Te density becomes higher for the amorphous layer/crystal interface.

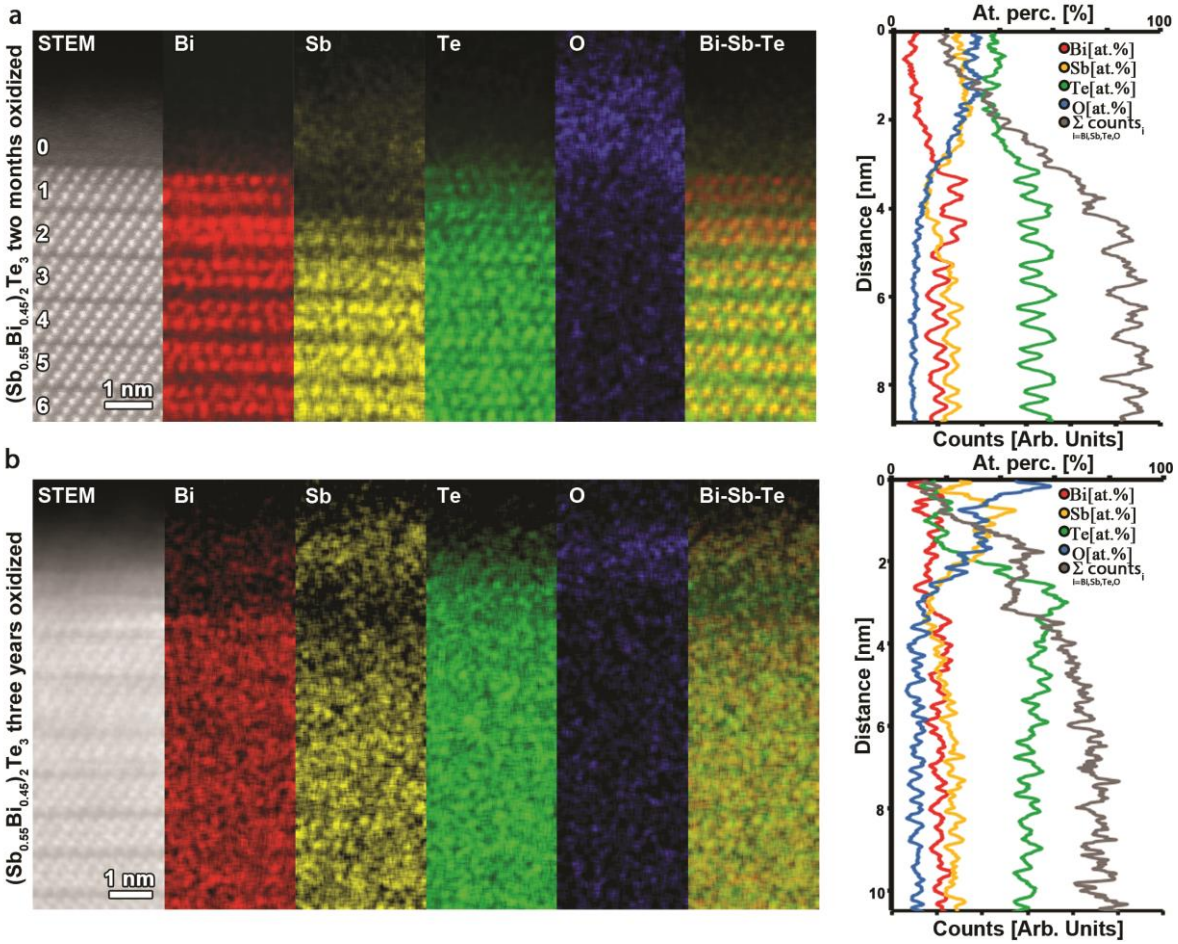

Figure 4.10 High resolution EDX maps in counts of the reaction zone for two months oxidized $(Sb_{0.55}Bi_{0.45})_2Te_3$ (a) and three years oxidized $(Sb_{0.55}Bi_{0.45})_2Te_3$ (b) with the corresponding line profiles in atomic percent. On all graphs, the sum of Bi, Sb, Te and O in counts (grey) is also displayed to illustrate that the top layer consists of less material, resulting in lower counts and accuracy.

4.1.3.3 Reaction mechanism

The following oxidation model for $(Bi_{1-x}Sb_x)_2Te_3$ is again based on the combination of XP-spectra, HAADF STEM imaging and EDX mapping.

The oxygen reactivity of the mixed Bi_2Te_3-Sb_2Te_3 crystals is not a linear combination of the oxygen reactivity of the separate constituents. The constituent with the highest reactivity has more influence. This is especially clear from the EDX maps (Figure 4.10) where a clear Sb depletion in the first quintuple layers is noticeable combined with the Sb enriched oxide layer on top. Sb has the most beneficial bonding with oxygen, compared to Te and Bi. Furthermore, the probability that oxygen attacks the Te-Sb bonds determines the surface reactivity and is directly proportional to the number of Te atoms bonded to one or more Sb atoms.

First, the oxide layer gets enriched in Sb, forming Sb_2O_3. To make this happen, oxygen attacks the Sb-Te bonds, leading to oxidation saturation of the surface Te-Sb bonds and the Sb migration from $(Bi_{1-x}Sb_x)_2Te_3$ to the oxide. The negatively charged surface layer due to the

electron tunnelling from the Fermi-level of $(Bi_{1-x}Sb_x)_2Te_3$ to oxygen, causes the Sb cations to migrate towards the surface. Thus Te becomes more 'oxidized', creating elemental Te, Te^0. Next, the oxygen atoms can diffuse through the oxide layer, creating Te^{+4}, where Te is bonded to oxygen. This process stops when the insulating oxide layer becomes too thick for further tunnelling. Long air exposures lead eventually to Te accumulation at the interface and lattice defects. The overall process resembles the Cabrera-Mott mechanism.

Due to the high reactivity of Sb with oxygen, an Sb rich oxide layer exists for $(Sb_{0.55}Bi_{0.45})_2Te_3$ similar to Sb_2Te_3. However, the planar oxide layer is quite similar to Bi_2Te_3. This suggests that the addition of Bi lowers the amount of Sb_{Te} antisite defects, creating a more planar oxide layer. Furthermore, the same seven-layered defects start to appear in $(Sb_{0.55}Bi_{0.45})_2Te_3$ after long enough air exposure as for Bi_2Te_3, probably due to the addition of Bi in this sample.

4.1.4 $Ge_mBi_{2n}Te_{(m+3n)}$

4.1.4.1 Trigonal layered structures

Unlike $(Sb_xBi_{1-x})_2Te_3$, these materials have a trigonal layered structure at the surface which differs from its bulk structure. $GeBi_2Te_4$ and $GeBi_2Te_4$+I contain a quintuple layer at the surface, while the bulk material consists of respectively nine and seven-layered building blocks. Furthermore, above this quintuple layer a mixture of the distorted structure and a trigonal layered structure is present. On the other hand, $Ge_3Bi_2Te_6$+I has a mixture of a three-layered block and the distorted structure at the surface in comparison to the eleven-layered building blocks in the bulk. Above this, the distorted structure is present. For all three compounds the final top layer is an amorphous layer. So, $GeBi_2Te_4$, $GeBi_2Te_4$+I and $Ge_3Bi_2Te_6$+I all contain an amorphous layer intermixed with a distorted structure and a layered trigonal structure different from the bulk, followed by the bulk structure (Figure 4.11).

The ordered atoms of the distorted structure match with the Te layers of the trigonal layered structure. So, upon oxidation the Te layers remain ordered while the layers in between get disordered. This structure is similar to the Te structures of previous discussed materials (Sb_2Te_3, Bi_2Te_3 and $(Sb_{0.55}Bi_{0.45})_2Te_3$). EDX (Figure 4.12) indicates that the amorphous layer is Ge oxide, suggesting that the Ge atoms are mobile and move towards the surface to create this oxide layer.

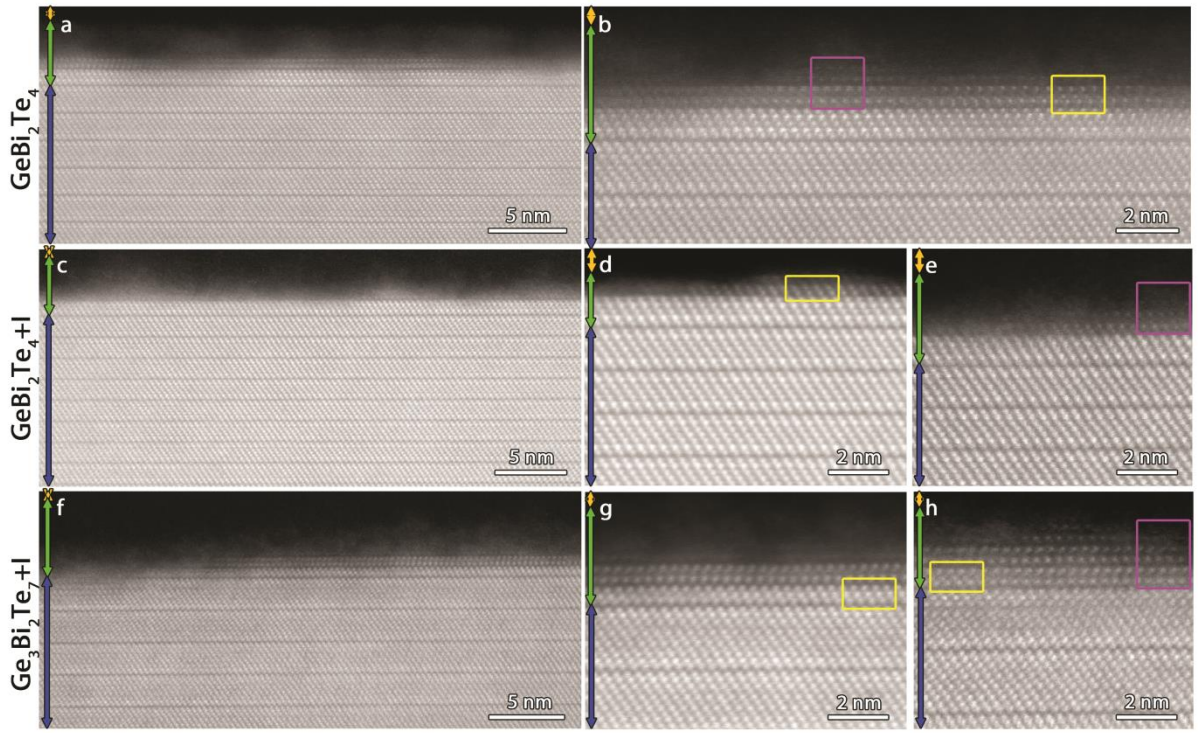

Figure 4.11 (a), (c), (f) Cross-sectional HAADF STEM overviews of zone $[010]_H$ of the oxidized layers and the subsurface from respectively $GeBi_2Te_4$, $GeBi_2Te_4$+I and $Ge_3Bi_2Te_6$+I. From top to bottom, a carbon protection layer (orange) is visible, followed by an amorphous layer intermixed with a distorted crystalline layer combined with a trigonal layered structure different from the bulk structure (green), and the trigonal layered bulk structure (blue). (b) shows the oxidized layers and the subsurface of (a) in more details, (d,e) do the same for (c) and (g,h) for (f). Some trigonal layered areas are marked with yellow squares, while some areas containing the distorted structure are indicated with purple squares.

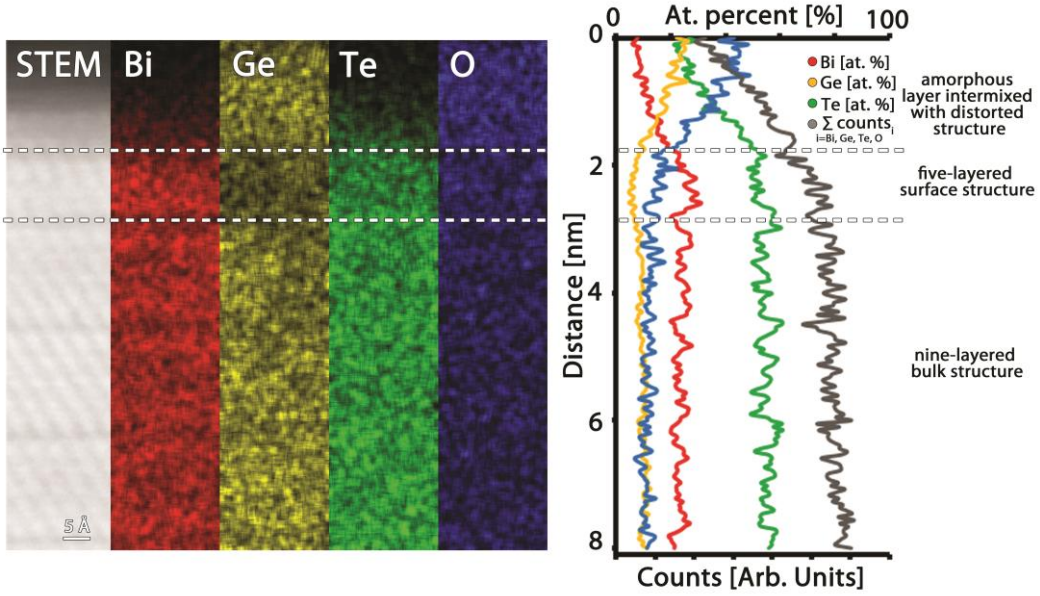

Figure 4.12 EDX map of the surface layers of $GeBi_2Te_4$ in counts combined with a line profile in atomic percent and the sum of the Bi, Ge, Te and O in counts: From top to bottom, the amorphous layer intermixed with a distorted crystalline structure enriched in Ge and O, followed by the Ge depleted five-layered surface structure and the nine-layered bulk structure.

4.1.4.2 Rock salt structures

The oxidized layers and subsurface structures for $Ge_3Bi_2Te_6$, $Ge_4Bi_2Te_7$ and $Ge_{6.8}Bi_2Te_{9.8}$ are similar, so only representative examples will be shown. The top oxidized layer is amorphous and intertwined with a distorted crystalline structure (Figure 4.13). This distorted structure consists of ordered Te layers, which is proposed from Figure 4.13e where the layered structure of $Ge_mBi_{2n}Te_{(m+3n)}$ deforms to the distorted structure. In between these Te layers periodic atoms are sometimes still visible, while in other areas the atoms are random distributed (Figure 4.13 c-e). This distorted structure is again similar to all previous discussed samples. No match was found in literature nor the ICSD structural database for the distorted structure with the ordered atoms in between the Te layers. A possible explanation is that the intermediate state during amorphization is too unstable to exist in a bulk structure.

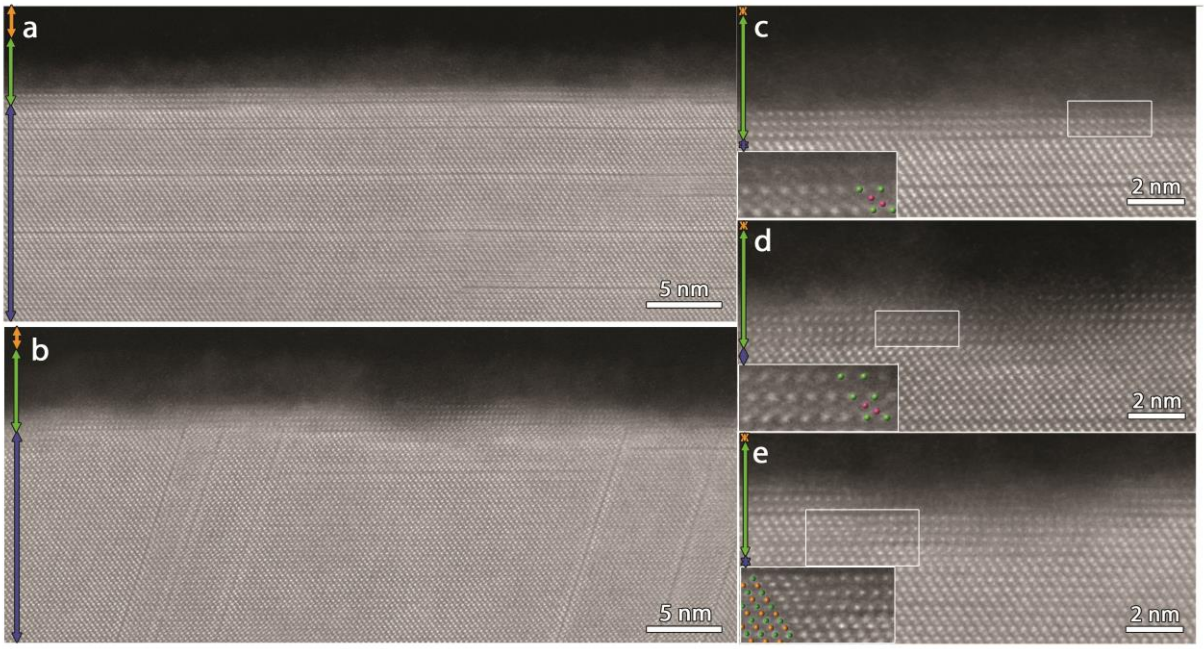

Figure 4.13 (a), (b) Cross-sectional HAADF STEM overviews of zone $[010]_H$ of the oxidized layers and the subsurface from $Ge_3Bi_2Te_6$. From top to bottom, a carbon protection layer (orange) is visible, followed by an amorphous layer intermixed with a distorted crystalline layer (green), and the on average cubic rock salt structure (blue). (c) and (d) are close-ups of the oxidized layers and the subsurface of respectively (a) and (b) where in the left corner the white marked regions are enlarged with a different contrast. Inset (c): In between the bottom two Te layers (green) the atoms are still ordered (pink), while the structure above it is already more disordered. Inset (d): In between the top two Te layers (green) the atoms are more random distributed than in between the bottom two Te layers. The ordered atoms are indicated with pink. (e) HAADF STEM image of $Ge_4Bi_2Te_7$, visualising that the Te atoms keep roughly their original positions, while the layers in between get disordered. The white indicated area is enlarged with changed contrast in the left corner overlaid with the rock salt structure. Te (mixed Bi/Ge) columns are represented with green (orange) spheres.

The oxide layer itself is a mixture of rougher and more planar areas. This could be due to the different kinds of planar defects at the surface (Figure 4.13 a-b) and the difference in formation enthalpies, even though no clear and direct correlation between the roughness of the surface with the defect type and the formation enthalpy can be found from the images. The Ge-O standard formation enthalpy comprises approximated -580 kJ/mol[253], -287

kJ/mol[253] for Bi-O and -319 to -323 kJ/mol[253,254] for Te-O. For this estimation we divided the formation enthalpy of Bi_2O_3 (574kJ/mol[253]) by two, and took the formation enthalpy of TeO_2 and GeO_2. So, the ranking from more to less beneficial bonding is Ge-O, Te-O and Bi-O. EDX proves that the amorphous oxide layer consists mostly of Ge and O (Figure 4.14).

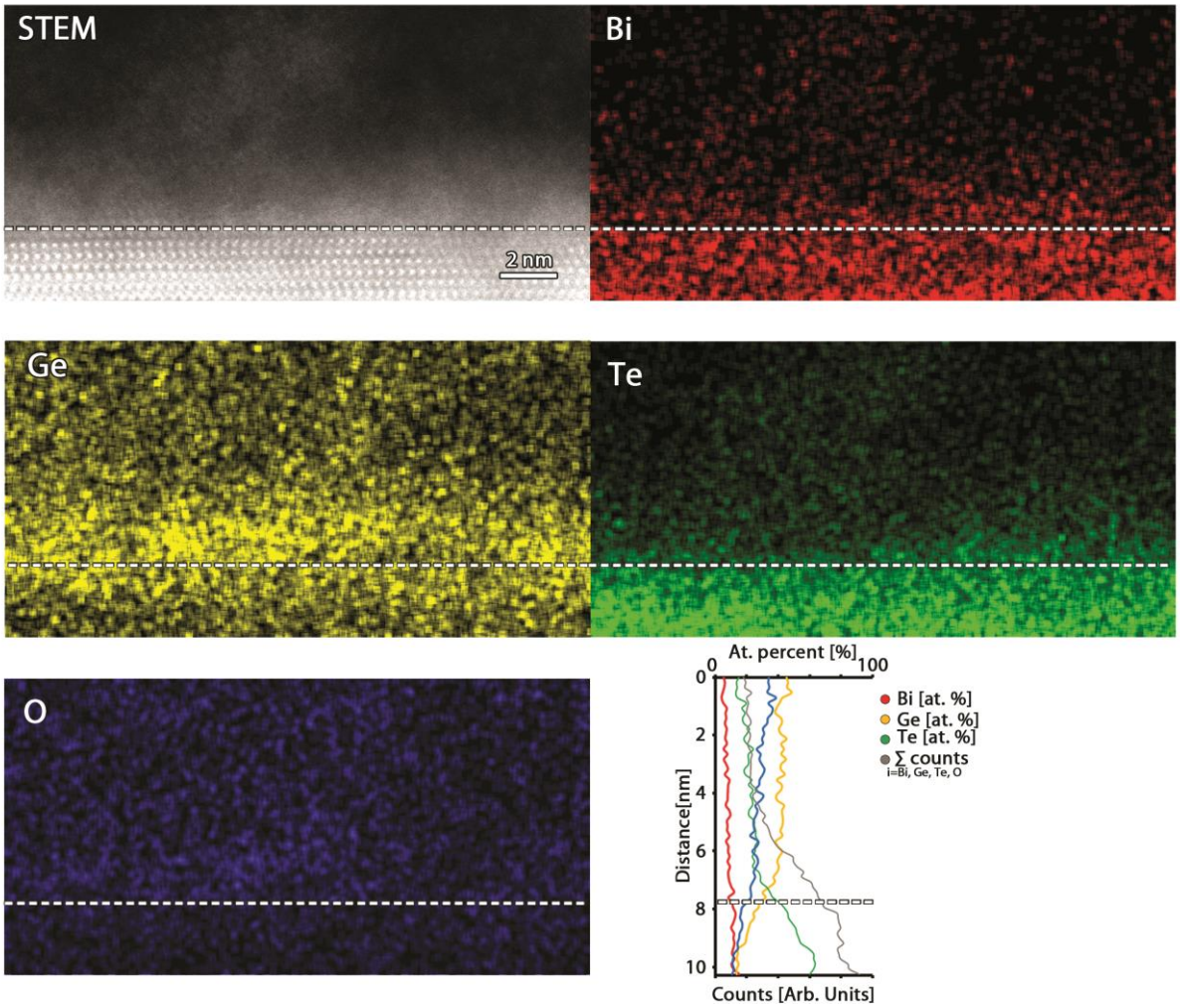

Figure 4.14 EDX maps of the surface of $Ge_{6.8}Bi_2Te_{9.8}$ in counts combined with a line profile in atomic percent and the sum of the Bi, Ge, Te and O counts: A dashed line indicates the interface between the crystalline subsurface (bottom) and the amorphous layer (top). Right above this dashed line, the amorphous layer is enriched in Ge and O.

4.1.4.3 Reaction mechanism

The surface layers of $Ge_mBi_{2n}Te_{(m+3n)}$ have a lot in common with the surface layers of Bi_2Te_3, Sb_2Te_3 and $(Sb_{0.55}Bi_{0.45})_2Te_3$. All materials have an amorphous oxide layer and distorted structure with ordered Te layers and disordered layers in between at the surface. Due to this, we suggest that a similar oxidation mechanism happens in $Ge_mBi_{2n}Te_{(m+3n)}$. EDX maps and HAADF STEM images prove that the oxide layer gets enriched in Ge: a Ge oxide layer[260,261] forms. To initiate this procedure, the Ge-Te bonds will be broken by oxygen, electrons from the Fermi-level of $Ge_mBi_{2n}Te_{(m+3n)}$ will tunnel to oxygen, inducing a negatively

charged surface layer and creating a potential. The latter causes the Ge^{2+} cations to migrate towards the surface, forming the Ge oxide layer.

We suspect that the electron tunnelling probability decreases with the oxide layer growth. When the oxide layer and the distorted crystalline structure underneath containing ordered Te layers are too thick, the oxidation of these ordered Te layers can be more advantageous, leading to the formation of a $(Ge,Bi)_nTe_mO_x$ layer and the initiation of the sequential step. However, conclusive evidence of the creation of a $(Ge,Bi)_nTe_mO_x$ layer could not be obtained using EDX. Possible explanations are that we didn't reach this oxidation step yet or that the oxidation layers are too thin leading to a low amount of counts and thus unreliable quantifications.

Unlike $(Sb_xBi_{1-x})_2Te_3$, the trigonal $Ge_mBi_{2n}Te_{(m+3n)}$ materials have a trigonal layered structure at the surface which differs from its bulk structure, *e.g.* $GeBi_2Te_4$ has a surface quintuple layer instead of the bulk nine-layered structure. A possible explanation is the change in chemical concentration in the subsurface region due to the diffusion of Ge towards the surface upon oxidation to form the amorphous oxide layer. With the removal of Ge the chemical composition will lean closer to Bi_2Te_3, which consist of five-layered building blocks. This can make the existence of a quintuple layer combined with the distorted structure more energetically favourable. The same reasoning can be applied to $GeBi_2Te_4$+I. For $Ge_3Bi_2Te_7$+I the oxidation can already be at a more advanced stage: only a trigonal layered structure still exists at the subsurface and not even everywhere. So, the quantity of Ge atoms can determine if the structure is still trigonal layered or already distorted. We suggest that the difference in the amount of layers in the surface trigonal layers of the different $Ge_mBi_{2n}Te_{(m+3n)}$ compounds compared to the bulk are a result of oxidation and were not present before oxidation, because cleaning the surface with scotch tape would preferentially break the weak van der Waals bonding between the Te-Te layers before the stronger bondings inside the building block.

4.1.5 Conclusion

Topological insulators have ideally conducting surface states and bulk insulating states. However, in regular circumstances, the preparation, handling and operation of future devices happens in contact with oxygen, making the knowledge of the surfaces' stability upon surface oxidation important. A step in better understanding the surfaces' stability is knowing what happens at an atomic level and how the surface oxidizes. For this, the atomic surface and subsurface layers were studied for Bi_2Te_3, Sb_2Te_3, $(Sb_{0.55}Bi_{0.45})_2Te_3$ and $Ge_mBi_{2n}Te_{(m+3n)}$ and oxidation mechanisms were suggested.

We found similarities between the surface and subsurface layers of the different materials. All materials contained an amorphous oxide layer at the top, intertwined with a distorted structure containing ordered Te layers with disordered layers in between and the final bulk structure. However, differences also occurred: $(Sb_{0.55}Bi_{0.45})_2Te_3$ and Bi_2Te_3 contained seven-layered defects in the subsurface, while the trigonal layered $Ge_mBi_{2n}Te_{(m+3n)}$ materials had a different layered building block at the surface compared to the bulk layering. The latter can

possibly be explained by the change in chemical concentration in the subsurface region due to the diffusion of the most reactive element, Ge, towards the surface. The reason for the existence of the seven-layered defects is unclear; however, they will enable atomic mobility.

Due to the similarities between the surface and subsurface layers of Bi_2Te_3, Sb_2Te_3, $(Sb_{0.55}Bi_{0.45})_2Te_3$ and $Ge_mBi_{2n}Te_{(m+3n)}$ we suggest that all these materials have similar oxidation mechanisms. Oxygen will try to break the bonding and react with the most reactive element of the material. Electrons from the Fermi level of the material will tunnel to the oxide, creating a negative surface layer. The most reactive element will then migrate to the surface, forming an amorphous oxide and leading to the distorted structure containing ordered Te layers with disordered layers in between. Afterwards, other elements will start to oxidize and form a more complex oxide $A_nB_mO_x$. However, also clear differences were observed *e.g.* for Bi_2Te_3 Te oxidizes first, followed by congruent oxidation of the first quintuple layer via oxygen transport, creating $Bi_2(TeO_3)_3$.

4.2 Fe deposition

This section is based on the paper: Sanchez-Barriga Jaime, Ogorodnikov Ilya I., Kuznetsov Mikhail V., Volykhov Andrey A., Matsui Fumihiko, Callaert Carolien, Hadermann Joke, Verbitskiy Nikolay I., Koch Roland J., Varykhalov Andrei, Rader Oliver, Yashina Lada V., *Observation of hidden atomic order at the interface between Fe and topological insulator* , Physical chemistry, chemical physics 19(2017), p.30520-30532[262]. I performed the TEM study, EDX study and FIB preparation. The latter was executed using the transfer module from Kammrath and Weiss GmbH to keep the sample in inert Ar gas during transport to and from the FIB microscope. No carbon layer could be applied onto the material for extra protection during FIB, because this layer is deposited onto the material outside the FIB microscope which was impossible due to the air limitation. To further limit air exposure, the samples were mounted in the holder in a glove box filled with inert Ar gas. Afterwards they were transported in an inert atmosphere and only exposed to air shortly before and after Ar plasma cleaning.

4.2.1 Fe/Bi_2Te_3

4.2.1.1 Introduction

Magnetic materials combined with topological insulators have many potential applications in spintronic devices[27,223,263,264], making detailed structural information important. Due to the spin-momentum locked property of the surface conduction, the spin of the electrons is perpendicular to their movement, leading to a very high efficient spin current and thus a high spin-orbit torque (SOT) efficiency[4]. This SOT can switch the direction of the magnetic

[4] To measure this SOT efficiency, a sweeping dc current and a bias magnetic field along the current direction is applied. The Hall resistance versus the current is plotted, which exhibit a shift which corresponds to the current-induced effective field H_z^{eff}. The SOT efficiency is then commonly defined as the ratio between H_z^{eff} and the current density J_e[340,341].

layer in a magnetic layer/topological insulator system. For example, recently Jiahao *et al.*[27] observed a high spin-orbit torque efficiency on the magnetic layer CoTb by Bi_2Se_3. Also, Wang *et al.*[263] showed this at room temperature for the NiFe/Bi_2Se_3 system using a low current density. It can lead to applications in low power consumption and high integration density memory devices and logic devices.

To use these interfaces between topological insulators and ferromagnets in applications, the surface conducting states should still exist after applying a magnetic layer. However, the surface states can mediate a coupling between the magnetic impurities that are uniformly deposited on the surface of a topological insulator, causing them to align perpendicular to the surface forming a ferromagnetic ordered film when the chemical potential of the electrons lies near the Dirac point[227]. The field which results from this, can break the time reversal symmetry and open up an energy gap at Dirac point[227]. When the easy magnetization of a ferromagnet lies inside the surface layer then no surface band opening happens, only a shift of the Dirac point. When it lies perpendicular to the surface plane, it causes a surface bandgap[265]. However, different situations are discussed in literature with different results on the surface states. The magnetic layer can be *e.g.* disordered[266], ferromagnetic[267] or paramagnetic[268], also bulk doping[267,269] can be performed. For example, single adatoms on Bi_2Se_3 (coverage range ≈1%) causing an in-plane magnetic anisotropy[270], a disordered Fe monolayer on Bi_2Te_3[266] and adsorbed Fe adatoms on Bi_2Te_3 resulting in a large paramagnetic out of plane magnetic anisotropy produce a Dirac point shift without opening a bandgap. In contrast, Fe substituted on the Bi sites of Bi_2Se_3 results in a theoretically favourable out of plane net magnetic moment and a small surface bandgap opening[269]. Also magnetic doping and ferromagnetic surface doping with Fe and Mn leads to a surface bandgap[267]. Even interfacial superconductivity was found for an antiferromagnetic ordered FeTe monolayer grown on Bi_2Te_3[271]. Furthermore, Kim *et al.*[272] detected that ultra-high vacuum annealing can restore the inherent topological surface states from an antiferromagnetic Gd-doped Bi_2Te_3.

To realize efficient spin injection in future topological insulator based devices, the conductive surface state should be robust upon addition of the magnetic layer and the Bi_2Te_3 family has the easiest linear surface state dispersion with one Dirac point. Also the bulk conductivity should be suppressed and the topological properties in the neighbourhood of the interface preserved. This is in order to achieve high spin current densities, also explaining the choice of Fe deposition: Fe owns the largest exchange splitting among the 3d transition metals[5,273–275]. Fe is a ferromagnet, like Co and Ni. A material is ferromagnetic, when the material has an exceptionally large density of states at the Fermi level[5]. In this material, the spin up and spin down energy bands are shifted (exchange splitting) with respect to each other and filled up to the Fermi level, leading to more electrons in one spin state (the majority spin) compared to the other spin state (a minority spin)[5]. The magnetic field is thus caused by the exchange interaction, which is the result of the collaboration of the Coulomb repulsion of two nearby electrons and the Pauli exclusion principle forbidding the same quantum state for two electrons[5]. Also ab initio calculations showed that a transition metal substituted on a Bi site causes magnetic moments due to the spin-polarization of the

transition-metal 3d electrons and Fe-doped Bi_2Te_3 had the highest magnetic moment compared to Ti, V, Cr and Mn doping[276].

We will discuss the interface structure upon deposition of a thick Fe film. Low coverage is already discussed in literature[266,268,270], however thick magnetic layers also useful for applications remained largely unexplored. Polyakov *et al.*[277] found that annealing at 520K after Fe deposition results in the formation of an α-FeSe structure. The complex atomic interface structure should be taken into account while fine tuning the parameters for the optimization of spin injection efficiency in devices. To investigate this, we used high-resolution scanning transmission electron microscopy (STEM) imaging and energy dispersive energy (EDX) spectroscopy.

4.2.1.2 Results

The deposition of a thick Fe film in the form of a compact layer results in a modification of the interface structure. The structure obtained after deposition of a 20 nm Fe layer was studied with HAADF STEM on a cross-sectional sample (Figure 4.15-Figure 4.16). The Fe layer is found to be crystalline. All Fourier transforms of different areas of the STEM image (bottom panels of Figure 4.15) extracted from some regions (labelled 1 and 2 in red and green colour, respectively) within the Fe layer can be indexed using cell parameters a=b=c≈3.5 Å. There are random distortions from the $Fm\bar{3}m$ structure as one would expect for bulk Fe with these cell parameters. For example, in the Fourier transform of region 1, the reflections correspond to a primitive cell rather than to an F-centred one. On the other hand, in the case of region 2 only few reflections can be obtained. The angle between the c-axis of Bi_2Te_3 and the (111) direction of the Fe lattice comprises 25°–30°. Normally, we would expect this angle to be close to 0° due to the energetically favourable stacking of Fe along the (111) direction[276].

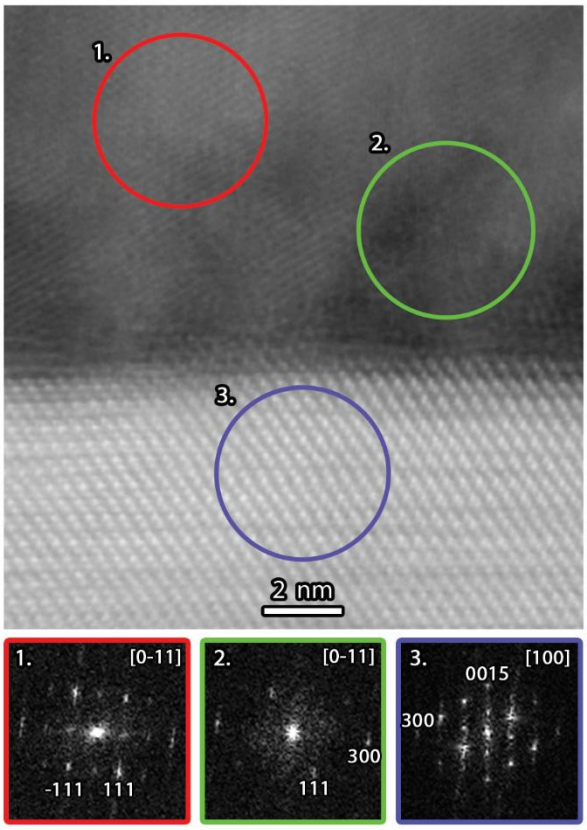

Figure 4.15 Characterization of the interface structure for 20 nm thick Fe on Bi_2Te_3 using high-resolution STEM: (top) Cross-sectional HAADF STEM image. (bottom) Corresponding Fourier transforms obtained from the green, blue and red regions labelled from 1 to 3, respectively.

Just below the Fe layer an amorphous layer (≈ 3.5 nm) mostly consisting of Te and Fe is formed as demonstrated in Figure 4.15 by the interface morphology seen in the STEM images, as well as by the corresponding depth profiles obtained using energy dispersive X-ray (EDX) nanoprobe analysis shown in Figure 4.17. The STEM images displayed in Figure 4.16 also show that the top layer of the substrate consists of a mixture of quintuple layers (Bi_2Te_3, Te–Bi–Te–Bi–Te), septuple layers (Bi_3Te_4, Te–Bi–Te–Bi–Te–Bi–Te) and quintuple layers with double layers. Frangis *et al.*[206,249] and Jiang *et al.*[250] already discovered these seven-layered defects in respectively Bi_2Te_3 and $Bi_{2+\delta}Te_3$. Jiang *et al.*[250] observed that these septuple layers do not stay at a fixed depth from the interface but this depth fluctuates stepwise parallel to the interface of the material. When Bi_3Te_4 (Te-Bi-Te-Bi-Te-Bi-Te) splits into a quintuple layer (Te-Bi-Te-Bi-Te) and two excessive Bi-Te layers, the order of those two excessive layers will change, so a Bi-Te layered ordering becomes a Te-Bi layered ordering. Those excessive layers will move to the adjacent QL, creating a new seven-layer lamella with the same sequence. The switch in chemical composition can be explained by the higher preference of the Bi-Te bonding compared to the Te-Te bonding[250]. Like already mentioned, these different building blocks - quintuple layers, septuple layers and quintuple layer with a double layer- are visible in subsurface area of the substrate. Furthermore, a high amount of these septuple layers occurs in the studied material, not comparable to the untreated material of Jiang *et al.*[250].

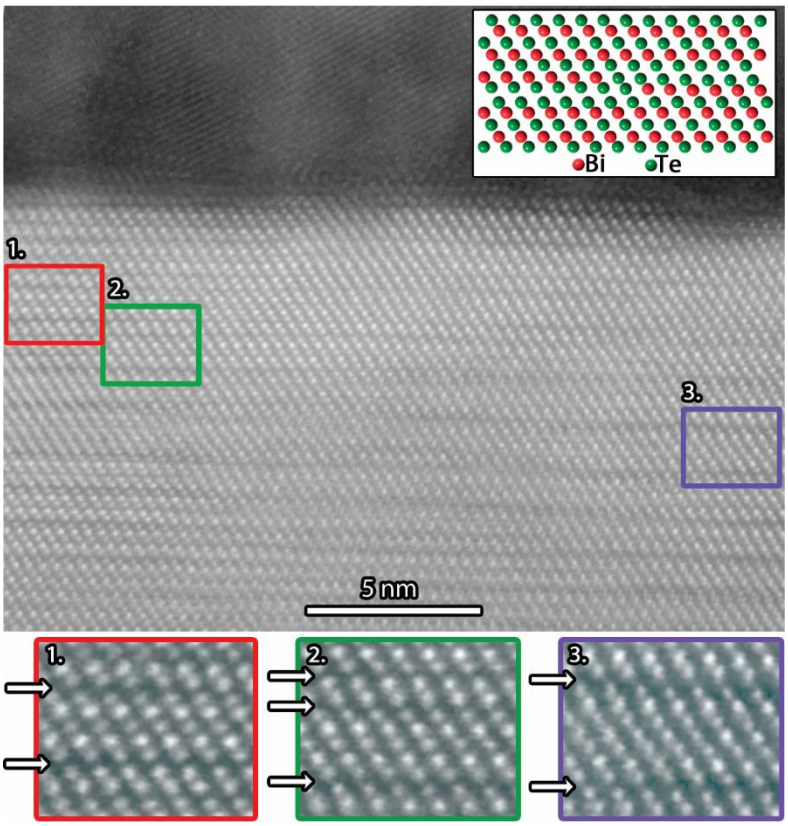

Figure 4.16 Details on the interface structure of 20 nm Fe on Bi_2Te_3: The top Bi_2Te_3 layer is shown with enlargements of three indicated areas. Red (1): quintuple layer; green (2): quintuple layer with a double layer; blue (3): septuple layer. The arrows mark the van der Waals gaps. The inset on the top right shows the transition from a quintuple layer to a septuple layer, using the model proposed in Jiang *et al.* [250]

The septuple layers are mostly localized within a distance of ~25 nm from the interface. This is consistent with the EDX observation evidencing a Bi/Te ratio notably higher than 2:3. This ratio is displayed as a light-blue curve in the corresponding depth profile shown in the bottom panel of Figure 4.17. The excessive Bi arising as a consequence of the FeTe layer formation is forced back into the bulk, forming septuple layers. In addition, the depth profile reveals the presence of minor amounts of Fe in the top layer of the substrate which decrease rapidly over the next 6 nm. Exact visualization of these Fe positions with EDX or HAADF STEM was hardly possible. This indicates that the Fe atoms show no long-range order over the structure and thus give too low signal in the possible individual positions, as the Fe positions along the whole thickness of the column are not completely occupied. A quantitative treatment of the HAADF STEM images to derive the exact amount of Fe per column was difficult to achieve due to the mixture of quintuple and septuple layers along the projection direction. For the 20 nm textured Fe layer grown on Bi_2Te_3, the interface structure contains a ≈3.5 nm amorphous FeTe interface layer, with excessive Bi migrating to the shallow bulk and forming septuple layers of Bi_3Te_4 that are randomly distributed within approximately 25 nm in depth from the interface. Manna *et al.*[278] observed interfacial superconductivity after applying a thin FeTe film on top of Bi_2Te_3. Interfacing topological insulators with superconductors is *e.g.* studied for Majorana fermions[279], which are fermions

that are their own antiparticle. This is an interesting direction to study, but lies outside the scope of this thesis.

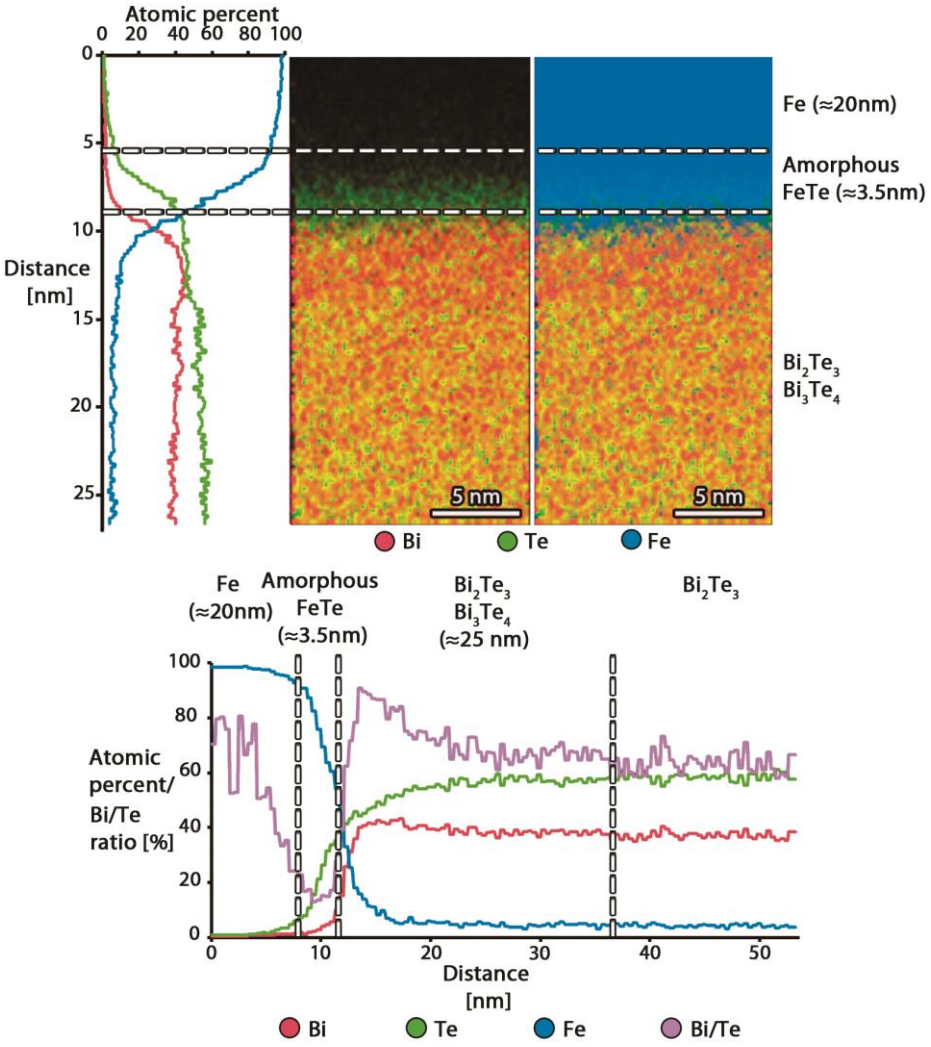

Figure 4.17 Interface composition of 20 nm Fe on Bi_2Te_3: (top) STEM-EDX maps and corresponding line profiles. (bottom) Line profiles taken over a larger depth emphasize the deviation of the Bi:Te ratio in the top layer and the regularization of this ratio when going deeper into the bulk.

The group of Lada Yashina[262] discovered using angle-resolved photoemission spectroscopy (ARPES) that the Dirac point is shifted towards higher binding energy after Fe deposition (up to 0.4 monolayer), so the magnetic moment of Fe is preferentially ordered parallel to the surface (Figure 4.18a). However, canted magnetic moments with a polar angle θ below 45° also exist (Figure 4.18b). This results in a maximum possible gap of ~20 meV. Using a combination of techniques (X-ray core-level photoemission spectroscopy (XPS), X-ray photoelectron diffraction (XPD), X-ray photoelectron holography (XPH), DFT calculations, electron diffraction in atomic clusters (EDAC) simulations of diffraction pattern) it was found that after one to three monolayers Fe deposition clear ordering of the Fe atoms at the interface can be observed, despite the disorder revealed with scanning tunnelling microscopy (STM) (atomic defects, clusters and islands) at the Bi_2Te_3 surface. Fe occupies two different positions in this local structure: hollow adatoms positions between the first

(Te) and the second (Bi) layer deeply relaxed into the quintuple layers of the Bi_2Te_3 material and an interstitial position between third (Te) and fourth (Bi) layer (Figure 4.18c).

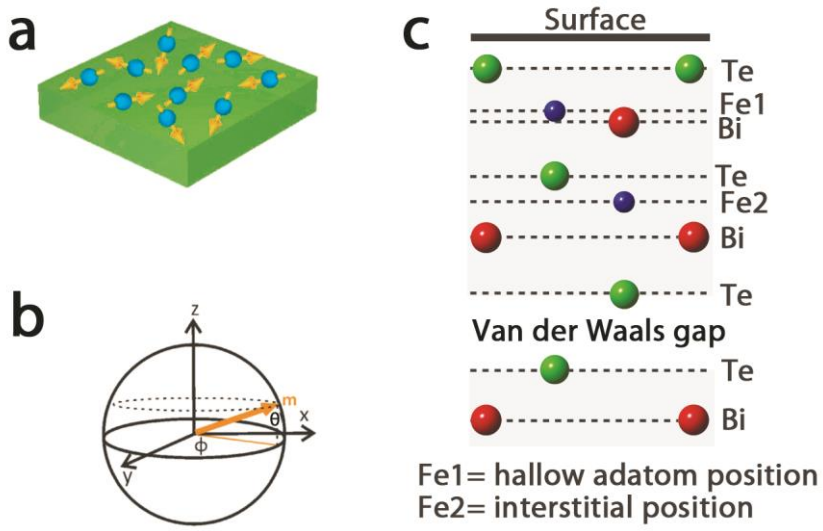

Figure 4.18 (a) Schematics of the Fe magnetic impurities on the Bi_2Te_3 surface (b) Fe magnetic moment in three dimensions, where the pole coordinates θ and ϕ are shown. (c) Local structure of Fe: Fe hollow adatoms between the first (Fe) and second (Bi) layer and the interstitial position between the third (Te) and fourth (Bi) layer.

4.2.1.3 Conclusion

We studied the atomic interface structure between the largely unexplored thick Fe deposition and the topological insulator Bi_2Te_3. Knowing the interface structure between this magnetic layer and Bi_2Te_3 is important, because this can have an influence on the conducting surface states of Bi_2Te_3, especially since these conducting surface states are not robust under magnetic impurities and the aim is to use these conducting surface states for applications in spintronic devices. A 20 nm thick bulk Fe layer was deposited onto Bi_2Te_3. This deposition leads to a ≈3.5 nm amorphous FeTe interface layer, with excessive Bi migrating to the shallow bulk (≈25 nm) and forming septuple layers of Bi_3Te_4. Also literature found interfacial superconductivity at the interface between Bi_2Te_3 and a thin FeTe film interesting *e.g.* for Majorana fermions. This raises the question if this interfacial superconductivity also exists in our case, but this lies outside the scope of this thesis.

Chapter 5 Structurally related materials

This chapter will discuss the defect structure of α-GeTe and the commensurate and incommensurate structures of Fe_2Ge_3. Both materials are not topological insulators. However, they are related to structures that are (see section 1.1.2). Both also have been researched for their thermoelectric properties.

5.1 GeTe

This section is based on the manuscript '*Atomic and electronic structure of a multidomain GeTe crystal surface*' by Alexander S. Frolov, Carolien Callaert, Joke Hadermann, Alexander V. Fedorov, Dmitry Y. Usachov, Alexander Chaika, Brian Walls, Kuanysh Zhussupbekov, Igor V. Shvets, Matthias Muntwiler, Jaime Sánchez-Barriga, Lada V. Yashina.

I made the sample using FIB milling. Afterwards, I performed the TEM study including SAED diffraction, DF and BF TEM imaging, STEM imaging and strain analysis.

5.1.1 Introduction

GeTe is a narrow bandgap semiconductor with a bandgap of ~0.1-0.2 eV[280,281] and is a thermoelectric material with a thermoelectric figure-of-merit ZT up to 1.37[39], which can be increased with doping[190,282]. The thermoelectric figure-of-merit ZT depends on the temperature T, the electrical conductivity σ, Seebeck coefficient S and the thermal conductivity κ which is the sum of the electronic κ_{el} and lattice κ_{lat} contributions: $ZT = S^2\sigma T/\kappa$. The thermal conductivity can be lowered by point defects[283], nanostructuring[283], domain boundaries and twins[284,285]. Especially the latter is present in α-GeTe[284,286–289], one of the crystalline phases of GeTe. α-GeTe is also a diatomic ferromagnetic semiconductor[290]. Despite its domain structure, it is a self-poling ferromagnet at room temperature due to preferential ferromagnetic order[291].

The phase transition of amorphous to crystalline GeTe is studied for phase change memory applications[211,292]. GeTe undergoes also a crystalline-crystalline phase transition at ~700K. The exact transition temperature depends on the specific composition[221]. Above this temperature, the atoms reorganize in a rock salt structure with space group $Fm\bar{3}m$[293], the β-GeTe structure, while below this temperature it takes on a rhombohedral R3m structure, the already mentioned α-GeTe[18] (Figure 5.1). At lower temperatures the structure is less symmetric and one of the cubic $<111>_C$ directions elongates and becomes the polar rhombohedral $[111]_R$ or the hexagonal $[001]_H$ direction[288]. On top of this, the 90° angles of the cubic phase distort[221]. A relative displacement of the Ge and the Te sublattices along the $[111]_R$ direction makes the planar distances between successive $(111)_R$Ge and $(111)_R$Te planes unequal as 1.57 Å and 1.98 Å, with the corresponding Ge-Te bond lengths of 2.87 Å and 3.12 Å[18]. During the phase transformation to the rhombohedral structure, the structure loses its inversion centre and becomes non-centrosymmetrical, which leads to its polar properties.

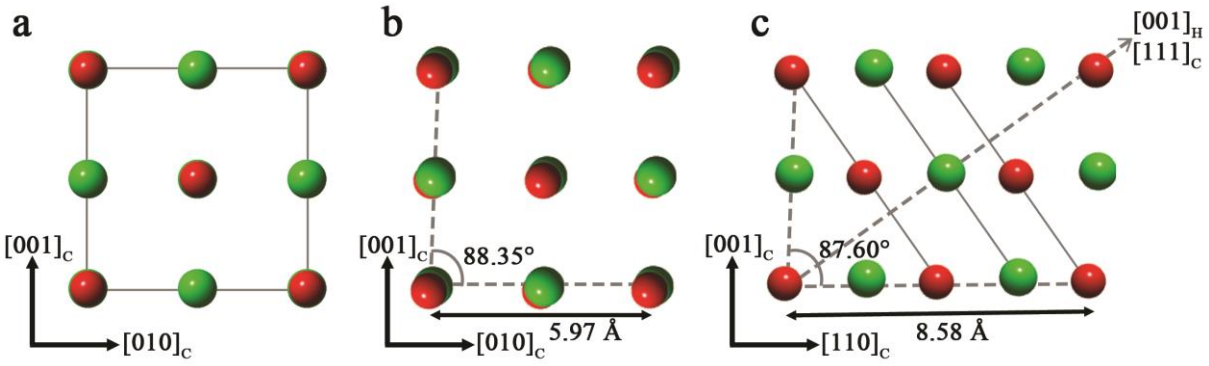

Figure 5.1 (a) The β-GeTe structure or the rock salt type structure along the a_C axis (b), (c) The α-GeTe structure along the a_c axis (b) and the [1-10] direction. (b) visualises that the planar distances between successive $(111)_R$Ge and $(111)_R$Te planes are unequal. Te atoms are represented with green spheres, while Bi atoms with red spheres. The figure is adapted from Vermeulen *et al.*[287].

The spin-orbit coupling in α-GeTe does not make it a topological insulator, but a ferroelectric Rashba semiconductor. Spin-orbit coupling combined with ferroelectricity, a consequence of the lack of inversion symmetry, can lead to giant Rashba spin splitting causing k-depended spin-splitting in the band structure.[294] This is a topological trivial state and leads to ferroelectric Rashba semiconductors. α-GeTe belongs to this class[294–297], exhibiting a giant spin splitting with a Rashba parameter α_R around 4.2 eV[298], the highest of the so-far known materials. First-principles calculations indicate that the large lattice distortion of α-GeTe is the key reason for this spin splitting[299]. Through an electric field, the spin texture in this type of material can be controlled and switched, interesting for spintronics applications[294]. Switching means that domain walls move to enlarge the domains with the favourable orientation and to decrease the domains with a less favourable polarization to raise the macroscopic polarization in the field's direction[300]. However, the large concentration of free-carriers[301,302] screens the electrical field and impedes its coupling with the internal polarization[303]. So Nukala *et al.*[289] proved that by applying electrical pulsing the polar domains can also be inverted in GeTe.

The cubic high symmetry structure has four different $<111>_C$ directions that are equivalent due to symmetry. While going through the phase transition, every one of the cubic $<111>_C$ can become the polar axis, leading to the formation of domains. Also the relative shift along the $[111]_C$ direction can happen in two different senses. According to Snykers *et al.*[288], two types of interfaces exist: twin boundaries and inversion domain boundaries. For the inversion domain boundaries the polar axis is parallel but in opposite senses, while for the twin boundaries the direction of the polar axis of different domains have different directions. The twin boundaries are subdivided in reflection twins showing head to head coupling (Figure 5.2a,c) along (100) and (110) planes and rotation twins with head to tail coupling along (100) and (110) planes (Figure 5.2b,d). The angle between the polarization vectors of the $(100)_C$ domains is 109° and of the $(110)_C$ domains 71°. Inversion boundaries of planar arrangement are formed by rotation twins, when the boundary is parallel to the trigonal axis (Figure 5.2e), and reflection twins when the boundary is perpendicular to the

trigonal axis (Figure 5.2f-i). The angle between the polarization vectors of the inversion domain boundaries is 180°. From common structural consideration, for the latter case (reflection twin inversion boundary) four types of domain walls are possible: two with shorter distances and two with longer distances around Ge or Te (Figure 5.2f-i).

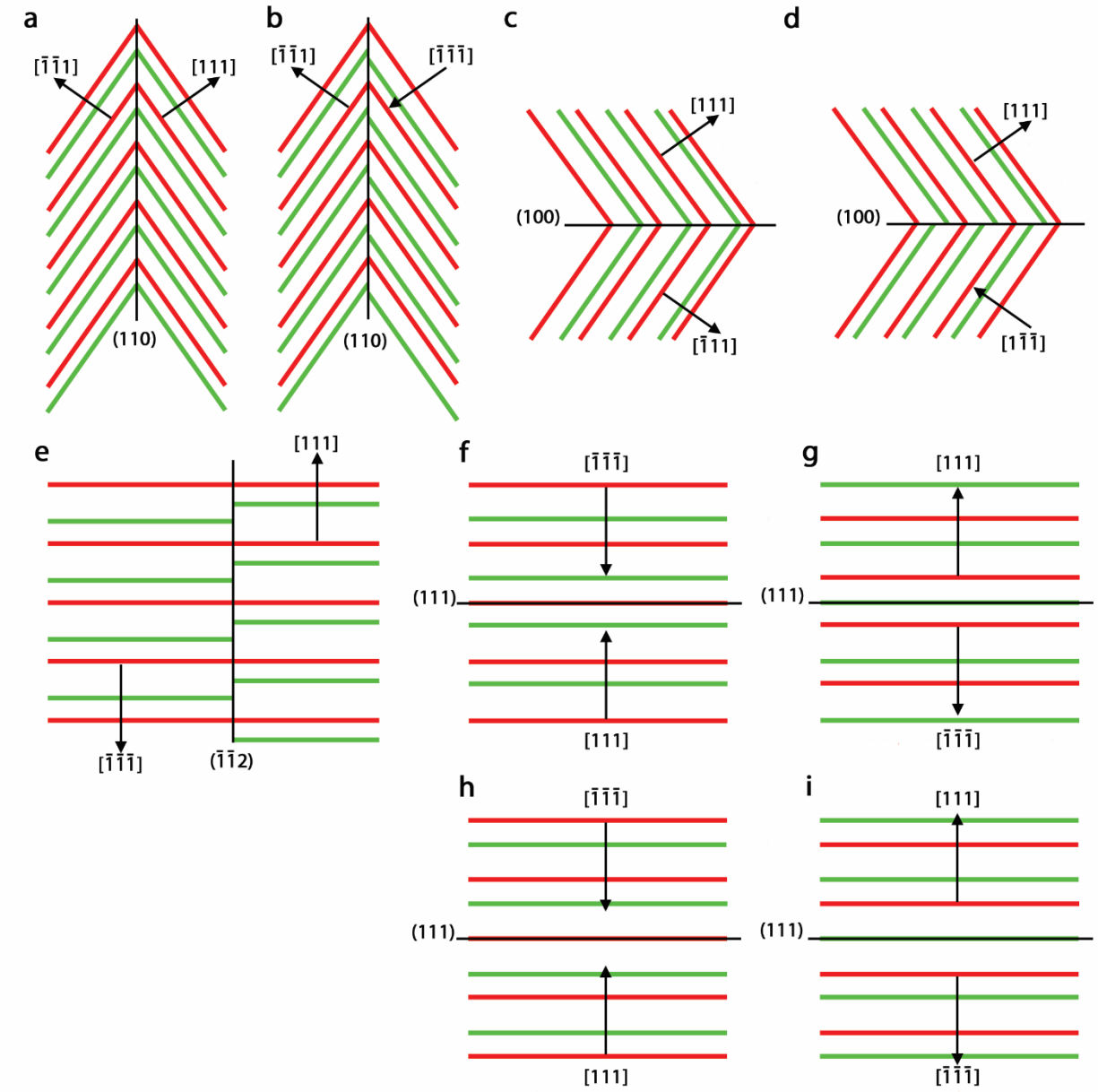

Figure 5.2 Domain structures: (a)-(d) represent different twin boundaries subdivided in $(110)_C$ (a) and $(100)_C$ (c) reflection twins and $(110)_C$ (b) and $(100)_C$ (d) rotation twins. The angle between the polarization vectors of the $(100)_C$ domains is 109° and of the $(110)_C$ domains 71°. (e)-(i) represent inversion boundaries subdivided in rotation twins (e) and (f)-(j) reflection twins. The angle between the polarization vectors in the inversion domain boundaries is 180°. Ge rows are displayed in red and Te rows in green. Figure adapted from Snykers *et al.*[288].

These different domain types can be visualized using microscopy[288]. Generally, α-GeTe materials studied before in literature reveal a domain structure of the herringbone type[284,286,287]. A herringbone structure is similar to a fish skeleton built from rows of slanted

parallel lines with a row by row alternating direction of the slant[286]. Vermeulen *et al.*[287] and Lee *et al.*[286] examined this herringbone structure in depth, but described it differently. Vermeulen *et al.*[287] used a mixed system of $\{100\}_C$ and $\{110\}_C$ twin boundaries, while Lee *et al.*[286] suggested a combination of inversion domains boundaries and twin boundaries. However, BF and DF TEM images should be taken to study inversion domain boundaries[288], which was not done in the case of Lee *et al.*[286]. Furthermore, the size of the inversion boundaries observed on the HR TEM images is smaller than the domains seen on the low magnification TEM image, which leads to more questions. But Snykers *et al.*[288] did observe inversion domain boundaries under the right conditions, next to twin boundaries, proving their existing in GeTe. Wu *et al.*[190] studied the domain structure for $(GeTe)_{0.975}(Bi_2Te_3)_{0.025}$ in detail. The material had an α-GeTe structure with 71° and 109° domain walls. After cyclic heat treatment, the existing vacancy clusters evolved in van der Waals gaps and 180° domain walls. Also, the appearance of domain structures like the size and form (well-defined/irregular) of the domain boundaries depends on the quantity of Ge vacancies, post-annealing temperature and thermal cycling[284]. This gives a hint how to control domain arrangement in the sample.

Future GeTe-based spintronic devices require knowledge about the type and atomic structure of the domain structure. We observed the defect structure of the studied α-GeTe at the atomic level, which was done for the first time. Atomic structural knowledge of the domain boundaries is important, because it can influence the domain wall movement. Only 180° domain walls existed in the material instead of the general herringbone structure in literature. 180° domain walls tend to be more mobile than other type of domain walls, because they react only to an electrical field and not a stress field[300]. On top of this, due to only the existence of 180° domain walls and the absence of 71° or 109° domain walls, interaction between different types of domains is absent leading to simpler domain movement[304] which can aid understanding this domain movement and application.

5.1.2 Results

For the studied crystals, solely inversion domain boundaries perpendicular to $[001]_H$ ($[111]_R$) are revealed. It is clearly seen from the zeroth order BF and DF TEM images of zone $[1\bar{1}0]_H$ ($[2\text{-}1\text{-}1]_R$) of the same area presented in Figure 5.3a-b. In detail, in bright field mode, successive domains with inversion domain boundaries have the same background contrast independent of the diffraction conditions; while in dark field mode, the domains have an opposite contrast (dark-bright) under multiple beam condition and the specific selection of the active reflections (more details are provided in the paper of Snykers *et al.*[288]). In both bright- and dark field modes we clearly observe an alternation of wavy and sharp (stepwise) interfaces perpendicular to $[001]_H$ ($[111]_R$), which we identify as the AA and BB interfaces respectively. Both AA and BB are inversion domain boundaries, which appear due to the loss of the inversion symmetry upon the phase transition. The median distance between two BB domain boundaries is 12.3 nm with an average of 13.6(7) nm. A structure containing only inversion domain boundaries is different from the literature, where if they observe inversion domain boundaries, they also observe twin boundaries[284,286–288]

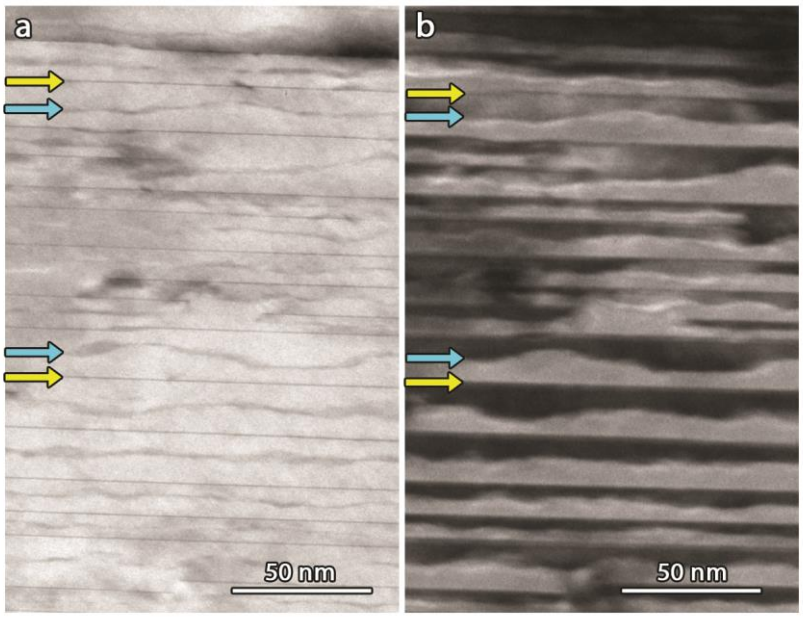

Figure 5.3 (a) Zeroth order BF TEM image and (b) corresponding DF TEM image, while selecting the 003 and 006 reflections, of zone $[1\bar{1}0]_H$ where a couple of type BB (AA) domain boundaries are marked with yellow (blue) arrows.

Further investigation of the domain boundaries with HR-STEM confirms the existence of two different types of inversion boundaries and uncovers that the atomic structure of both type of interfaces is different from what we anticipated from common structural consideration above. In more detail, Figure 5.4a and Figure 5.5a,b evidence that the flat BB boundaries are atomically flat while the stepwise AA interfaces go through different layers. The latter are similar to twinning dislocations, a term commonly used for deformation twins when applying an external force[305]. However, in our case the phase transition from the high symmetric cubic structure to this rhombohedral structure induces local strain, *i.e.* a change in the Te-Te distance. Irregularities in the periodicity of the crystal lattice, here planar defects perpendicular to the c_H axis, cause streaks along the c_H* axis in the corresponding diffraction pattern exhibited in Figure 5.5e.

Figure 5.4b shows the strain map calculated from the projected interatomic distances in the HR-STEM image using StatSTEM[306]. First, the program locates all the projected Te atomic columns inside the STEM image using a peak finder routine, which looks for local maxima in the image. Manual changes can be made *i.e.* adding or removing wrongly assigned columns. Next, every column will be fitted with a Gaussian peak with the same width to obtain the coordinates of the projected atomic Te columns. These coordinates will be used in the further column coordinate based analysis of the data and to calculate the strain map. First, we give the program the column positions and cell parameters of the projected unit cell. With this information, the program can find the lattice direction and index the columns in reference to the distance in unit cells from a chosen reference Te site, which in our case is manually chosen and away from the defects. The lattice direction is found automatically by calculating the distance between the reference Te column and the neighbouring columns

and by comparing these values with the given projected cell parameters. Also the given lattice parameters are optimized by the program using an area containing NxN unit cells where N is manually chosen. Then, for every Te column the vector difference between the expected coordinates using the projected cell and the experimental coordinates are calculated. Finally, the first derivative of this vector with respect to the projected distance between the Te columns is taken to generate the strain map, where positive values indicate an increase in the projected Te-Te distance and negative ones a decrease. The relative shift of the Ge and the Te sublattices along the $[001]_H$ ($[111]_R$) direction[288] occurs in opposite senses in neighbouring domains, explaining the observed expansion (AA interfaces) and compression (BB interfaces) at the interface in Figure 5.4b.

For the AA interface, an expansion of the projected Te-Te distance is found (Figure 5.4b) and either a centred Ge signal or two Ge sites between the Te layers are visible in the HAADF STEM images (Figure 5.4a and Figure 5.5a). However, only one of two potential Ge positions in every unit cell at the AA interface can be occupied due to geometric restrictions. On top of this, at the AA interface two Gaussian peaks could be fitted between the Te layers to a line profile shown in Figure 5.5d from the HAADF STEM image of zone $[100]_H$ in Figure 5.5a. This indicates two separate Ge positions. Both peaks also have a lower peak intensity compared to the Ge peaks further away from the AA interface. The latter combined with the geometric restrictions suggest that parallel to $(001)_H$ a gradual occupancy transition occurs between the two Te rows, possibly accompanied with small deviations on the Ge position. This domain interface is similar to the model based on common structural consideration in Figure 5.2h, however the coordinates of the atoms at the domain interface are different. We observed that there exists a gradual occupancy transition between the two Ge sites between the Te-Te layers, while the model indicates that Ge is centred between the Te-Te layers at the interface. Lee *et al*.[286] also observed an expansion strain at a similar domain boundary, but suggested a centred Ge atom. In their case, however, the domain boundary is 5 nm thick, while the size of our domain boundaries is at the atomic scale. The stepwise AA domain boundary contains negatively charged and uncharged sections (Figure 5.5c), indicating a weakly charged domain wall, possibly aiding the stability of the domain wall. Weak charged domain walls might exist without charge screening[307].

For the BB interface, a uniform compressive strain around the BB boundary is found (Figure 5.4b). This stress can be released by pushing Ge atoms out or, in other words, by the accumulation of cation vacancies, which leads to two consecutive $(001)_H$Te planes. Such vacancies are available and always present in GeTe since its equilibrium homogeneity range is completely shifted to Te-rich side, so the vacancy concentration can be ~1 at.% giving vacancy concentrations of ~10^{19}-10^{20} cm^{-3} [301,302]. More Ge vacancies exist under Te-rich conditions than in Ge- rich conditions[301,302]. The studied samples are Te-enriched and, therefore, the bulk density of vacancies is higher than the value needed to form BB interfaces with a mean spacing of 10-15 nm. Sist *et al.*[308] already speculated the possibility of vacancy accumulation at domain boundaries in GeTe and He *et al.*[309] already showed this for tetragonal $PbTiO_3$ using first-principles density functional calculations where oxygen vacancies tended to migrate to 180° domain walls. The BB interface is similar to the VdW gap

in layered Bi_2Te_3 and a defect type in $Ge_mBi_{2n}Te_{m+3n}$, which is discussed in more details in the section 3.3. Also the released stress by pushing the Ge atoms out of this boundary explains why only in rare cases we saw the existence of Ge atoms at the interface (Figure 5.5f). This domain interface is similar to the model based on common structural consideration in Figure 5.2f, however in our case Ge vacancies are present at the interface, while in the model no Ge vacancies are taken into account. The BB domain boundary is also strongly positively charged (Figure 5.5c) and thus can attract the negative Ge vacancies. Screening of the bound charge around a charged domain wall by electrons, holes and/or mobile ions is necessary for the stability of a charged domain wall[307]. The structure of the BB domain boundaries implies their lower mobility and, hence, longer time of switching, than those for Snyker's model and the previous AA domain boundaries, since this includes atomic motion from one layer to another. Lee *et al.*[286] also observed a compression strain at a similar domain boundary, but do not mention vacancies at these interfaces. Our final model showing both AA and BB boundaries is displayed in Figure 5.6.

Both AA and BB domain walls are partly or completely charged. Charged domain walls can contain high two dimensional conductivity along the wall, which can be used in 'domain wall nanoelectronics' like ferroelectric domain wall memory devices[307]. For the latter, the existence or absence of conductive domain walls determine the binary state of the memory device. Sharma *et al.*[310] made and examined a prototype and found promising results such as its non-destructivity for voltages below 3V and relative high OFF-ON ratios with excellent endurance and retention characteristics.

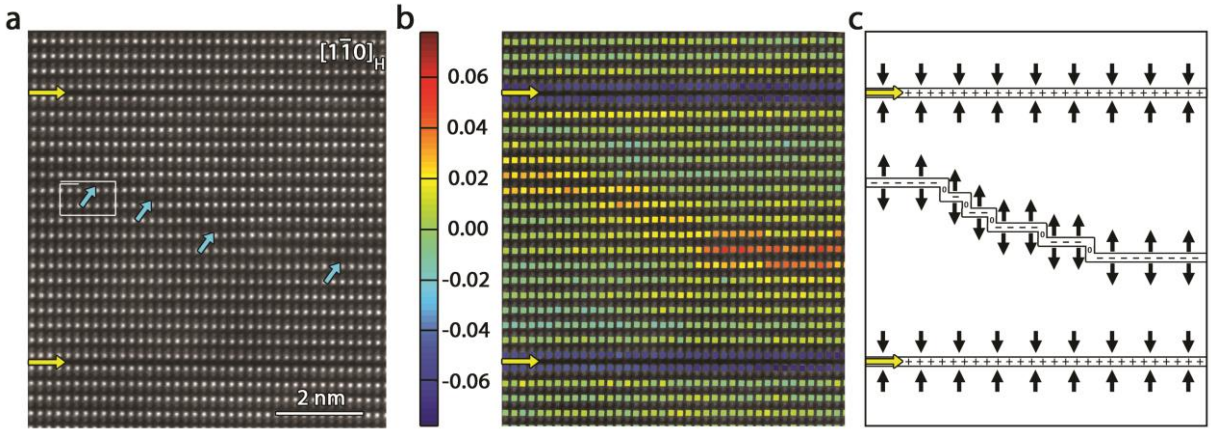

Figure 5.4 (a) Averaged HAADF STEM image of zone $[1\bar{1}0]_H$ using a short frame time (2.52s) to limit distortions, showing a sharp BB interface in a single layer (yellow arrows) and a stepwise AA interface (blue arrows) with a marked Burgers vector. (b) Strain map of the HAADF STEM image in (a) calculated with StatSTEM[306] using the projected Te-Te interlayer distance onto the c_H direction. Positive values indicate an increase in the projected interlayer Te-Te distance, while negative a decrease. c) Visualization of the positive charged BB domain wall and the negative AA domain wall containing neutral vertical parts. The polarization vectors (dipole moment per unit volume) are displaced with black arrows.

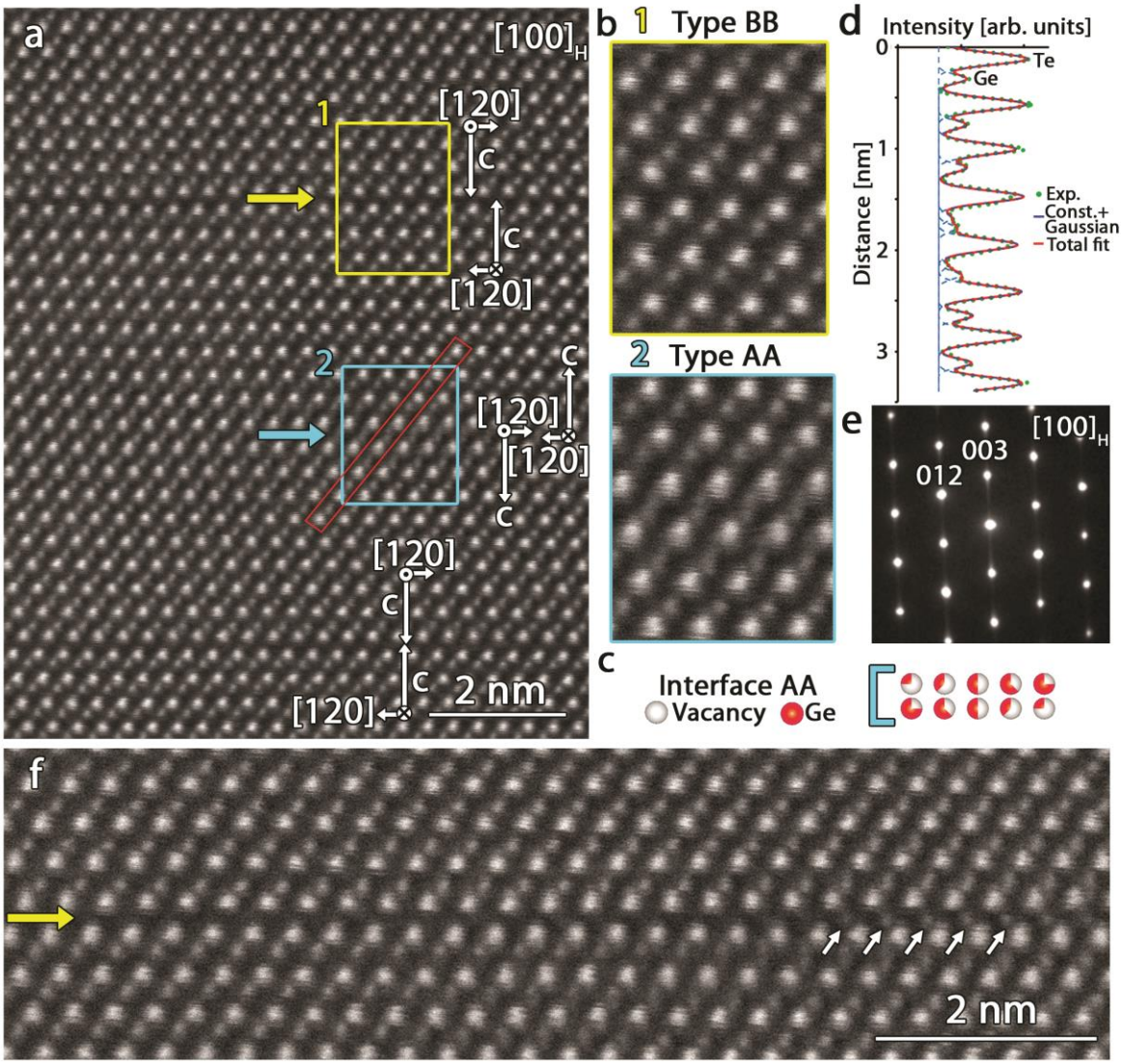

Figure 5.5 (a) HAADF STEM image of zone $[100]_H$ with type BB (yellow) and type AA (blue) interfaces, where (e) shows a diffraction pattern of the corresponding zone with slight streaks along the c_H^* axis. (b) Enlargement of the two areas in (a). (c) Parallel to $(001)_H$, a gradual occupancy transition occurs at the AA interface between the two Ge rows. (d) Line profile of the red area in (a), fitted with Fityk[195], showing the experimental data (green dots), the total fitted curve (red line) and the separate Gaussian fits with a constant background (blue striped line): At the AA interface, the two separate Ge positions between the Te layers have clearly a lower intensity. (f) Interstitial Ge atoms inside the BB interface, where some examples are marked with white arrows.

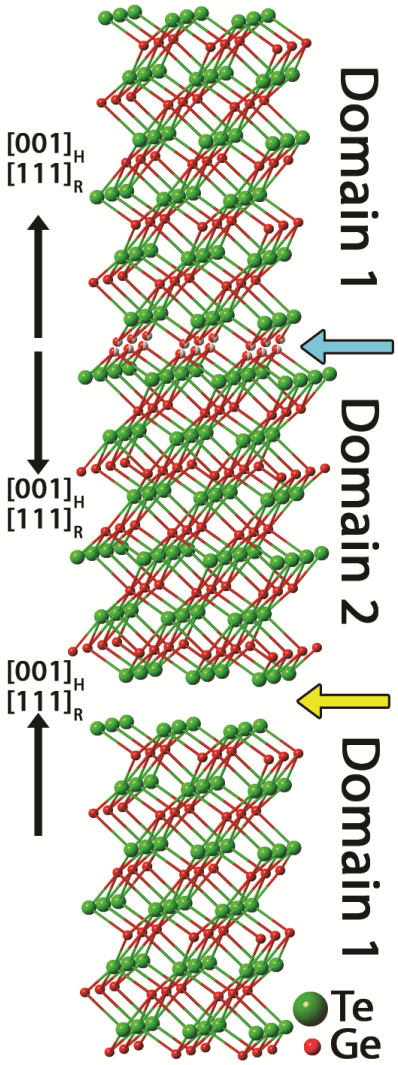

Figure 5.6 Our proposed model for the domain structure showing both AA and BB type domain structures. Red spheres represent Ge and green Te.

Wu *et al.*[190] observed a similar domain wall construction for heat treated $(GeTe)_{0.975}(Bi_2Te_3)_{0.025}$. However, it was in that case accompanied with 71° and 109° domain wall formation. Furthermore, they[190] observed light contrast features in their HAADF STEM images and suggested that at these positions a charged nano-domain wall existed. These positions correlate to what we call the type AA domain boundary, but we do not observe contrast differences in our HAADF STEM images around our AA domain boundary. Possibly, these lighter features could be due to Bi excess around the domain boundaries similar to our observations in 3.3.2.2 for the rock salt $Ge_mBi_{2n}Te_{m+3n}$ structure.

Note that the data is described equally well by 180° rotation twins with twin boundaries perpendicular to the c_H-axis and with rotation axis a_H (a symmetry element lost by the phase transition) instead of inversion twins. The hexagonal structure contains a mirror plane perpendicular to the a_H axis, so that a 180° rotation twin along a_H cannot be distinguished from an inversion twin[311].

5.1.3 Conclusion

In order to use GeTe in spintronic devices, atomic information about the type and the structure of the domain walls in GeTe is necessary since it can influence domain wall movement. We revealed for the first time the atomic interfaces of the so called inversion domain boundaries or 180° domain walls of GeTe using transmission electron microscopy. GeTe contains the α-GeTe structure with two atomically different domain walls perpendicular to the c_H-axis. Atomically flat BB boundaries, where one complete Ge plane is removed creating a van der Waals bond between the Te layers and stepwise AA interfaces going through different layers with different Ge positions between the two Te layers. In contrast to the herringbone structure in literature, only 180° domain walls exist in this material leading to simpler domain movement due to the lack of interaction between different domain types which can aid understand the domain wall movement and applications. Also 180° domain walls react only to electric fields and not to stress fields, making them inclined to be more mobile in comparison to other types of domain walls. From the atomic domain wall structure we suspect that the AA domain wall will be more mobile thus with lower switching times than the BB domain walls. Furthermore, both AA and BB domain boundaries are completely or partly charged domain walls interesting for 'domain wall nanoelectronics'.

5.2 Fe_2Ge_3

This section is based on the paper: Verchenko Valeriy Yu., Wei Zheng, Tsirlin Alexander A., Callaert Carolien, Jesche Anton, Hadermann Joke, Dikarev Evgeny V., Shevelkov Andrei V., *Crystal growth of the Nowotny chimney ladder phase : exploring new Fe-based narrow-gap semiconductor with promising thermoelectric performance*, Chemistry of materials 29(2017), p.9954-9963 [17].

I prepared the TEM sample by crushing the sample, dissolving it in ethanol and placing it on a Cu grid. Afterwards, I performed the TEM study including SAED diffraction, STEM imaging and STEM simulation and the analysis of the resulting data thereof.

5.2.1 Introduction

Fe_2Ge_3, a combination of a transition metal (Fe) and a metalloid (Ge), belongs to the class of intermetallic compounds or intermetallics. Intermetallics are a mixture of at least two metallic elements where the structure of the mixture differs from the separate constituents[312]. Intermetallics have many attractive physical and mechanical properties such as high melting points, low density, high strength and ductility at elevated temperatures. However, they suffer from brittleness, inadequate ductility and strength at low temperature[313]. More specific, the studied Fe_2Ge_3 structure belongs to the Nowotny chimney ladder phases (NCLs), a subdivision of intermetallics. They have the general formula T_tE_m and unique structural flexibility. The transition metal T is generally a group IVb-VIII element and the E element a main group IIIa-Va element[31,32].

The Nowotny chimney ladder phase is built using two sublattices that are intertwined with each other. You have the squared T sublattice which forms 4-fold helical channels arranged in a flattened diamond network of the β-Sn-type structure (Figure 5.7). The E atoms form helices inside the T helical channels. So we get helix-within-a-helix motif.

The stoichiometry of the material determines the relative spacing and the helicity of the E atoms, giving rise to complex structures and even incommensurately modulated structures when the period of the E helix is a non-integer amount of the period of the T helix[30,314–317]. When the T element belongs to the element group VIIb or higher (Fe belong to group VIII), then the stoichiometry will depend on the fact that every T atom wants 14 valence electrons[30], the '14-electron rule'. So, for Fe_2Ge_3 this means that every Fe contributes 8 valence electrons and every Ge 4 valence electrons leading to 14 electrons per Fe atoms ((2*8+3*4)/2=14). This special electronic condition leads in most cases to an electronic band gap with the Fermi level located inside this band gap, thus creating narrow band gap semiconductors[318–324]. An empirical rule for these NCL is that a pseudoperiodicity is present, related to the stoichiometry by $(2t - m)\boldsymbol{c}_{pseudo} = \boldsymbol{c}$.[319]

The thermoelectric properties of these materials are being studied for their semiconductor property combined with possible low lattice thermal conductivity caused by their structural complexity while maintaining the electrical conductivity [325–328]. Ru_2Sn_3 was even found to be a topological insulator[33]. The T atoms in the β-Sn-type structure (Figure 5.7) have four neighbouring T atoms forming flattened tetrahedrons. The T atoms in T_tE_m achieve a closed shell 18 electron configuration by covalently sharing electrons with the four neighbouring T atoms[329]. Due to this covalent sharing, the ideal 18 electrons require only 14 electrons (=18-n, where n is the amount of T-T bondings)[329], in agreement with the general 18-n role of intermetallics[330]. The E atoms bond to the T atoms and stabilize this T-T bonding, leading to homogenous E distribution inside the T channels[329]. Chemical pressure due to the short T-E distance perpendicular to the channels and large spaces along the channels leads to the formation of helixes of E atoms inside the T channels[331].

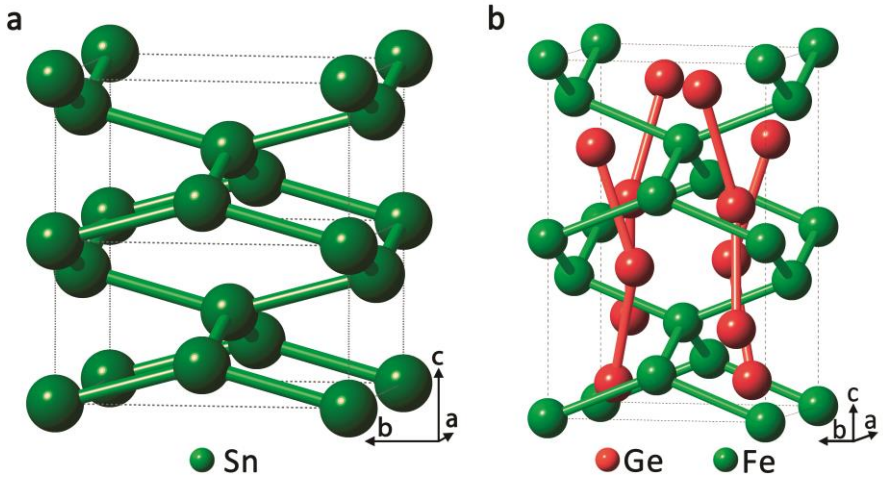

Figure 5.7 (a) β-Sn structure[332] with a=5.8326 Å, c=3.1821 Å and space group $I4_1/amd$, where the same bindings were formed as for the Fe_2Ge_3 structure (b) for easy comparison.

The new phase discovered recently in the Fe-Ge system by Gerasimov *et al.*[333] has a Ru_2Sn_3 type structure, which is a Nowotny chimney ladder structure, and a suggested 2:3 Fe:Ge ratio. However, they did not perform a Rietveld refinement or proper indexing of the polycrystalline two-phase sample[333]. Li *et al.*[316] studied this new phase in more details using X-ray diffraction, SAED and HR TEM and found an incommensurately modulated structure for $FeGe_{1.52}$. However, no space group was determined. Sato *et al.*[334] predicted using first-principle calculations that Fe_2Ge_3 with the Ru_2Sn_3 structure has glass-like low lattice thermal conductivity κ_{lat} and a large power factor ($S^2\sigma$), leading to a thermoelectric figure-of-merit ZT ($ZT = S^2\sigma T/(\kappa_{lat} + \kappa_{ele})$) of 0.57[334].

The sample that we studied in this section is made using a synthetic approach based on chemical transport reactions to overcome the kinetic passivity of Fe and Ge at low temperatures, leading to high-quality polycrystalline samples of the Nowotny chimney ladder phase Fe_2Ge_3. We determined the space group and cell parameters of two coexisting structures, one commensurately and one incommensurately modulated structure, from SAED which was not done up until now. The coexistence of these two structures was not reported before in literature. Using HAADF STEM, we observed the structure's similarities with the tetragonal model deduced by Verchenko *et al.*[17] from SCXRD. On top of this, we found additional defects through HAADF STEM.

5.2.2 Results

The PXRD pattern of $FeGe_\gamma$ for γ = 1.5 taken by the group of Andrei Shevelkov[17] could not be indexed neither in the primitive tetragonal lattice that was expected for the Ru_2Sn_3-type of crystal structure[335] nor in the orthorhombic system expected for the Ru_2Ge_3-type chimney ladder phase[336]. Moreover, the observed reflections were shifted from the positions calculated for the idealized structure in a complex manner implying possible incommensurability, necessitating a TEM investigation of the polycrystalline samples of $FeGe_\gamma$.

According to the TEM results, an orthorhombic commensurate structure with cell parameters approximately a ≈ 5.45 Å, b ≈ 5.6 Å, and c ≈ 8.95 Å is present in the sample. Representative selected area electron diffraction (SAED) patterns of this phase along the main zone axes are shown in Figure 5.8. Tilt series collected from different crystals allow to derive the reflection conditions 0*kl*: $l = 2n$; *h*0*l*: $l = 2n$; 00*l*: $l = 2n$; and *hkl*, *hk*0, *h*00, and 0*k*0: no conditions, which indicates extinction symbol *Pcc*- and allows two orthorhombic space groups, *Pcc*2 and *Pccm*. From SAED patterns alone, differentiation between these groups is not possible. Furthermore, for application of converged beam electron diffraction (CBED) point group determination one has to be sure of having single phase crystallites, which is not the case in this situation.

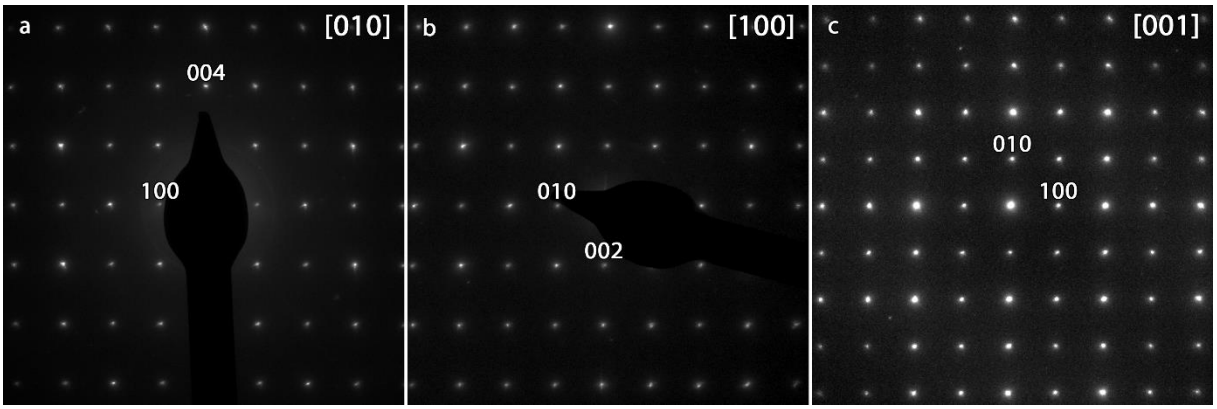

Figure 5.8 SAED patterns taken along [010], [100], and [001] directions for the commensurate orthorhombic phase.

Further investigations show that the phase with the incommensurate structure is also present in the sample. The SAED patterns taken along the [1$\bar{1}$0] and [100] directions (Figure 5.9a and c) can be indexed with cell parameters approximately $a \approx 5.6$ Å, $c \approx 4.6$ Å, and $q = 0.49(3)\,c^*$. With this q-vector, the [001] SAED patterns are indistinguishable from those of the commensurate phase (Figure 5.8c), because of the absence of nonzero components along a^* and b^*. However, also slightly different q-vectors were found, as shown in Figure 5.9b and the bottom inset in Figure 5.9c, where the components along a^* and b^* differ from zero. The split reflections in Figure 5.9b close to the hk00: h≠2n, k≠2n do not lie in the (001) plane, but slightly above and below and are satellites of reflections in the hk-1, hk1, hk-2 and hk2 reciprocal planes. Due to the fact that the crystal is not infinite, the reflections in reciprocal space have the form of rods instead of points and these rods can still cut the Ewald sphere (and thus be visible on the electron diffraction patterns) even if the reflection itself is slightly out of the hk0 plane. The patterns in Figure 5.9a and b with $q = 0.49(3)\,c^*$ are similar to those in the article of Li *et al.*[316], and are in agreement with the reflection conditions of the superspace group $I4_1/amd(00\gamma)00ss$ proposed in literature for incommensurately modulated NCLs[35], *i.e.* $hklm$: $h + k + l = 2n$, $0klm$: $m = 2n$, $00lm$: $l + 2m = 4n$, $hhlm$: $2h + l = 4n$, and $hk00$: $h = 2n$.

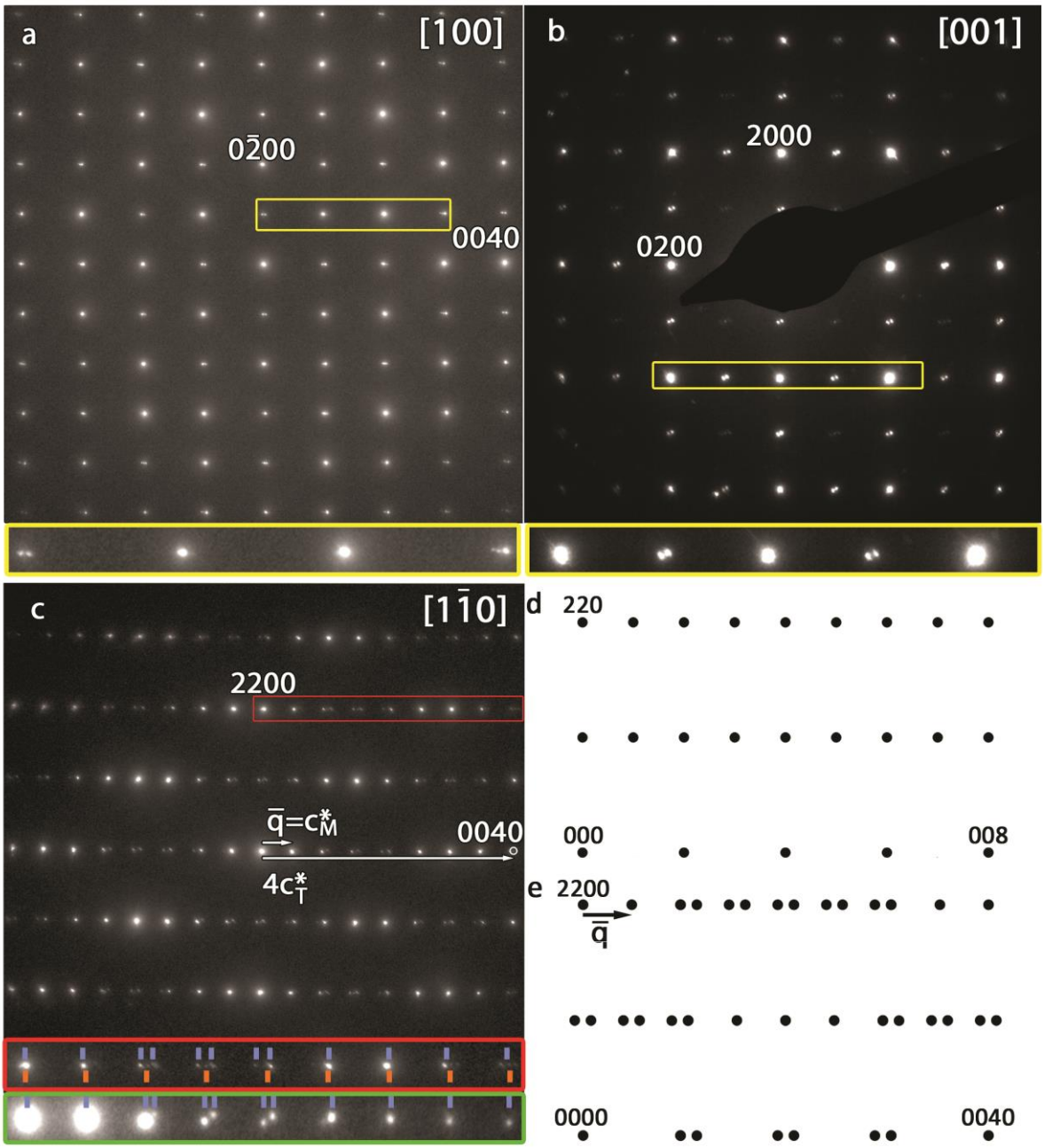

Figure 5.9 (a)-(c) Representative SAED patterns of $FeGe_\gamma$ along the [100], [001] [$1\bar{1}0$] directions for the incommensurately modulated phase. The insets show enlargements of the parts indicated on the figures, except the inset indicated by a green border, which is an enlargement of an SAED pattern from another crystal for comparison. In the two insets of Figure 5.9c the reflections of the incommensurate structure is indicated by blue markers and the commensurate with orange ones. Schematic representation of the diffraction patterns of zone [$1\bar{1}0$] for (d) the commensurate structure and (e) the incommensurate structure.

The commensurate and incommensurate phases are present as domains next to each other. This can be seen from the occurrence (see the top inset of Figure 5.9c) of reflections at the centre of some pairs of satellites, which originate from domains of the commensurate phase (for a schematic representation, see Figure 5.9d-e). Furthermore, the domains of the commensurate and incommensurate structure are too small to observe separately with

selected area electron diffraction microscopy using the smallest selected area (≈200 nm) and carried out on the thinnest areas of the crystal to minimize coexistence of both phases.

In the earlier mentioned domains, where the *q*-vector has nonzero a^* and b^* components, the tetragonal symmetry is necessarily broken[315,317,337–339]. The tetragonal model of the Fe_2Ge_3 single crystal structure from Verchenko *et al.*[17] (Figure 5.10c,d) was used for generating the calculated STEM image with MULTEM[83] shown as an inset in Figure 5.10b. It shows a good agreement for the basic feature seen in the STEM image. However, small deviations for the atomic positions are present, which can be explained using the incommensurate model elaborated by Ye *et al.*[315] for the NCL compound $MnSi_{2-x}$. According to Ye *et al.* [315], the "orientation anomaly" is caused by systematic shifting of the helical arrangement of the metalloid atoms along the "chimney" in the transition metal sublattice. This effect can effectively be observed in the HAADF STEM image in Figure 5.10a indicated by the white lines. The local variations in the *q*-vector are most likely due to local differences in chemical composition. [30,316] Using the formula proposed by Li *et al.*[316], $Ge/Fe = 2 - c^*_{Ge}/c^*_{Fe}$, results in a composition $FeGe_{1.51(3)}$ for q = 0.49(3) c^*. Such deviations from the stoichiometric composition with γ = 1.5 are unfortunately too small to confirm with EDX analysis, as they are beyond the precision of EDX on a TEM instrument. In summary, two main phases appear in the polycrystalline sample of $FeGe_\gamma$ ($\gamma \approx 1.5$): (i) an orthorhombic commensurate structure with cell parameters $a \approx 5.45$ Å, $b \approx 5.6$ Å, and $c \approx 8.95$ Å and space group *Pcc*2 or *Pccm*; and (ii) an incommensurate phase that can be indexed with the superspace group used in literature for NCLs[314,337], *i.e.* $I4_1/amd(00\gamma)00ss$, and with approximate cell parameters $a \approx 5.6$ Å, $c \approx 4.6$ Å, and variable q, most frequently q = 0.49(3) c^*. The patterns agree with the patterns characteristic of NCLs, however, the simultaneous presence of a commensurate and several slightly different incommensurate phases, and minor amounts of admixtures hindered fitting of the PXRD pattern of $FeGe_\gamma$ for γ = 1.5.

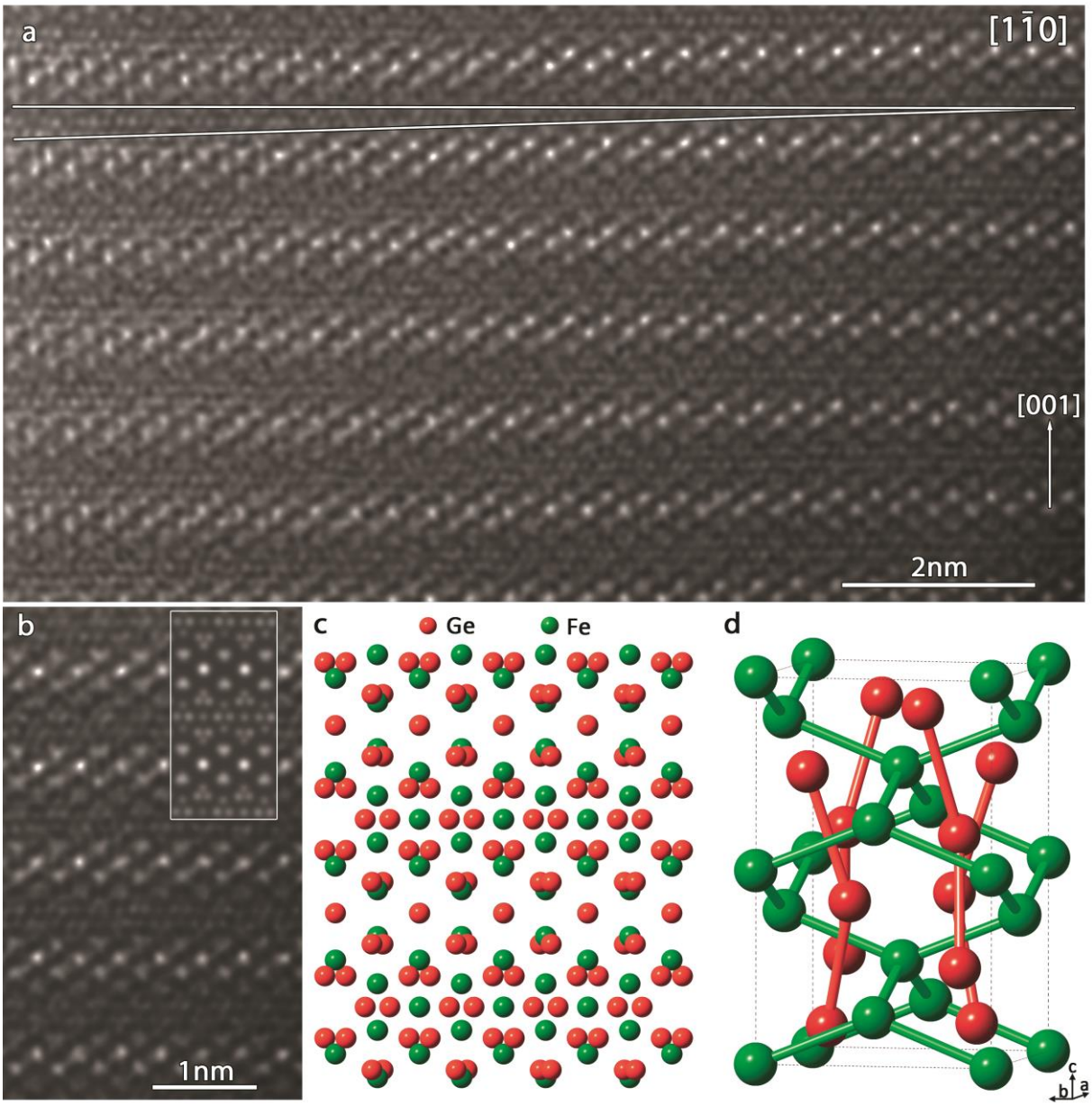

Figure 5.10 (a) HAADF STEM image of a typical $FeGe_\gamma$ crystal. The white lines indicate the shift of the Ge helices in successive Fe chimneys. (b) Enlarged view of (a), including an STEM image simulation calculated using MULTEM[83] using the Fe_2Ge_3 single crystal structure from Verchenko *et al.*[17]. Slight differences are visible due to the incommensurate character of $FeGe_\gamma$. (c) shows the projection of the model from Verchenko *et al.*[17] along the [1$\bar{1}$0] directions, while (d) represents the structure in 3D.

Verchenko *et al.*[17] performed transport and thermoelectric properties measurements on these polycrystalline samples, more specific temperature-dependent resistivity, Seebeck coefficient and thermal conductivity measurements. They found that $FeGe_\gamma$ ($\gamma \approx 1.5$) is a ~30 meV narrow bandgap semiconductor and exhibits high absolute values of the Seebeck coefficient at elevated temperatures. Furthermore, low glass-like thermal conductivity exists in a wide temperature range which might be a consequence of the complex microstructure. These characteristics are good for thermoelectric materials.

5.2.3 Conclusion

We determined the space group of the polycrystalline $FeGe_\gamma$ ($\gamma \approx 1.5$) using transmission electron microscopy which was impossible using the standard PXRD technique. The polycrystalline $FeGe_\gamma$ sample possesses both commensurately and incommensurately modulated chimney ladder structures. We are the first to observe this coexistence of these two structures. The commensurate structure has cell parameters $a \approx 5.45$ Å, $b \approx 5.6$ Å, and $c \approx 8.95$ Å and space group Pcc2 or Pccm. The incommensurate structure has cell parameters $a \approx 5.6$ Å, $c \approx 4.6$ Å, and $q = 0.49(3)\, c^*$ and space group $I4_1/amd(00\gamma)00ss$. Furthermore, an orientation anomaly, not previously mentioned for $FeGe_\gamma$, is observed caused by the systematic shifting of the helical arrangement of the Ge atoms along the Fe helix structure. Also good thermoelectric characteristics are found for this material, such as semiconductivity with a ~30 meV narrow bandgap, high absolute values of the Seebeck coefficient at elevated temperatures and low glass-like thermal conductivity in a wide temperature range. The latter can be caused by the observed complex microstructure.

Chapter 6 General Conclusions

Adding defects (point-, line-, planar- and 3D defects), modulating the structure or interfacing the material with another material is a common practice to obtain the desired properties for applications. In this thesis, I studied different kinds of adaptations of topological insulators and structurally related materials, that were all also examined in literature for their thermoelectric properties. The focus of this work was on the determination of the atomic structure of the materials, because this in the end will affect the properties of the material. More research needs to be done in order to connect the structure to the properties; however this was outside the scope of this thesis. I started with the first step, understanding the structure.

I applied different transmission electron microscopy (TEM) techniques to characterize the structure and supported some findings with first-principles calculations using the VASP code and compared them with powder X-ray diffraction (PXRD), a standard technique. The different applied TEM techniques include high-angle annular dark-field scanning transmission electron microscopy (HAADF STEM) to define the structure; atomic resolution energy dispersive X-ray (EDX) spectroscopy to determine the structural chemical character at an atomic level; selected area electron diffraction (SAED) to deduce the space group; electron diffraction tomography (EDT) to quantify the amount of a certain defect type and finally bright-field and dark-field transmission electron microscopy (BF and DF TEM) imaging to characterize domain structures on the nanoscale. Utilizing all these techniques allowed me to obtain local structural information.

The thesis can be divided into three parts: (I) the study of the bulk structure of topological insulators, (II) the interface of a topological insulator with a gas or another material and (III) two materials structurally related to topological insulators.

In the first part, I studied the bulk structure of (i) an undoped topological insulator, (ii) doped topological insulators and (iii) modulated structures of a topological insulator. For applications where the conducting surface states are important, the focus lies on obtaining a material where the Dirac cone and the Fermi level are located in the bulk band gap. For thermoelectric applications, defects and higher conductivity can help to increase the figure-of-merit (ZT). Both types of applications require their own modification.

The undoped material was Bi_2Se_3, consisting of a quintuple-layered structure (Se-Bi-Se-Bi-Se) with van der Waals interaction in between the quintuple layers. I observed interstitial defects in an octahedral coordination in the van der Waals gap, with mainly a Bi character. I proposed that this defect makes the material more n-doped, unfavourable for spintronic applications but favourable for thermoelectric applications. Furthermore, atomic mobility along and across the van der Waals gap was observed, which is negative for Li or Na battery applications but also a sign that the material can withstand a certain amount of stimuli, in my case the electron beam, without completely deforming its structure.

Next, I studied two types of doped topological materials: $(Bi_{1-x}In_x)_2Se_3$ and $Sb_2(Se_xTe_{1-x})_3$. Both are a mixture of a topological insulator and a normal insulator. For $(Bi_{1-x}In_x)_2Se_3$, In occupies the Bi sites and an interstitial site in the van der Waals gap. I suggested that the latter makes the material n-doped. Also atomic mobility is observed in this material similar to Bi_2Se_3. The same conclusions as for Bi_2Se_3 are valid for this material. For $Sb_2(Se_xTe_{1-x})_3$, I found that the crystal contained voids where part of a quintuple layer was removed, which is interesting since this sort of defects can drastically increase the thermoelectric properties. Furthermore, Se will occupy in small quantities the outer Te layers, before the middle layer is completely filled. This small quantity of Se defects in the outer Te layers (Te1) can probably influence the concentration of the commonly accepted Sb_{Te1} antisite defects more than the Se atoms in the middle Te layers. In this way, the Fermi level can be indirectly modified, which influences the properties. This is in contradiction to literature where no distinction was made between the two different Se sites and their influence on the properties of the material.

I also investigated the $Ge_mBi_{2n}Te_{(m+3n)}$ series, where I observed that samples made with the transport growth method always resulted in a trigonal l-layered structure (l=7,9,11, 5-7), while the Bridgman method led to trigonal layered structures or rock salt structures with planar defects. I determined the layered composition and the amount of layers in a building block, which is the first step to determine the topological insulator character and their characteristics for later use in applications. Differences with the GeTe-Sb_2Te_3 system were found, like the higher structural stability due to the absence of atomic van der Waals gap reconfiguration, suggested to be relevant for phase change applications. The rock salt structure contained two types of planar defects along the $(11\bar{1})_C$ or $(1\bar{1}\bar{1})_C$ Ge planes. The first defect type is the absence of a complete $(11\bar{1})_C$ or $(1\bar{1}\bar{1})_C$ Ge plane with an excess of Bi on the Ge sites and a structural distortion around it to α-GeTe, described by a twin domain formation or van der Waals gap formation. This type only exists in Bi rich $Ge_mBi_{2n}Te_{(m+3n)}$ materials. Literature indicates its positive effect on the thermoelectric properties. The second defect type is the Ge vacancy rich $(11\bar{1})_C$ or $(1\bar{1}\bar{1})_C$ Ge planes, with excess of Bi around the defect. The specific effect of this defect type is unknown.

In the second part, I investigated the interface between a topological insulator with oxygen and an Fe layer. Oxidation characterization is necessary, because we are interested in the conducting surface states and under normal circumstances the samples are made, handled and operated under oxygen environment. Interfacing a topological material with a magnetic material, like Fe, is useful for spintronic applications. However, these conducting surface states we want to use are not robust under magnetic impurities. The atomic interface will also have an influence, which was the driving force for this research.

All materials (Bi_2Te_3, Sb_2Te_3, $(Sb_{0.55}Bi_{0.45})_2Te_3$ and $Ge_mBi_{2n}Te_{(m+3n)}$) had an amorphous oxide layer at the top which was intertwined with a distorted structure containing ordered Te layers with disordered layers in between. However, in the subsurface layer of $(Sb_{0.55}Bi_{0.45})_2Te_3$ and Bi_2Te_3 seven-layered defects occurred, while in the subsurface layer of the trigonal layered $Ge_mBi_{2n}Te_{(m+3n)}$ crystals a layered building block with a different layering

than the bulk structure was present. The first enables atomic mobility although the reason for their occurrence is unknown. The second could be a consequence of the chemical change at the subsurface due to the mobility of the most reactive element, Ge, towards the surface. Due to the similarities between the different materials, I proposed similar oxidation mechanisms. First, oxygen will react with the most reactive element of the material and thus break their bonding with the bulk. Next, the surface layer will become negatively charged due to the electrons that will tunnel from the Fermi level of the material towards the oxide, followed by the migration of the most reactive positive cation element towards the surface due to the created potential. The latter leads to the formation of an amorphous oxide layer and the distorted structure containing ordered Te layers with disordered layers in between. Afterwards, a more complex oxide $A_nB_mO_x$ will take shape due to the oxidation of other elements. However, Bi_2Te_3 underwent first a congruent oxidation of the first quintuple layer, forming $Bi_2(TeO_3)_3$, by oxidizing Te first via oxygen transport.

Onto Bi_2Te_3 a 20 nm Fe layer was deposited. This led to the formation of an Fe layer, followed by an amorphous FeTe layer, where the excess of Bi migrated towards the Bi_2Te_3 bulk creating seven-layered defects close to the FeTe interface. In literature, a thin FeTe film onto Bi_2Te_3 created interfacial superconductivity, interesting for Majorana fermions. The question remains if the same happens for our case.

In the third part of my thesis, I investigated the α-GeTe and $FeGe_\gamma$ (γ≈ 1.5) structures which are structurally related to topological insulators. Both are thermoelectric materials, without being a topological insulator.

α-GeTe contains the so-called inversion domain boundaries or 180° domain boundaries, which I atomically characterized. I found two atomically differently charged 180° domain walls perpendicular to the c_H-axis. For the atomically flat BB boundaries one complete Ge plane is removed creating a van der Waals binding between the Te layers. The stepwise AA interface goes through different layers with a variable Ge position between the two Te layers. For spintronic applications, the mobility of domain walls is important. I suggested that the AA domain wall will be more mobile leading to lower switching times than the BB domain walls. Furthermore, the existence of only 180° domain walls makes these crystals good study samples due to their simple domain movement. They are charged domain walls, interesting for 'domain wall nanoelectronics'.

I determined the space group and cell parameters of the two coexisting structures of the polycrystalline $FeGe_\gamma$, which was not possible using PXRD. The incommensurate structure had cell parameters a ≈ 5.6 Å, c ≈ 4.6 Å, and q = 0.49(3) c^* and space group $I4_1/amd(00\gamma)00ss$ and the commensurate structure had cell parameters a ≈ 5.45 Å, b ≈ 5.6 Å, and c ≈ 8.95 Å and space group Pcc2 or Pccm. Both are Nowotny chimney ladder structures, build using a Ge helix inside a four-fold Fe helix. The material also contained an orientation anomaly, not previously mentioned in literature for $FeGe_\gamma$, causing the helical arrangement of the Ge atoms to shift systematically along the Fe helix structure. The complex structure probably led to the low glass-like thermal conductivity in a wide temperature range, a good

thermoelectric characteristic. Other good thermoelectric properties were the ~30 meV narrow band gap and the high absolute values of the Seebeck coefficient at elevated temperatures.

Algemene conclusies

Het toevoegen van defecten (punt-, lijn-, vlakke- en 3D defecten), het moduleren van de structuur of het toevoegen van een toplaag bestaande uit een ander materiaal is een gebruikelijke praktijk om gewenste eigenschappen te verkrijgen voor toepassingen. In deze thesis werden verschillende soorten modificaties van topologische isolatoren en structureel gerelateerde materialen bestudeerd, die allen in de literatuur al onderzocht werden voor hun thermo-elektrische eigenschappen. De focus van dit werk lag op het determineren van de atomaire structuur van het materiaal, omdat deze uiteindelijk de eigenschappen van het materiaal zullen bepalen. Meer onderzoek is nodig om de structuur te verbinden aan zijn eigenschappen; dit ligt echter buiten het bereik van deze thesis. Ik begon met de eerste stap, namelijk de structuur begrijpen.

Ik heb verschillende transmissie elektronenmicroscopie (TEM) technieken toegepast om de structuur te karakteriseren, waarbij sommige bevindingen onderbouwd werden met *ab initio* berekeningen met behulp van de VASP code en vergeleken met poeder X-stralen diffractie, wat een standaard methode is. De verschillende toegepaste TEM technieken bevatten onder meer HAADF STEM om de structuur te definiëren, EDX spectroscopie om het structureel chemische karakter te bepalen op atomair niveau, SAED om de ruimtegroep af te leiden, EDT om de hoeveelheid van een bepaald type defect te kwantificeren en ten slotte BF en DF TEM om de domeinstructuren op nanoschaal te karakteriseren. Door gebruik te maken van al deze methoden was ik in staat om lokale structurele informatie te verkrijgen.

De thesis kan opgedeeld worden in drie delen: (I) de studie van de bulkstructuur van topologische isolatoren, (II) de interface tussen een topologische isolator met een gas of een ander materiaal en (III) twee materialen die structureel gerelateerd zijn met topologische isolatoren.

In het eerste deel, heb ik de bulk structuur bestudeerd van (i) een ongedopeerde topologische isolator, (ii) gedopeerde topologische isolatoren en (iii) gemoduleerde structuren van een topologische isolator. Voor toepassingen waarbij de geleidende oppervlaktetoestanden belangrijk zijn ligt de focus op het verkrijgen van een materiaal waarbij de Dirac kegel en het Fermi niveau gelegen zijn in de bandenkloof van de bulk. Voor thermo-elektrische toepassingen kunnen defecten en een hogere geleiding bijdragen tot het verhogen van de ZT waarde. Beide soorten toepassingen vereisen een eigen modificatie.

Bi_2Se_3 was het ongedopeerde materiaal, die bestond uit een vijflagige structuur (Se-Bi-Se-Bi-Se) met een van der Waals interactie tussen deze vijflagen. Ik heb interstitiële defecten geobserveerd met voornamelijk een Bi karakter in een octahedrale coördinatie in de van der Waals kloof. Ik heb voorgesteld dat dit defect het materiaal waarschijnlijk meer n-gedopeerd maakt, wat ongewenst is voor spintronica toepassingen maar gewenst voor thermo-elektrische toepassingen. Atomaire mobiliteit was geobserveerd langs en over de van der Waals kloof, wat een nadeel is voor Li of Na batterijtoepassingen maar tegelijk een indicatie

is dat het materiaal een zekere externe invloed kan verdragen, in mijn geval de elektronenbundel, zonder de structuur volledig te vervormen.

Vervolgens heb ik twee soorten gedopeerde topologische materialen bestudeerd: $(Bi_{1-x}In_x)_2Se_3$ en $Sb_2(Se_xTe_{1-x})_3$. Beiden zijn een mengeling van een topologische isolator en een normale isolator. Voor $(Bi_{1-x}In_x)_2Se_3$ bezet In de Bi sites en een interstitiële site in de van der Waals kloof. Ik stelde voor dat de laatstgenoemde het materiaal n-gedopeerd maakt. In dit materiaal werd gelijkaardig aan Bi_2Se_3 atomaire mobiliteit geobserveerd. Dezelfde conclusies van Bi_2Se_3 zijn ook van toepassing op dit materiaal. Voor $Sb_2(Se_xTe_{1-x})_3$ vond ik dat het kristal leegtes had waar een deel van de vijflagige bouwblok verwijderd was, wat interessant is sinds dit soort defecten de thermo-elektrische eigenschappen sterk kunnen verhogen. Bovendien zal Se in kleine hoeveelheden de buitenste Te lagen bezetten voordat de middelste laag volledig opgevuld is. Deze kleine hoeveelheid aan Se defecten in de buitenste Te lagen (Te1) kunnen waarschijnlijk de concentratie van de algemeen aanvaarde Sb_{Te1} antisite defecten meer beïnvloeden dan de Se atomen op de middelste Te lagen. Op deze manier kan het Fermi niveau onrechtstreeks gemodificeerd worden, wat een invloed heeft op de eigenschappen. Dit is in tegenspraak met de literatuur waar er geen onderscheid gemaakt werd tussen de twee verschillende Se sites en hun invloed op de eigenschappen van het materiaal.

Ik heb ook de $Ge_mBi_{2n}Te_{(m+3n)}$ series onderzocht waarbij ik opmerkte dat de materialen gemaakt met de transport groei methode steeds resulteerden in een l-trigonaal gelaagde structuur (l=7,9,11,5-7), terwijl de Bridgman methode zowel trigonaal gelaagde structuren als NaCl structuren met planaire defecten opleverde. Ik heb de gelaagde compositie bepaald en het aantal lagen in een bouwsteen, wat de eerste stap is in het bepalen van het topologische isolator karakter en hun karakteristieken voor toekomstig gebruik in toepassingen. Verschillen werden gevonden in vergelijking met het GeTe-Sb_2Te_3 systeem, zoals de hogere structurele stabiliteit vanwege de afwezigheid van een atomaire van der Waals kloof reconfiguratie, gesuggereerd nuttig te zijn voor fasetransitie toepassingen. De NaCl structuur bevatte twee soorten planaire defecten langs de $(11\bar{1})_C$ of $(1\bar{1}\bar{1})_C$ Ge vlakken. De eerste defectsoort is de afwezigheid van een volledig $(11\bar{1})_C$ of $(1\bar{1}\bar{1})_C$ Ge vlak met errond een overmaat aan Bi op de Ge sites en een structurele distortie naar α-GeTe, beschreven door de vorming van een tweelingdomein of de vorming van een van der Waals kloof. Dit soort bestaat enkel in Bi rijke $Ge_mBi_{2n}Te_{(m+3n)}$ materialen. De literatuur geeft aan dat het een positief effect heeft op de thermo-elektrische eigenschappen. De tweede defectsoort bestaat uit Ge vacaturen rijk $(11\bar{1})_C$ of $(1\bar{1}\bar{1})_C$ Ge vlakken met een overmaat aan Bi rond het defect. Het specifieke effect van dit defect is onbekend.

In het tweede gedeelte heb ik de interface onderzocht tussen een topologische isolator met zuurstof en een ijzerlaag. Oxidatie karakterisatie is noodzakelijk omdat we geïnteresseerd zijn in de geleidende oppervlaktetoestanden en de specimens onder normale omstandigheden gemaakt, behandeld en bestudeerd worden in een zuurstof omgeving. Het toevoegen van een magnetische toplaag, zoals ijzer, op een topologisch materiaal kan nuttig zijn voor spintronica toepassingen. Deze geleidende oppervlaktetoestanden zijn echter niet

robuust bij magnetische onzuiverheden. De atomaire interface zal bovendien een invloed hebben, wat de motivatie was achter dit onderzoek.

Alle materialen (Bi_2Te_3, Sb_2Te_3, $(Sb_{0.55}Bi_{0.45})_2Te_3$ en $Ge_mBi_{2n}Te_{(m+3n)}$) hadden een amorfe oxide laag aan de top die verwoven was met een vervormde structuur bestaande uit geordende Te lagen met wanordelijke lagen ertussen. In de sublaag van $(Sb_{0.55}Bi_{0.45})_2Te_3$ en Bi_2Te_3 kwamen ook zevenlagige defecten voor, terwijl in de sublaag van de trigonaal gelaagde $Ge_mBi_{2n}Te_{(m+3n)}$ kristallen een gelaagde bouwsteen voorkwam met een anders gelaagde structuur dan de bulk. Het eerste vergemakkelijkt atomaire mobiliteit ook al is de reden voor hun bestaan onbekend. De tweede zou een gevolg kunnen zijn van de chemische verandering in de sublaag vanwege de mobiliteit van het meest reactieve element, Ge, naar het oppervlak. Vanwege de gelijkenissen tussen de verschillende materialen stelde ik voor dat de oxidatie mechanismes gelijkaardig zijn. Eerst zal zuurstof reageren met het meest reactieve element van het materiaal en dus hun binding breken met de bulk. Vervolgens zal de oppervlaktelaag negatief geladen worden vanwege de elektronen die zullen verplaatsen van het Fermi niveau van het materiaal naar de oxide, gevolgd door een migratie van het meest reactieve kation element naar het oppervlak vanwege de gecreëerde potentiaal. Het laatstgenoemde zal leiden tot de vorming van een amorfe oxidelaag en de vervormde structuur met geordende Te lagen en wanordelijke lagen ertussen. Achteraf zal een complexere $A_nB_mO_x$ oxide vormen vanwege de oxidatie van andere elementen. Bi_2Te_3 heeft echter eerst een congruente oxidatie ondergaan van de eerste vijfdelige laag, waarbij $Bi_2(TeO_3)_3$ gevormd werd door Te eerst te oxideren via zuurstof transportatie.

Een ijzerlaag van 20 nm was gedeponeerd op Bi_2Te_3. Dit leidde tot de vorming van een ijzerlaag, gevolgd door een amorfe FeTe laag, waarbij het overmaat aan Bi migreerde naar de Bi_2Te_3 bulk om zo zevenlagige defecten te creëren dicht bij de FeTe interface. In de literatuur leidde een dunne FeTe film op Bi_2Te_3 tot superconductiviteit op de interface, wat interessant is voor Majorana fermionen. De vraag blijft of hetzelfde gebeurd in mijn geval.

In het derde deel van mijn thesis heb ik de α-GeTe en $FeGe_\gamma$ ($\gamma \approx 1.5$) structuren onderzocht die structureel gerelateerd zijn tot topologische isolatoren. Beiden zijn thermo-elektrische materialen, maar geen topologische isolatoren.

α-GeTe bevat de zogenaamde inversie domeingrenzen of 180° domeingrenzen, die ik atomair karakteriseerde. Ik vond twee atomair verschillend geladen 180° domeinmuren die loodrecht op de c_H as staan. Bij de atomair vlakke BB grenzen is één volledig Ge vlak verwijderd, waardoor een van der Waals binding ontstaat tussen de Te lagen. De stapsgewijze AA interface gaat door verschillende lagen heen met een variabele Ge positie tussen de twee Te lagen in. Voor spintronica toepassingen is de mobiliteit van de domeingrenzen belangrijk. Ik suggereerde dat de AA domeinmuur mobieler is waardoor deze een lagere wisseltijd heeft dan de BB domeinmuren. Bovendien maakt het bestaan van enkel de 180° domeinmuren deze kristallen tot geschikte studie specimens vanwege hun simplistische domeinbeweging. Het zijn geladen domeinmuren, wat interessant is voor ‘domeinmuur nano-elektronica’.

Ik heb de ruimtegroep en celparameters bepaald van twee co-existerende structuren van het polykristallijne $FeGe_\gamma$ specimen, wat niet mogelijk was met PXRD. De incommensurabele structuur heeft als celparameters $a \approx 5.6$ Å, $c \approx 4.6$ Å, en $q = 0.49(3)\, c^*$ en ruimtegroep $I4_1/amd(00\gamma)00ss$, terwijl de commensurabele structuur als celparameters $a \approx 5.45$ Å, $b \approx 5.6$ Å, and $c \approx 8.95$ Å heeft en als ruimtegroep Pcc2 of Pccm. Beiden zijn Nowotny schoorsteenladder structuren, opgebouwd uit een Ge helix in een viervoudige Fe helix. Het materiaal bevatte ook een oriëntatie anomalie, wat nog niet eerder in literatuur was vernoemd voor $FeGe_\gamma$, wat er voor zorgde dat de schroefvormige rangschikking van de Ge atomen systematisch verschoof langs de Fe helix structuur. De complexe structuur zorgde waarschijnlijk voor een lage thermische geleiding gelijkaardig aan glas in een breed temperatuursbereik, wat een goede thermo-elektrische eigenschap is. Andere goede thermo-elektrische karakteristieken waren de ~30 meV dunne bandkloof en de hoge absolute waarden van de Seebeck coëfficiënt bij verhoogde temperaturen.

References

1. Kane, C., Moore, J., Topological insulators 32–36 (2011).
2. Thouless, D. J., Kohmoto, M., Nightingale, M. P. & den Nijs, M. *Phys. Rev. Lett.* **49**, 405–408 (1982).
3. Murakami, S., Nagaosa, N. & Zhang, S.-C. *Science.* **301**, 1348–1351 (2003).
4. Sinova, J. *et al. Phys. Rev. Lett.* **92**, 1–4 (2004).
5. Coey, J. M. D. *Magnetism and Magnetic Materials*. (Cambridge University press, 2013).
6. Fu, L., Kane, C. L. & Mele, E. J. Phys. Rev. Lett. **98**, 106803 (2007)..
7. Hsieh, D. *et al. Nature* **452**, 970–974 (2008).
8. Bansil, A., Lin, H. & Das, T. *Rev. Mod. Phys.* **88**, 1–37 (2016).
9. Qi, X. L. & Zhang, S. C. *Phys. Today* **63**, 33–38 (2010).
10. Heremans, J. P., Cava, R. J. & Samarth, N. *Nat. Rev. Mater.* **2**, (2017).
11. Moore, J. E. *Nature* **464**, 194–198 (2010).
12. Malik, K. *et al. J. Appl. Phys.* **112**, (2012).
13. Atuchin, V. V. *et al. Solid State Commun.* **152**, 1119–1122 (2012).
14. Agaev, K. A. & Semiletov, S. A. *Kristallografiya* **10**, 109–112 (1965).
15. Poutcharovsky, D. J., Yvon, K. & Parthe, E. *J. Less-Common Met.* **40**, 139–144 (1975).
16. Goldak, J., Barrett, C. S., Innes, D. & Youdelis, W. *J. Chem. Phys.* **44**, 3323–3325 (1966).
17. Verchenko, V. Y. *et al. Chem. Mater.* **29**, 9954–9963 (2017).
18. Bauer Pereira, P. *et al. Phys. status solidi* **250**, 1300–1307 (2013).
19. Wondratschek & H., Müller *International Tables for Crystallogray A1*. (Kluwer Academic Publishers, 2004).
20. Pérez Vicente, C. *et al. Inorg. Chem.* **38**, 2131–2135 (1999).
21. Mansour, A. N. *et al. J. Appl. Phys.* **116**, 0–14 (2014).
22. Anderson, T. & Krause, H. B. *Acta Crystallogr. B* **30**, 1307–1310 (1974).
23. Chen, Y. L. *et al. Science.* **325**, 178–181 (2009).
24. Hsieh, D. *et al. Nature* **460**, 1101–1105 (2009).

25. Xia, Y. *et al. Nat. Phys.* **5**, 398–402 (2009).

26. Pauly, C. *et al. Phys. Rev. B - Condens. Matter Mater. Phys.* **86**, 1–8 (2012).

27. Zhang, H. *et al. Nat. Phys.* **5**, 438–442 (2009).

28. Tokura, Y., Yasuda, K. & Tsukazaki, A. *Nat. Rev. Phys.* **1**, 126–143 (2019).

29. Eremeev, S. V. *et al. Nat. Commun.* **3**, 4–10 (2012).

30. Lu, G. *et al. J. Solid State Chem.* **164**, 210–219 (2002).

31. Nowotny, H. Crystal Chemistry of Transition Element Defect Silicides and Related Compounds. in *The Chemistry of Extended Defects in Nonmetallic Solids* (eds. Eyring, L. & O'Keeffe, M.) (North-Holland Publishing Co., 1970).

32. Elder, I., Lee, C.-S. & Kleinke, H. *Inorg. Chem.* **41**, 538–545 (2002).

33. Gibson, Q. D. *et al. Sci. Rep.* **4**, 1–6 (2014).

34. Sun, G. *et al. J. Alloys Compd.* **639**, 9–14 (2015).

35. Goldsmid, H. Bismuth Telluride and Its Alloys as Materials for Thermoelectric Generation *Materials* **7**, 2577–2592 (2014).

36. Müchler, L., Casper, F., Yan, B., Chadov, S. & Felser, C. *Phys. Status Solidi - Rapid Res. Lett.* **7**, 91–100 (2013).

37. Tritt, T. M. *Annu. Rev. Mater. Res.* **41**, 433–448 (2011).

38. Tritt, T. M. & Subramanian, M. A. *MRS Bull.* **31**, 188–198 (2006).

39. Li, J. *et al. NPG Asia Mater.* **9**, e353–e353 (2017).

40. Liu, Y., Zhou, M. & He, J. *Scr. Mater.* **111**, 39–43 (2016).

41. Saremi, S., Gao, R., Dasgupta, A. & Martin, L. W. *Am. Ceram. Soc. Bull.* **97**, 16–23 (2018).

42. Repula, A. & Grelet, E. *Phys. Rev. Lett.* **121**, 097801 (2018).

43. International Union of Crystallography, Report of the Executive Committee for 1991, *Acta Crystallographica Section A Foundations of Crystallography* **48**, (1992).

44. Jones, R. O. *J. Phys. Condens. Matter* **30**, 153001 (2018).

45. Pecharsky, V. & Zavalij, P. *Fundamentals of Powder Diffraction and Structural Characterization of Materials*. (Springer US, 2009).

46. De Graef, M. *Introduction to conventional transmission electron microscopy*. (Cambridge University Press, 2003).

47. Batuk, D., Batuk, M., Abakumov, A. M. & Hadermann, J. *Acta Crystallogr. Sect. B*

Struct. Sci. Cryst. Eng. Mater. **71**, 127–143 (2015).

48. van Smaalen, S. *Incommensurate Crystallography*. (Oxford University Press, 2007).

49. Janssen, T. & Janner, A. *Adv. Phys.* **36**, 519–624 (1987).

50. Kolb, U., Gorelik, T., Kübel, C., Otten, M. T. & Hubert, D. *Ultramicroscopy* **107**, 507–513 (2007).

51. Kolb, U., Gorelik, T. & Otten, M. T. *Ultramicroscopy* **108**, 763–772 (2008).

52. Gorelik, T. E., Stewart, A. A. & Kolb, U. *J. Microsc.* **244**, 325–331 (2011).

53. Karakulina, O. Quantitive electron diffraction tomography for structure characterization of cathode materials for Li-ion batteries, PhD thesis (University of Antwerp, 2018).

54. Williams, D. B. & Carter, C. B. *Transmission Electron Microscopy*. (Springer US, 2009).

55. Bhattarai, N., Khanal, S., Velazquez-Salazar, J. J. & Jeose-Yacaman, M. Advanced Transmission Electron Microscopy: Applications to nanomaterials (eds. Deepak, F. L., Mayoral, A. & Arenal, R.) (Springer International Publishing, 2015).

56. Pennycook, S. J. & Boatner, L. A. *Nature* **336**, 565–567 (1988).

57. Pennycook, S. J. Imaging in the STEM in *Transmission Electron Microscopy: Diffraction, Imaging, and Spectrometry* (eds. Carter, C. B. & Williams, D. B.) 283–342 (Springer International Publishing, 2016).

58. Zhang, Y. *et al. Beilstein J. Nanotechnol.* **5**, 946–955 (2014).

59. Toby, B. H. *Powder Diffr.* **21**, 67–70 (2006).

60. Born, M. & Oppenheimer, R. *Ann. Phys.* **389**, 457–484 (1927).

61. Kohanoff, J. *Electronic-Structure Calculations for Solids and Molecules*. (Cambridge University Press, 2006).

62. Springborg, M. *Methods of Electronic-Structure Calculations: From Molecules to Solids*. (John Wiley & Sons Inc, 2000).

63. Hohenberg, P. & Kohn, W. *Phys. Rev.* **136**, B864–B871 (1964).

64. Perdew, J. P., Burke, K. & Ernzerhof, M. *Phys. Rev. Lett.* **77**, 3865 (1996).

65. Klimeš, J. & Michaelides, A. *J. Chem. Phys.* **137**, 120901 (2012).

66. Klimeš, J., Bowler, D. R. & Michaelides, A. *J. Phys. Condens. Matter* **22**, 022201 (2010).

67. Klimeš, J., Bowler, D. R. & Michaelides, A. *Phys. Rev. B* **83**, 195131 (2011).

68. Dion, M., Rydberg, H., Schröder, E., Langreth, D. C. & Lundqvist, B. I. *Phys. Rev. Lett.* **92**, 246401 (2004).

69. Dirac, P. A. M. *The Principles of Quantum Mechanics*. (Clarendon Press, 1930).

70. Weissbluth, M. *Atoms and molecules*. (Academic Press, 1978).

71. Capelle, K. *Phys. Rev. B* **63**, 052503 (2001).

72. Ching, W. Y. & Rulis, P. *Electronic Structure Methods for Complex Materials*. (Oxford University Press, 2012).

73. Koelling, D. D. & Harmon, B. N. *J. Phys. C Solid State Phys.* **10**, 3107–3114 (1977).

74. Blöchl, P. E. *Phys. Rev. B* **50**, 17953–17979 (1994).

75. Rostgaard, C. The Projector Augmented Wave Method. *arXiv* 1–25 (2009).

76. Feynman, R. P. *Phys. Rev.* **56**, 340–343 (1939).

77. Hellmann, H. Einführung in die Quantenchemie (F. Deuticke, 1937).

78. Boioli, F. *et al. Multiscale Modeling of the Mantle Rheology: The RheoMan Project*. (eds. Cordier, P. & Goryaeva, A.M.) (Print Forum, 2018).

79. Henkelman, G., Uberuaga, B. P. & Jónsson, H. *J. Chem. Phys.* **113**, 9901–9904 (2000).

80. Henkelman, G. & Jónsson, H. *J. Chem. Phys.* **113**, 9978–9985 (2000).

81. Shtanov, V. I. & Yashina, L. V. *J. Cryst. Growth* **311**, 3257–3264 (2009).

82. Lund, J. C., Olschner, F. & Burger, A. Chapter 11 Lead Iodide Crystals and Detectors in *Semiconductors and Semimetals* **43**, (eds. Schlesinger, T.E. & James, R. B.) 443–464 (ACADEMIC PRESS, 1995).

83. Lobato, I. & Van Dyck, D. *Ultramicroscopy* **156**, 9–17 (2015).

84. Koch, C. Determination of core structure and point defect density along dislocations, PhD thesis (2002).

85. Kresse, G. & Hafner, J. *Phys. Rev. B* **47**, 558 (1993).

86. Kresse, G. & Hafner, J. *Phys. Rev. B* **49**, 14251 (1994).

87. Kresse, G. & Furthmüller, J. *Comput. Mater. Sci.* **6**, 15 (1996).

88. Kresse, G. & Furthmüller, J. *Phys. Rev. B* **54**, 11169 (1996).

89. Palatinus, L. PETS–Program For Analysis Of Electron Diffraction Data Prague. Czech Republic: Institute of Physics of the AS CR (2011).

90. Petrícek, V., Dušek, M. & Palatinus, L. *Zeitschrift fur Kristallographie* **229**, 345–352 (2014).

91. Callaert, C., Bercx, M., Lamoen, D. & Hadermann, J. *Acta Crystallogr. Sect. B Struct. Crystallogr. Cryst. Chem.* **75**, 717–732 (2019).

92. Hor, Y. S. *et al. Phys. Rev. B - Condens. Matter Mater. Phys.* **79**, 195208 (2009).

93. Tumelero, M. A., Faccio, R. & Pasa, A. A. *J. Phys. Condens. Matter* **28**, 425801 (2016).

94. Ramachandran, V., Halfpenny, P. J. & Roberts, K. J. Crystal Science Fundamentals in *Engineering Crystallography: From Molecule to Crystal to Functional Form* (eds. Roberts, K. J., Docherty, R. & Tamura, R.) 3–19 (Springer Netherlands, 2017).

95. Dai, J. *et al. Phys. Rev. Lett.* **117**, 106401 (2016).

96. Wu, K. K., Ramachandran, B., Kuo, Y. K., Sankar, R. & Chou, F. C. *J. Alloys Compd.* **682**, 225–231 (2016).

97. Ando, Y. *J. Phys. Soc. Japan* **82**, 102001 (2013).

98. Mann, C. *et al. Nat. Commun.* **4**, 2277 (2013).

99. Zhu, T., Hu, L., Zhao, X. & He, J. *Adv. Sci.* **3**, 1600004 (2016).

100. Ali, Z. *et al. J. Power Sources* **229**, 216–222 (2013).

101. Xu, H. *et al. CrystEngComm* **15**, 1618–1625 (2013).

102. Xie, L. *et al. Nano-Micro Lett.* **10**, 50 (2018).

103. Tominaga, J. *MRS Bull.* **43**, 347–351 (2018).

104. Tominaga, J., Simpson, R. E., Fons, P. & Kolobov, A. V. *Appl. Phys. Lett.* **99**, 152105 (2011).

105. Simpson, R. E. *et al. Nat. Nanotechnol.* **6**, 501–505 (2011).

106. Han, N. *et al. Adv. Mater.* **23**, 1871–1875 (2011).

107. Mishra, S., Satpathy, S. & Jepsen, O. *J. Phys Condens. Matter* **9**, 461–470 (1997).

108. Scanlon, D. O. *et al. Adv. Mater.* **24**, 2154–2158 (2012).

109. Unzueta, I. *et al. Phys. Rev. B* **94**, 43–46 (2016).

110. Devidas, T. R. *et al. EPL (Europhys. Lett.)* **108**, 67008 (2014).

111. Alpichshev, Z. *et al. Phys. Rev. Lett.* **108**, 206402 (2012).

112. West, D., Sun, Y. Y., Wang, H., Bang, J. & Zhang, S. B. *Phys. Rev. B - Condens. Matter Mater. Phys.* **86**, 121201 (2012).

113. Wang, L. L. *et al. Phys. Rev. B - Condens. Matter Mater. Phys.* **87**, 125303 (2013).

114. Xue, L. *et al. AIP Adv.* **3**, 052105 (2013).

115. Urazhdin, S. *et al. Phys. Rev. B* **66**, 161306 (2002).

116. Huang, F. T. *et al. Phys. Rev. B - Condens. Matter Mater. Phys.* **86**, 081104 (2012).

117. Jia, G., Wang, X., Li, Q. & Yao, J. *Superlattices Microstruct.* **66**, 33–38 (2014).

118. Urazhdin, S. *et al. Phys. Rev. B* **69**, 085313 (2004).

119. P., V., Khoviv, A. M. & Zavrazhnov, A. J. Physicochemical Analysis and Synthesis of Nonstoichiometric Solids in *Materials Science - Advanced Topics* (ed. Mastai, Y.) (InTech, 2013).

120. (Pierre Villars. Pauling file in Inorganic solid phases, SpringerMaterials (online database) http://www.himikatus.ru/art/phase-diagr1/diagrams.php (Springer Materials, 2016).

121. Offergeld, G. & van Cakenberghe, J. *J. Phys. Chem. Solids* **11**, 310-314 (1959).

122. Palatinus, L., Petříček, V. & Corrêa, C. A. *Acta Crystallogr. Sect. A Found. Adv.* **71**, 235–244 (2015).

123. Palatinus, L. *et al. Acta Crystallogr. Sect. A Found. Crystallogr.* **69**, 171–188 (2013).

124. Palatinus, L. *et al. Acta Crystallogr. Sect. B Struct. Sci. Cryst. Eng. Mater.* **71**, 740–751 (2015).

125. Finger, L. W., Cox, D. E. & Jephcoat, A. P. *J. Appl. Crystallogr.* **27**, 892–900 (1994).

126. March, A. *Zeitschrift für Krist. - Cryst. Mater.* **81**, 285–297 (1932).

127. Dollase, W. A. *J. Appl. Crystallogr.* **19**, 267–272 (1986).

128. Zolotoyabko, E. *J. Appl. Crystallogr.* **42**, 513–518 (2009).

129. Kresse, G. & Joubert, D. *Phys. Rev. B* **59**, 1758 (1999).

130. Blöchl, P. E. *Phys. Rev. B* **50**, 17953 (1994).

131. Freysoldt, C. *et al. Rev. Mod. Phys.* **86**, 253–305 (2014).

132. Hashibon, A. & Elsässer, C. *Phys. Rev. B - Condens. Matter Mater. Phys.* **84**, 144117 (2011).

133. Van de Walle, C. G. & Neugebauer, J. *J. Appl. Phys.* **95**, 3851–3879 (2004).

134. Novoselov, K. S. *et al. Science.* **306**, 666–669 (2004).

135. Wang, Z., Lv, X. & Weng, J. *Carbon N. Y.* **62**, 51–60 (2013).

136. Sun, L. *et al. Sci. Rep.* **4**, 4794 (2014).

137. Azar, L. Cavitation in Ultrasonic Cleaning and Cell Disruption in *Control. Environ.* 14–17 (2009).

138. Sánchez-Barriga, J. *et al. Phys. Rev. B* **98**, 235110 (2018).

139. Bouanani, H. G., Eddike, D., Liautard, B. & Brun, G. *Mater. Res. Bull.* **31**, 177–187

(1996).

140. Bals, S., Tirry, W., Geurts, R., Yang, Z. & Schryvers, D. *Microsc. Microanal.* **13**, 80–86 (2007).

141. Meyer, J. C. *et al. Phys. Rev. Lett.* **108**, 196102 (2012).

142. Zhu, G. -z. & Botton, G. A. *Micron* **68**, 141–145 (2015).

143. Jiang, N. *Reports Prog. Phys.* **79**, 016501 (2016).

144. Egerton, R. F., Li, P. & Malac, M. *Micron* **35**, 399–409 (2004).

145. van Genderen, E. *et al. Acta Crystallogr. Sect. A Found. Adv.* **72**, 236–242 (2016).

146. Nederlof, I., van Genderen, E., Li, Y.-W. & Abrahams, J. P. *Acta Crystallogr. Sect. D Biol. Crystallogr.* **69**, 1223–1230 (2013).

147. Momma, K. & Izumi, F. *J. Appl. Crystallogr.* **44**, 1272–1276 (2011).

148. Semenkovich, S. A. & Melekh, B. T. Thermodynamic Properties of Bi_2Te_3, Bi_2Se_3, Sb_2Te_3, and Sb_2Se_3 in *Chemical Bonds in Solids Volume 3: X-Ray and Thermodynamic Investigations* (ed. Sirota, N.N.) 159–162 (Springer US, 1972).

149. Sheppard, D., Terrell, R. & Henkelman, G. *J. Chem. Phys.* **128**, 134106 (2008).

150. Deringer, V. L., Lumeij, M., Stoffel, R. P. & Dronskowski, R. *Chem. Mater.* **25**, 2220–2226 (2013).

151. Young, D. Finding transition structures in *Computational Chemistry: A Practical Guide for Applying Techniques to Real World Problems* 147 (John Wiley & Sons, Inc, 2001).

152. Dai, Y., Ni, S., Li, Z. & Yang, J. *J. Phys. Condens. Matter* **25**, 405301 (2013).

153. Yashina, L. V., Shatalova, T. B., Bobruiko, V. B., Belyansky, M. P. & Zlomanov, V. P. *Solid State Ionics* **101**–**103**, 533–538 (1997).

154. Car, R., Kelly, P. J., Oshiyama, A. & Pantelides, S. T. *Phys. Rev. Lett.* **52**, 1814–1817 (1984).

155. Shackelford, J. Diffusion in *Introduction to Material Science for engineers* (ed. George, D. A.) 157–185 (Pearson Education Limited, 2005).

156. Wang, Y. L. *et al. Phys. Rev. B - Condens. Matter Mater. Phys.* **84**, 075335 (2011).

157. Egerton, R. F. *Micron* **119**, 72–87 (2019).

158. Liu, B. *et al. AIP Adv.* **8**, 115327 (2018).

159. Hobbs, L. W. Murphy's law and the uncertainty of electron probes in *Introduction to analytical electron microsopy* (eds. Hren, J. J., Goldstein, J. I. & Joy, D. C.) 437–480 (Springer Science+Business Media, 1979).

160. Hobbs, L. W. *J. Non. Cryst. Solids* **182**, 27–39 (1995).

161. Fahey, P. M., Griffin, P. B. & Plummer, J. D. *Rev. Mod. Phys.* **61**, 289–384 (1989).

162. Sultana, R., Gahtori, B., Meena, R. S. & Awana, V. P. S. Synthesis and structural characterization of bulk Sb2Te3 single crystal in *AIP Conference Proceedings* **1953**, 070021 (2018).

163. Sultana, R., Gurjar, G., Patnaik, S. & Awana, V. P. S. *Mater. Res. Express* **5**, 046107 (2018).

164. Horák, J., Karamazov, S., Nesládek, P. & Lošťák, P. *J. Solid State Chem.* **129**, 92–97 (1997).

165. Jiang, Y. *et al. Phys. Rev. Lett.* **108**, 066809 (2012).

166. Mehta, R. J. *et al. Nano Lett.* **12**, 4523–4529 (2012).

167. Uher, C. Materials Aspect of Thermoelectricity (CRC Press, 2016).

168. Scherrer, H., Martin-Lopez, R., Lenoir, B., Dauscher, A. & Scherrer, S. Thermoelectric materials of P and N type from the (Bi, Sb, Te) phase diagram 20th *Int. Conf. Thermoelectr.* 13–17 (2001). doi:10.1109/ict.2001.979606

169. Wolf, S. A. *Science.* **294**, 1488–1495 (2001).

170. Teramoto, I. & Takayanagi, S. *J. Phys. Chem. Solids* **19**, 124–129 (1961).

171. Lošťák, P., Novotný, R., Beneš, L. & Civiš, S. *J. Cryst. Growth* **94**, 656–662 (1989).

172. Lee, C.-K. *et al. Sci. Rep.* **6**, 36538 (2016).

173. Hsieh, D. *et al. Phys. Rev. Lett.* **103**, 2–5 (2009).

174. Zhang, H. *et al.* Topological Insulators at Room Temperature *arXiv* 1–6 (2008).

175. Pan, Z.-H. *et al. Phys. Rev. Lett.* **106**, 257004 (2011).

176. Li, W. *et al. Phys. Rev. B* **98**, 165134 (2018).

177. Vadapoo, R., Krishnan, S., Yilmaz, H. & Marin, C. *Phys. Status Solidi Basic Res.* **248**, 700–705 (2011).

178. Osamura, K., Murakami, Y. & Tomiie, Y. *J. Phys. Soc. Japan* **21**, 1848–1848 (1966).

179. Likforman, A. *et al. J. Solid State Chem.* **33**, 91–97 (1980).

180. Voutsas, G. P., Papazoglou, A. G., Rentzeperis, P. J. & Siapkas, D. *Zeitschrift für Krist. - Cryst. Mater.* **171**, 261–268 (1985).

181. Ren, Z., Taskin, A. A., Sasaki, S., Segawa, K. & Ando, Y. *Phys. Rev. B* **84**, 165311 (2011).

182. Horák, J., Strarý, Z., Lošťák, P. & Pancíř, J. *J. Phys. Chem. Solids* **51**, 1353–1360 (1990).

183. Ji, H. *et al. Mater. Res. Bull.* **48**, 2517–2521 (2013).

184. Procarione, W. & Wood, C. *Phys. status solidi* **42**, 871–878 (1970).

185. Ullner, H.-A. *Ann. Phys.* **476**, 45–56 (1968).

186. Lošťák, P., Novotný, R. & Horák, J. *Czechoslovak Journal of Physics* **39**, 308–315 (1989).

187. Zhang, W., Yu, R., Zhang, H.-J., Dai, X. & Fang, Z. *New J. Phys.* **12**, 065013 (2010).

188. Wang, H. *et al. Phys. E Low-Dimensional Syst. Nanostructures* **98**, 66–73 (2018).

189. Horák, J., Starý, Z., Lošťák, P. & Pancír, J. *J. Phys. Chem. Solids* **51**, 1353–1360 (1990).

190. Wu, D., Xie, L., Xu, X. & He, J. *Adv. Funct. Mater.* **29**, 1806613 (2019).

191. Khan, A. U. *et al. Nano Energy* **31**, 152–159 (2017).

192. Anderson, T. L. & Krause, H. B. *Acta Crystallogr. Sect. B Struct. Crystallogr. Cryst. Chem.* **30**, 1307–1310 (1974).

193. Lu, P., Zhou, L., Kramer, M. J. & Smith, D. J. *Sci. Rep.* **4**, 1–5 (2014).

194. Lu, P., Xiong, J., Benthem, M. Van & Jia, Q. *Appl. Phys. Lett.* **102**, 173111 (2013).

195. Wojdyr, M. *J. Appl. Crystallogr.* **43**, 1126 (2010).

196. Kuypers, S., van Tendeloo, G., van Landuyt, J. & Amelinckx, S. *J. Solid State Chem.* **76**, 102–108 (1988).

197. Eremeev, S. V. *et al. Nat. Commun.* **3**, 635 (2012).

198. Xu, S.-Y. *et al.* Discovery of several large families of Topological Insulator classes with backscattering-suppressed spin-polarized single-Dirac-cone on the surface. *arXiv* 1-11 (2010).

199. Karpinskii, O. G., Shelimova, L. E. & Kretova, M. *Inorg. Mater.* **33**, 793–797 (1997).

200. Urban, P., Simonov, A., Weber, T. & Oeckler, O. *J. Appl. Crystallogr.* **48**, 200–211 (2015).

201. Matsunaga, T. *et al. Acta Crystallogr. Sect. B Struct. Sci. Cryst. Eng. Mater.* **63**, 346–52 (2007).

202. Petrov, I. I. & Imamov, R. M. *Kristallografiya* **15**, 168–170 (1970).

203. Karpinskii, O. G., Shelimova, L. E., Kretova, M. A. & Lubman, G. U. *Inorg. Mater.* **30**, 1406–1411 (1994).

204. Agaev, K. A., Talybov, A. G. & Semiletov, S. A. *Kristallografiya* **13**, 59–62 (1968).

205. Zhukova, T. B. & Zaslavskii, A. I. *Kristallografiya* **16**, 796–800 (1971).

206. Frangis, N. *et al. J. Solid State Chem.* **84**, 314–334 (1990).

207. Matsunaga, T. *et al. Inorg. Chem.* **45**, 2235–2241 (2006).

208. Kooi, B. J. & De Hosson, J. T. M. *J. Appl. Phys.* **92**, 3584–3590 (2002).

209. Zhang, W. *et al. Nat. Mater.* **11**, 952–956 (2012).

210. Lee, T. *et al. Appl. Phys. Lett.* **92**, 101908 (2008).

211. Wuttig, M. & Yamada, N. *Nat. Mater.* **6**, 824–832 (2007).

212. Madar, N., Givon, T., Mogilyansky, D. & Gelbstein, Y. *J. Appl. Phys.* **120**, 035102 (2016).

213. Geim, A. K. & Grigorieva, I. V. *Nature* **499**, 419–425 (2013).

214. Watanabe, M. *et al. Microsc. Microanal.* **12**, 515–526 (2006).

215. Kraxner, J. *et al. Ultramicroscopy* **172**, 30–39 (2017).

216. Wang, J.-J. *et al. Chem. Mater.* **30**, 4770–4777 (2018).

217. Shekhar, C. *et al.* Single crystal growth for topology and beyond. *Chemical metals science & solid state chemistry* (2018).

218. Momand, J. *et al. Nanoscale* **7**, 19136–19143 (2015).

219. Kolobov, A. V, Fons, P., Saito, Y. & Tominaga, J. *ACS Omega* **2**, 6223–6232 (2017).

220. Lotnyk, A. *et al. Acta Mater.* **141**, 92–96 (2017).

221. Leger, J. M. *et al. J. Phys. C Solid State Phys.* **20**, 1431–1440 (1987).

222. Shelimova, L. E., Karpinskii, O. G., Zemskov, V. S. & Konstantinov, P. P. *Inorg. Mater.* **36**, 235–242 (2000).

223. Hasan, M. Z. & Kane, C. L. *Rev. Mod. Phys.* **82**, 3045–3067 (2010).

224. Thomas, C. R. *et al. Phys. Status Solidi - Rapid Res. Lett.* **8**, 997–1002 (2014).

225. Analytis, J. G. *et al. Nat. Phys.* **6**, 960–964 (2010).

226. Kong, D. *et al. ACS Nano* **5**, 4698–4703 (2011).

227. Liu, Q., Liu, C. X., Xu, C., Qi, X. L. & Zhang, S. C. *Phys. Rev. Lett.* **102**, 1–4 (2009).

228. Volykhov, A. A. *et al. J. Mater. Chem. C* **6**, 8941–8949 (2018).

229. Yashina, L. V *et al. ACS Nano* **7**, 5181–5191 (2013).

230. Ngabonziza, P., Wang, Y. & Brinkman, A. *Phys. Rev. Mater.* **2**, 044204 (2018).

231. Bathon, T. *et al. Adv. Mater.* **28**, 2183–2188 (2016).

232. Wang, J., Chen, X., Zhu, B.-F. & Zhang, S.-C. *Phys. Rev. B* **85**, 235131 (2012).

233. Zhang, J. *et al. Nat. Commun.* **2**, 574 (2011).

234. Caillat, T., Carle, M., Pierrat, P., Scherrer, H. & Scherrer, S. *J. Phys. Chem. Solids* **53**, 1121–1129 (1992).

235. Grosvenor, A. P., Kobe, B. A. & McIntyre, N. S. *Surf. Sci.* **574**, 317–321 (2005).

236. Fehlner, F. P. & Mott, N. F. *Oxid. Met.* **2**, 59–99 (1970).

237. Cabrera, N. & Mott, N. F. *Reports Prog. Phys.* **12**, 308 (1949).

238. Davis, J. R. *Specialty Handbook: Heat-Resistant Materials*. (ASM International, 1997).

239. Eley, D. D. & Wilkinson, P. R. *Proc. R. Soc. London. Ser. A. Math. Phys. Sci.* **254**, 327–342 (2006).

240. Smeltzer, W. W. & Perrow, J. M. *an I/EC Chem. Eng. Fundam. Rev.* **53**, 319–324 (1961).

241. L. Cocke, D., Dorms, K., G. Naugle, D. & R. Hess, T. *MRS Proc.* **355**, 421 (1994).

242. Schennach, R., Promreuk, S., Naugle, D. G. & Cocke, D. L. *Oxid. Met.* **55**, 523–541 (2001).

243. Wagner, C. *J. Electrochem. Soc.* **99**, 369 (2007).

244. Mott, N. F., Rigo, S., Rochet, F. & Stoneham, A. M. *Philos. Mag. B* **60**, 189–212 (1989).

245. Morita, M., Ohmi, T., Hasegawa, E., Kawakami, M. & Ohwada, M. *J. Appl. Phys.* **68**, 1272–1281 (1990).

246. Wilmsen, C. W., Kee, R. W. & Geib, K. M. *J. Vac. Sci. Technol.* **16**, 1434–1438 (1979).

247. Wilmsen, C. W. *Thin Solid Films* **39**, 105–117 (1976).

248. Morita, M., Ohmi, T., Hasegawa, E., Kawakami, M. & Ohwada, M. *J. Appl. Phys.* **68**, 1272–1281 (1990).

249. Frangis, N., Kuypers, S., Manolikas, C., Van Landuyt, J. & Amelinckx, S. *Solid State Commun.* **69**, 817–819 (1989).

250. Jiang, Y. *et al. Nano Lett.* **13**, 2851–2856 (2013).

251. Brebrick, R. F. *J. Phys. Chem. Solids* **30**, 719–731 (1969).

252. Aspiala, M., Sukhomlinov, D. & Taskinen, P. *Solid State Ionics* **265**, 80–84 (2014).

253. Haynes, W. M. *Standard thermodynamic properties of chemical substances*. (CRC Handbook of Chemistry and Physics, 2012).

254. Teo, B. *J. Chem. Thermodyn.* **19**, 369–375 (1987).

255. Sirotina, A. P., Callaert, C., Volykhov, A. A. & Frolov, A. S. *The J. Phys. Chem.* C **123**, 26201-26210 (2019).

256. Thonhauser, T., Jeon, G. S., Mahan, G. D. & Sofo, J. O. *Phys. Rev. B* **68**, 205207 (2003).

257. Wang, J.-J. *et al. Chem. Mater.* **30**, 4770–4777 (2018).

258. Mansour, A. N. *et al. J. Appl. Phys.* **116**, 083513 (2014).

259. Adenis, C., Langer, V. & Lindqvist, O. *Acta Crystallogr. Sect. C Cryst. Struct. Commun.* **45**, 941–942 (1989).

260. Kolb, A. N. D. *et al. ACS Appl. Electron. Mater.* **1**, 701–710 (2019).

261. Yashina, L. V., Kobeleva, S. P., Shatalova, T. B., Zlomanov, V. P. & Shtanov, V. I. *Solid State Ionics* **141**–**142**, 513–522 (2001).

262. Sánchez-Barriga, J. *et al. Phys. Chem. Chem. Phys.* **19**, 30520–30532 (2017).

263. Wang, Y. *et al. Nat. Commun.* **8**, 6–11 (2017).

264. Yokoyama, T. & Murakami, S. *Phys. E Low-Dimensional Syst. Nanostructures* **55**, 1–8 (2014).

265. Shelford, L. R. *et al. Phys. Rev. B* **86**, 081304 (2012).

266. Scholz, M. R. *et al. Phys. status solidi - Rapid Res. Lett.* **7**, 139–141 (2013).

267. Chen, Y. L. *et al. Science.* **329**, 659–662 (2010).

268. Eelbo, T. *et al. Phys. Rev. B* **104424**, 1–6 (2014).

269. Abdalla, L. B., Seixas, L., Schmidt, T. M., Miwa, R. H. & Fazzio, A. *Phys. Rev. B - Condens. Matter Mater. Phys.* **88**, 1–12 (2013).

270. Honolka, J. *et al. Phys. Rev. Lett.* **108**, 256811 (2012).

271. Manna, S. *et al. Nat. Commun.* **8**, 14074 (2017).

272. Kim, J. *et al.* Restoration of Topological Surface State by Vacuum Annealing in Magnetically Doped Topological Insulator. *ArXiv* 1-29 (2017).

273. Eastman, D. E., Himpsel, F. J. & Knapp, J. A. *Phys. Rev. Lett.* **44**, 95–98 (1980).

274. Santoni, A. & Himpsel, F. J. *Phys. Rev. B* **43**, 1305–1312 (1991).

275. Gerhardt, U., Maetz, C. J., Schütz, A. & Dietz, E. *J. Magn. Magn. Mater.* **15**–**18**, 1141–1142 (1980).

276. Ju, L. *et al.* **28**, 173–178 (2015).

277. Polyakov, A. *et al. Phys. Rev. B* **92**, 045423 (2015).

278. Manna, S. *et al. Nat. Commun.* **8**, 14074 (2017).

279. Fu, L. & Kane, C. L. *Phys. Rev. Lett.* **100**, 096407 (2008).

280. Esaki, L. *J. Phys. Soc. Japan* **21**, 589 (1966).

281. Tsu, R., Howard, W. E. & Esaki, L. *Phys. Rev.* **172**, 779–788 (1968).

282. Weintraub, L. *et al. J. Nanomater.* **2014**, 1–7 (2014).

283. Sootsman, J. R., Chung, D. Y. & Kanatzidis, M. G. *Angew. Chemie - Int. Ed.* **48**, 8616–8639 (2009).

284. Bayikadi, K. S. *et al. J. Mater. Chem. A* **7**, 15181–15189 (2019).

285. Medlin, D. L. & Snyder, G. J. *Curr. Opin. Colloid Interface Sci.* **14**, 226–235 (2009).

286. Lee, H. S. *et al. Acta Mater.* **91**, 83–90 (2015).

287. Vermeulen, P. A., Kumar, A., ten Brink, G. H., Blake, G. R. & Kooi, B. J. *Cryst. Growth Des.* **16**, 5915–5922 (2016).

288. Snykers, M., Delavignette, P. & Amelinckx, S. *Mater. Res. Bull.* **7**, 831–840 (1972).

289. Nukala, P. *et al. Nat. Commun.* **8**, 1–9 (2017).

290. Pawley, G. S., Cochran, W., Cowley, R. A. & Dolling, G. *Phys. Rev. Lett.* **17**, 753–755 (1966).

291. Kriegner, D. *et al. Crystals* **9**, 335 (2019).

292. Bruns, G. *et al. Appl. Phys. Lett.* **95**, 043108 (2009).

293. Wiedemeier, H. & Siemers, P. A. *Zeitschrift für Anorg. und Allg. Chemie* **431**, 299–304 (1977).

294. Picozzi, S. *Front. Phys.* **2**, 1–5 (2014).

295. Di Sante, D., Barone, P., Bertacco, R. & Picozzi, S. *Adv. Mater.* **25**, 509–513 (2013).

296. Liebmann, M. *et al. Adv. Mater.* **28**, 560–565 (2016).

297. Elmers, H. J. *et al. Phys. Rev. B* **94**, 201403 (2016).

298. Krempaský, J. *et al. Phys. Rev. B* **94**, 205111 (2016).

299. Krempaský, J., Springholz, G., Minár, J. & Dil, J. H. α-GeTe and (GeMn)Te semiconductors: A new paradigm for spintronics in *AIP Conference Proceedings* **1996**, 020026 (2018).

300. Chen, I.-W. Dielectric and Ferroelectric Ceramics: Interfaces in *Encyclopedia of Materials: Science and Technology* 2152–2157 (Elsevier, 2001).

301. Edwards, A. H. *et al. J. Phys. Condens. Matter* **17**, L329–L335 (2005).

302. Edwards, A. *et al. Phys. Rev. B* **73**, 045210 (2006).

303. Kalinin, S. V., Morozovska, A. N., Chen, L. Q. & Rodriguez, B. J. *Reports Prog. Phys.* **73**,

056502 (2010).

304. Pérez, R., García, J. E., Albareda, A., Gomis, V. & Ochoa, D. A. *Mech. Mater.* **42**, 374–382 (2010).

305. Hahn, T. & Klapper, H. Twinning of crystals in *International Tables for Crystallography Volume D: Physical properties of crystals* (ed. Authier, A.) 393–448 (Springer Netherlands, 2003).

306. De Backer, A., van den Bos, K. H. W., Van den Broek, W., Sijbers, J. & Van Aert, S. *Ultramicroscopy* **171**, 104–116 (2016).

307. Bednyakov, P. S., Sturman, B. I., Sluka, T., Tagantsev, A. K. & Yudin, P. V. *npj Comput. Mater.* **4**, 65 (2018).

308. Sist, M., Kasai, H., Hedegaard, E. M. J. & Iversen, B. B. *Phys. Rev. B* **97**, 094116 (2018).

309. He, L. & Vanderbilt, D. *Phys. Rev. B* **68**, 134103 (2003).

310. Sharma, P. *et al. Sci. Adv.* **3**, 1–9 (2017).

311. Koch, E. Twinning in *International Tables for Crystallography Volume C: Mathematical, physical and chemical tables* (ed. Prince, E.) 10–14 (Springer Netherlands, 2004).

312. Guloy, A. M. Polar Intermetallics and Zintl Phases along the Zintl Border in *Inorganic Chemistry in Focus III* (eds. Meyer, G., Naumann, D. & Wesemann, L.) 157–171 (Wiley-VCH Verlag GmbH & Co. KGaA, 2006).

313. Stoloff, N. S. Intermetallics: Mechanical Properties in *Encyclopedia of Materials: Science and Technology* **2**, 4213–4225 (Elsevier, 2001).

314. Rohrer, F. E., Lind, H., Eriksson, L. & Lidin, S. *Zeitschrift fur Krist.* **216**, 190–198 (2001).

315. Ye, H. Q. & Amelinckx, S. *J. Solid State Chem.* **61**, 8–39 (1986).

316. Li, W., Li, Y., Ma, X. & Zhang, Z. *Mater. Chem. Phys.* **148**, 490–493 (2014).

317. De Ridder, R., Van Tendeloo, G. & Amelinckx, S. *Phys. Status Solidi* **30**, 99–101 (1975).

318. Fredrickson, D. C., Lee, S. & Hoffmann, R. *Inorg. Chem.* **43**, 6159–6167 (2004).

319. Fredrickson, D. C., Lee, S., Hoffmann, R. & Lin, J. *Inorg. Chem.* **43**, 6151–6158 (2004).

320. Lange, H., Migas, D. B., Shaposhnikov, V. L., Dorozhkin, N. N. & Borisenko, V. E. *Phys. Rev. B - Condens. Matter Mater. Phys.* **60**, 16494–16498 (1999).

321. Wolf, W., Bihlmayer, G. & Blügel, S. *Phys. Rev. B* **55**, 6918–6926 (1997).

322. Pecheur, P. & Toussaint, G. *MRS Proc.* **234**, 157 (1991).

323. Migas, D. B., Miglio, L., Shaposhnikov, V. L. & Borisenko, V. E. *Phys. status solidi* **231**, 171–180 (2002).

324. Imai, Y. & Watanabe, A. *Intermetallics* **13**, 233–241 (2005).

325. Kishida, K., Ishida, A., Tanaka, K. & Inui, H. *Mater. Sci. Forum* **561**–**565**, 463–466 (2007).

326. Barczak, S. A. *et al. J. Solid State Chem.* **227**, 55–59 (2015).

327. Higgins, J. M., Schmitt, A. L., Guzei, I. A. & Jin, S. *J. Am. Chem. Soc.* **130**, 16086–16094 (2008).

328. Heremans, J. & Dresselhaus, M. *Thermoelectr. Handb.* **48**, 39-1-39–24 (2005).

329. Yannello, V. J. & Fredrickson, D. C. *Inorg. Chem.* **53**, 10627–10631 (2014).

330. Yannello, V. J. & Fredrickson, D. C. *Inorg. Chem.* **54**, 11385–11398 (2015).

331. Lu, E. & Fredrickson, D. C. *Inorg. Chem.* **58**, 4063–4066 (2019).

332. Deshpande, V. T. & Sirdeshmukh, D. B. *Acta Crystallogr.* **15**, 294–295 (1962).

333. Gerasimov, K. . & Pavlov, S. . *Intermetallics* **8**, 451–452 (2000).

334. Sato, N., Ouchi, H., Takagiwa, Y. & Kimura, K. *Chem. Mater.* **28**, 529–533 (2016).

335. Schwomma, 0., Nowotny, H. & Wittmann, A. *Monatshefte für Chemie* **95**, 1538–1543 (1964).

336. Poutcharovsky, D. L. & Parthe, E. *Acta Crystallogr. B* **30**, 2692–2696 (1974).

337. Rohrer, F. E., Lind, H., Eriksson, L., Larsson, A. K. & Lidin, S. *Zeitschrift fur Krist.* **215**, 650–660 (2000).

338. De Ridder, R., van Tendeloo, G. & Amelinckx, S. *Phys. Status Solidi* **33**, 383–393 (1976).

339. De Ridder, R. & Amelinckx, S. *Mater. Res. Bull.* **6**, 1223–1234 (1971).

340. Han, J. *et al. Phys. Rev. Lett.* **119**, 077702 (2017).

341. Pai, C. F., Mann, M., Tan, A. J. & Beach, G. S. D. *Phys. Rev. B* **93**, 1–7 (2016).

Scientific contributions

Published publications

- **Callaert Carolien**, Bercx Marnik, Lamoen Dirk, Hadermann Joke, *Interstitial defects in the van der Waals gap of Bi_2Se_3*, Acta Crystallographica B, Structural Crystallography and Crystal Chemistry B75 (2019), p.717-732.

- Sirotina Anna, **Callaert Carolien**, Volykhov Andrey, Frolov Alexander, Sánchez-Barriga Jaime, Knop-Gericke Axel, Hadermann Joke, Yashina Lada, *Mechanistic Studies of Gas Reactions With Multicomponent Solids: What Can We Learn by Combining NAP XPS and Atomic Resolution STEM/EDX?,* Journal of Physical Chemistry C 123 (2019), p.26201-26210.

- Volykhov Andrey A., Sanchez-Barriga Jaime, Batuk Maria, **Callaert Carolien**, Hadermann Joke, Sirotina Anna P., Neudachina Vera S.,Belova Alina I., Vladimirova Nadezhda V., Tamm Marina E., Khmelevsky Nikolay O., Escudero Carlos, Perez-Dieste Virginia, Knop-Gericke Axel, Yashina Lada V., *Can surface reactivity of mixed crystals be predicted from their counterparts? A case study of topological insulators*, Journal of materials chemistry C : materials for optical and electronic devices 6 (2018), p.8941-8949.

- Sanchez-Barriga Jaime, Aguilera Irene, Yashina Lada V, Tsukanova D. Y., Freyse Friedrich, Chaika Alexander N., **Callaert Carolien,** Abakumov Artem M., Hadermann Joke, Varykhalov Andrei, Rienks Emile D. L., Bihlmayer Gustav, Blugel Stefan, Rader Oliver, *Anomalous behavior of the electronic structure of across the quantum phase transition from topological to trivial insulator*, Physical review B 98 (2018), p. 235110-1 - 235110-9.

- Verchenko Valeriy Yu., Wei Zheng, Tsirlin Alexander A., **Callaert Carolien**, Jesche Anton, Hadermann Joke, Dikarev Evgeny V., Shevelkov Andrei V., *Crystal growth of the Nowotny chimney ladder phase : exploring new Fe-based narrow-gap semiconductor with promising thermoelectric performance*, Chemistry of materials 29 (2017), p.9954-9963.

- Sánchez-Barriga Jaime, Ogorodnikov Ilya I., Kuznetsov Mikhail V., Volykhov Andrey A., Matsui Fumihiko, **Callaert Carolien**, Hadermann Joke, Verbitskiy Nikolay I., Koch Roland J., Varykhalov Andrei, Rader Oliver, Yashina Lada V., *Observation of hidden atomic order at the interface between Fe and topological insulator* , Physical chemistry, chemical physics 19 (2017), p.30520-30532.

Submitted publications

- Tunca Bensu, Lapauw Thomas, **Callaert Carolien**, Hadermann Joke, Delville Remi, Caspi El'ad N., Dahlqvist Martin, Rosén Johanna, Amalraj Marshal, Pradeep Konda G., Schneider Jochen M., Vleugels Jozef, Lambrinou Konstantina *Compatibility of Zr2AlC MAX phase-based ceramics with oxygen-poor, static liquid lead-bismuth eutectic,* submitted to Corrosion Science.

Posters

- Local structure in Bi_2Se_3:In using transmission electron microscopy on the BCS-9, organized by National Committee for Crystallography, at Academy House, Hertogsstraat 1, 1000 Brussels.

- Local structure in Bi_2Se_3:In using transmission electron microscopy on RBSM Golden Jubilee Meeting, organized by Royal Belgian Society of Microscopy, at Palais des Académies, Brussels.

Presentation

- Local structure in Bi_2Se_3:In using transmission electron microscopy on the BCS-9, organized by National Committee for Crystallography, at Academy House, Hertogsstraat 1, 1000 Brussels.

Acknowledgement

First and foremost, I want to thank my promoter Prof. Joke Hadermann for the opportunity to perform this thesis and for her guidance not only during my PhD but also during my bachelor and master thesis. During the latter she stayed until late to give me enough time to perform my experiment. She taught me the basic steps to align a microscope and how to perform selected area electron diffraction. She was always available in case I needed help or had questions. I also want to thank my co-promoter Prof. Dirk Lamoen who helped me a lot during the density functional calculations and was always (even until quite late) available for many discussions.

I also want to thank the members of my PhD committee Prof. Bart Partoens, Prof. Wim Wenseleers, Prof. Lada Yashina and Prof. Simon Clarke who found the time in their busy schedules to read my thesis.

I want to express my gratitude to the group of Prof. Lada Yashina who made most of my samples. The samples were really nicely produced and interesting. Furthermore, I want to thank the group of Prof. Andrei Shevelkov who made the Fe_2Ge_3 sample and Prof. Artem Abakumov for Bi_2Se_3.

I want to thank all my EMAT colleagues: Prof. Altantzis, Prof. Abakumov, Prof. Bals, Prof. Hadermann, Prof. Hosni, Prof. Lamoen, Prof. Pennycook, Prof. Schryvers, Prof. Van Dyck, Prof. Van Tendeloo, Prof. Verbeeck, Aäron, Abner, Adrián, Alania, Alexander M., Alexander N., Alexander S., Andrey, Annelies, Annick, Antonios, Armand, Bárbara, Bart, Behnam, Chen, Da, Daen, Daniel, Daniele, Dileep, Dmitry, Ece, Eva, Evangelia, Frédéric, Gerardo, Giulio, Gizem, Gunnar, Hamed, Hans, Ivan, Jarmo, Kirsten, Julie, Kadir, Kai, Karel, Koen, Kristof, Laura, Lien, Liesbet, Lipeng, Lucian, Lydia, Magnus, Maria B., Maria F., Maria M., Marnik, Martin, Mert, Miek, Mikhail, Mylène, Naomi, Nathalie, Nesli, Nico, Nicolaas, Niels, Olesia, Pei, Qiongyang, Ricardo, Robert, Roeland, Ruben, Saeid, Shanshan, Shyam, Silvia, Stijn, Stuart, Svetlana, Thais, Thomas, Tine, Tom, Ursula, Vahid, Vivek, Wiebke, Xiayang, Yang, Zezhong and Zhi-Yi. I want to especially express my gratitude to my colleagues who were also guided by Prof. Joke and Prof. Lamoen, who helped me and with whom I had many scientific and non-scientific discussions: Robert, Olesia, Maria, Marnik and Mylène. Furthermore, I want to thank Barbara, Olesia, Maria, Mylène, Nathalie, Saied, Thais and Vahid, most of them were my former office mates, who were there to support me during the difficult times in my four year journey and with whom I also enjoyed lots of nice conversations.

I also want to express my thanks to Iris Van Camp, a physics- and math teacher during high school, who was the cause of my interest in physics, without her knowing. Without that interest, I would not be where I am today.

I also want to thank my parents Dirk Callaert and Claudine Van Mele, my older sister Karen Callaert and her partner Kristof Galle for their support all these years. I know I can count on them if I need it. Finally I want to thank my fiancé Gunnar Lumbeeck, who stayed by my side and supported me during the PhD and during my university studies. For example, he kept me company during my way past midnight Friday evening sessions which I often took, even though he is definitely a morning person. He accompanied me during the good and the crazy days, and I hope he will keep on doing this for the rest of my life.